N° d'ordre : 2562

THESE

présentée pour obtenir le titre de

DOCTEUR DE L'INSTITUT NATIONAL POLYTECHNIQUE DE TOULOUSE

École doctorale : Mécanique, Energétique, Génie Civil, Procédés

Spécialité : Génie des Procédés et de l'Environnement

and

submitted in fulfilment of the requirements for the degree of

DOCTOR OF PHILOSOPHY

School of Chemical and Biomolecular Engineering

The University of Sydney

by

Jean-Philippe TORRÉ

QUENCHING RUNAWAY REACTIONS:

HYDRODYNAMICS AND JET INJECTION STUDIES

FOR AGITATED REACTORS WITH A DEFORMED FREE-SURFACE

Thesis presentation: 6th December 2007, Toulouse, France

BERTRAND J.	Directeur de Recherches CNRS, Université de Toulouse, INPT, LGC, France	Jury President
BRANLY M.	Industrial Development Manager, Tessenderlo Group, Mazingarbe, France	Jury Member
FLETCHER D. F.	Adjunct Associate Professor, The University of Sydney, Australia	Jury Member
HAYNES B. S.	Professor, The University of Sydney (USYD), Australia	Internal USYD Examiner
HUERRE P.	Directeur de Recherches CNRS, LadHyX, Ecole Polytechnique, Palaiseau, France	Rapporteur
LASUYE T.	PVC Synthesis and Process Research Manager, Tessenderlo Group, Mazingarbe, France	Jury Member
MAVROS P.	Professor, Aristotle University, Greece	Rapporteur
XUEREB C.	Directeur de Recherches CNRS, Université de Toulouse, INPT, LGC, France	Jury Member

ABSTRACT

To quench a thermal runaway reaction in a chemical rector, an efficient approach is the introduction of a small quantity of a liquid inhibiting agent, named a "killer", into the mixing vessel. In this thesis, an experimental approach has been coupled tightly with numerical modelling using Computational Fluid Dynamics (CFD). The first part of this thesis is devoted to a study of the hydrodynamics of partially-baffled mixing vessels, including the free-surface deformation caused by the central vortex. The use of an inhomogeneous, multiphase approach allowed simulation of the free-surface deformation. The capability of this novel method was demonstrated by very good agreement between the numerical predictions and experimental data. In the second part, liquid jet injection at the free-surface was coupled with the vessel hydrodynamics. Numerical results, obtained using an Eulerian-Lagrangian approach, have again shown good agreement with experimental data. These results allowed the jet trajectory to be modelled and its penetration into the agitated vessel was quantified. New mixing criteria were introduced that are specific to this application. Finally, the numerical methods validated at the pilot scale were applied at the industrial scale and allowed the proposal of practical improvements to the safety of the synthesis reactors studied.

Key words: Agitation and mixing; Computational Fluid Dynamics (CFD); Partially-baffled agitated vessel; Free-surface; Particle Image Velocimetry (PIV); Jet injection; Thermal runaway; S-PVC.

RESUME

Pour stopper un emballement thermique dans un réacteur chimique, un moyen efficace consiste à introduire une faible quantité d'un inhibiteur liquide appelé « killer » dans la cuve agitée. Tout au long de cette thèse, l'approche expérimentale a été fortement couplée à la modélisation numérique par Computational Fluid Dynamics (CFD). La première partie du manuscrit porte sur l'hydrodynamique des réacteurs partiellement chicanés incluant la prise en compte du vortex central qui se forme à leur surface. L'utilisation d'une approche numérique multiphasique, non-homogène a permis de modéliser la déformation de la surface-libre, et la faisabilité de cette méthode innovante a été démontrée par un très bon accord entre prédictions numériques et données expérimentales. Dans une deuxième partie, l'introduction d'un jet de liquide sur la surface libre a été couplée à l'hydrodynamique du réacteur. Les résultats numériques, obtenus avec une approche Eulerienne-Lagrangienne, ont également montré un bon accord avec les données expérimentales. Ces résultats ont permis de modéliser la trajectoire du jet, de quantifier sa pénétration dans la cuve agitée, et de définir de nouveaux critères de mélange. Enfin, les méthodes numériques validées à l'échelle pilote ont été étendues à l'échelle industrielle et ont permis de proposer des améliorations concrètes pour une meilleure sécurité des réacteurs industriels étudiés.

Mot clés: Agitation et mélange; Mécanique des fluides numérique (CFD); Cuve agitée partiellement chicanée; surface libre; Vélocimétrie par images de particules (PIV); Jet ; Emballement thermique; S-PVC.

La recherche est un métier de passion, à exercer avec passion, ou à ne pas choisir.

Research is a career you should love and carry out with enthusiasm, or do something else.

Albert Szent-Györgyi

Rien n'est impossible, ça prend juste plus longtemps.

Nothing is impossible, it just takes time.

Philo T. Farnsworth

ACKNOWLEDGEMENTS

LIST OF PAPERS

Journal papers

o **Torré, J.P.**, Fletcher, D.F., Lasuye, T. and Xuereb, C. (2008). An experimental and CFD study of liquid jet injection into a partially-baffled mixing vessel: a contribution to process safety by improving the quenching of runaway reactions. *Chemical Engineering Science*, 63, 924-942.

o **Torré, J.P.**, Fletcher, D.F., Lasuye, T. and Xuereb, C. (2007c). Single and multiphase CFD approaches for modelling partially-baffled stirred vessels: comparison of experimental data with numerical predictions. *Chemical Engineering Science*, 62(22), 6246-6262.

o **Torré, J.P.**, Fletcher, D.F., Lasuye, T. and Xuereb, C. (2007b). Transient hydrodynamics and free surface capture of an under-baffled stirred tank during stopping. *Chemical Engineering Research and Design*, 85(A5), 1-11.

o **Torré, J.P.**, Fletcher, D.F., Lasuye, T. and Xuereb, C. (2007a). An experimental and computational study of the vortex shape in a partially baffled agitated vessel. *Chemical Engineering Science*, 62(7), 1915-1926.

Conference papers

o **Torré, J.P.**, Fletcher, D.F., Lasuye, T., Triopon, S. and Xuereb, C. (2007). Hydrodynamics and quenching of PVC synthesis reactors. *Proc. of ECVM Annual Health, Safety & Environment Conference*, 7-8 June 2007, Lille, France.

o **Torré, J.P.**, Fletcher, D.F., Lasuye, T. and Xuereb, C. (2006b). CFD modelling of partially baffled agitated vessels with free surfaces. *Proc. Fifth International Conf. on CFD in the Process Industries*, CSIRO, 13-15 December 2006, Melbourne, Australia.

The author was awarded the prize for *Best Student Paper* at the above conference.

o **Torré, J.P.**, Fletcher, D.F., Lasuye, T. and Xuereb, C. (2006a). Transient hydrodynamics of a stirred tank during stopping, *Proc. of the 12th European Conference on Mixing*, 27-30 June 2006, Bologna, 551-558.

CONTENTS

NOTATION

A, B, C, D, E	notation factors for DoE
A, B, C	characteristic points on power curves of industrial reactors
A_b	projected agitator blade surface, m²
A_1, A_2, B	coefficients of the jet trajectory correlation, (-)
B'	distance baffle – reactor, m
B_l	baffles length, m
B_t	baffle thickness, m
B_w	baffle width, m
b_{ij}	Reynolds stress anisotropy tensor in the SSG model
C	scalar concentration, (-)
C	centre point of the experimental domain (for DoE)
C_D	drag coefficient, (-)
C_{inf}	scalar equilibrium concentration at infinite time, (-)
C_{min}	minimum concentration of stopper to quench the reaction, (-)
C^*	normalised stopper concentration (= C/C_{min}), (-)
C^*_{min}	normalized minimum concentration necessary to quench the reaction (=C_{min}/C_{inf}), (-)
$C_{\varepsilon 1}$	k-ε model constant, (-)
$C_{\varepsilon 2}$	k-ε model constant, (-)
C_μ	k-ε model constant, (-)
c	agitator clearance, m
D	agitator diameter, m
D_p	diameter of the control volume (used in pumping capacity calculation), m
d	injection pipe diameter, jet diameter, m
d_b	bubble diameter, m
df	degree of freedom (for DoE)
DoE	abbreviation for Design of Experiments
d_{32}	Sauter mean bubble diameter, m
d_{50}	mean particle diameter of PVC resin, m

D_ϕ^{lam}	kinematic diffusivity of the scalar, m²/s
D^{turb}	turbulent diffusivity, m²/s
e	residual (for DoE)
F	scale-up factor, (-)
Fr	Froude number (= ND^2/g), (-)
f_s	FFT sampling frequency, Hz
G	gain value of the IRIS image treatment software, (-)
g, g	acceleration due to gravity, m s^{-2}
H_d	bottom dish height, mm
H_{init}	initial water level used in the experiments, m
H_{liq}	liquid height, m
H_{max}	maximum tank height, m
H_p	jet penetration depth, m
H_p^*	dimensionless jet penetration depth, (-)
$H_{PIV, min}$	bottom height of the PIV plane, m
$H_{PIV, max}$	top height of the PIV plane, m
H^*	normalized vessel height, (-)
I	agitator motor current, A
I	initial injection point (for DoE)
I_G	agitation index, %
i, j	indecies (for DoE)
K	constant in the dimensionless mixing time law, (-)
k	turbulent kinetic energy, m^2 s^{-2}
k	number of experimental factors (for DoE)
L_{vK}	von Karman length scale, m
L_t	turbulent length, m
M	jet momentum flux, kg m s^{-2}
M$_{gl}$	drag force per unit volume, N m^{-3}
M$_{ip}$	interfacial force per unit volume, N m^{-3}
MS	mean square (for DoE)
MSE	mean squared error (for DoE)
N	agitator rotation speed, RPM or s^{-1}
N_F	number of frames superimposed during the imaging process, (-)

N_m	initial impeller velocity before agitator stopping, RPM or s^{-1}
$N_{nom.}$	nominal agitator speed (Industrial Mazingarbe reactor), RPM or s^{-1}
N_p	agitator power number (=$P/(\rho N^3 D^5)$), (-)
N_q	agitator pumping number, (=$Q_p/(ND^3)$), (-)
N_r	number of agitator revolutions, (-)
N_{r1}	minimum number of agitator rotations to reach the quasi-steady state, (-)
N_{r2}	minimum number of agitator rotations to obtain meaningful statistics, (-)
n	number of experimental runs (for DoE)
n_b	number of agitator blades, (-)
n_B	number of baffles, (-)
P	injection pressure, bar relative
$\tilde{P}$	turbulence energy production, kg m^{-1} s^{-3}
P	shear production term, kg m^{-1} s^{-3}
P	power consumption, W
p	pressure, Pa
p', p"	modified pressure, Pa
Q_p	agitator pumping flow rate, m^3/s
R	mixing vessel radius, m
R	effective velocity ratio (R = u_j / u_{cf}), (-)
R_a	agitator radius, m
R_b	agitator blade projected length, m
R²	statistical indicator for fitting methods (%)
Re	Reynolds number, Re = $\rho_l ND^2 / \mu_l$, (-)
Re_p	Particle Reynolds number, $Re_p = \rho_l d_b \lvert u_g - u_l \rvert / \mu_l$, (-)
r	radial coordinate
S	sum of squares (for DoE)
Sc^{turb}	turbulent Schmidt number, (= (μ^{turb}/ρ) / D^{turb}), (-)
S_{ij}	mean rate of strain tensor in the SSG model
T	tank diameter, m
T	bulk reactor temperature, °C
T_{inj}	time at the end of jet injection, s
T_m	mixing time, s
T_o	impeller torque, Nm

t	time, s
t_b	agitator blade thickness, m
t_{50}	the time required to quench 50% of the vessel volume, s
t_{90}	the time required to quench 90% of the vessel volume, s
U_a	axial velocity, m s^{-1}
U_r	radial velocity, m s^{-1}
U_a*	normalized axial velocity (= U_a/U_{tip}), (-)
U_{ar}	axial-radial velocity, m s^{-1}
$U_{ar}*$	normalized axial-radial velocity (=$(U_a^2+U_r^2)^{0.5}/U_{tip}$), (-)
U_{tip}	impeller tip velocity (=πND), m s^{-1}
U_{ijk}	liquid speed, m s^{-1}
$U*_{ijk}$	liquid speed normalized by the tip speed, (-)
$\langle U \rangle$	volume averaged velocity, m s^{-1}
$\langle U_o \rangle$	initial volume averaged velocity, m s^{-1}
u	Cartesian velocity component of the liquid velocity, m s^{-1}
u	velocity, m s^{-1}
u'	velocity fluctuation, m s^{-1}
u_{cf}	cross-flow velocity (for jet in cross-flow), m s^{-1}
u_j	jet velocity (for jet in cross-flow), m s^{-1}
$\vec{u}(\underline{x}, t)$	local velocity of the liquid, m s^{-1}
V	jet velocity, m s^{-1}
V_i	injected volume, m^3
V_{ijk}	volume of liquid in the cell with coordinates i j k, m^3
V_o	current industrial jet velocity, m s^{-1}
V1, V2, V3	experimental validation points for DoE
v	Cartesian velocity component of the liquid velocity, m s^{-1}
W_{ij}	mean vorticity tensor in the SSG model
w	Cartesian velocity component of the liquid velocity, m s^{-1}
w_b	agitator blade width, m
X, Y	Cartesian coordinates for the injection location (for DoE)
X, Y, Z	reference frame directions
X_o, Y_o, Z_o	coordinates of the injection point, m
X^*, Y^*, Z^*	coordinates in the transformed reference frame

X_j	X coordinate of the jet centre, m
X	standard notation factor (for DoE)
x	generic variable for mathematical function definitions
$\underline{x}$	local position of a tracer particle (PIV), m
Y	axial coordinate
Y	standard notation response (for DoE)
$\hat{Y}$	predicted value of the response obtained by the DoE model
Z_{FFT}	number of samples collected for the FFT, (-)
Z_j	Z coordinate of the jet centre, m

Greek letters

α	volume fraction, (-)
Δt	time interval, s
$\Delta \vec{x}$	displacement of a tracer particle (PIV) during time Δt, m
ε	dissipation rate of turbulent energy per unit volume, $m^2\ s^{-3}$
ε	experimental error (for DoE)
Φ_B	fully-baffled criterion, (-)
ϕ	scalar variable, (-)
ϕ_{ij}	pressure-strain correlation in the SSG model, $kg\ m^{-1}\ s^{-3}$
φ	current-tension phase angle, °
κ	von Karman constant ($\kappa = 0.41$), (-)
η	agitator motor efficiency, %
λ	wavelength, nm
λ_{cut}	cut wavelength for the high pass filer of the PIV camera, nm
μ	dynamic viscosity, $kg\ m^{-1}\ s^{-1}$
θ	agitator retreat angle, degrees
ρ	density, $kg\ m^{-3}$
σ	standard deviation
σ_k	k-ε model constant, (-)
σ_ε	k-ε model constant, (-)
Ψ_{90}	scale-up criterion for optimal jet velocity (=M_a/M_j), (-)

Subscripts

A, B, C	relative to the points *A*, *B* and *C* on industrial power curves
a	agitator
exp	experimental
g	gas phase
i	interfacial
i j k	relative to the Cartesian coordinates i, j, k
i j	relative to the i and j indexes used for DoE
ind	industrial scale
j	jet
l	liquid phase
lab	laboratory (pilot) scale
m	mean
mod	modelling
opt	optimal
p	phase index

Superscripts

BEEK	Beek industrial reactor
CFD	numerical
eff	effective
exp	experimental
in	directed toward the interior of the agitator control volume
lam	laminar
MAX	configuration with the baffles in maximal perturbation
MIN	configuration with the baffles in minimal perturbation
MZG	Mazingarbe industrial reactor
out	directed towards the exterior of the agitator control volume
T	matrix transposition
t	threshold
turb	turbulent
+	in the same direction as the direction considered

-                         in the opposite direction to the direction considered

Mathematical functions

f( )   generic mathematical function

$\xi(x)$ filter function in the agitation index definition

H(x)   Heaviside function

Other symbols

(-)   dimensionless

Chapter 1

INTRODUCTION AND OUTLINE

"What does society need; what are the desirable outcomes and how can chemical engineers work in partnership with others to make it happen?" These difficult questions start the *Roadmap of 21st Century Chemical Engineering* published in 2007 by the Institution of Chemical Engineers (IChemE). Twenty priority tasks, included in six key themes were defined as the basis of the most important issues of Chemical Engineering for the 21st century. Health, Safety, Environment and Public Perception of Risk is one of the major outcomes for the future.

Thermal runaway remains a problem in the process industries with poor or inadequate mixing contributing significantly to these incidents. The consequences of such accidents (loss of containment, destruction of buildings, toxic releases, etc) are very dangerous for plant workers, the environment, the production process and the surrounding plant. An efficient way to quench such an uncontrolled chemical reaction is via the injection of a liquid jet containing a small quantity of a very active inhibiting agent (often called a "killer") that must be mixed into the bulk of the fluid to quench the reaction. Despite its efficacy, there exists a lack of published information concerning this injection system, particularly its mixing efficiency and factors affecting the distribution of the inhibitor within the bulk.

The studies carried out in this thesis were motivated initially from a request made by Tessenderlo Group, the 6th largest manufacturer of PVC in Europe in 2007. As the PVC polymerization reaction is strongly exothermic, runaway conditions can create hot spots and cause a dramatic increase in the vessel pressure. In November 2003, during a power shutdown in one of the PVC plants, pressure build up was noticed on most of the synthesis reactors despite the fact that the killer was dosed. On another occasion, a runaway reaction occurred although the agitator was functioning normally. As several important points remained poorly understood, in particular the hydrodynamics of the PVC synthesis reactors and the effects of agitation parameters on the killer mixing, this study was carried out.

Even if the guidelines of this work were inspired by the industrial case, the strategies adopted during this thesis were chosen to obtain results which serve the largest possible framework. A strong association between experimental and numerical work, using Computational Fluid Dynamics (CFD), has been maintained during the different studies carried out. On one hand, Computational Fluid Dynamics has become a powerful and promising tool that it is already a part of the future of engineering and academic research. In addition, the hazards associated with such runaway events mean that a validated CFD model would be extremely useful. On the other hand, the important growth of CFD methods and numerical models has generated the need for accurate experimental data to validate the predicted results. Therefore, a pilot installation, comprising a mixing vessel and an injection system designed in geometrical similarity with the industrial vessels, was used to visualize various phenomena (vortex shape, macro-instabilities, dead-zones, etc.) and to obtain quantitative experimental data such as mixing times, velocity fields (using Particle Image Velocimetry), jet trajectories in the mixing vessel, power input, etc. Concerning the numerical part of this work, all the simulation were performed with the commercial CFD code ANSYS-CFX, which solves the fluid flow equations using a finite volume method and a coupled solver. Numerous step-by-step comparisons between the experimental and numerical data allowed accurate models for the pilot reactor to be built by increasing progressively the complexity of the simulations carried out, to finally investigate the real industrial synthesis reactors.

The manuscript consists of fourteen Chapters (including this general introduction) which have their own literature review when needed. The following Chapters are outlined as follows:

Chapter 2 presents the background and industrial motivation of this thesis. A literature review of the quenching of runaway reactions starts the Chapter, and is followed by the reasons as to why Computational Fluid Dynamics is carried out for this study. Then, the experimental/numerical co-validation strategy followed during the remainder of the thesis is briefly discussed.

In Chapter 3, the experimental apparatus and the Particle Image Velocimetry technique are detailed.

After a literature review of unbaffled and partially-baffled agitated vessels, Chapter 4 presents an experimental and computational study of the vortex shape which develops in these partially-baffled mixing vessels.

In Chapter 5, a brief literature survey of the turbulence models used in CFD simulations of mixing vessels is given. Then, the results presented compare numerical predictions obtained in a transient manner using single and multiphase CFD approaches with experimental PIV data.

Chapter 6 extends the methods used in Chapters 4 and 5 to the study of hydrodynamics and free-surface shape in the same partially-baffled mixing vessel but during the agitator stopping phase and the inertial period after the agitator has stopped.

Chapter 7 is devoted to mixing time experiments, which were used in a large part to develop a mixing time model by using a Design of Experiment (DoE) approach. The Chapter starts with a brief literature review of the different techniques used for measuring the mixing time. Then, the DoE approach is presented, and is followed by the construction and use of the mixing time model.

Chapter 8 is the first chapter which considers the fluid jet injection on the flat free-surface of the partially-baffled stirred vessel studied in the previous Chapters. This Chapter presents CFD studies, complemented by experimental investigations.

Chapters 9 and 10 are devoted to the industrial application of this thesis. Chapter 9 presents the hydrodynamics, vortex shape, power input and pumping capacity of the industrial S-PVC synthesis reactors of Mazingarbe and Beek plants of Tessenderlo Group. In Chapter 10, one of the industrial vessels presented in Chapter 9 is studied numerically with jet injection of the killer. Current industrial injection conditions, quenching studies, scale-up tools and optimization proposals are discussed.

Chapter 11 is devoted to the analysis of the jet trajectories obtained using CFD at the pilot and industrial scales. The establishment of a general correlation to describe the jet trajectory and to quantify the penetration depth is presented.

Chapter 12 presents briefly two promising approaches in which only preliminary results were obtained during the course of this thesis: use of the SAS-SST turbulence model and a new way to simulate mixing vessels with a deformed free-surface.

Chapter 13 gives a summary of the results obtained, complemented by concluding remarks.

Finally, perspectives and recommendations for future work are given in Chapter 14.

Chapter 2

INDUSTRIAL MOTIVATION AND SCIENTIFIC STRATEGY

This Chapter presents a short literature survey of the quenching of runaway reactions in mixing vessels, particularly focussed on the quenching by jet injection. The use of Computational Fluid Dynamic (CFD) during this study is then discussed. As this PhD thesis was motivated by an industrial request concerning the suspension polymerization of Poly Vinyl Chloride (S-PVC), the industrial case is analysed to highlight the complexity of the whole problem and the key-points and guidelines of this study. Finally, the studies carried out and reported in this manuscript have been conducted with a strong interaction between experimental and numerical modelling (CFD) work. This co-validation strategy is presented at the end of this Chapter.

2.1. QUENCHING RUNAWAY REACTIONS BY JET INJECTIONS

Many reactions within the process industry are exothermic. When the heat generated by chemical reaction exceeds that removed by cooling, an uncontrolled increase of temperature can occur. This loss of control is termed a thermal runaway. In 2002, Balasubramanian and Louvar used several government and private sector-safety-related databases, in addition to other published safety resources, to review major accidents and summarized some lessons learned. The authors revealed, by determining the number of runaways resulting in a major incident in the chemical industries, that 26.5% of the major accidents in the petrochemical industries for the 40 year period from 1960 to 2000 were the result of runaway reactions. In the United States of America alone, a two year investigation of the Chemical Safety and Hazard Investigation Board (CSB) carried out in 2002 (U.S. CSB, 2003), using more than 40 different data sources (public-domain databases, technical literature and news accounts), examined 167 serious chemical accidents occurring from 1980 to 2002 that involved uncontrolled chemical reactions in the U.S.A. The report revealed that 35% of these accidents, which caused 108 deaths as well as hundreds of millions of dollars of property damage, were due to runaway reactions. Butcher and Eagles (2002) declared that on average around eight

runaway incidents a year occurred in the UK, with poor mixing being a significant contributor to these incidents. More precisely, an analysis of Barton and Nolan in 1989 of 189 incidents which occurred in industrial batch reactors in the UK chemical industry between 1962 and 1987 revealed that polymerization reactions account for almost 50% of the classified incidents for which there was a high potential for loss of control and runaway, as shown in Figure 2.1.

Process	Percentage
polymerizations (including condensations)	47.8%
Nitration	11.2%
Sulphonation	9.7%
Hydrolysis	7.5%
Salt formation	6.0%
Halogenation (Chlorination and Bromination)	6.0%
Alkylation usin Friedel and Crafts synthesis	3.7%
Amination	3.0%
Diazotisation	3.0%
Oxidation	1.5%
Esterification	0.7%
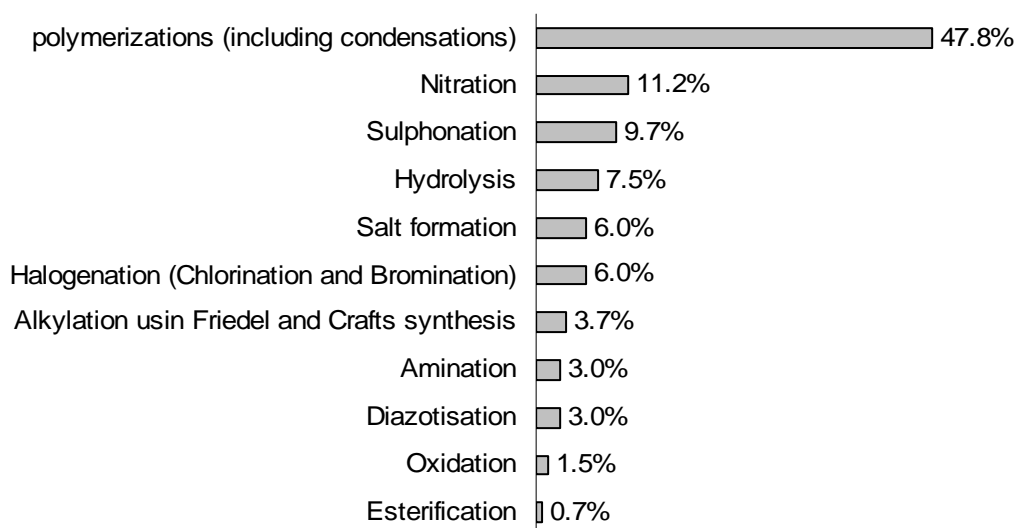
Figure 2.1. Percentage of incidents per specified chemical process involving thermal runaway (from the data of Barton and Nolan, 1989).

In the analysis presented in Figure 2.1, agitation problems were responsible for 10% of 169 incidents (20 incidents were not classified) which led to overheating and eventual thermal-runaway with the principle causes being:

- inadequate stirrer specification;
- mechanical failure (for example: stirrer blades sheared off due to the solidification of the residue from the previous batch; too powerful motor for the paddle securing bolts);
- operator either failed to switch on agitator or switched it on too late leading to reaction throughout the vessel;
- loss of power supply;
- agitator stopped by operator to make an addition.

In addition, the Health and Safety Executive reported that for Great Britain in the four year period from 1994 to 1998, 203 incidents involving exothermic runaway or thermal decompositions occurred, with the majority of these being due to the inadvertent mixing of

chemicals (Fowler and Hazeldean (1998), Fowler and Baxter (2000)). Etchells (1996), in a paper which explains why exothermic runaway is a cause of great concern, declared that in the 135 exothermic runaways incidents analysed from 1986 to 1991, inadequate agitation of reacting materials was significant (12% of the total incidents).

As analysed by Westerterp and Molga (2004), most of these runaway events caused at best loss and disruption of production and perhaps equipment damage, at worst they had the potential for a major accident that could affect not only the reactor itself but also represent a hazard for plant workers and the surrounding plant.

Despite the fact that much progress has been made to understand and limit such runaway reactions, this problem still occurs. According to Westerterp and Molga (2006), three "lines of defence" have to be considered to prevent a reactor incident: (a) the choice of the right operating conditions, (b) an early warning detection system, and (c) a suitable system to handle runaway reactions. Although the prevention of such accidents requires detailed knowledge of the reaction process, the "first two lines of defence" (items (a) and (b)) have received considerable attention (Etchells (1997), Gustin (1991), McIntosh and Nolan (2001), Westerterp and Molga (2006) and Zaldivar *et al.* (2003)) over the last 30 years following the accident that occurred in Seveso (Italy) in 1976, and are not discussed further here.

Concerning the quenching of an exothermic reaction once the runaway reaction is in progress, an efficient process to avoid runaway is the injection and the mixing of a small quantity of an efficient inhibiting agent (also called a "stopper" or "killer" in the polymer industry) into the bulk. These substances can act in several ways: (i) stopping the reaction by deactivating a catalyst (e.g. sulphides can irreversibly deactivate platinum of carbon catalysts); (ii) stopping a chain reaction by deactivating the active end of the expanding chain and preventing further propagation; (iii) stopping the reaction by providing an alternative reaction with one of the reactants that is not as energetic as the normal process (Rowe *et al.*, 1994).

This inhibition process is often associated with important mixing problems (McIntosh and Nolan (2001)). Particularly, the problem is worse after a breakdown of the agitation system (Platkowski and Reichert (1999)) due to the poor mixing which results from a decreasing agitation speed. The mixing of small quantities of very active substances in free-radical-

initiated reaction systems, such as for polymerisations products, foaming mixtures or highly viscous fluids, requires an injection system with optimal design and efficiency. Experimental studies which couple the quenching efficiency of the "killer" and hydrodynamics of both the stirred vessel and the injection system are rare in the literature. The problem is so-complex that the jet and the mixing vessel are often studied separately, as for example by Kammel *et al.* (1996), who studied bottom entering jet tracer injections using model fluids in a vessel without mechanical agitation. They found that the mixing time, $t_{m95\%}$, was dependent on the jet Reynolds number ($Re_j = v_j d_j \rho_j / \mu_j$) and the liquid height (filling ratio).

Related to jet injection, extensive research has also been undertaken to understand the physical phenomena that control by-product formation via competitive or consecutive reactions, conducted in turbulent mixing conditions. Although experiments are carried out with very low feed velocities, leading to laminar flow in the feed pipes, the studies of Baldyga *et al.* (1993) or Baldyga and Pohorecki (1995) discuss the processes of micro, meso and macromixing in the vessel where the flow is turbulent. Concerning high velocity feeds, Verschuren *et al.* (2001) provided a method for the calculation of the time-scale of turbulent dispersion of the feed stream introduced inside a stirred vessel. Recently, Bhattacharya and Kresta (2006) used a mixing-sensitive chemical reaction to analyse the effects of the feed time and the jet velocity on the performance of a reactor fed with a high velocity surface jet. Their theoretical analysis suggested that rapid convection of the reagents from the surface to the impeller swept region can potentially improve the performance, but their experimental results revealed otherwise.

A complete description of the different inhibition systems and the possible alternatives is reviewed by McIntosh and Nolan (2001) and is not repeated here. A jet injected at the surface of a stirred vessel can be used to quench an uncontrolled reaction for many reaction mixtures. McIntosh and Nolan (2001) highlighted that one of the main reasons that this system is not popular for industrial applications, despite its efficacy, is the lack of published information concerning the injection system, together with uncertainties over the mixing efficiency and distribution of the inhibitor within the bulk. The same conclusion was previously made by Rowe *et al.* (1994), who declared that the technique of reaction inhibition was a poorly researched topic. Mark *et al.* (1987) noted that few studies on the subject have been reported. Recently, in inhibition studies of the styrene polymerization reaction, Snee and Cusco (2005) stated that only limited guidance was available on the design of a reaction inhibition system,

with the main difficulty being the prediction of the rate of dispersion of the inhibitor in the full-size industrial reactor using the small-scale data. In summary, in 2007, one continues to note an important lack of published information concerning the inhibition process by jet injection.

Bhattacharya and Kresta (2006) concluded that the behaviour of a feed stream with more momentum than the ambient fluid is largely unknown, compounding the problems of this approach. In contrast, the stability and fragmentation of liquid jets has been studied extensively over the past one hundred and seventy years. Since the earliest investigations into jet flow phenomena, which appear to have been carried out by Bidone (1829) and Savart (1833), many studies have been performed on jet hydrodynamics, as reviewed by McCarthy and Molloy in 1974. As a detailed analysis of jet theory is not the aim of this thesis, the reader can consult Rajaratnam (1976) and more recently Pope (2000) and Sallam *et al.* (2002) for reviews of experimental results and theoretical developments concerning turbulent jets. Surprisingly, no studies were found in the literature concerning the trajectories of a fluid jet injected at the free-surface of an agitated vessel under batch operation conditions.

2.2. THE IMPORTANT ROLE OF CFD IN THIS STUDY

Over the years, mixing vessels have been widely used in the process industries to carry out various objectives, such as homogenization, gas dispersion, heat transfer, solid suspension, etc. Since the early studies on mixing vessels published by Rushton *et al.* (1950a, b) and Kramers *et al.* (1953) in the early 1950's, many studies have been carried out to investigate their characteristics under varying conditions. For mixing vessels, the knowledge of the hydrodynamics, and of local or global parameters which can be deduced (for example velocity fields, concentration fields, distribution of solids, gaseous retention, turbulent kinetic energy, energy dissipation, power input, etc.) is fundamental to the understanding of the physical phenomena involved. This allows better selection of the vessel geometry, the agitator model, as well as allowing a better choice of process conditions and the scale-up of the results. Particularly, the need for local flow information is increasing since many processes exhibit substantial spatial variation in, for example, bubble or drop size, crystal size, mixing rate, etc (Van den Akker, 2006). For an introduction (in French) to mixing vessels, see

Roustan *et al.* (1997) and Xuereb *et al.* (2006). In 2004, Paul *et al.* compiled in a book, containing more than one thousand pages, topics varying from fundamental notions of mixing to the very recent engineering applications and design guidelines. This "Handbook of Mixing" is considered by the author to be a very helpful and reliable source of information for academic or industrial purposes and the reader is encouraged to consult it for further details of the theory and practice of mixing vessel usage.

The governing fluid flow equations form a set of coupled, non-linear, partial differential equations which cannot be solved analytically for most engineering problems. Computational Fluid Dynamics (CFD) is a computer-based method for simulating the behavior of systems involving fluid flow, heat transfer, and other related physical processes. In the last twenty years, the considerable advances made in computing efficiency, coupled with the development of advanced solvers and algorithms which enable robust solution of the flow field, have made CFD an efficient and powerful tool for both industrial and research purposes. As a result, Computational Fluid Dynamics is nowadays used in various domains such as process engineering, aeronautics, electronics cooling, environmental sciences, agriculture, medical applications, etc. Concerning the role of CFD for mixing vessels, Van den Akker published very recently in 2006 an excellent article which reviews turbulent mixing processes carried out in stirred vessels and their simulation using CFD. He declared that "the advances attained in recent years in the field of CFD really matter for the degree of accuracy and confidence at which the performance of stirred reactors and of others operations carried out in stirred vessels can be simulated". However, as CFD methods grow in importance and new models and numerical methods are developed, it is more important than ever to obtain accurate experimental data to validate the predicted results.

In addition, due to the hazards linked to thermal runaways, laboratory and pilot-plant scale experiments in runaway conditions are difficult to carry out, thus the use of Computational Fluid Dynamics is extremely important. Some authors have used CFD to study the mixing of an inhibiting agent in a stirred vessel. Balasubramanian *et al.* (2003), Dakshinamoorthy *et al.* (2004 and 2006) and Dakshinamoorthy and Louvar (2006) showed CFD to be a powerful tool in the quest to understand the mixing of an inhibiting agent in an agitated vessel, as it can be used to study the effect of different injection positions and the quantities of inhibitor introduced. For a fully-baffled stirred vessel, they extended the hydrodynamics study, using a Multiple Reference Frame (MRF) approach (Harvey *et al.* 1995, Luo *et al.*, 1994), to simulate

under transient conditions the instantaneous runaway and inhibition reactions by coupling the reaction kinetics equations (for propylene oxide polymerisation) with the flow and transport equations. In the CFD model developed, the entire volume of inhibiting agent was added instantaneously to a part of the tank, and then the transport equations were solved in a transient manner. As stated by the authors in Dakshinamoorthy *et al.* (2004), this assumes that the addition of stopper does not influence the fluid dynamics inside the stirred vessel.

As Computational Fluid Dynamics is now a very popular tool, the subject is covered in many papers (e.g. Sommerfeld and Decker (2004), Aubin *et al.* (2004), Shang (2004), Van den Akker (2006)) and multiples books. The reader is referred to Versteeg and Malalasekera (1995) for an excellent introduction to the theory of CFD, with well presented derivations of the equations, a standard text on the details of numerical methods is given in Patankar (1980), more engineering aspects are detailed in Abbott and Basco (1989), and for engineering guidelines about CFD modeling of mixing vessels (in French), see Fletcher and Xuereb (2004). Therefore, generalities concerning the different modeling approaches, discretization schemes, turbulence models, as well as the governing equations will not be presented here. The information needed to understand the work of this thesis is presented in each Chapter as it is needed.

2.3. INDUSTRIAL CASE-STUDY

Brooks declared in 1997 that the high potential for thermal runaway is one feature of polymerization reactors which cannot be ignored. More than ten years later, improving the quenching of chemical reactors is more than ever an important task. The subject of this PhD thesis came directly from an industrial request. Since the methods developed and the results obtained in this thesis had to be applicable to the widest possible framework, the initial investigations were devoted to the mixing of inhibitors for industrial PVC synthesis reactors used by Tessenderlo Group, in order to improve the quenching of a possible runaway reaction. The following sub-section presents a brief description of the real industrial case to highlight the key-points and guidelines of the present study.

2.3.1. <u>Suspension polymerization of vinyl chloride</u>

PVC (Poly Vinyl Chloride) is a synthetic polymer obtained by radical polymerization of vinyl chloride monomer (VCM), carried out in batch autoclave reactors. PVC is now one of the world's major polymers and a large amount of PVC is produced worldwide because of its superior mechanical and physical properties (Endo, 2002). In 2007, the suspension process represented more than 80% of the world PVC production (the remaining 20% is made by bulk, emulsion and solution polymerization processes). In the suspension process, the VCM, quasi-insoluble in the water, is dispersed under agitation in an aqueous phase. The coalescence of the monomer droplets is prevented by both the agitation conditions and the addition of suspending agents. The polymerisation of PVC is initiated by the decomposition of an initiator soluble in the monomer, and each monomer droplet behaves as a bulk polymerization micro-system. At the beginning of the polymerization process, the monomer droplets are spherical, with an external membrane formed by polymer molecules at the interface (Barclay (1976), Davidson and Witenhafer (1980)). As the conversion increases, the PVC, which is insoluble in the monomer, precipitates into monomer droplets. The growth of the PVC particles inside the monomer droplets continues until a critical conversion, at which point the droplets begin to aggregate and to form a non-spherical PVC particle from 50 to 250 μm in diameter. For further detailed information on the chemical reactions, PVC particle morphology and different production processes, the reader is referred to papers by Xie *et al.* (1991a, b,c), reviews of Endo (2002) and Saeki and Emura (2002) and books of Allsopp and Vianello (1992) and Burgess (1982).

2.3.2. <u>Mixing in PVC synthesis reactors</u>

In the suspension polymerization PVC process, the agitator has the functions of producing the necessary droplet sizes, maintaining these droplets and ultimately keeping the PVC particles in suspension, and ensuring good heat transfer from the polymerising mass to the reactor walls. In the early days of PVC production, it was normal to agitate the vessel with a single simple 45° or 90° paddle on the end of a shaft entering from the top of relatively small (up to 10 m^3) vessels. Under these conditions, the VCM passes through the area of high turbulence to the impeller sufficiently frequently to ensure the correct droplet size and distribution, and to ensure adequate circulation in the whole batch of fluid. The ability of the agitator to produce a

particular droplet size can be predicted from classical fluid mechanics and this research topic, which is not covered in the present work, represents a large amount of published work (Armenante and Huang (1992), Church and Shinnar (1961), Lesek and Eichler (1975), Zerfa and Brooks (1996a, b)). As the reactor size increased, the length of the shaft from the top of the vessel to the impeller became very long and wide. To avoid vibrations and to cope with the power required, the shaft and bearing became very expensive. Thus, it is common practice for new large reactors to be agitated by means of an impeller close to the bottom of the vessel, driven by a short bottom entry shaft. Changes of reactor shape with reactor volume are shown in Figure 2.2.
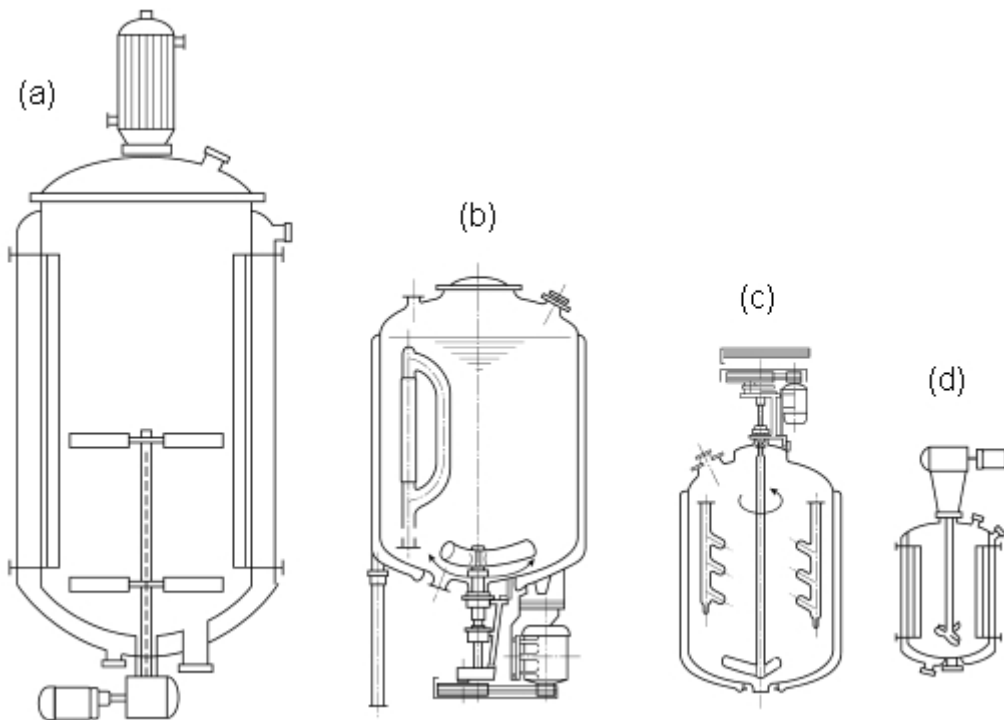
Figure 2.2. Changes of reactor shape for different reactor volumes. (a) 60 ~ 200 m^3; (b) 30 ~ 60 m^3; (c) 10 ~ 30 m^3; (d) 4 m^3 (from Saeki and Emura, 2002).

The real industrial case treated in this example concerns reactor volumes ranging from 30 to 60 m^3, and as shown in Figure 2.2(b), the configuration of the mixing vessels are far from the so-called "standard configuration" (further details are given in Chapter 9). "Standard configuration" mixing vessels have received considerable attention in the literature since Rushton *et al.* (1950a, b). The dimensions of this standard agitated vessel, provided with 4 wall-baffles and usually equipped with a Rushton turbine or a propeller, are in the metric European standard: the tank diameter is equal to the liquid height ($T = H_{liq}$); the diameter of

the agitator is D = T/3; the height of the impeller from the bottom tank (agitator clearance) is c = D = T/3; the baffle width is equal to B_w = T/10; the baffle- reactor shell distance is B′ = T/50. Nevertheless, many industrial reactors have non-standard geometries (and our case is one of these), are provided with a non-conventional set of baffles and specific single or multiple impeller. Very few published works are therefore available concerning the hydrodynamics, the impeller characteristics, the power input, etc, with these non-standard configurations.

The industrial vessel studied in this thesis is equipped with only two baffles instead of the four classically used. The baffling effect is not sufficient to prevent free-surface deformation and the assumption of a flat free-surface, generally assumed in common mixing vessels studies, is not appropriate here (this point is discussed in more detail in Chapter 4). Therefore, in the hydrodynamic study, the deep and unstable vortex formed at the free-surface of these stirred reactors must be taken into account.

Finally, the worse critical situation is obtained when the reactor has to be quenched after an event that stops agitator rotation, this situation being frequently encountered after a power shutdown of the PVC plant (see Chapter 6). Due to the total power necessary to supply all the agitator motors (greater than two MW in this case), the impellers cannot be restarted using the supply generator. From a process-safety point of view, a failure of the stirring system is very dangerous. For polymerization reactions, local hot spots caused by inefficient mixing can lead to a global thermal runaway, triggering dangerous side or decomposition reactions (Milewska and Molga, 2007).

2.3.3. <u>Quenching the polymerization reaction</u>

The polymerization of Vinyl Chloride can lead to severe consequences in the reactor, and in the worst case, release of VCM to the environmental (Braga Jr. *et al.*, 2006). The reaction is strongly exothermic (approximately 100 kJ/mol) and efficient removal of the heat of reaction is very critical for the operation of large scale reactors (Mejdell *et al.*, 1999). For quenching this polymerisation reaction, the emergency stopper (named "killer") introduced in the vessel must react with the free radicals present in the reaction medium. The killers are classically inhibitors or retarders, both acting on the same mechanism, but with a different effectiveness.

They react with the initiating and propagating radicals and convert them either to non radical species or radicals of reactivity too low to undergo propagation. As shown on Figure 2.3, an inhibitor stops every radical and the polymerization is completely halted until they are consumed. After an inhibition period, polymerisation proceeds at the same rate as in absence of inhibitor. A retarder stops only a portion of the radicals and polymerisation occurs at a slower rate.
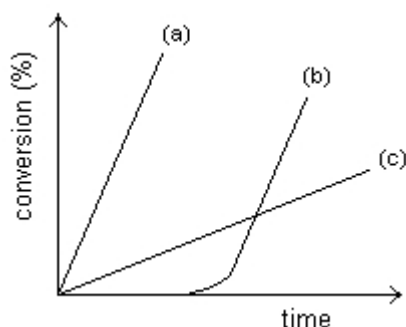
Figure 2.3. Schematic curves showing the effect of inhibitors and retarders on the rate of polymerization: (a) no additive; (b) with inhibitor present; (c) with retarder present; (inspired from Bovey and Winslow, 1979).

The killers are classically vinyl monomers, phenols and quinone based aromatic compounds, amines or aromatic nitro-compounds (Tüdós and Földes-Berezsnich, 1989) and can be stabilized in an organic or aqueous solvent, fine emulsions or solid dispersions. The choice of a specific killer agent is not only based on its reaction efficiency but other qualities have to be considered, such as its stability, solubility, colour, toxicity, cost and volatility. In the case studied here, the killer agent used is an organic solution composed of a phenolic crystalline solid (active agent) dissolved in an organic solvent.

The problem is thus increased in complexity when both the PVC synthesis and the quenching process are considered together. The killer is introduced as a liquid jet at the free-surface into the bulk. It is contained initially inside a steel vessel, isolated from the synthesis reactor by a rupture disk (this apparatus is detailed in Chapter 10). As shown schematically in Figure 2.4, before impacting the surface of the stirred fluid, the jet passes through a gaseous, pressurized space.
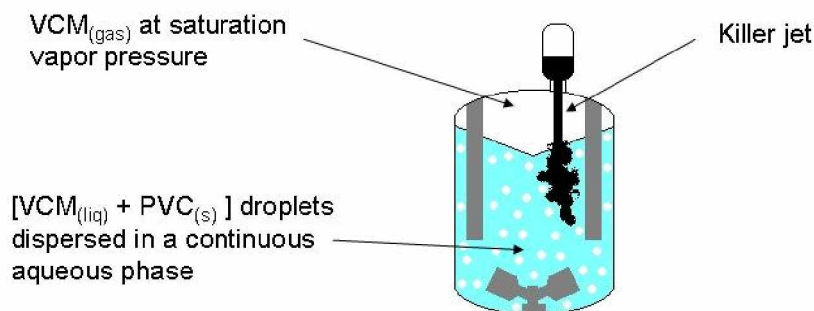
Figure 2.4. Schematic of killer injection into a PVC synthesis reactor

As described above, in the polymerization of VCM suspension, the reaction medium is a heterogeneous mixture with three phases: a water phase, a polymer phase and a monomer phase, the last two kept homogeneously dispersed in the water phase. The monomer phase is in liquid-vapour equilibrium at the reaction temperature. The initiator is initially distributed inside the monomer droplets, which will form the PVC particles during conversion. Thus, the inhibitor must be capable of diffusing through the water phase and/or polymer phase to reach the monomer droplets, where the radicals are located (Malmonges and Santos, 1996).

During the introduction of the killer agent into the bulk, if the precipitation of the stopper agent when it enters the continuous water phase is neglected, the real problem involves four different phases: three phases are already in the bulk — water (liquid, continuous phase), VCM (liquid, dispersed phase) and PVC (solid, dispersed phase) — and an organic supplementary phase is added with the killer agent. Therefore, complex physico-chemical phenomena are involved, such as diffusion and interface transfer from one phase to another. These transfer phenomena are coupled with the convective and turbulent transport of the killer agent in the bulk, provided by the jet injection and the agitator stirring effect.

2.4. A CO-VALIDATION STRATEGY: FROM THE SIMPLE TO THE COMPLEX

The entire quenching problem is very complex and requires competences in various research domains from basic chemistry, going through physico-chemistry, physics, chemical engineering, fluid mechanics, etc. It was outside of the scope of this thesis to study the entire

inhibition process. However, the advantages of such a "real case" study and the development of validated models allows a better understanding of the process.

With a coupled experimental and numerical CFD approach, this study is focussed on the agitation of a model fluid (water) and on jet injection studies, keeping the same non-standard reactor geometries as used in the industrial cases. As killer agents may vary largely depending on the development of new efficient products on the market, the present study was not based on a specific product but used water as a generic fluid.

For most of the results presented in this thesis, the experiments were performed in conjunction with numerical predictions. The two approaches, experimental and numerical, were developed in parallel and in a strongly coupled manner. Instead of carrying out experiments for validating the numerical methods, it is better here to speak about a co-validation strategy, as these two domains have progressed simultaneously and are now capable of delivering useful results. On one hand, the numerical CFD methods are growing in importance and many studies have already demonstrated the capability of this tool in many different situations. In another way, experimental techniques must occupy a fundamental place in the engineering and research community. Obviously, the current tendency in the process industries is to drastically reduce the use of pilot-scale experimental studies for time and cost constraints, and to replace it by simulation work. This tendency is shown for mixing applications, but has also happened in basic chemical engineering, as for example in chemical reactors, distillation, etc. In certain cases, numerical sciences have reached such a level of accuracy that they may replace the use of experimental validations. The author shares the point of view of Sahu *et al.* (1991) who declared in 1991, in a period where CFD was in constant acceleration, that "CFD may not eliminate altogether the necessity for experiments because the complexity of the flows (…) it is true that where it cannot eliminate the necessity for experiments, CFD can synergistically guide the experiments and accelerate the progress". For this study, a strong association of numerical and experimental work has been chosen.

In this thesis, a mixing vessel equipped with its injection system in exact geometrical similarity with the industrial stirred reactor is designed and built, in order to have reliable and easily scalable experimental data. Then, CFD methods were developed to co-validate numerical predictions and experimental data. Numerous step-by-step comparisons between the experimental and numerical data allowed an accurate model for the pilot reactor to be built

by increasing progressively the complexity of the simulations carried out. Finally, the numerical know-how and background learnt for pilot-scale simulations to investigate with confidence the hydrodynamics, free-surface-shape, jet trajectories and reactor quenching at the industrial scale.

Figure 2.5 summarises how the computational work that has been performed by increasing the level of complexity of the simulations.

The simplest case is the agitated vessel, modelled using a steady-state Multiple Reference Frame (MRF) approach, single phase model, flat free-surface and constant agitator speed, as shown in Figure 2.5(a). The first improvement of the basic case was to replace the single phase model by an inhomogeneous multiphase model while the MRF approach was kept (see Chapter 4) to take in account the free-surface deformation (Figure 2.5(b)).

In order to highlight the complex, unsteady nature of the fluid flow, the mixing vessel was simulated at constant agitator speed using a transient "sliding mesh" approach (see Chapter 5) instead of the MRF and a single phase model (Figure 2.5(c)). This last situation was then modified by replacing the single phase by a multiphase approach at a rotation speed which allows a flat free-surface (Figure 2.5(d)), and this modelling was finally extended to a deformed free-surface case as shown in Figure 2.5(e) (see Chapter 5). Figure 2.5(f) shows the higher complexity level in our simulations which consider only the mixing vessel (without the jet injection). In this latter case, a decreasing agitator speed function was added using a transient multiphase model and deformed free-surface shown in Figure 2.5(e), to simulate the agitator stopping phase and the inertial period after the agitator has stopped completely.

When the numerical background learned about the mixing vessel was sufficient and the numerical models used were validated by experimental data (free-surface shape, transient macro-instabilities, use of the k-ε turbulence model instead of Reynolds Stress model), the jet injection dynamics was considered. This was an important gap in the complexity of the modelling compared with the modelling of the mixing vessel alone and required a number of assumptions to be made (discussed in Chapter 8). The MRF steady-state approach was used for the impeller motion whilst a transient model was used to study jet injection, as shown in Figure 2.5(g). Using this configuration, simulations with jet injection were performed for the pilot-scale and industrial-scale reactors.

MRF: *Multiple Frame of Reference*
SM: *Sliding Mesh*
SP_m: *Single-phase model*
MP_m: *Multi-phase model*
f. s.: *free-surface*

Steady state (MRF)
Multi-phase model
Deformed free-surface
Constant rot. speed **(b)**

$SP_m \rightarrow MP_m$

Steady state (MRF)
Single-phase model
Flat free-surface
Constant rot. speed **(a)**

Lagrangian particle tracks
and passive scalar transport

$+ \mathbf{JET}$

$MRF \rightarrow SM$

Transient (SM)
Single-phase model
Flat free-surface
Constant rot. speed **(c)**

$SP_m \rightarrow MP_m$

Transient (SM)
Multi-phase model
Flat free-surface
Constant rot. speed **(d)**

Flat f.s.
$\rightarrow$ deformed f.s.

Transient (SM)
Multi-phase model
Deformed free-surface
Constant rot. speed **(e)**

$N = cst$
$\rightarrow N \neq const$

Transient (SM)
Multi-phase model
Deformed free-surface
Decreasing rot. speed **(f)**

Steady state (MRF): impeller
Transient: jet injection
Single-phase model
Flat free-surface
N = constant
JET (Euler. and Lagr.) **(g)**

Flat f.s.
$\rightarrow$ deformed f.s.

Steady state (MRF): impeller
Transient: jet injection
Single-phase model
Deformed free-surface
N = constant
JET (Euler. and Lagr.) **(h)**

Figure 2.5. Summary of the CFD strategies developed in the thesis. The diagram shows the linkages between the different simulations performed.

The last improvement of the modelling was developed at the very end of this thesis (see Chapter 12). As it was not possible to couple the inhomogeneous multiphase approach (used to predict the vortex shape) with jet injection located on the free-surface (see Chapter 8), this problem was bypassed by proposing a new way of thinking for the modelling of agitated vessels with a free-surface. The free-surface obtained at a high rotation speed using the multiphase model presented in Figure 2.5(b) has been used to represent the free-surface in a single phase simulation. This allowed a single phase model to be used with jet injection, as presented in Figure 2.5(h) to model jet injection with a deformed free-surface.

The details of these methodologies form the body of this thesis and are presented in the following chapters.

Chapter 3

EXPERIMENTAL RIG AND MEASUREMENT EQUIPMENT

This Chapter presents the experimental rig and measurement equipment used in this study. The pilot installation used for all the experiments carried out in this thesis, which comprises a mixing vessel equipped with a liquid injection system, scaled-down from industrial reactors, is described. Then, the technical details of the cameras used in this study are presented. Finally, the Particle Image Velocimetry (PIV) technique, used here to study the hydrodynamics in the agitated vessel, is presented together with technical details and PIV settings.

3.1. MIXING VESSEL AND INJECTION SYSTEM

The experiments carried out for this study have been conducted in a pilot reactor designed for polymer and fine chemicals industrial applications. This equipment was designed and assembled in the Chemical Engineering Laboratory of Toulouse. The dimensions of the equipment have been calculated in strict geometrical similarity with the real industrial suspension polymerization reactors of Tessenderlo Group which are studied in details in Chapter 9. For confidentiality reasons, the scale-down procedure is not detailed in this manuscript.

3.1.1. Overview of the installation

To carry out hydrodynamics studies with the possibility of injecting additives, this reactor is composed of two main sections, which are the mixing vessel and the liquid injection system. Before describing each of them, the entire equipment is shown in Figure 3.1.
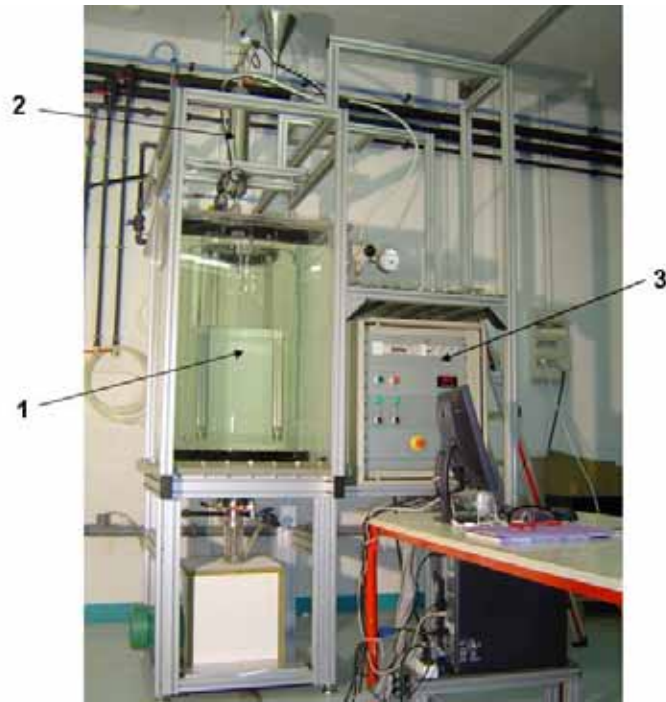
Figure 3.1. Experimental rig: 1. mixing vessel, 2. liquid injection system, 3. control equipment.

3.1.2. <u>The mixing vessel</u>

The mixing vessel is shown in Figure 3.2. Information and technical details for the model of equipment used on the mixing vessel is presented in Table 3.1.
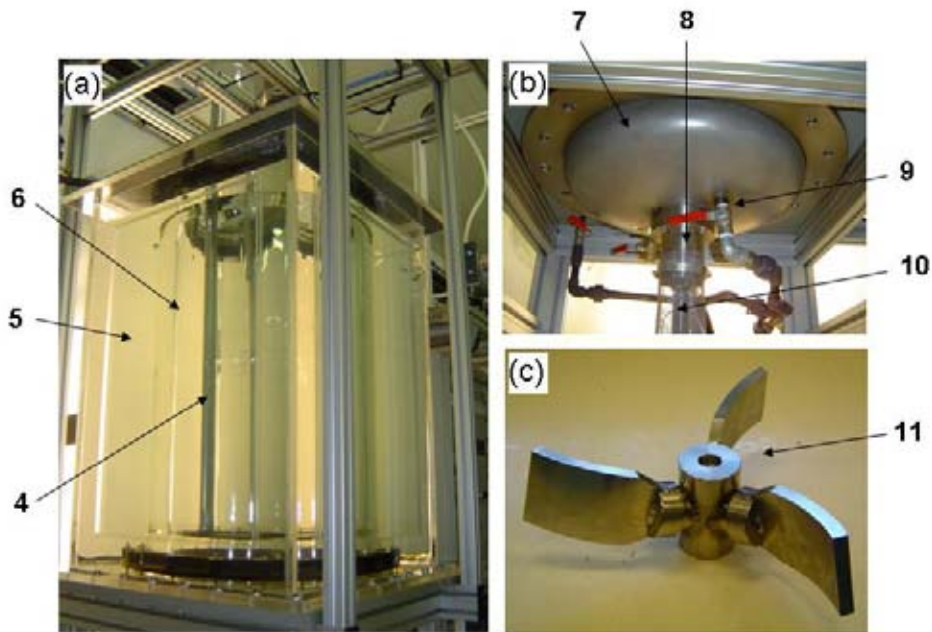
Figure 3.2. Pictures of the different elements of the mixing vessel: (a) vessel shell and jacket; (b) bottom dish; (c) agitator.

Table 3.1. Legend for Figure 3.2. and technical details of the mixing vessel equipment

Number	Equipment	Technical details
4	Beaver-tail baffle	Steel 304L
5	Squared jacket around the vessel	Methacrylate for lateral panels Fortal aluminium for bottom lid
6	Cylindrical vessel shell in glass	De Dietrich process systems, type B 450/1000
7	Curved bottom dish	304L steel, 457.2×2.9
8	Gland packing	Carbon/Viton D.22 Ball bearing RIG.BIL 20×42×12 Ball bearing CT.OBL 20×47×20.6
9	Reactor draining valve	Standard inox valve
10	Agitator shaft	Hand made, 316L steel
11	Agitator	Hand made, 316L steel

The bottom dish is a curved dish fabricated in steel, drilled in the centre to accommodate a gland packing for rendering the vessel leak tight. The curved shape of the vessel bottom allows the impeller to be placed very close to the bottom, making the reactor suitable for suspending heavy dispersions effectively (Li *et al.*, 2005). The cylindrical part of the stirred vessel is composed of a transparent glass column element of 450 mm diameter and 1 m height, allowing a maximum filling volume of 150 L. This stirred vessel was designed to allow Particle Image Velocimetry (PIV) measurements, so the cylindrical vessel is completely contained in a square-section water-filled jacket, made of transparent materials (glass and Perspex Altuglass®) in order to minimize shell curvature and refraction problems at the cylindrical surface of the inner vessel. The refraction effects could be totally eliminated by a fluid with the same refractive index as that of the glass (n ~ 1.5) for both the fluid in the stirred vessel and in the square tank. This technique would require a large volume of fluid which could be aqueous solutions of zinc iodide, sodium iodide, potassium thiocyanate or organic liquids (Budwig (1994), Hendricks and Aviram (1982)). This modification is not necessary for the experimental apparatus used in this study as the curvature radius of the vessel shell is sufficiently large to avoid high refraction effects, and a simple calibration using water was sufficient.

The agitated vessel is equipped with only two beaver-tail baffles which are supported by a flat steel lid fixed on the top of the glass cylindrical vessel part. This type of baffle support, as well as the fact that the vessel is a partially-baffled system, will be discussed in Chapter 4. The three-blade agitator used is shown in Figure 3.2(c). This agitator is a copy of a real

industrial design used in suspension polymerization reactors. This model is derived from the classical Retreat Curve Impeller (RCI), developed by the Pfaudler Company specifically for glass-lined reactors, but with larger blades. Note the industrial agitator is glass-coated and has smoother surfaces than the steel model used here but it is not expected that this would change the results significantly. This agitator is powered by a 1.5 kW variable speed motor, located below the bottom dish, with a maximum rotation speed of 500 RPM and is controlled by a speed controller (Leroy Somer Proxidrive®). A torque transducer (HBM GmbH, T5 model, 20 N m of nominal torque) located on the agitator shaft, coupled to a measuring amplifier (SCOUT55 from HBM GmbH) enabled measurement of the impeller torque to be made to estimate the power dissipated in the fluid. The precision of the torque measurements was ± 0.1 Nm in the range 0-20 Nm.

3.1.3. The injection system

The injection system is shown in Figure 3.3. Information and technical details relating to the model of the equipment used for the injection system is presented in Table 3.2.
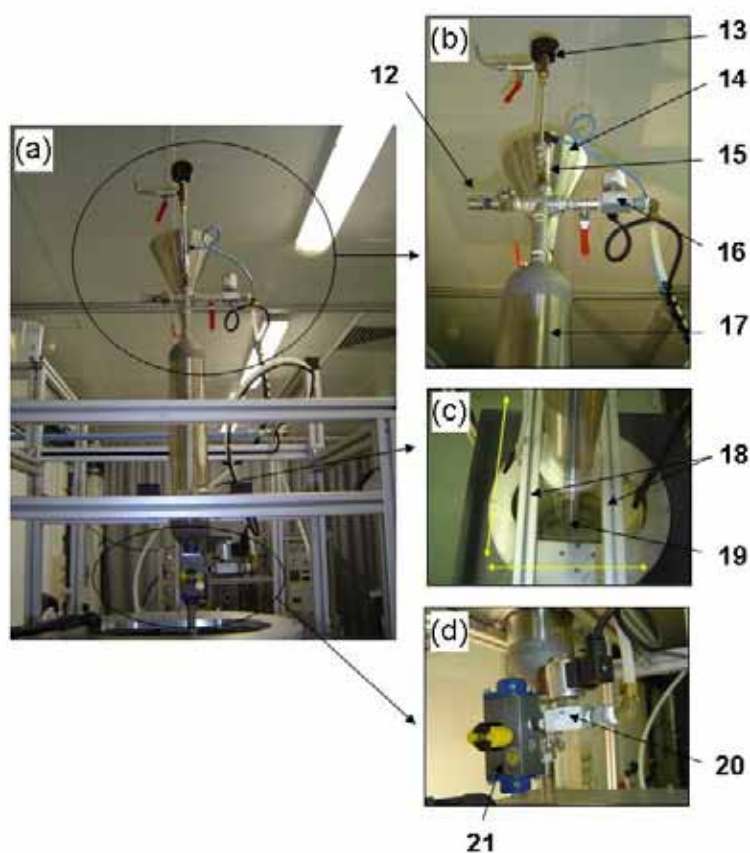
Figure 3.3. Pictures of the different elements of the injection system: (a) the top of the injection system; (b) the bottom of the injection system and sash; (c) the draining equipment.

Table 3.2. Legend for Figure 3.3 and technical details of the injection system equipment

Number	Equipment	Technical details
12	Safety relief valve	Max pressure 3.5 – 34 bars
13	Vent valve and safety pressure gauge	Standard equipment.
14	Loading steel funnel	Hand made, 304 L steel
15	Pressure sensor	Keller, model PR21/10b, 4/20mA, ¼ GM
16	Electro-valve	Eugen Seitz AG, DN 2.2, 0-8 bars (used for pressurization)
17	Killer vessel	Hoke, 304L inox sampling cylinder, 125 bars, double orifice ½ npt female, 3 litres of capacity, certified pressurized equipment DESP97/23/CE
18	Movable sash supporting the killer vessel	Hand made
19	Injection pipe	Steel and PVC, diameters 7.2, 10, 12.5, 15n 17.8 mm
20	Electro-valve	Eugen Seitz AG, DN 2.2, 0-8 bars (for draining valve actuator)
21	Pneumatic actuator and draining valve	Fluid services Pneumatic actuator: 10 bar max Valve: Inox, simple effect, model 746XS G1/2 (Cv = 17)

The liquid injection system consists of a 3 litres high pressure (max 125 bars) steel vessel manufactured by Hoke (commonly called a "sampling cylinder" because it is used to take a fluid sample from a chemical process unit and store it safely for future analysis). This vessel, of diameter and height equal to 102 mm and 559 mm, respectively, has two orifices of 15 mm diameter each located at the top and bottom. The top orifice is fitted with a four junction piping element which is used: (i) to mount a steel funnel (isolated from the vessel by a manual valve) to feed the liquid, (ii) to feed the air to pressurize the vessel, (iii) to mount the pressure sensor and (iv) to mount a safety relief valve. A constant pressure reducing valve located on the air feed pipe is used to maintain a constant pressure in the vessel during draining. A high-speed automatic valve, controlled via a pneumatic actuator (using air at 8 bars), is mounted directly at the bottom of the vessel. A 15 mm diameter passage with no obstruction exists when the valve is open. The liquid volume present initially in the killer vessel is introduced into the stirred vessel via a single pipe. The liquid jet impacts directly on the free-surface of the stirred liquid and the pipe outlet is located at a distance of, $L^{'}$, 220 mm above the liquid free-surface for all the experiments. Five different injection pipes of different diameters were used for the experiments carried out in this study. The internal pipe diameters were equal to 7.2 mm, 10 mm, 12.5, 15 mm and 17.8 mm with the same total pipe length (L = 300 mm).

3.1.4. <u>Drawings and dimensions</u>

Table 3.3 summarizes all the geometric information for the stirred vessel and the injection system. All the dimensions and the position of the different elements inside the vessel are shown schematically in Figures. 3.4. The PIV plane presented in this figure corresponds to the area where measurements were carried out using the Particle Image Velocimetry technique. This PIV plane is discussed in more depth in the paragraph §3.3.6 relating to the PIV measurements.

Table 3.2. Dimensions of the agitated vessel and the injection system

	Symbol	Value
Tank diameter	T	450 mm
Maximum tank height	H_{max}	1156 mm
Bottom dish height	H_d	122.9 mm
Agitator diameter	D	260 mm
Number of agitator blades	n_b	3
Agitator blade width	w_b	58 mm
Agitator blade thickness	t_b	9 mm
Agitator retreat angle	θ	15°
Agitator clearance	c	47.2 mm
Baffles length	B_l	900 mm
Number of baffles	n_B	2
Baffle width	B_W	46 mm
Baffle thickness	B_t	27 mm
Distance baffle – shell	B'	38.5 mm
Initial liquid height	H_{liq}	700 mm
Injected volume	V_j	533 ml
Injection pipe diameter	d	7.2, 10, 12.5, 15 , 17.8 mm
Injection pipe length	L	300 mm
Distance pipe outlet - free-surface	L'	220 mm
Bottom height of the PIV plane	$H_{PIV, min}$	278 mm
Top height of the PIV plane	$H_{PIV, max}$	738 mm

In addition, the mixing vessel and the injection system are monitored via a process supervision system completely designed and developed in the laboratory. Suitable electronic, electric equipments and a standard PC (P4 3Ghz, 1 Go RAM) equipped with an acquisition card (Elexis, DaqBoard 2000) monitored by the software DasyLab 7.0, allowed the pilot reactor to be operated manually or in a completely automated fashion.
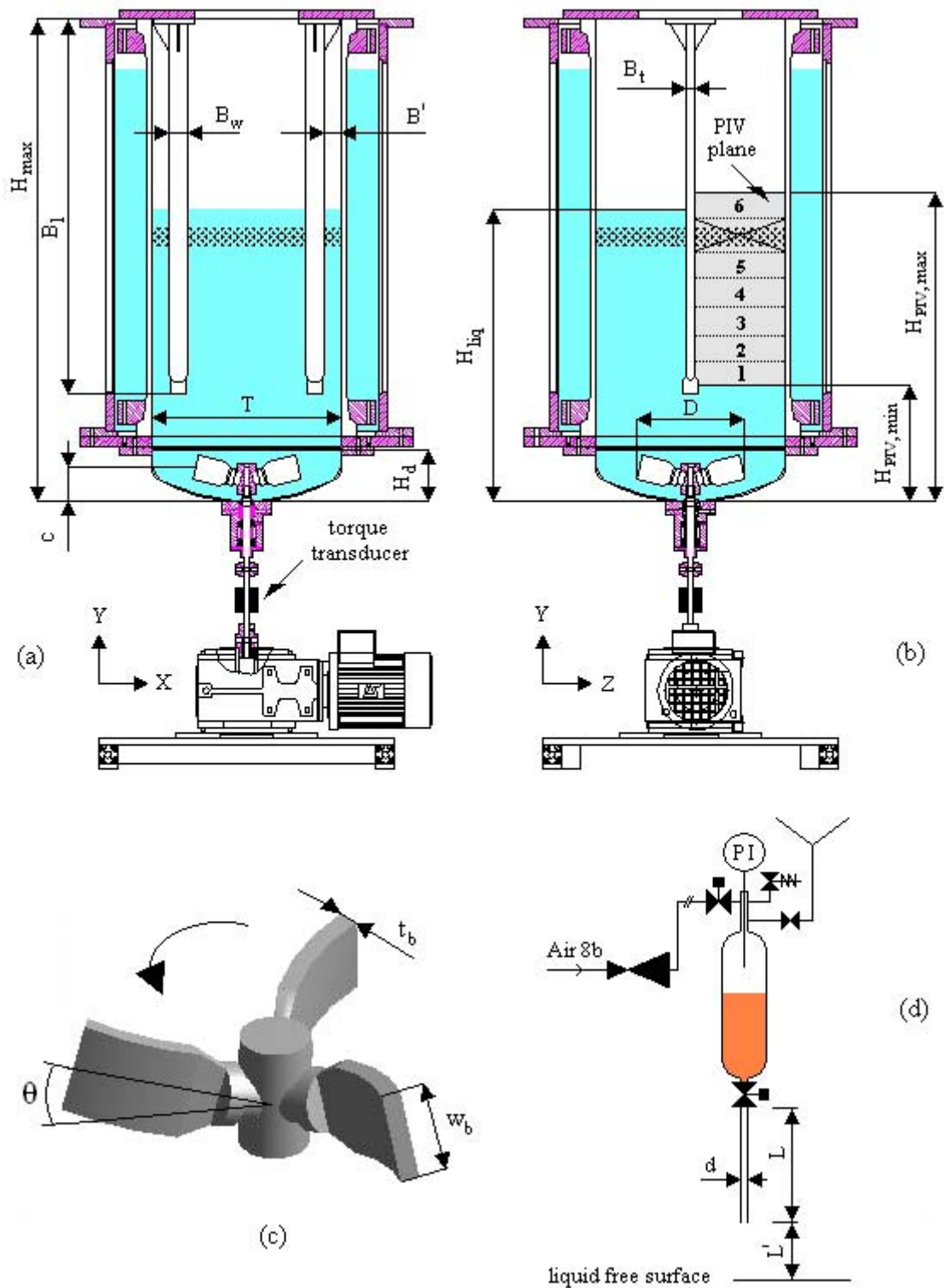
Figure 3.4. Schematic of the mixing vessel: (a) XY view of the mixing vessel; (b) YZ view of the mixing vessel; (c) details of the agitator; (d) injection system.

3.2. VIDEO CAMERAS

Two different video cameras were used to record videos or to take snapshots of various phenomena observed in this study. The technical details of each can be found in this paragraph. Detail of the CCD camera which was used for the Particle Image Velocimetry is given in §3.3.

3.2.1. <u>Webcam Philips Toucam Pro II</u>

Significant progress has been made in the development of digital systems for processing and handing large amount of data at increasing speeds. This is the case with webcams, a very popular and cheap device which has arisen in parallel with the increasing use of the Internet, the presence of high-speed connections and the advanced software for domestic or business video-conferences (Dorr *et al.*, 2007). Today, millions of webcams provide views of homes, offices and other buildings, providing panoramic views of cities and of the countryside, etc.

In addition to these applications, some recent literature papers have illustrated that this very simple and inexpensive camera performs well for scientific purposes and deserves interest. As examples, Togasaki *et al.* (2005) achieved automated quantitative measurement of movement in primates, Chung *et al.* (2005) performed laparoscopic studies, Dorr *et al.* (2007) adapted a webcam in a microscope to measure membrane water permeability of nervous system cells, and Tort *et al.* (2006) evaluated the position and locomotion of rodents in an arena. Finally, a large number of amateur astronomers (as I am!) have adopted the Webcam instead of CCD cameras for deep sky or planetary photography (Legault, 2007).

For this study, some videos and snapshots (vortex shape in Chapter 4, precessing vortex motion in Chapter 5, mixing time experiments in Chapter 7) have been made using a webcam (Philips Toucam Pro II) linked to a standard PC. This webcam is a commercially-available camera equipped with a CDD sensor and its technical details are listed in Table 3.4.

Table 3.4. Technical specifications of the Webcam Philips Toucam Pro II

	Technical specifications	Picture of the camera
Model	Toucam Pro II	
Supplier	Philips	
Sensor	1/3″ VGA CCD	
Pixel size	5.6 μm × 5.6 μm	
Picture resolution	640 × 480	
Max acquisition frequency	60 frames per second	
System	Microsoft Windows XP, USB link	
Monitoring software	IRIS 4.17	
Dimensions (mm)	70 (H) × 50 (W) × 35 (D)	

The information is transferred from the camera to the computer via a USB link and the frame rate available can be set from 5 frames/s to 60 frames/s. The Webcam was located either in front of the tank in order to cover the field necessary to visualise the entire vortex shape or mounted above the top reactor lid to visualise the trajectory of the precessing vortex.

3.2.2. High speed CMOS camera HCC-1000

When the webcam presented in the §3.2.1 could not provide a sufficiently high frame rate and resolution to carry out the observation and/or the measurement, a high speed CMOS camera (HCC-1000 model from VDS Vosskühler) monitored by the NV1000 software from New Vision Technologies was used. The technical details relative to this camera are presented in Table 3.5.

Table 3.5. Technical specifications of the HCC-1000 camera

	Technical specifications	Picture of the camera
Model	HCC-1000	
Supplier	VDS Vosskühler	
Sensor	10.24 mm × 10.24 mm CMOS sensor	
Pixel size	10 μm × 10 μm	
Picture resolution	1024 × 1024 pixels²	
Max acquisition frequency	640 frames per second	
System	Microsoft Windows 98 USB connexion	
Monitoring software	NV1000 from New Vision Technologies	
Dimensions (mm)	90 × 71 × 37	

This camera was used to capture experimentally, with a high image resolution of 1024×1024 pixels², the vorticity filaments which develop and rotate in the stirred vessel (Chapter 5), to capture the transient evolution of the free-surface during impeller stopping (Chapter 6), to measure the jet velocities by following the jet leading edge versus time during the killer vessel draining and to capture the jet trajectory during its mixing into the stirred vessel as presented in Chapter 8. This camera was used either with a telephoto lens Nikon – Nikkor (50 mm focal length, 1.2 maximum relative aperture) or a telephoto lens Rainbow S6X11 (11.5-69 mm focal length, 1:1.4 maximum relative aperture).

3.3. PARTICLE IMAGE VELOCIMETRY

The term ''Particle Image Velocimetry'' (PIV) first appeared in the literature 27 years ago, and continues to be linked to intensive research work by being applied to a wide range of flow problems, varying from the flow over an aircraft wing in a wind tunnel to vortex formation in prosthetic heart valves. Particle image Velocimetry (PIV) is nowadays a standard tool which is used to analyse various flow fields, including micro-flow, nano-flow, high-speed flow, bio-flow, etc, and this is one of the most successful measurement techniques developed in this decade (Okamoto, 2005). Although the targets of PIV research focus nowadays on the improvement of accuracy, the applications of PIV to complicated nonlinear analysis, or to the development of stereoscopic and holographic PIV, Particle Image Velocimetry remains a very useful and interesting experimental technique which enables measurements of the instantaneous fluid velocities in a two-dimensional plane. For a detailed historical and very interesting presentation of PIV since its beginning, the reader is invited to consult Adrian (2005).

3.3.1. <u>Principles of PIV</u>

The basic principle of determining instantaneous velocities of a flow field using PIV consists of measuring the distance that a seeding particle in the fluid has travelled during a time interval, assuming the movement of this particle is representative of the fluid. If during a time

interval Δt, a particle moves from position $\underline{x}$ to position $\underline{x} + \Delta\vec{x}$, the local velocity of the liquid $\vec{u}(\underline{x}, t)$ can be defined by relation (3.1):

$$\vec{u}(\underline{x}, t) = \frac{\Delta\vec{x}(\underline{x}, t)}{\Delta t} \qquad\qquad (3.1)$$

The determination of the local fluid velocity therefore depends on the measurement of the displacement of seeding particles at two instants of time, t and $t + \Delta t$. To do this, two images of the particle in the flow field are recorded at two successive instants of time. Analysis of theses images enables the local displacement of the seeding particles to be determined, and as Δt is known, the local velocity of the flow may be calculated.

As illustrated schematically in Figure 3.5, the image acquisition is carried out by adding small seeding particles to the flow and then illuminating them with a thin two dimensional laser sheet. When the particles pass through the illuminated zone, they scatter the laser light. This scattered light is then received by a photo-sensitive captor, which is often a CCD camera placed perpendicular to the laser sheet. The images are received by the captor and are recorded digitally on photo-sensitive material, resembling a spatial distribution of luminous points on a dark background.
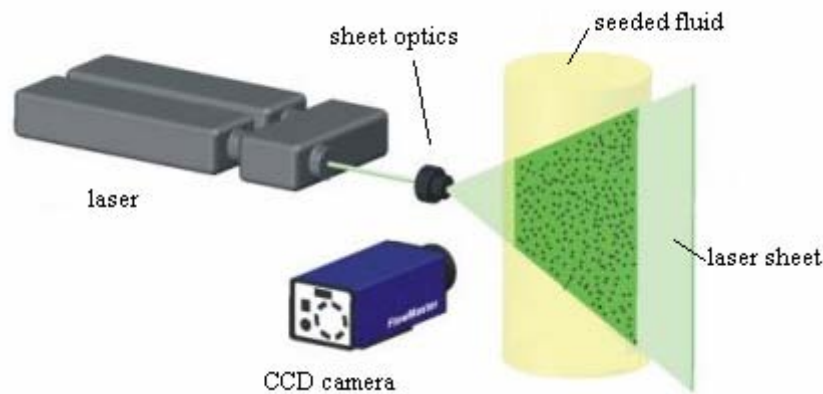
Figure 3.5. System components for PIV (inspired from www.piv.de).

As shown in Figure 3.6, the digital images of luminous points are divided using a grid and each statistical calculation is carried out in every grid cell containing the group of particles. The corresponding areas, named interrogation area, from both frames are searched for identical particles to calculate the displacements. This processing is done by Fast Fourier

Transforms (FFT) giving several peaks where the peak height is a measure of the probability for that particular displacement value. Finally, calculations extract the velocity from the correlation and a vector for this interrogation window is obtained.
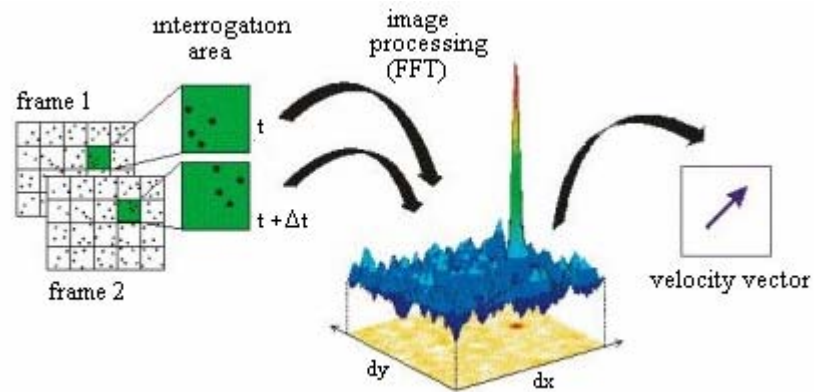
Figure 3.6. PIV image evaluation (inspired from www.piv.de).

The PIV apparatus installed on the mixing vessel is shown in Figure 3.7. The synchronization between the laser and the camera, the calculations and image processing as well as the post processing of the results was performed using the commercial software Davis 7.01.

Figure 3.7. PIV apparatus on the pilot reactor: 1. mixing vessel; 2. CCD camera; 3. camera support; 4. PC and timing controller; 5. laser support; 6. laser and light optics.

3.3.2. <u>Light sources</u>

As previously mentioned, a laser sheet of light is required to illuminate the seeding particles in the flow field in order to determine the instantaneous velocity of the fluid. Two different types of lasers may be used: continuous and impulse lasers. The continuous laser allows a light sheet with a uniform thickness to be emitted continuously. The time interval between two successive images may be fixed by the shutter of the photo-sensitive captor or by rotating a mirror in front of the laser beam, about an axis that is perpendicular to the illuminated two-dimensional flow area. The advantage of such lasers that emit continuously is that they provide a constant stable flux of light. However, continuous laser emission is costly and therefore this type of laser emits only with a low luminous energy, which restricts this type of light source to be used for low velocity flows of less than 1 ms^{-1} (Aubin, 2001). For flows of higher velocities, the impulse laser is better adapted (to give an order of magnitude, the tip velocity for N = 100 RPM in our case is equal to 1.36 ms^{-1}). Impulse lasers emit the light sheet as short pulses with high luminous energy allowing velocities in fast flowing fluids to be measured. In recent applications, a commonly used impulse laser is the Nd-YAG laser (Neodymium doped Yttrium Aluminium Garnet, Nd:$Y_3Al_5O_{12}$). This laser emits green light with a wavelength of 532 nm and can produce pulses with a luminous energy of up to a few hundred millijoules. The Nd-YAG does however posses a disadvantage in that the luminous energy varies from one light pulse to the other and is not spread uniformly in the beam. This problem can be resolved by using a dual cavity Nd-YAG that emits each light pulse from a separate laser. For our study, the laser used was a dual cavity Nd-YAG of 25 mJ, 15Hz max.

3.3.3. <u>Sheet optics</u>

The geometrical characteristics of the laser sheet depend on the set-up of the optical equipment, as well as the distribution of the luminous energy within the laser beam. The set-up of the optical equipment includes the types of lenses and their positions. The organisation of lenses in the optic assembly is used to create the laser sheet from a single laser beam. In the case of a dual cavity impulse laser, where two laser sheets are formed, the optic assembly is also used to ensure that the two sheets have identical characteristics and form in the same plane in the flow field. Figure 3.8 describes the set up of the optical equipment of the laser used for the creation of a laser sheet from a laser beam.
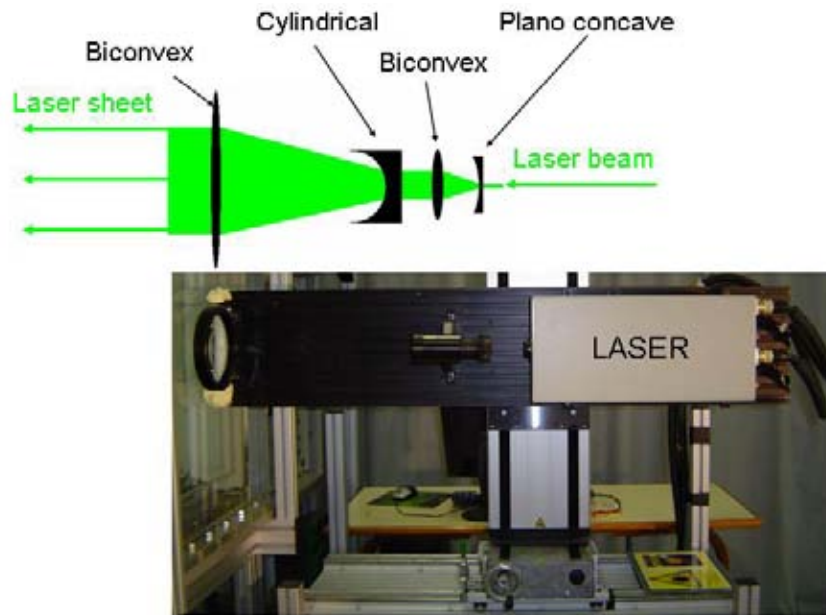
Figure 3.8. Lens assembly for the creation of a laser sheet from a laser beam

The plano-concave lens causes the laser beam to diverge. This diverging beam passes through a biconvex lens which induces the beam to become straight with a larger diameter than the original beam. Then, the cylindrical lens forms the laser sheet from the incident beam and finally the biconvex lens straightens up the laser sheet into a parallel sheet.

After controlling that the laser was perfectly horizontal and normal to the front jacket wall of the vessel, the laser sheet had to be adjusted to go through exactly the centre of the vessel. This was done by matching a plumb line suspended from the top vessel lid and passing though the agitator shaft hole (agitator in the bottom dish).

3.3.4. Seeding

The light of the laser sheet must be scattered in order to be captured by the photo-sensitive device. To do this, the studied fluid must be seeded with tracer particles. These particles are of small size, usually ranging from about 1 mm to about 30 μm, and are assumed to follow the flow faithfully. The tracer particles used here were PMMA impregnated with Rhodamine-B (molecular formula given in Figure 3.9(a)), provided by Microparticles GmbH (excitation/emission wavelengths: 575 nm/584 nm, 1 μm < diameter < 20 μm). An example

of water seeded with Rhodamine B captured photographically in the pilot reactor is shown Figure 3.9(b).
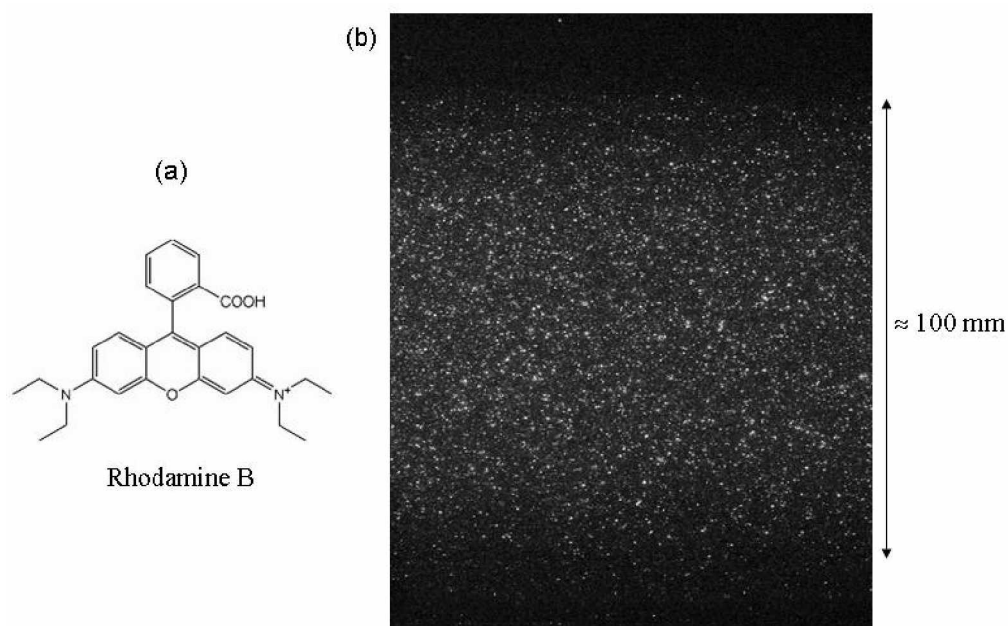
Figure 3.9. Molecular formula of the Rhodamine-B; (b) water and Rhodamine B exposed by the Nd-YAG

The seeding concentration is one of the most important operational parameters and is one of the most common factors responsible for erroneous vectors (Huang *et al.*, 1997). If the seeding concentration is too low, there are not a sufficient number of particles to statistically represent the flow which results in a poor correlation between the two successive images. In contrast, increasing the seeding to too high a concentration does not always have a beneficial effect. When the number of seeding particles in the flow is increased, the optical transparency of the fluid is not only reduced (Adrian and Yao, 1985) but two phase effects are also enhanced due to the increased influence of the seeding on the flow (Westerweel, 1994). In our case, a concentration of seeded particles adjusted to have between 5 and 10 particles in each 32×32 pixels² interrogation window was found to be a good seeding concentration value. This concentration value has been maintained in all the experiments using PIV

3.3.5. <u>Recording particle images</u>

When the seeding particles in the fluid are illuminated and scatter laser light, a photo sensitive device collects the light signals and records them as images. Several devices which have been

used for recording particle images are photographic film, high speed cinematography, etc. Nowadays, it is the Charged Coupled Device (CCD) cameras which are generally used because they allow acquisition in near-real time with a high image resolution and direct numerical image processing. In this study, a black and white CCD camera La Vision Imager Intense was used to capture the frames exposed by laser pulses (technical details in Table 3.6). The camera was equipped with the telephoto lens (Nikon – Nikkor 50mm/1.2) that was used to focus on the laser sheet. A high pass filter was placed in front of the camera which enabled capture of light with a wavelength greater than 550 nm, protecting the CCD sensor from unwanted light reflections from gas bubbles and improving contrast. The camera, the telephoto lens and the filter are shown in Figure 3.10(a), (b) and (c), respectively.

Table 3.6. Technical specifications of the PIV camera

	Technical specifications
Model	Imager intense
Supplier	LaVision
Sensor	CCD
Pixel size	$6.45\mu m \times 6.45\mu m$
Picture resolution	1376×1024 pixels^2
Max acquisition frequency	10 Hz
Monitoring software	DAVIS (version 7.01), Windows XP
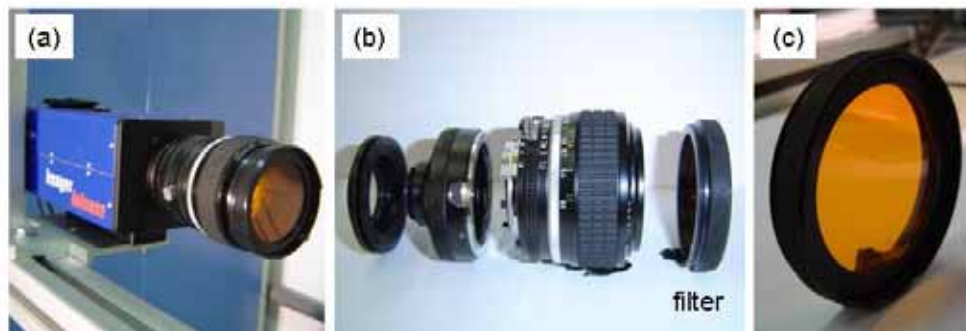
Figure 3.10. PIV camera: (a) camera equipped with the telephoto lens and the filter; (b) telephoto lens Nikkor 50 mm and its mounting rings ; (c) high pass filter $\lambda_{cut} = 550$ nm.

3.3.6. **Measurements in the stirred vessel**

The maximal size of the measurement area which can be covered in the mixing vessel for a given position of the laser is directly given by the height of the laser sheet. In our case, the biconvex lens which forms the parallel laser sheet shown previously in Figure 3.8 allowed a

maximum laser sheet height of 100 mm. Therefore, covering the whole vessel height was impossible by using one single position of the laser as shown in Figure 3.11(a). To cover the entire half tank, the measurements required the construction of a mosaic composed of six different sectors. This measurement area forms the PIV plane drawn in Figure 3.4. To locate the laser vertically at a good position, a calibration panel was made by sticking plasticized sheets of cross-section paper on a PVC plate and by suspending the whole system from the top of the reactor lid, as shown in Figure 3.11(b). The height of each sector was 80 mm so that it would be smaller than the dimension of the laser sheet and therefore allow optimal intensity in this area. As shown in Figures 3.11(c) and (d), the sectors were adjusted vertically on specific Y coordinates to allow 10 mm of superimposition of two adjacent sectors, thus making a junction area. In each junction area, the velocity value considered for the velocity field was the result of the arithmetic average of the two velocities coming from the two adjacent sectors. Horizontally, each sector covered the entire half tank (225 mm). An irregular glass welding around the vessel led to significant light distortions and made it impossible to obtain reliable data acquisition in the vicinity of Y = 633 mm. Thus, the area from Y = 609 mm to 658 mm has not been considered.
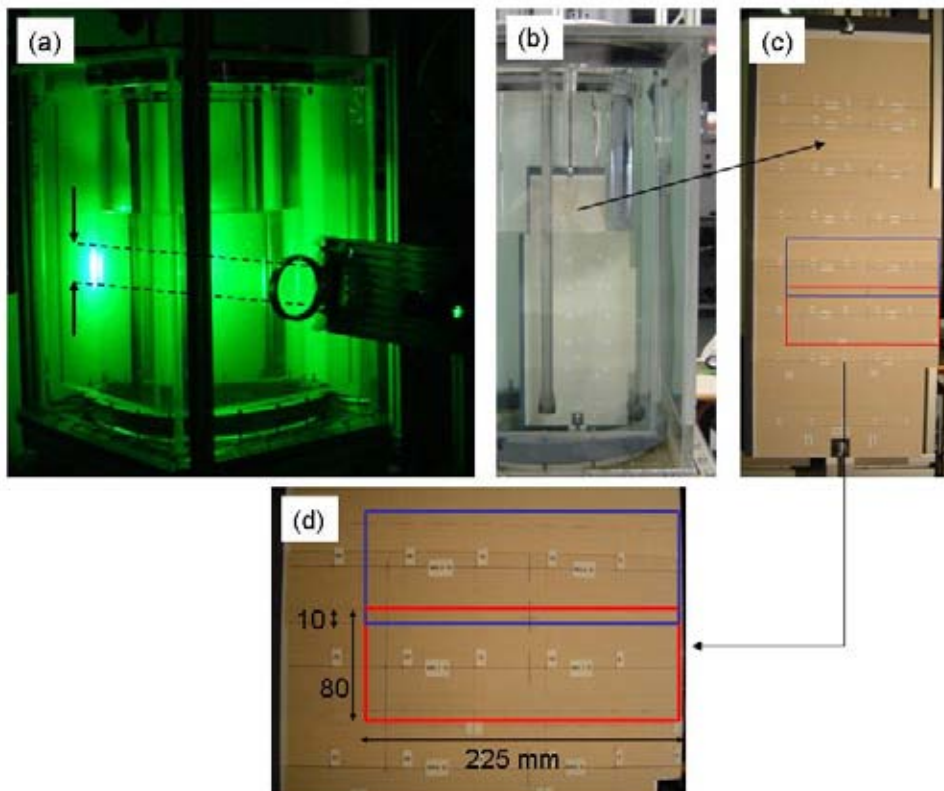
Figure 3.11. (a) laser sheet height compared with the liquid height; (b) PIV calibration panel immersed in the water in the stirred vessel; (c) PIV calibration panel alone; (d) zoom of two main sectors and a sector junction.

3.3.7. **Methods of image analysis**

The aim of the image analysis method is to determine the velocity vector in a defined area that contains a large number of particles. This zone can be defined by dividing the image into small areas, named interrogation areas, whose dimension may be set by the user. In each interrogation area, the most probable particle displacements are determined, in our case by calculating the cross correlation function, developed initially by Whillert and Gharib (1991). Readers interested in the details of the mathematics of the cross correlation function are referred to Rouland (1994). In this calculation, two hypotheses are assumed: the first is the iso-velocity hypothesis that assumes that the displacement of every particle in a single grid cell is identical; the second hypothesis is that the number of particles in the flow field is assumed to be statistically sufficient. The result of the correlation is the number of events that have occurred relative to a specific displacement. This is often represented using the three dimensional graph shown in Figure 3.12, where each displacement is represented by a peak and the highest corresponds to the most probable average displacement. Figure 3.12(a) shows only noise and 3.12(b) an example of a correlation peak obtained with our measurements.
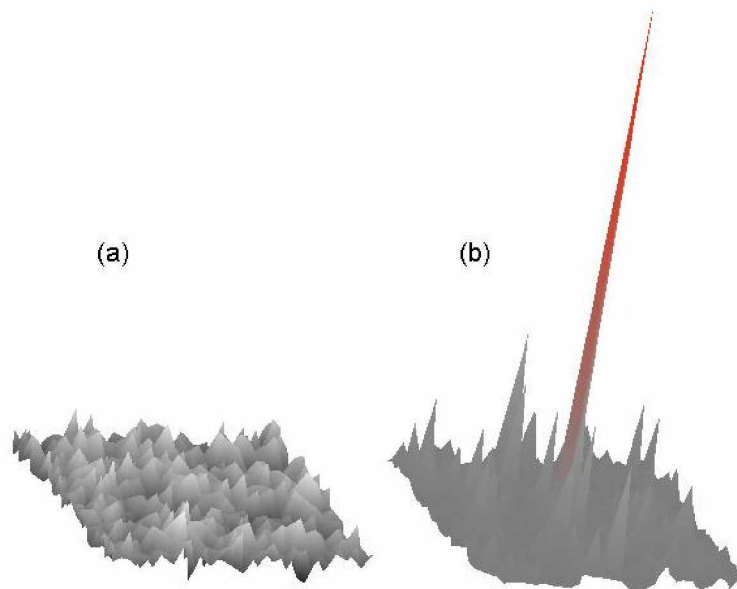
Figure 3.12. Three dimensional plot representing results of a cross correlation calculation: (a) only noise: (b) correlation peak

3.3.8. Results post processing

The calculation of the velocity vector in each interrogation area can be done with a single-pass or with multiple-passes. In our case, all the calculations were done with multi-pass, where the interrogation cell size was set to 64 pixels² for the preliminary step and reduced to 32 pixels² with 50% overlap for the final step, as shown in Figure 3.12.
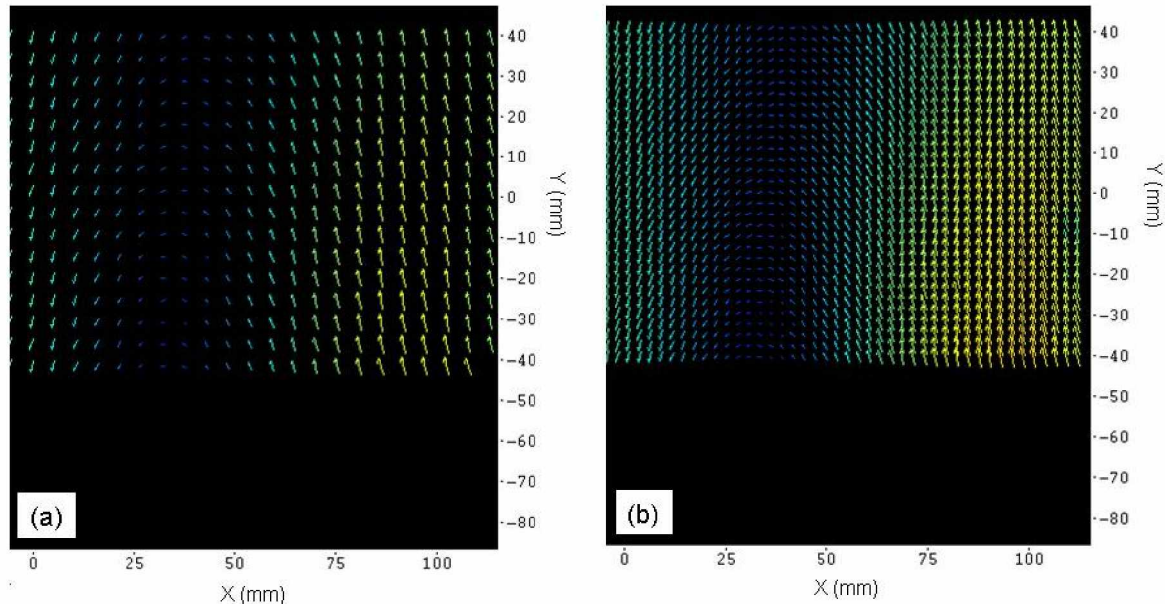
Figure 3.12. Multi-pass calculation and influence of the size of the interrogation area for an averaged velocity field (a) first step: 64 pixels²; (b) last step: 32 pixels² with 50% overlap. Y = 0 corresponds to the centre of the laser sheet.

A too large interrogation area removes the smaller turbulent structures that become apparent when a smaller interrogation area is used. A final interrogation area of 32 pixels² was sufficient to enable the complex nature of the flow field to be distinguished.

Several criteria concerning the post processing of the results have been optimized to obtain good resolution of the instantaneous and average flow fields. All the vectors which have one of their velocity components higher than the agitator tip speed were considered out of the allowable range and were deleted. In the same way, vectors having a peak-ratio less than 1.2 and all the isolated groups of vectors of less than five were also deleted. Finally, each accepted averaged velocity vector was calculated with the threshold of a minimum of five instantaneous vectors. For further details on each post-processing parameter, see the DAVIS 7.01 user's guide.

The purpose of this paragraph was not to be exhaustive on all the principles, technical details or mathematical developments relative to the PIV technique, but to provide useful information to allow the reader a good understanding of the following sections. As this experimental technique is covered in many papers and books, the reader is advised to consult one of the following list for additional information: Adrian (1991), La Fontaine and Shepherd (1996), Raffel *et al.* (1998) and Mavros (2001) for a review of the subject.

Chapter 4

CAPTURE OF THE FREE-SURFACE SHAPE

In this Chapter, the vortex shape of the free-surface formed in the pilot mixing vessel has been investigated using both experimental and numerical approaches for an air/water system for different rotation speeds of the agitator. The introduction presents a literature review of unbaffled and partially-baffled agitated vessels. In the following sections, a simple and flexible experimental strategy for determination of the time-averaged location of the unstable free-surface using a processes involving superimposition of images is described. CFD simulations were performed to predict the vortex shape using an Eulerian-Eulerian multiphase model coupled with a homogenous turbulence model. The simplifying assumptions of a constant bubble size, a constant drag coefficient and use of the k-ε turbulence model were made. An assessment of the capability of the numerical method to predict the vortex shape was carried out through comparison between experimental data and numerical results. Considering for comparison purposes an iso-surface for the water volume fraction equal to 0.9, to account for the existence of air/water mixture present at the interface in the experiments, instead of the classical value of 0.5, gave very good agreement with the experimental data.

4.1. INTRODUCTION

Fluid mixing is carried out in mechanically stirred vessels for a variety of objectives, including for homogenizing single or multiple phases in terms of concentration of components, physical properties and temperature. The choice of the tank geometry, the impeller type and the number and type of baffles can vary depending on the operation carried out. In the classical geometry, agitated vessels are fitted with baffles which are generally used in the transitional and turbulent flow regimes. Many agitated vessels use standard wall baffles which consist of four flat vertical plates, directed radially, spaced at 90 degree intervals around the vessel periphery, starting at the bottom tangent line of the lower vessel head and

running the length of the vessel side to the top tangent line of the upper head. Most vessels have at least three baffles, with four being the most common, often referred to as a fully-baffled condition. When a low viscosity liquid is stirred, the rotating impeller imparts a tangential motion to the liquid and if no baffles are present, the bulk fluid undergoes a swirling motion which approximates solid body rotation. The fluid moves along circular trajectories with high circumferential velocity creating poor mixing and a vortex is created at the free-surface. The fully-baffled condition destroys the vortex, keeping the free-surface flat, leading to an improved mixing rate and the swirling flow is converted into a preferred flow pattern desirable for process objectives, such as axial flow for blending and solids suspension, or radial flow for dispersions (Myers *et al*., 2002). For these reasons, baffled tanks are the most widely used in industrial applications and have received much more attention both by experimentalists and modellers (Alcamo *et al*., 2005, Ciofalo *et al*., 1996). For further information about baffled tanks, see Brucato *et al*. (1998) and Harris *et al*. (1996), who have performed extensive literature reviews of experimental and CFD simulation work on baffled vessels.

Although baffled configurations are encountered in most industrial stirred vessels, there are numerous applications where unbaffled tanks are used. Baffles are rarely used for side entering mixers in large product tanks and for angled mixers in small agitated tanks (Paul *et al*., 2004) or with close-clearance impellers, such as gates, anchors and helical ribbons, for which the impeller to tank diameter ratio is typically greater than 90%. In square or rectangular tanks, the corners break up the tangential flow pattern by providing some natural baffling in the sharp corners, which suppress to a considerable extent formation of the central vortex (Novák and Rieger, 1973), and wall baffles may not be needed (Myers *et al*., 2002). In some other special cases listed by Myers *et al*. (2002), internals such as heat-exchanger tubes contained inside the vessel provide sufficient baffling that additional baffles are not necessary. In fact, some reactors used to carry out highly exothermic reactions may contain so many heat exchangers tubes that the vessel is over-baffled, making it difficult for the agitator to promote sufficient flow. For further details on other applications where baffles are rarely used (e.g. side entering mixers in large product tanks, etc), see Paul *et al.* (2004) and Myers *et al*. (2002).

The reported minimum impeller Reynolds number for which the use of baffles is not required varies depending on the authors considered. According to Nagata (1975), baffles

should be eliminated if the flow is not in the fully turbulent region because this may lead to stagnant zones behind the baffles and the depression of the liquid surface is not significant. Alcamo *et al.* (2005) and Ciofalo *et al.* (1996) state that baffles are usually omitted for Re < 20, since for this laminar flow regime the dead zones created behind the baffles may actually worsen the mixing performance. According to Bakker and Gates (1995) and Myers *et al.* (2002), no baffles or only narrow baffles should be used for Re < 50, where the viscous action of the liquid at the vessel wall causes a natural baffling effect, eliminating the nearly solid-body rotation. The reader can refer to Alcamo *et al.* (2005), Bakker and Gates (1995), Ciofalo *et al.* (1996) and Nagata (1975) for detailed considerations on the minimum impeller Reynolds number for which the use of baffles is not required.

In comparison with baffled vessels, it should be noted that the unbaffled case has been poorly studied in the literature. The vortex, usually regarded as a drawback, may be desirable in a number of situations as listed by Smit and Düring (1991): the vortex created has proved to be useful for suspending floating or unwettable solid particles (see also Freudig *et al.* (1999), Joosten *et al.* (1977), Siddiqui (1993)); a vortex can be used for removing gas bubbles rapidly from the liquid and is often itself sufficient for preventing foam formation; if the heat transfer is a limiting process factor, the use of a vortex is advantageous because the available wall surface area increases and also the wall velocity is greater. Rousseaux *et al.* (2001) highlighted other advantages linked to the vortex formation as unbaffled vessels consume less power than those with baffles (Markopoulos and Kontogeorgaki (1995), Nagata (1975)), a better performance is noted for some cases of heat and mass transfer in unbaffled devices (Uhl and Gray, 1966); surface aeration and air entrapment can be observed when the vortex reaches the stirrer which is of great interest for gas/liquid reactions or phenomena (Brennan and Lehrer, 1976); unbaffled vessels are technologically easier to implement than classical vessels provided with baffles or draft tubes (Rousseau *et al.* (2001)).

In addition to fully-baffled, unbaffled and special cases, there exist non-standard baffling applications and in particular partially-baffled systems. This category of systems represents stirred baffled tanks that are equipped with baffles but where the baffling effect is not sufficient to prevent vortex formation. More quantitatively, the fully-baffled condition can be defined in terms of power consumption. Power consumption (P) in a mixing vessel is increased by the insertion of baffles and reaches a maximum value at a certain level of baffling, due to the impediment to the tangential flow and to the suppression of the central

vortex. Nagata (1975) has investigated the influence of the number of baffles plates on the power consumption and was the first to give a quantitative definition of the fully-baffled condition by the term Φ_B, which is proportional to the total area of the baffle plates, defined by Eq. (4.1):

$$\Phi_B = n_B \left(\frac{B_W}{T} \right) = 0.5 \tag{4.1}$$

or more exactly by Eq. (4.2):

$$\Phi'_B = n_B \left(\frac{B_W}{T} \right)^{1.2} = 0.35 \tag{4.2}$$

However, Sano and Usui (1987) found the same form of law but reported that the fully-baffled condition is attained when $\Phi_B = 0.4$. The same result ($\Phi_B = 0.4$) was found by Nishikawa *et al.* (1979) from the point of view of heat transfer and power consumption (cited by Sano and Usui (1987)). Lu, Wu and Ju (1997), who studied the effect of width and number of baffles in stirred vessels for systems with and without aeration, reported that the fully-baffled condition is more difficult to achieve if: (i) if the number of baffles is less than three; (ii) the rotational speed is increased, as found previously in Lu *et al.* (1997) that $\Phi'_B = 0.45$, 0.67 and 0.74 for N = 200, 300 and 400 RPM, respectively. In this study, a mixing vessel was considered fully-baffled if $\Phi_B > 0.4$, which corresponds to the minimum value of Φ_B found in the literature.

These partially-baffled conditions are usually encountered in glass-lined vessels. Although a minimum of three baffles are usually used in classical systems to avoid mechanical instability, a one or two baffle configuration is frequent for glass-lined vessels. The type of baffles usually found in glass lined reactors used for fine chemical and pharmaceutical productions are beaver-tail, H or D type, finger, flattened pipe, fin or concave baffles, as described by Paul *et al.* (2004). They have no contact with the reactor shell and are usually supported on the vessel head, rather than being mounted on the vessel wall, in order to prevent chemical fouling and dead zones. To produce good mechanical stability these baffles hang from flanges attached to the top of the vessel. Due to the limited space available on the head, no more than two baffles are used in glass-lined tanks. Myers *et al.* (2002) explain that

one of the main challenges for baffling in glass-lined vessels arises from the production process. The surface of the baffles must be contoured because sharp corners cannot be coated with glass. As a result, the most common type of baffle used is a pipe flattened to yield an elliptical cross section, commonly called a beaver-tail baffle, and this is the type used in this study. In addition, with only two baffles present, it can be difficult to provide sufficient baffling and glass-lined vessels are usually under-baffled. Concerning the beaver-tail baffle model used in this study, its width may be directly introduced in the Φ_B calculation formula of Eq (4.1), as this type of baffle, which is a flattened pipe, acts like a thick plate in cross-section. The calculation of Φ_B, using the geometrical data of the pilot reactor detailed in Chapter 3, gives $\Phi_B = 0.2$. In fact, Equations (4.1) and (4.2) were established using wall-baffles attached on the vessel shell. In the case studied here, the baffles are not attached to the shell and, in addition, the baffle-shell distance is much larger than the distance usually recommended in the standard configuration ($B'/T \approx 1/12$ instead of $B'/T = 1/50$). The influence of the baffles displaced from the wall on the tangential motion is less than that for the same baffles attached to the wall. Thus, the real value of the baffling factor Φ_B (which could be compared with literature values obtained using Eq. (4.1)) could be much lower than 0.2. Therefore, the experimental configuration used in this study is classified, without any doubt, as a partially-baffled system.

In this chapter, we examine the free-surface shape in a non-standard partially-baffled agitated vessel and the results obtained can be considered as a preliminary analysis of glass-lined, under-baffled stirred vessels. The existing experimental methods for the determination of the vortex shape and the numerical method used to simulate it, relative to unbaffled and glass-lined agitated vessels, are briefly reviewed. For unbaffled stirred vessels, construction of a model for the vortex geometry, experimental study of the vortex shape, construction of correlations for the vortex depth and determination of the critical impeller speed at which the gas/liquid interface reaches the impeller, have all received considerable attention from numerous authors for more than fifty years.

Nagata (1975) proposed a simplified theory to describe the vortex geometry. This theory is not detailed in this article but the reader can refer to Ciofalo *et al*. (1996) who took into account the modified formulation of Smit and Düring (1991). Le Lan and Angelino (1972) measured the vortex shape, by electrical contact between a vertical cylindrical electrode of 1

mm diameter and a conducting solution, along the entire tank radius. A potential difference was applied between this electrode and an auxiliary electrode represented by the tank itself, the contact between the electrode and the liquid gave a current flow and allowed the vortex shape to be determined. Zlokarnik (1971) observed the vortex through the wall of a transparent vessel and the depth was determined by a plate whose height was infinitely variable and free of parallax. Brennan (1976), who highlighted numerous variables affecting the vortex depth, made graduated marks on the impeller shaft and the vessel wall for measuring the vortex depth and elevation. Photographic analysis was carried out only for stirrer speeds corresponding to stable symmetrical vortices. An addition of NaOH from the surface to the stirred fluid (water, phenolphthalein solution and sufficient HCl solution for decolourization) revealed a red vortex core which was photographed after stabilization.

Rieger *et al*. (1979) have also carried out experimental investigations of vortex depth based on visual observations of marks made on the shaft and the vessel wall corresponding to the initial liquid surface position. Ciofalo *et al*. (1996) have made an assessment of the free-surface height by using a vertically adjustable finger movable through the tank diameter. Serra *et al*. (2001), who investigated turbulent flows in a Continuously Stirred Tank Reactor (CSTR) with a free-surface, used the interface elevation at the vessel wall to validate the accuracy of the calculations carried out. For a review of the correlations proposed for the prediction of the vortex depth in unbaffled agitated vessels with various types of single and multiple impeller systems, the reader is referred to Markopoulos and Kontogeorgaki (1995).

Experimental investigations using Laser Doppler Velocimetry (LDV) and Particle Image Velocimetry (PIV) techniques are extensively reviewed by Mavros (2001), and have also been used to investigate the flow field in unbaffled tanks. In parallel, due to the spectacular progress in digital computing, Computational Fluid Dynamics (CFD) has become a popular and powerful tool and provides detailed analysis of stirred vessels. Armenante and Chou (1994), Armenante *et al*. (1997) and Dong *et al*. (1994a and 1994b) determined experimentally the flow field using LDV and numerically predicted it in unbaffled vessels, equipped with a top lid with no head space (i.e. tank completely filled with water inhibiting vortex formation). Lamberto *et al*. (1999) investigated the laminar flow structure in a stirred tank by PIV and numerical computations, considering the upper surface of the fluid to be flat under conditions where vortex formation did not occur. Murthy Shekhar and Jayanti (2002) carried out flow field simulation of an unbaffled vessel stirred by an eight-blade paddle in

laminar, transitional and turbulent flow without a lid and compared the results with the experimental data of Dong *et al*. (1994a). They considered the top surface as flat with free slip and stated that this may introduce some errors in the formulation of the numerical model, especially at high Reynolds numbers. It was apparent that effects associated with vortex formation and free-surface deformation had to be taken into account in the simulation in order to get the correct results. Alcamo *et al*. (2005) have computed the flow field in an unbaffled stirred tank using Large Eddy Simulation (LES), but again they assumed a flat surface that inhibited vortex formation and any surface aeration. Montante *et al.* (2006), who have investigated experimentally and numerically the hydrodynamics of an unbaffled vessel stirred with a Ruston turbine located coaxially or eccentrically, assumed a flat free-surface and did not report any results concerning the free-surface shape. Hitomi *et al.* (2006) have avoided the simulation of the free-surface by choosing an agitator Reynolds number sufficiently low to provide a negligible variation of the free-surface level (less than 10 mm) and therefore the free-surface was fixed to a flat configuration with a free slip boundary condition.

Glass-lined vessel configurations equipped with a retreat blade impeller have also been investigated by some authors. Campolo and Soldati (2002) and Campolo *et al*. (2002) performed simulations of an industrial size CSTR, equipped with two beaver-tail baffles in a non-symmetrical position, from the laminar to the fully turbulent regime, for predicting power consumption and pumping efficiency, but they assumed a flat free-surface to limit the computational requirements. Li *et al.* (2004, 2005) carried out LDV measurements and CFD modelling of a stirred vessel equipped with a retreat blade impeller and one cylindrical baffle. The free-surface was also treated as a flat, free slip surface.

Very few authors have undertaken the challenge of simulating the flow field including the free-surface deformation. In 1996, Ciofalo *et al*. presented the first simulations of the free-surface profile for an unbaffled vessel. The simulations were performed without any empirical data and used a second order turbulence closure model (Differential Stress Model) including the effect of Coriolis forces, implemented in the computer code Harwell-FLOW3D®. An iterative method used with a treatment of non-orthogonal body fitted grids allowed prediction of a vortex shape in good agreement with Nagata's theory (1975) and with vortex height experiments conducted in a model tank. Serra *et al*. (2001) simulated a baffled CSTR, with coupling between the free-surface deformation and a full transient simulation of the flow field. They used a Volume of Fluid (VOF) method (Jeong and Yang, 1998) with a piecewise

linear interface calculation (PLIC) technique (Scardovelli and Zaleski, 1999; Tang *et al*., 2004) to reconstruct the temporal evolution of the free-surface profile. The time-averaged computed interface trend was captured correctly but some discrepancies between the numerical and experimental results were noted by the authors.

More recently, Haque *et al.* (2006) carried out numerical simulation of the turbulent flow with a free-surface vortex in unbaffled vessels agitated by a paddle impeller and a Rushton turbine using the standard Volume Of Fluid (VOF) method (also known as a homogeneous multiphase flow model). Cartland Glover and Fitzpatrick (2007), who have also noted very recently that for the majority of numerical studies of stirred tanks the liquid surface is not considered to deform with agitation, used the VOF approach with an MRF model with eight and six bladed paddle impellers. Their simulations showed that, using the standard VOF method, the predicted liquid surface profiles could be captured generally in good agreement with the experimentally-determined profiles of Haque *et al.* (2006), and in reasonable agreement with experimental data for Cartland Glover and Fitzpatrick (2007), but their cases resulted in smooth, parabolic-shaped interfaces and no entrainment of gas into the impeller swept region.

As can be seen from the state of the art described above, the free-surface treatment in numerical simulations has often been simplified to allow either comparisons with experimental apparatus equipped with a lid and full of liquid in order to avoid simulating the gas/liquid interface or by assuming a flat, stress free-surface and neglecting the vortex effects. Concerning the vortex shape which develops in these partially-baffled systems, as far as the authors are aware, no experimental or numerical results have been published to date. Thus, two innovative approaches: an experimental one to determine the vortex shape and a numerical one to calculate it using a CFD approach are presented.

4.2. EXPERIMENTAL METHODOLOGY

4.2.1. <u>Strategy for the experimental acquisition of the vortex shape</u>

One of the main motivations was to develop a simple and effective method for making vortex shape acquisition. The literature study presented earlier highlighted the fact that the experimental methods used by previous authors could only be applied to a stable free-surface, as encountered in unbaffled stirred vessels, but could not be used for unstable free-surfaces. In contrast, the experimental strategy presented in this Chapter is simple, flexible and requires only readily-available equipment. All the video data acquisition has been made using the Webcam (Philips Toucam Pro II) presented in §3.2.1. The Webcam was located in front of the tank in order to cover the field necessary to visualise the entire vortex shape. The software used for video post treatment was IRIS 4.17, usually used by amateur astronomers for deep sky or planetary photography. This freeware was downloaded from the internet (<u>http://www.astrosurf.org/buil/iris/iris.htm</u>).

The stirred tank studied here is the partially-baffled pilot reactor described previously in Chapter 3. The two beaver-tail baffles do not have sufficient impact on the solid-body rotation of the fluid to prevent vortex formation, and the vortex free-surface is unstable making visualization difficult. Nevertheless, the air/water interface generates a light/dark contrasted area and can be seen qualitatively as a dark shape without well-defined boundaries, as seen in Figure 4.1.
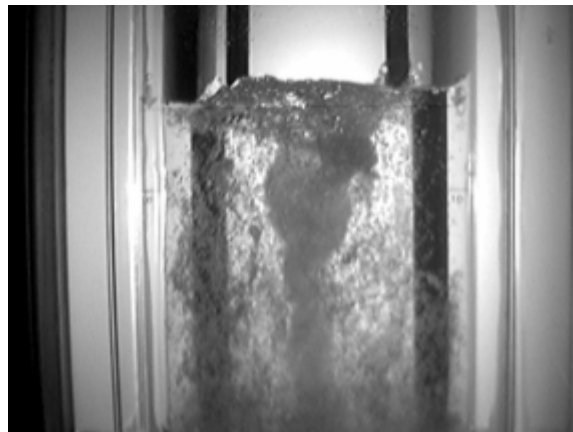
Figure 4.1. Picture of the vortex, webcam ToucamProII in Black and White mode, N = 275 RPM, the tank contains 109 L of water giving an initial height of $H_{init} = 700$ mm.

These fluctuating free-surface boundaries can be considered as an unstable phenomenon which has a variable position with time, and the method developed in this Chapter allows easy determination of these boundaries. The basic idea is that if a phenomenon observed has preferential positions in time, then a video recording with a given frame rate, decomposed into N_F individual frames and the subsequent superimposition of these N_F frames can highlight the most probable area. This idea has been developed with success in this study to highlight a clear vortex shape. The final number of individual frames resulting from the video decomposition is the product of the frame rate and the acquisition time. Classically, the frame rate must be fixed to fit the characteristic time of the physical phenomenon observed. Moreover, the computer buffer limits must be taken into account, as the requirements can become prohibitive if a relative high frame rate from a Webcam is used (> 30 frames/s). The characteristic time of the phenomenon observed does not require a higher frame rate but it can be easily changed for other observations, in smaller tanks for example. Recording during 60 s with a 5 frames/s frame rate was found to be a good compromise between the physical timescales of the system, the acquisition time, the memory allocation and the working computer limits. Thus, all the videos of the following experiments presented in this paper have been recorded with the Webcam during 60 seconds at a framing rate equal to 5 frames/s. The camera has been set to black and white mode because the experiments carried out did not require a coloured video acquisition. A black and white acquisition allows treatment of only one channel component during the image post treatment, as opposed to the red, green and blue components, if colour is used. The AVI file generated after acquisition was decomposed into N_F single frames by IRIS and gave 300 frames after decomposition. Then, these N_F frames were superimposed to make the final picture. Several tests with different acquisition times showed that the quality of the final superimposed picture was not improved with a number of frames higher than 300 for the experiments carried out here. The final picture obtained by the superimposition process is called the raw picture. This raw picture can be easily transformed using IRIS by setting of the image gain, denoted G, with $0 < G < 32,767$, which is used for improving the contrast and increasing the accuracy of free-surface mapping. Figure 4.2 presents the raw image (a) and three images (b, c and d) obtained by modification of the visualisation parameters following the basic settings available in IRIS from the raw picture. This raw picture was obtained with an initial water level of 700 mm, a rotation speed equal to 275 RPM, an acquisition time of 60s with a frame rate of 5 frames/s and a superposition of 300 frames to form the final picture. The raw picture (a) can be transformed into a black and white negative (b), a coloured picture proportional to the grey levels of the

black and white raw one (c) and finally a negative of the coloured picture presented with the optimal gain equal to 21,000 (d).
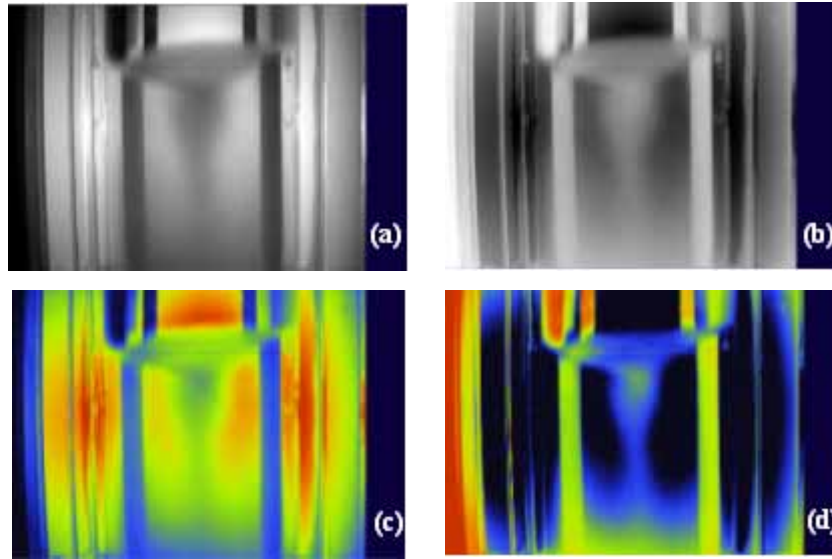
Figure 4.2. Final vortex pictures, N = 275 RPM. (a) black and white raw picture; (b) black and white negative picture; (c) coloured picture by transformation of the grey levels of (a); (d) negative coloured picture from (c) with G = 21,000.

The case of optimal gain, where a compromise has been made between image quality (low gain) with some loss of information and high gain, where the image quality is poor but all information is retained, gives the best definition of the free-surface. As shown in Figure 4.3, using the optimal gain of 21,000 allows the same free-surface contours to be obtained as when the maximum gain of 32,767 was used.
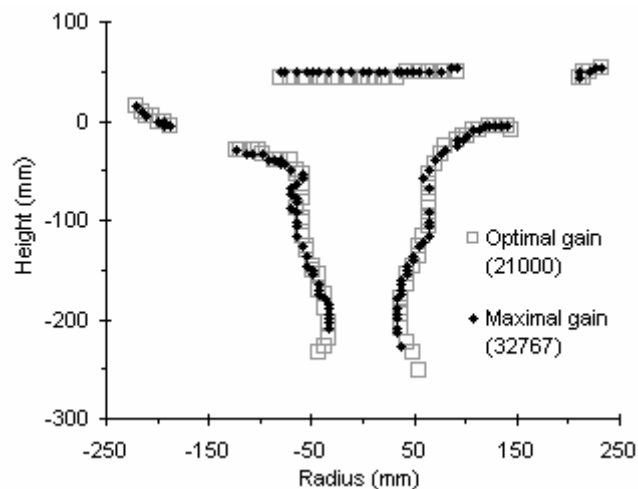
Figure 4.3. Comparison of the capture of the experimental free-surface shape obtained by using the optimal gain (G_{opt}) and the maximum gain (G_{max}).

Therefore, we used this basic contrast optimization strategy for all the free-surface contour mappings.

4.2.2. Calibration procedure

Using IRIS, it is possible to obtain the pixel coordinates of each point of the picture just by clicking with the mouse on the desired point of the computer screen. Then, an output window allows export of a set of pixel coordinates (X, Y) as a text file which can be used in a spreadsheet program. Due to the change of the refraction index between air, water and glass, refraction effects prevent the direct determination of the real geometrical dimensions and these appear larger than they are in reality. So, it was important to calibrate the acquisition method to transform a pixel map given by IRIS into a real geometric map useful for the studies carried out. For the calibration experiments, the stirred vessel was filled with 109 litres of water at ambient temperature and the square jacket around the cylindrical part of the reactor was also filled with water at the same temperature to the maximum level. The volume of liquid in the stirred vessel corresponded to the initial water level of 700 mm used in all of the following experiments. A rectangular grid (360 mm×600 mm) with regular cells (15 mm×30 mm) was plunged vertically into the reactor in the vortex measurement area, just behind the baffles to determine whether the curvature of the shell led to a non-uniform deformation of lengths in the tank. It was demonstrated that the modification of the grid size was regular on the entire grid and the curvature of the shell had no visible effect. Thus, only one standard for X and one for Y were sufficient for the calibration. The horizontal standard was the distance between the two baffles (281 mm) and the vertical standard was a metallic ruler with two phosphorescent marks spaced 200 mm apart, suspended from the reactor lid into the liquid in a central position. The calibration procedure has been tested for the determination of the real contour and position of the baffles, the initial liquid level and the position of the vertical standard marks.

Figure 4.4 represents the comparison between experimental measured points obtained by conversion from the pixel map to the real dimensions with conversion factors for X and Y equal to 5.38 and 4.85, respectively. Good agreement with the reference locations was observed and it was concluded that this method can determine the geometrical shapes and positions of locations within the tank with an uncertainty of +/- 10 mm.
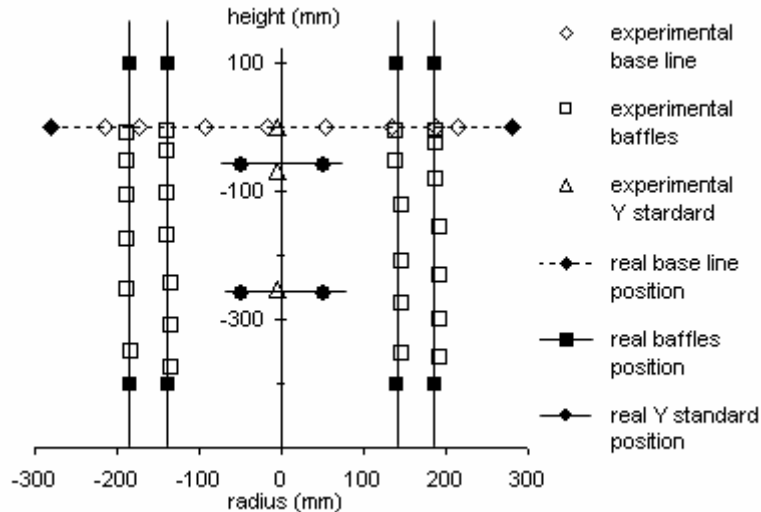
Figure 4.4. Comparison between the experimental positions determined from IRIS after calibration (hollow symbols) and real geometrical data of the vessel (full symbols).

4.3. CFD MODELLING

The numerical simulations were carried out with a commercial CFD package (ANSYS CFX 10.0) to predict the turbulent flow field and the free-surface shape in the stirred vessel. The simulation of a free-surface implies a separation between gas and liquid caused by the action of body forces and can only be captured by treating the fluid with a multiphase model. The fluids used were water and air at 25°C in a steady-state simulation. Free-surface flows are usually modelled by a Volume of Fluid (VOF) model which solves the Navier-Stokes equations, to obtain a common phasic velocity, together with an additional equation that allows determination of the free-surface location. In this study, the free-surface calculation is made using an Eulerian-Eulerian multiphase model. An inhomogeneous model was chosen to allow phase separation, as a homogeneous model assumes no slip between the liquid and gas, and therefore once fluids mix there is no means to separate them. The interfacial momentum transfer between the two phases was modelled using a disperse phase model in which the liquid phase is continuous and the gas phase is dispersed.

This model is characterized by the solution of an individual set of continuity and momentum equations for each phase. The flow field predictions are made via the numerical resolution of the Reynolds-Averaged Navier-Stokes equations. The volume fractions of the

phases are tracked with the condition that the volume fractions of all phases sum to unity. The inhomogeneous model applied for the velocity field was coupled with a homogenous turbulence model assuming the turbulent quantities are the same for the two phases, as the phases only co-exist in a small interfacial region. The k-ε turbulence model (Launder and Spalding, 1974) was used for reasons of stability and computational efficiency, and has proved to perform very well with our system. The literature review relative to the comparison of different turbulence models is detailed in Chapter 5 of this thesis, together with simulation results.

The continuity equation, written for each phase p, is expressed in Eq. (4.3) by:

$$\frac{\partial(\alpha_p \rho_p)}{\partial t} + \nabla \cdot (\alpha_p \rho_p \mathbf{u_p}) = 0 \qquad (4.3)$$

where α_p is the volume fraction, ρ_p is the density and $\mathbf{u_p}$ the phase averaged velocity.

The momentum equation for phase p is written in Eq. (4.4) as:

$$\frac{\partial(\alpha_p \rho_p \mathbf{u_p})}{\partial t} + \nabla \cdot (\alpha_p \rho_p \mathbf{u_p} \otimes \mathbf{u_p}) = -\alpha_p \nabla p$$
$$+ \nabla \cdot \left[\mu_p^{eff} \alpha_p \left(\nabla \mathbf{u_p} + (\nabla \mathbf{u_p})^T \right) \right] + \alpha_p \rho_p \mathbf{g} + \mathbf{M_{ip}} \qquad (4.4)$$

where $\mathbf{g}$ is the acceleration due to gravity and the interfacial forces acting on each phase are represented by the term $\mathbf{M_{ip}}$ due to the interaction between the two phases.

μ_p^{eff} is the effective viscosity defined by :

$$\mu_p^{eff} = \mu_p^{lam} + \mu_p^{turb} \text{ with } \mu_p^{turb} = \rho_p C_\mu \frac{k^2}{\varepsilon} \text{ and } C_\mu = 0.09 \qquad (4.5)$$

Only drag forces were included for momentum exchange between the two phases. The total drag exerted on the continuous phase by the gas per unit volume is given by Eq. (4.6):

$$\mathbf{M_{ip}} = \mathbf{M_{gl}} = \frac{3}{4} \frac{\alpha_g \rho_l}{d_b} C_D |\mathbf{u_g} - \mathbf{u_l}| (\mathbf{u_g} - \mathbf{u_l}) \qquad (4.6)$$

where C_D is the drag coefficient and d_b is an assumed bubble size.

For modelling the vortex shape, two models have been tested for the calculation of the drag coefficient C_D. The first is the modified Schiller-Naumann drag model presented in Eq.

(4.7), and available in ANSYS CFX 10.0, in which the drag coefficient is modified to ensure the correct limiting behaviour in the inertial regime. Thus, C_D is automatically bounded below with increasing particle Reynolds number (Eq. (4.9)) and takes a minimum value of 0.44. The second model tested is a constant drag coefficient model (Eq. (4.8)) usually applied when the particle Reynolds numbers (Eq. (4.9)) is sufficiently large for inertial effects to dominate over viscous effects (Dhotre and Smith (2007), Pfleger and Becker (2001)).

$$C_D = \text{Max}\left\{ \frac{24}{\text{Re}_p}(1 + 0.15\text{Re}_p^{0.687}), 0.44 \right\}, \quad 0.1 \leq \text{Re}_p \leq 1 \text{ - } 2\times 10^5 \qquad (4.7)$$

$$C_D = 0.44, \quad 1000 \leq \text{Re}_p \leq 1 \text{ - } 2\times 10^5 \qquad (4.8)$$

$$\text{where } \text{Re}_p = \frac{\rho_l d_b |u_g - u_l|}{\mu_l} \qquad (4.9)$$

The values of k and ε come directly from the partial differential transport equations for the turbulent kinetic energy and the turbulence energy dissipation rate, which are expressed in Eq. (4.10) and (4.11), respectively:

$$\frac{\partial(\rho_m k)}{\partial t} + \nabla \cdot (\rho_m \mathbf{u_m} k) = \nabla \cdot \left[\left(\mu_m^{\text{lam}} + \frac{\mu_m^{\text{turb}}}{\sigma_k} \right) \nabla k \right] + \tilde{P} - \rho_m \varepsilon \qquad (4.10)$$

$$\frac{\partial(\rho_m \varepsilon)}{\partial t} + \nabla \cdot (\rho_m \mathbf{u_m} \varepsilon) = \nabla \cdot \left[\left(\mu_m^{\text{lam}} + \frac{\mu_m^{\text{turb}}}{\sigma_\varepsilon} \right) \nabla \varepsilon \right] + \frac{\varepsilon}{k} \left(C_{\varepsilon 1} \tilde{P} - C_{\varepsilon 2} \rho_m \varepsilon \right) \qquad (4.11)$$

with $\rho_m = \alpha_g \rho_g + \alpha_l \rho_l$, $\mu_m^j = \alpha_g \mu_g^j + \alpha_l \mu_l^j$ (j = lam or turb), $\mathbf{u_m} = \dfrac{\alpha_g \rho_g \mathbf{u_g} + \alpha_l \rho_l \mathbf{u_l}}{\rho_m}$ and $C_{\varepsilon 1}$, $C_{\varepsilon 2}$, σ_k and σ_ε are the k-ε turbulence model constants equal to 1.44, 1.92, 1.0 and 1.3, respectively.

The turbulent kinetic energy production due to shear is given in Eq. (4.12):

$$\tilde{P} = \mu_m^{\text{turb}} \nabla \mathbf{u_m} \cdot \left(\nabla \mathbf{u_m} + (\nabla \mathbf{u_m})^T \right) - \frac{2}{3} \nabla \cdot \mathbf{u_m} \left(3\mu_m^{\text{turb}} \nabla \cdot \mathbf{u_m} + \rho_m k \right) \qquad (4.12)$$

A Multiple Reference Frame (MRF) model was used in this study. The stirred vessel was separated into regions modelled in rotating and stationary frames: the rotating frame is used for the bottom dish containing the rotating impeller, and the stationary frame was used for the cylindrical part of the vessel, containing the cylindrical part of the vessel walls and the two

baffles. A no slip condition was set at all solid/liquid interfaces. The boundary condition used on the upper surface of the vessel was the free slip condition, which prevents any flow through the boundary and sets zero gradients for all other quantities. This boundary condition is removed far from the areas of interest and has no significant impact on the results. A frozen rotor condition is set at the interface between the rotating and stationary frames, implying a change of reference frame across the interface but with the relative orientation of the components remaining fixed.

An unstructured grid was used in the simulations. The density of cells was optimized to be fine enough to capture flow details without being excessive. Figure 4.5 shows the grid used in the proximity of the right baffle end.
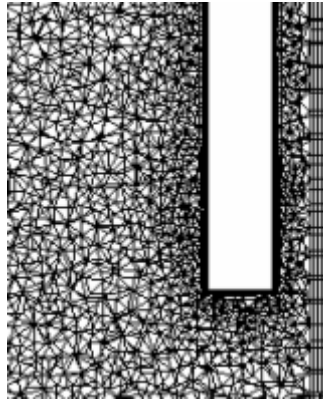
Figure 4.5. Unstructured grid used in the simulations in the region near the right baffle bottom tip and the reactor shell.

Note that inflation meshing was used at all walls. The final mesh, based on sensitivity studies, was composed of 208,000 nodes. All simulations were performed using a second order bounded differencing scheme for the momentum and volume fraction equations to limit numerical diffusion as much as possible, with upwind differencing used the turbulence equations for stability. The convergence criterion adopted for the simulations is based on the RMS (root mean square) normalised values of the equation residuals. The runs were terminated when the residuals for the mass, momentum and turbulence equations were below 10^{-4}, and below 10^{-3} for the volume fraction equations.

The simulations carried out assumed a liquid height of 700 mm, with 100 mm of gas above it. A reference density equal to that of the gas phase was used in the simulations to

assist with convergence. The simulation was initialized with a hydrostatic pressure profile in the liquid phase defined as $p(y) = \rho_l\, g\, (H_{liq} - y)$, for $y \le H_{liq}$.

4.4. RESULTS AND DISCUSSION

For unstable free-surfaces, as is the case in this study, the process of air bubble formation at the air/water interface, pumping of these down into the liquid due to the liquid velocity field and escape into the gas phase due to the buoyancy force leads to a dynamical system which was hard to treat. The bubble size used for this study was chosen based on physical considerations and results provided by Laakkonen *et al*. (2005). They used a capillary suction probe technique to measure the local volumetric bubble size distributions in a 0.194 m^3 fully-baffled vessel agitated with a Rushton turbine equipped with a ring gas sparger located below the agitator. They found that the Sauter mean diameter measured in the baffle mid-plane close to the surface at 250 RPM for an air-tap water system was close to 3 mm for the two different gas flow rates tested (d_{32} equal to 2.7 mm and 3 mm, respectively, for air feed rate equal to 0.052 and 0.093 m^3 (gas) m^{-3} (dispersion) min^{-1}). Whilst this situation is different to ours, it provides a guide to the likely stable bubble size in this system.

The influence of the bubble diameter has been investigated through five simulations from $d_b = 1$ mm to 10 mm. Figure 4.6 shows the water volume fraction profiles on the XY plane and highlights a strong dependence of the water volume fraction profile on the air bubble size.
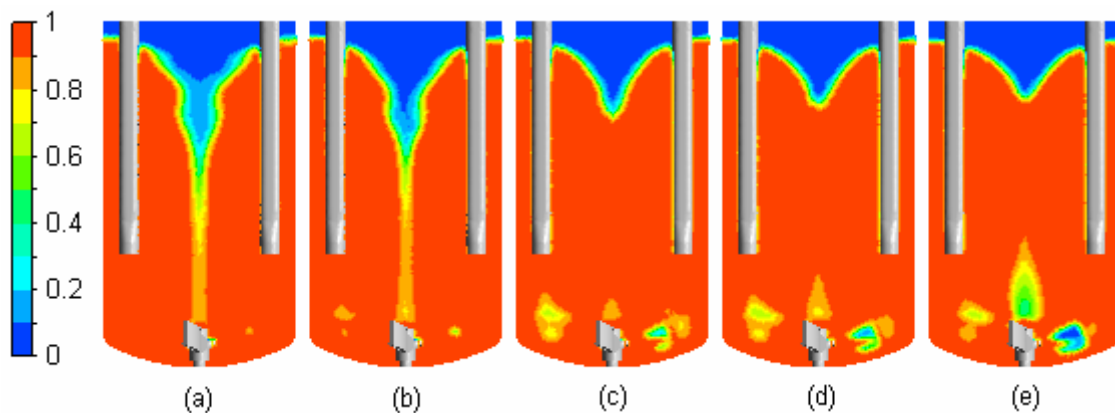
Figure 4.6. Water volume fraction profiles on the XY plane containing the baffles obtained using different air bubble diameter: (a) $d_b = 1$ mm; (b) $d_b = 3$ mm; (c) $d_b = 5$ mm; (d) $d_b = 7$ mm, (e) $d_b = 10$ mm.

In the range of d_b from 3 mm to 10 mm, the free-surface flattens out, the air column linking the top and the agitator region disappears and the gaseous retention around the agitator increases as the air bubble diameter increases. However, the results were found to be insensitive to a change of bubble diameter in the range 1 mm to 3 mm, with a 3mm size giving the best convergence. Thus, a constant bubble diameter of 3 mm was adopted for the following simulations.

Concerning the drag coefficient model, the comparison between numerical prediction of the vortex shapes at 275 RPM using a modified Schiller-Naumann drag coefficient model or a constant drag coefficient equal to 0.44 led to identical vortex shapes, as shown in Figure 4.7.
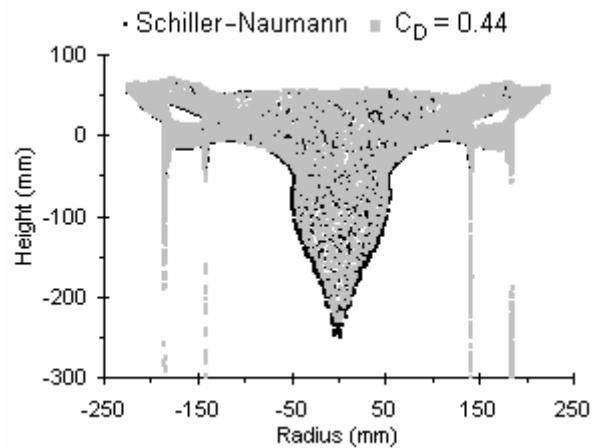
Figure 4.7. Comparison between the vortex shapes obtained using the Schiller-Naumann drag coefficient model or a constant drag coefficient equal to 0.44 (Isosurface of water volume fraction equal to 0.5).

Thus, the simplest model (Eq. (4.8)) was adopted for the remainder of the computational calculations. In this system there is obviously a complex interaction between the phases as bubbles of various sizes mix at the interface and disentrain due to buoyancy. The bubble size and drag coefficient were chosen to give a physically realistic estimate of the drag force between the gas and liquid. Here we are not trying to model this process in detail but rather we assume a fixed bubble size and a constant drag coefficient that provide sufficient slip at the interface to represent this process.

The vortex surface, being physically the interface between the gas and the liquid, was obtained from the simulations by the 3D representation of a water isosurface volume fraction.

Figures 4.8(a) and (b) show the water volume fraction profile obtained at 275 RPM and the corresponding vortex represented by a water volume fraction isosurface of 0.5, respectively.
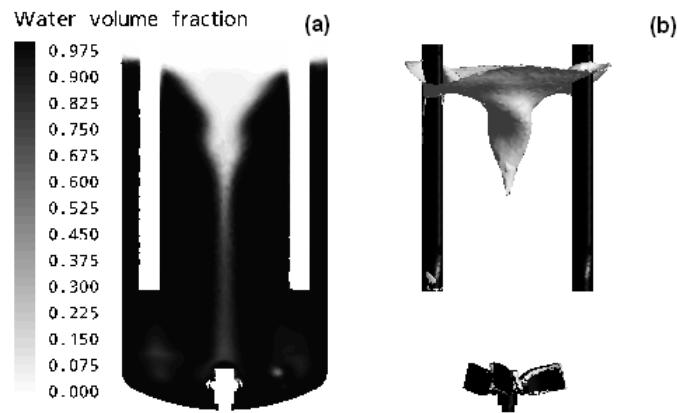
Figure 4.8. (a) Water volume fraction profile with N = 275 RPM; (b) isosurface of volume fraction equal to 0.5.

To compare the planar image view with the experimental results, a projection of the free-surface onto the vertical XY baffle plane has been made, considering only the X and Y coordinates of the vortex shape (the Z coordinate being normal to the baffle plane).

Firstly, the influence of the value of the water volume fraction used to determine the free-surface shape has been investigated for a constant rotation speed of 275 RPM and water volume fraction values ranging from 0.5 to 0.95. Figure 4.9 compares the experimental vortex shape determined at the optimal gain (21,000) with an isosurface of water volume fraction equal to 0.5 (Figure 4.9(a)) and 0.9 (Figure 4.9(b)).
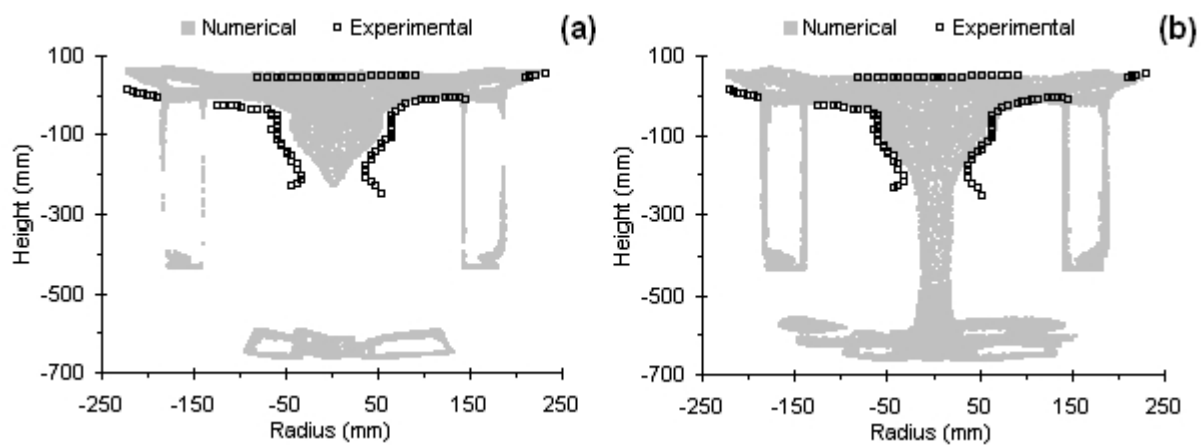
Figure 4.9 Comparison between experimental vortex shape profile (negative coloured picture, G = 21,000, N = 275 RPM) and the projection on the XY vertical plane of isosurfaces of water volume fraction (N = 275 RPM); (a) isosurface of water volume fraction equal to 0.5; (b) isosurface of water volume fraction equal to 0.9.

These comparisons lead to several comments. The experimental results and the numerical prediction give the same global vortex shape. It can be noted that the numerical predictions of the curvatures of the vortex boundary in its central part (the bulb shape) and the maximum liquid height (median or lateral parts) are in relatively good agreement with the experimental results.

In addition, the water volume fraction used for the calculation of the isosurface representing the vortex has a significant influence on the comparison. The small gradient of water volume fraction profile around the gas/liquid interface is sufficient to give a difference in the free-surface representation. It may be seen that the use of a water volume fraction of 0.9 instead of 0.5 leads to better agreement between the experimental results and the numerical predictions. This may be due to the experimental strategy for vortex shape capture. The image picture method is very sensitive to a small percentage of gas mixed into the liquid phase. It is clearly visible that the imaging process does not differentiate between the high volume fraction of gas present in the vortex core and the bubbles pumped down by the agitation effect into the liquid at the bottom tank. The free-surface boundary, which represents the vortex shape, is a region of dynamical equilibrium, where gas bubbles are introduced into the liquid and subsequently come out again into the vortex core. Thus, this dynamical area of intense gas movement could be captured by the camera and included in the free-surface shape. This may explain why the experimental data are closer to the numerical predictions made with a water volume fraction equal to 0.9. Alternatively, the numerical model and particularly the use of an interfacial momentum transfer term $\mathbf{M_{ip}}$ including only the drag force could play an important role in the prediction of the water volume fraction profile. The interfacial forces acting on the gas bubbles should also contain the Basset, virtual mass and lift forces, but these have been neglected in the present simulations. If they are included, one may arrive at a different value for the water volume fraction that best fits the experimental profiles. Figure 4.10 shows the comparison between the experimental image of the vortex shape for 275 RPM and the numerical isosurface of water volume fraction equal to 0.9 represented at the same scale. Very good agreement is shown between these two figures.
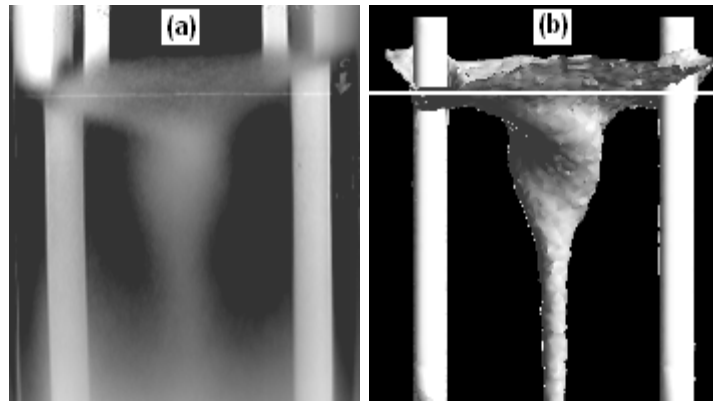
Figure 4.10. Comparison on the same scale of the experimental (a) and the numerical (b) vortex shapes; (a) negative coloured picture, G = 21000, N = 275 RPM; (b) isosurface of water volume fraction equal to 0.9 (N = 275 RPM).

Further results have been obtained for additional impeller speeds (200, 250, 300 and 350 RPM). Figures 4.11 and 4.12 contain the results.
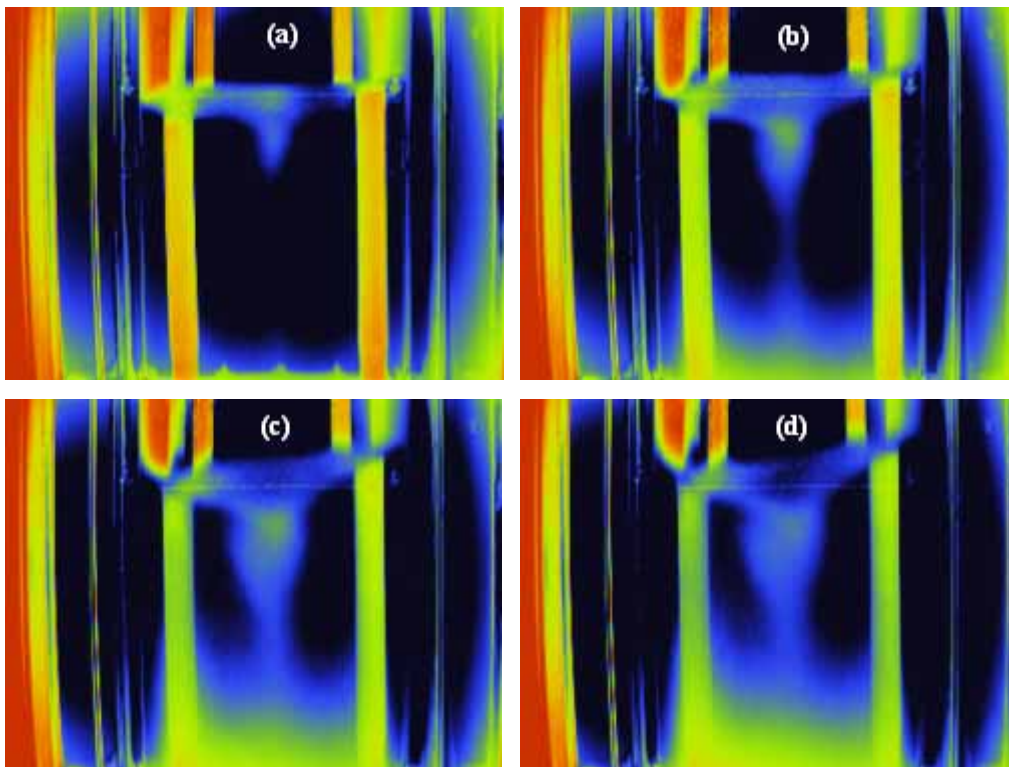
Figure 4.11. Experimental acquisitions of the vortex shapes, negative coloured pictures; (a) N = 200 RPM, G = 26000; (b) N = 250 RPM, G = 22500; (c) N = 300 RPM, G = 20000; (d) N = 350 RPM, G = 18000.

Good agreement between the experimental data and numerical predictions was observed with the global vortex shape at 250 and 300 RPM. The maximum height reached by the

liquid, the bottom vortex contour located between the baffles and the central vortex bulb and the periphery of the bulb shape vortex were predicted in satisfactory agreement with the experimental results. At 200 RPM, both the numerical and experimental vortex profiles showed a "closed" vortex, in the sense that the vortex bottom could be located precisely, contrary to the vortex shapes observed at higher rotation speeds. Nevertheless, some discrepancies were noted at the lowest (200 RPM) and the highest (350 RPM) impeller rotation speeds tested. At 200 RPM, the experimental vortex was deeper than the numerical results. It is hypothesised that the small central core was not captured in the numerical work, as the predicted flat base is not consistent with the expected shape. At 350 RPM, the experimental acquisition was uncertain due to the very high number of bubbles pumped down into the tank and rotating into the bulk. In addition, the thickness of the air/water zone around the free-surface was wider, increasing the measurement uncertainties of the vortex contour.
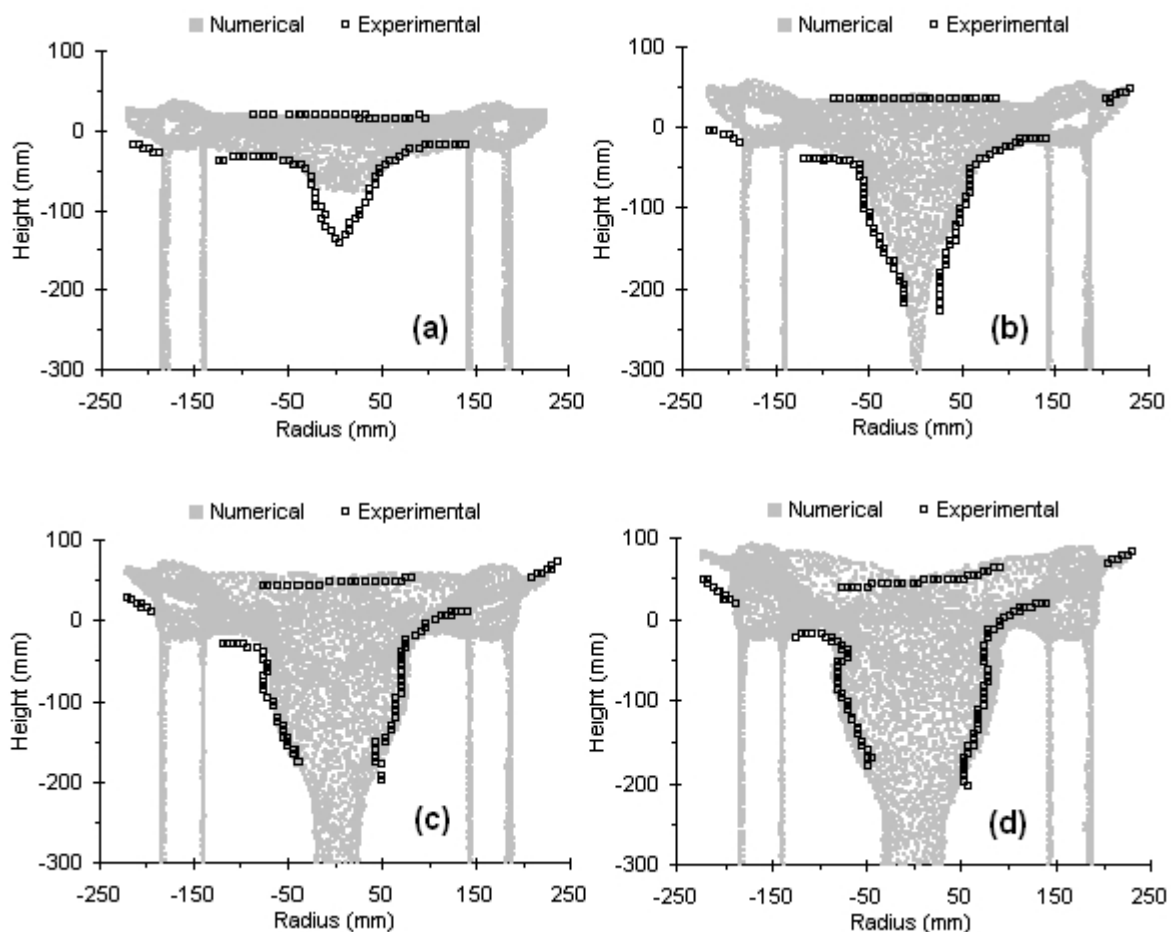
Figure 4.12. Comparison between experimental vortex shapes (negative coloured pictures with the optimal gain) and the projection on the XY vertical plane of isosurfaces of water volume fraction equal to 0.9; (a) 200 RPM; (b) 250 RPM; (c) 300 RPM; (d) 350 RPM.

4.5. CONCLUSIONS

The vortex shape that develops in a non-standard, partially-baffled, agitated vessel of 450 mm diameter, similar to glass-lined under-baffled stirred vessels, has been studied both experimentally and numerically. The strong instability of the free-surface due to the dynamic process of bubble formation and pumping at the air/water interface accompanied by gas disengagement lead to the development of a novel experimental strategy to measure the vortex shape. A video acquisition method based on the superposition of images was used and showed the capability to determine accurately the position of the vortex contours at different rotation speed from 200 to 350 RPM.

The vortex shape was also predicted numerically by CFD using an Eulerian-Eulerian multiphase approach, coupled with post-processing in the form of volume fraction isosurface profiles. An assessment of the capability of the numerical method to predict the vortex shape was carried out through comparison between experimental data and numerical results. Even with the use of a homogeneous k-ε turbulence model and the approximations of a single bubble diameter and a constant drag coefficient used in the CFD calculations, the numerical model was able to give a vortex shape in very good agreement with the experimental data from 250 to 350 RPM. Instead of the classical value of a water isosurface volume fraction equal to 0.5, a value of 0.9 gives the best agreement with experimental data due to the presence of the dynamical equilibrium zone of intense gas/liquid exchanges which occurs around the free-surface into the air zone. Although the modelling of the detailed gas entrainment and disentrainment process was not carried out in this study, it is a challenging problem to take into account in future work.

Chapter 5

VESSEL HYDRODYNAMICS

This Chapter starts with a brief literature survey of the turbulence models used in CFD simulations of mixing vessels. Then, the numerical predictions of the mean flow field, obtained by using the standard k-ε and the SSG Reynolds Stress turbulence models, are compared with experimental PIV data. At low rotation rates a flat free-surface is observed and the flow is simulated using a single phase model, whilst at high rotation rates an Eulerian-Eulerian multiphase model is used to capture the free-surface location. It is shown that there are significant transient effects that mean many of the "rules of thumb" that have been developed for fully-baffled vessels must be revisited. In particular such flows have central vortices that are unsteady and complex, transient flow-induced vortical structures generated by the impeller-baffle interactions and require a significant number of simulated agitator rotations before meaningful statistical analysis can be performed. Surprisingly, better agreement between CFD and experimental data was obtained using the k-ε than the SSG Reynolds stress model. The multiphase inhomogeneous approach used here with simplified physics assumptions gives good agreement for power consumption, and with PIV measurements with flat and deformed free-surfaces, making this affordable method practical to avoid the erroneous modelling assumption of a flat free-surface often made in such cases.

5.1. INTRODUCTION

Mixing is one of the most common and most important operations in the process industries. The situation most frequently encountered in industry is an agitated vessel which is fully-baffled, causing the destruction of the impeller-generated vortex and thus having a flat liquid surface. Although partially-baffled reactors are frequently encountered in the polymer, pharmaceutical and specialty chemicals industries, they have been poorly studied in the literature, where there is a lack of experimental and numerical studies. As a consequence, the

study of the hydrodynamics which develops in these stirred tanks, where the free-surface deformation cannot be neglected, is particularly interesting and challenging.

Extensive literature reviews of experimental and CFD simulation work have been provided for fully-baffled vessels (see Brucato *et al.* (1998), Van den Akker (2006)), with a great number of these works concentrated on turbulent, single phase flows in tanks stirred by Rushton turbines. In addition, most experimental studies have been carried out with the liquid surface covered by a lid to prevent vortex formation. The unbaffled case, in comparison with the baffled case, has been studied much less. Very few studies were found in the literature that relate to the computation of a turbulent flow in a stirred vessel, including free-surface deformation. A detailed literature review of simulations of unbaffled and partially-baffled vessels was presented in Chapter 4 and also in Torré *et al.* (2007a).

Various turbulence models have already been tested and compared for mixing vessel computational studies by several authors. The standard k-ε model (Launder and Spalding, 1974) has served the engineering community well for many years because it is robust, rapid and provides reasonable results for many flows (Paul *et al.*, 2004). This model, which uses the eddy viscosity hypothesis, is known to over-estimate turbulent viscosities in stagnant areas and may have limitations for systems with high streamline curvature, swirling flows or vortex generation, as mentioned in Alcamo *et al.* (2005), Ciofalo *et al.* (1996) and Jenne and Reuss (1999). Jaworski *et al.* (1997), who studied the flow generated by a Ruston turbine with a sliding mesh approach using the standard k-ε and RNG k-ε turbulences models, concluded that the mean velocity components predicted with the two models did not differ significantly in the whole tank and matched the experimental data well, except in the trailing vortex region. In addition, the same author (Jaworski and Zakrzewska, 2002) compared the CFD predictions of the mean velocity and the turbulent kinetic energy obtained by using six different turbulence models, with experimental data from LDA. The models used were the standard k-ε, the RNG k-ε, the realizable k-ε, the Chen-Kim k-ε, the optimized Chen-Kim k-ε and a Reynolds Stress Model. The best results were obtained using the standard k-ε model which gave good predictions for the mean velocity but a significant under-prediction of the turbulent kinetic energy (Jaworski and Zakrzewska, 2002). It would be expected that more accurate numerical results would be obtained through the use of models not based on the assumption of an isotropic eddy viscosity. The Algebraic Stress Model (ASM) used by Armenante *et al.*

(1997), and the Reynolds Stress Model (RSM) are known to perform better for highly swirling flows with anisotropic turbulence, such as those that develop in unbaffled vessels, or hydrocyclones (Narasimha *et al.*, 2007). This turbulence anisotropy is due to the fact that because of the constrained swirling flow field, turbulence fluctuations in the tangential and axial directions are increased in comparison with those in the radial direction (Cokljat *et al.*, 2006). Nevertheless, as mentioned in Aubin *et al.* (2004), this model is rarely used for the simulation of baffled agitated vessels due to convergence problems.

Haque *et al.* (2006) have performed a study which deserves special interest. They modelled an unbaffled agitated vessel using the Shear Stress Transport (SST) and RSM turbulence models and compared numerical predictions with experimental data for free-surface shape and the velocity on various lines in the tank. They concluded that there is better agreement between the experimental profiles and the SST model predictions in the inner region of the vortex, whereas in the outer region, the RSM model provides better agreement. Concerning their prediction of the surface shape profile, they declared: "it is, however, difficult to draw a definite conclusion on the performance of the SST and RSM models with regard to the quality of the surface-profile predictions at high impeller speeds". Concerning the comparison between the SST and the k-ε turbulence models, no quantitative data obtained with the k-ε model have been reported to judge the difference between the SST and the k-ε models. Using the RSM and k-ε models, they compared experimental data for radial velocity (obtained by Nagata (1975)) and numerical predictions at two vessel heights. In the impeller stream they obtained very good agreement using the RSM but there were no data in the inner half of the tank close to the vessel axis. Above the impeller blades, good agreement was obtained in the free-vortex region using the RSM but they concluded that "in the forced-vortex region, in contrast with measurements, both turbulence models return virtually zero radial velocity".

More fundamental approaches, such as LES and DNS, are discussed in a recent review by Van den Akker (2006) but these are generally too expensive for engineering applications. In this study, both the standard k-ε eddy viscosity model and a second moment Reynolds Stress Model, developed by Speziale, Sarkar and Gatski (Speziale *et al.* (1990), Basara and Younis (1995)) and denoted RSM-SSG, have been tested for single phase flows.

In Chapter 4, it was demonstrated that a steady, Eulerian-Eulerian multiphase method can predict the vortex shape in good agreement with experimental data for different agitator rotation speeds (Torré *et al.* (2007a)). However, no comparisons between the flow-field predictions and experimental data were reported. In the first part of this Chapter, guidelines on the simulation procedures required to obtain meaningful mean velocity data are obtained using single phase simulations for a case where the surface is flat. The single phase predicted results are then compared with results from the inhomogeneous multiphase flow model. Then, the capability of the numerical methods used to capture the free-surface shape and the hydrodynamics of partially-baffled systems are examined through comparisons between experimental observations and PIV results.

5.2. CFD MODELLING

Numerical simulations of the turbulent flow field have been carried out using the commercial CFD package ANSYS-CFX 10.0. The predictions were made in a fully transient manner using fluids at 25°C and the well-known sliding mesh approach. The flow fields obtained from the computations need to be averaged in time for comparison with the PIV data. This process has highlighted several important questions concerning the time required before averaging can be started and how many agitator rotations are necessary to obtain relevant numerical data. The answers to these questions have proved to be complex and are discussed later.

5.2.1. <u>Single phase simulations</u>

Single phase simulations with water only and a flat free-surface were run initially to understand certain elements of the problem before multiphase simulations were run. The governing equations and the turbulence closure models used in the single phase simulations are presented in this paragraph.

After averaging and selecting a closure hypothesis, the Reynolds-averaged equations, called URANS (Unsteady Reynolds Averaged Navier-Stokes equations), are obtained. For

clarity in the equations, the bar which represents averaged quantities is dropped, except for products of fluctuating quantities.

The continuity equation is expressed in Eq. (5.1) by:

$$\nabla \cdot \mathbf{u} = 0 \tag{5.1}$$

- **k-ε model:**

As the standard k-ε model employs the eddy-viscosity hypothesis, the momentum equation may be expressed as:

$$\frac{\partial(\rho \mathbf{u})}{\partial t} + \nabla \cdot (\rho \mathbf{u} \otimes \mathbf{u}) = -\nabla p' + \nabla \cdot \left[\mu^{\text{eff}} \left(\nabla \mathbf{u} + (\nabla \mathbf{u})^{\text{T}} \right) \right] \tag{5.2}$$

where μ^{eff} is the effective viscosity defined by :

$$\mu^{\text{eff}} = \mu^{\text{lam}} + \mu^{\text{turb}} \text{ with } \mu^{\text{turb}} = \rho C_{\mu} \frac{k^2}{\varepsilon} \text{ and } C_{\mu} = 0.09$$

p' is a modified pressure expressed in Eq. (5.3) as:

$$p' = p + \frac{2}{3}\rho k + \rho \mathbf{r}.\mathbf{g} \tag{5.3}$$

The values of k and ε come directly from the partial differential transport equations for the turbulent kinetic energy and the turbulence dissipation rate, which are expressed in equations (5.4) and (5.5), respectively:

$$\frac{\partial(\rho k)}{\partial t} + \nabla \cdot (\rho \mathbf{u} k) = \nabla \cdot \left[\left(\mu^{\text{lam}} + \frac{\mu^{\text{turb}}}{\sigma_k} \right) \nabla k \right] + \tilde{P} - \rho \varepsilon \tag{5.4}$$

$$\frac{\partial(\rho \varepsilon)}{\partial t} + \nabla \cdot (\rho \mathbf{u} \varepsilon) = \nabla \cdot \left[\left(\mu^{\text{lam}} + \frac{\mu^{\text{turb}}}{\sigma_\varepsilon} \right) \nabla \varepsilon \right] + \frac{\varepsilon}{k} \left(C_{\varepsilon 1} \tilde{P} - C_{\varepsilon 2} \rho \varepsilon \right) \tag{5.5}$$

with $C_{\varepsilon 1}$, $C_{\varepsilon 2}$, σ_k and σ_ε being model constants that are set to the usual values of 1.44, 1.92, 1.0 and 1.3, respectively.

The turbulence production due to shear is given is Eq. (5.6):

$$\tilde{P} = \mu^{\text{turb}} \nabla \mathbf{u} \cdot \left(\nabla \mathbf{u} + (\nabla \mathbf{u})^{\text{T}} \right) \tag{5.6}$$

▪ **Reynolds Stress Model (SSG)**

In the Reynolds Stress Model (RSM), the momentum equation to be solved is given by:

$$\frac{\partial(\rho\mathbf{u})}{\partial t} + \nabla\cdot(\rho\mathbf{u}\otimes\mathbf{u}) = -\nabla p'' - \nabla\cdot\left(\rho\overline{\mathbf{u}'\otimes\mathbf{u}'}\right) + \nabla\cdot(\mu\nabla\mathbf{u}) \qquad (5.7)$$

where p'' is again a modified pressure. Unlike in the eddy viscosity model, the modified pressure has no turbulence contribution and is related to the static pressure by:

$$p'' = p + \rho\mathbf{r}.\mathbf{g} \qquad (5.8)$$

In this model, separate equations are solved for the six components of the Reynolds stress tensor and for the turbulence energy dissipation rate (ε). The anisotropic diffusion coefficients of the original models have been replaced by an isotropic formulation, which increases the robustness of the Reynolds stress model, as expressed in Eq. (5.9), written in Cartesian-tensor notation:

$$\frac{\partial\left(\rho\overline{u_i'u_j'}\right)}{\partial t} + \frac{\partial\left(u_k\rho\overline{u_i'u_j'}\right)}{\partial x_k}$$
$$= P_{ij} + \phi_{ij} + \frac{\partial}{\partial x_k}\left[\left(\mu^{lam} + \frac{2}{3}C_S\rho\frac{k^2}{\varepsilon}\right)\frac{\partial\overline{u_i'u_j'}}{\partial x_k}\right] - \frac{2}{3}\delta_{ij}\rho\varepsilon \qquad (5.9)$$

ϕ_{ij} is the pressure-strain correlation, and P_{ij} is the shear production term which is given by:

$$\boldsymbol{P} = -\rho\left(\overline{\mathbf{u}'\otimes\mathbf{u}'}(\nabla\mathbf{u})^T + (\nabla\mathbf{u})\overline{\mathbf{u}'\otimes\mathbf{u}'}\right) \qquad (5.10)$$

As noted above, an additional equation is solved for the turbulence energy dissipation rate as given below in Eq. (5.11):

$$\frac{\partial(\rho\varepsilon)}{\partial t} + \frac{\partial(\rho u_k\varepsilon)}{\partial x_k} = \frac{\varepsilon}{k}\left(C_{\varepsilon 1}\tilde{P} - C_{\varepsilon 2}\rho\varepsilon\right) + \frac{\partial}{\partial x_k}\left[\left(\mu^{lam} + \frac{\mu^{turb}}{\sigma_{\varepsilon RS}}\right)\frac{\partial\varepsilon}{\partial x_k}\right] \qquad (5.11)$$

where

$$\mu^{turb} = \rho C_{\mu RS}\frac{k^2}{\varepsilon} \qquad (5.12)$$

and the turbulent kinetic energy comes directly from $k = \frac{1}{2}\overline{u_i'u_i'}$.

The complete pressure strain term can be modelled, after the application of various kinematical constraints (Basara and Younis (1995)), by the form expressed in Eq. (5.13):

$$
\begin{aligned}
\phi_{ij} = &-\left(C_{S1}\varepsilon + C_{R1}\tilde{P}\right)\rho b_{ij} - C_{S2}\rho\varepsilon\left(b_{ik}b_{ij} - \frac{1}{3}b_{mn}b_{mn}\delta_{ij}\right) \\
&+\left[C_{R2} - C_{R3}(b_{mn}b_{mn})^{1/2}\right]\rho k S_{ij} \\
&+ C_{R4}\rho k\left(b_{ik}S_{jk} + b_{jk}S_{ik} - \frac{2}{3}b_{mn}S_{mn}\delta_{ij}\right) \\
&+ C_{R5}\rho k\left(b_{ik}W_{jk} + b_{jk}W_{ik}\right)
\end{aligned}
\tag{5.13}
$$

where b_{ij}, S_{ij} and W_{ij} are the Reynolds stress anisotropy, the mean rate of strain and the mean vorticity tensors, and the turbulence energy production term defined, respectively, in Eqs. (5.14), (5.15), (5.16) and (5.17), as:

$$
b_{ij} = \frac{\overline{u_i' u_j'}}{k} - \frac{2}{3}\delta_{ij}
\tag{5.14}
$$

$$
S_{ij} = \frac{1}{2}\left(\frac{\partial u_i}{\partial x_j} + \frac{\partial u_j}{\partial x_i}\right)
\tag{5.15}
$$

$$
W_{ij} = \frac{1}{2}\left(\frac{\partial u_i}{\partial x_j} - \frac{\partial u_j}{\partial x_i}\right)
\tag{5.16}
$$

and

$$
\tilde{P} = \frac{1}{2}\text{trace}\left(\tilde{\mathbf{P}}\right) = -\rho\,\overline{\mathbf{u}' \otimes \mathbf{u}'} \cdot \nabla\mathbf{u}
\tag{5.17}
$$

The model coefficients have been calibrated for a number of simple homogeneous flows, details of which may be found in Abid and Speziale (1993) and Speziale *et al.* (1990). The reader is referred to Basara and Younis (1995) for further details. The values used here for the model constants are listed in Table 5.1.

Table 5.1. Constants used in the SSG Reynolds Stress model simulations

$C_{\mu_{RS}}$	$\sigma_{\varepsilon_{RS}}$	C_S	$C_{\varepsilon1}$	$C_{\varepsilon2}$	C_{S1}	C_{S2}	C_{r1}	C_{r2}	C_{r3}	C_{r4}	C_{r5}
0.1	1.36	0.22	1.45	1.83	1.7	-1.05	0.9	0.8	0.65	0.625	0.2

5.2.2. <u>Multiphase simulations</u>

The multiphase simulations were carried out using an Eulerian-Eulerian multiphase model which considers the water and air as the continuous and the dispersed phases, respectively. The model equations and the assumptions used for modelling of the free-surface are not repeated here as they were detailed in Chapter 4.

The stirred vessel was modelled using an unstructured grid of 230,000 and 209,000 nodes (958,000 and 832,000 elements) for the single and multiphase cases, respectively, optimised by sensitivity studies to be fine enough to capture the flow without being excessive, and to give grid independent velocity fields. The rotating domain was set to be the entire bottom dish which includes the agitator and the sliding interface was represented by the horizontal surface which connects the cylindrical part of the vessel and the bottom dish. A no-slip condition was applied to all walls (vessel and bottom dish walls, agitator and baffles) except at the very top surface of the vessel where the free-slip condition was set. This boundary condition prevents any flow through the surface and sets the normal gradients for all other quantities to zero, representing a lid that is well removed from the region containing liquid. The simulations were carried out with an initial liquid height of 700 mm, and for the inhomogeneous approach with 100 mm of gas above the liquid interface. The quantities of liquid and gas remain fixed in the simulation and the initial condition described above is used to enable the water to rise up the vessel walls as the vortex is generated with no liquid loss from the computational domain.

The simulations were run using the sliding mesh approach using the transient rotor-stator model available in ANSYS CFX 10.0, with a 2° rotation angle of the agitator per time-step and a maximum of 10 coefficient loops at each time-step, which ensured good convergence. The transient runs were initialized from steady-state results obtained using the Multiple Reference Frame (MRF) approach. The instantaneous velocity of the liquid was monitored during the simulation at fifteen monitor points located on the vertical median plane of the two baffles. These monitor points were located vertically at three different vessel heights (Y = 200, 400 and 600 mm) and radially at five positions which are r = 0, ± 75 mm and ± 150 mm.

5.3. EXPERIMENTAL METHODOLOGY USING PARTICLE IMAGE VELOCIMETRY

The stirred tank investigated is the partially-baffled pilot reactor described previously in Chapter 3. The instantaneous velocity fields were measured in this agitated vessel filled with 109 litres of tap water for all experiments and the flow in the stirred vessel was investigated using the Particle Image Velocimetry (PIV) technique. The principles of PIV have been detailed in Chapter 3, together with the technical details necessary for this chapter.

In short, the flow was seeded with fluorescent tracer particles of Rhodamine-B. A double pulsed Milite Nd:YAG continuum laser of wavelength 532 nm (green) was used to illuminate these particles with a short time difference (Δt = 1 ms and 0.4 ms for N = 100 RPM and 200 RPM, respectively). An appropriate lens and optical system allowed transformation of the laser beam into a vertical laser sheet of 100 mm height and about 1 mm thickness passing through the centre of the vessel and midway between the two baffles. To capture the frames exposed by laser pulses, the black and white CCD camera (La Vision Imager Intense) with a resolution of 1376×1024 pixels² was used. The camera was equipped with the telephoto lens (Nikon – Nikkor 50mm/1.2) that was used to focus on the laser sheet, protected with the high pass filter (see Chapter 3 for details). It was located 1087 mm away from the light sheet and normal to the jacket sidewall. The image acquisition rate was set to 3 Hz in order not to freeze the flow in the event that low frequency instabilities exist. The snapshots were not synchronized with the passage of impeller blades.

960 images were found to be necessary and sufficient to obtain the averaged flow field, as shown in Figure 5.1.

To cover the entire half tank, the measurements required the construction of a mosaic composed of six different sectors included in the PIV plane, as detailed in Chapter 3. The discrepancy in the velocity magnitude between the values measured at the same locations in adjacent fields of view and the averaged value in the junction areas was typically less than 10% for the axial and radial velocities along the entire vessel radius, as shown in Figure 5.2.
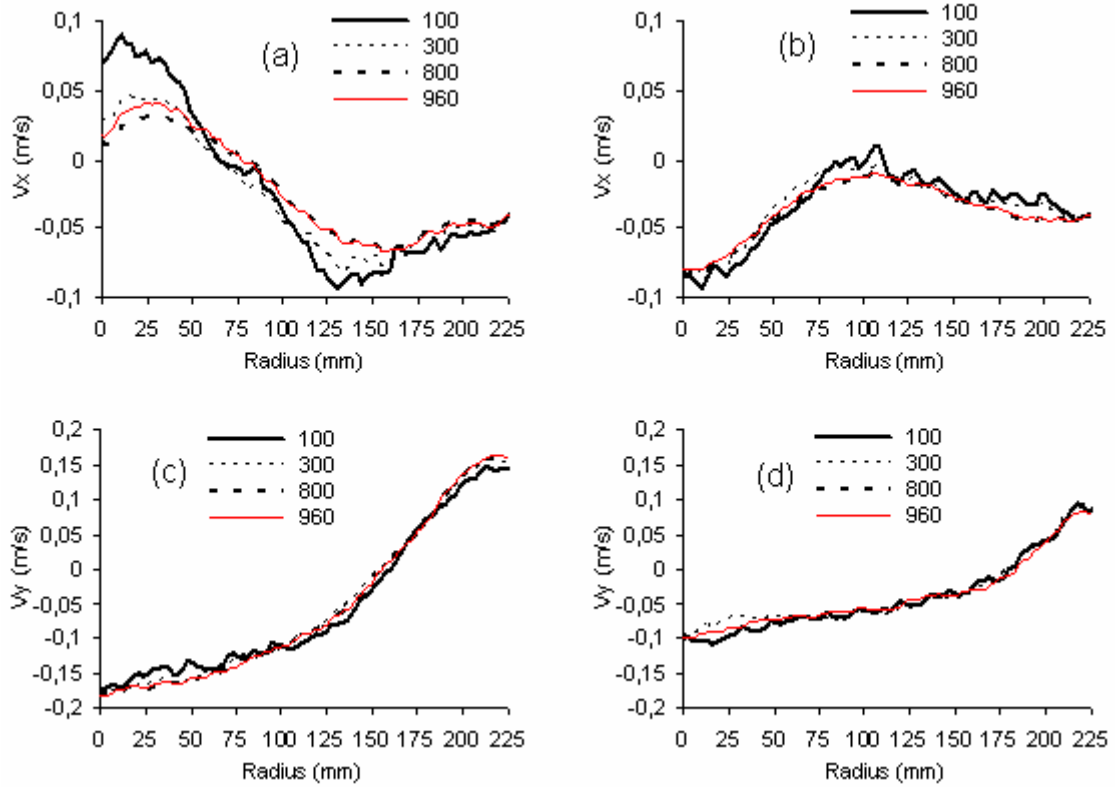
Figure 5.1. Experimental velocities for N = 100 RPM on the lines Y = 388 mm and Y = 528 mm for four different numbers of PIV images pairs: (a) radial velocity Vx at Y = 388 mm, (b) radial velocity Vx at Y = 528 mm, (c) axial velocity Vy at Y = 388 mm, (d) axial velocity Vy at Y = 528 mm.
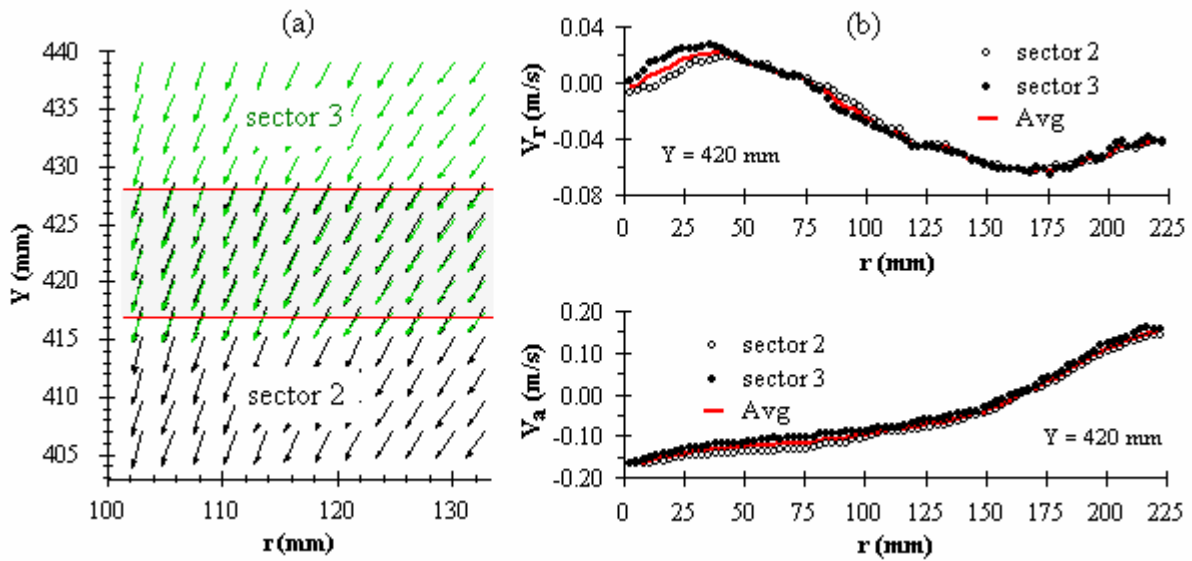
Figure 5.2. Overlapping region between two adjacent fields of view (sector 2 and sector 3). (a): superimposition of the vector fields; (b) radial and axial liquid velocities in each sectors measured on the horizontal line located at Y = 420 mm.

An exception was the radial velocities measured close to the vessel axis (r < 50 mm) where the discrepancy between the average value and the velocity measured in each sector was up to 50%. This relatively high difference is attributed to the very low value of the radial velocity near the vessel axis, combined with the uncertainties resulting from the transient effects in this area caused by rising bubbles and a precessing vortex. An irregular glass welding around the vessel led to significant light distortions and made it impossible to obtain reliable data acquisition in the vicinity of Y = 633 mm. Thus, the area from Y = 609 mm to 658 mm has not been considered. Two different cameras were used for experimental data capture. The vorticity filaments were filmed using the high resolution CMOS camera (HCC-1000 model from VDS Vosskühler) monitored by the NV1000 software from New Vision Technologies. The image resolution was 1024×1024 pixels². The camera was located normal to the vessel jacket sidewall, and was equipped with a telephoto lens (Nikon – Nikkor 50mm/1.2). The capture of the precessing vortex moving on the free-surface required the mounting of a camera above the free-surface. For these measurements, the video data acquisition was made using the commercial Webcam (Philips Toucam Pro II) detailed in Chapter 3. The data were transferred to the computer via a USB link and the frame rate was 15 frames/s.

5.4. RESULTS

5.4.1. <u>Transient instabilities and quasi-steady state</u>

Figure 5.3 presents the computed velocity field obtained using the k-ε turbulence model at nine of the monitoring-points versus the number of agitator rotations for N = 100 RPM. The velocities measured on the monitor points where r < 0 were found to have the same tendencies as those for r > 0. Thus, to simplify the figure, only the monitor points with r ≥ 0 are presented.

Although the normalized residuals of the momentum, continuity and turbulence equations were all below 10^{-4}, the evolution of the velocity during the first fifteen agitator rotations (N_r < 15) differs from the following rotations (N_r > 15). For 0 < N_r < 5, the velocity remains quasi-stable with weak oscillations. For 5 < N_r < 15, a pronounced decrease, followed by an

increase of the velocity magnitude for the points located at r = 0 and r = 75 mm is observed, while this variation is less pronounced for r = 150 mm. The reproducibility of the velocity profiles has been tested on two different simulations and it was found to be exactly the same. Thus, the initial agitator rotations were not included in the averaging process and the collection of transient statistics was started only after fifteen revolutions.
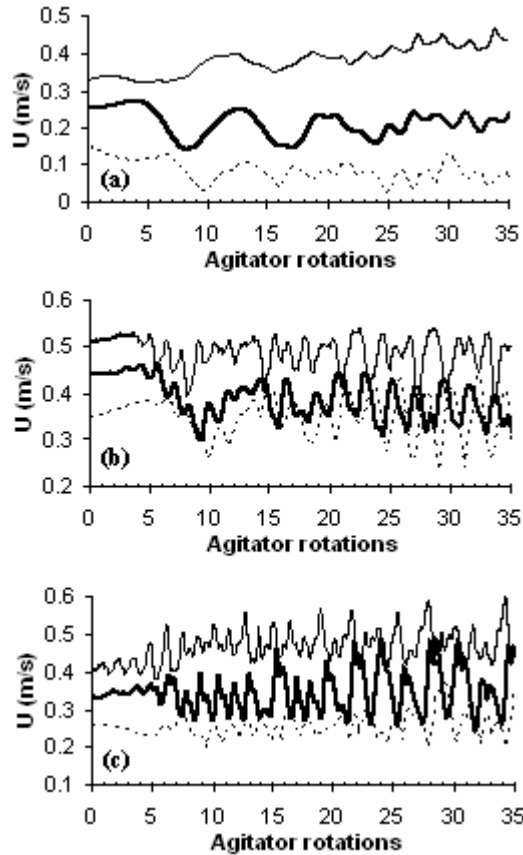
Figure 5.3. Instantaneous velocity evolution versus number of agitator rotations for different locations in the vessel and N = 100 RPM. Regular line: Y = 200 mm; bold line: Y = 400 mm; dashed line: Y = 600 mm. (a) r = 0; (b) r = 75 mm; (c) r = 150 mm.

The number of agitator revolutions needed to reach a quasi-steady state in our study is of the same order of magnitude as the number of revolutions needed by Li *et al.* (2004, 2005) to reach a quasi-steady state. Their numerical studies of a mixing vessel equipped with a retreat curve impeller and only one cylindrical baffle were carried out using a sliding mesh approach, the Shear Stress Transport turbulence model and used a steady-state result as initialization, required 9 - 10 agitator rotations to reach the quasi-steady state. In contrast, Campolo *et al.* (2002) ran their simulations during 30 - 40 agitator revolutions because they started their sliding mesh computations from conditions of a stationary fluid. As concluded also by Li *et al.* (2005), the use of a converged steady-state result as initialization of a transient sliding

mesh run greatly reduces the number of agitator revolutions needed before a quasi-steady state is reached.

Single phase simulations run in steady-state mode (SS) lead to good convergence (residuals $< 10^{-4}$). Contrary to this, the multiphase runs do not converge as well (residuals between 10^{-4} and 10^{-3}) when the agitator rotation speed was set to a value below 200 rpm. As shown in Figure 5.4(b), the free-surface shape predicted by the inhomogeneous model for $N =$ 100 RPM starts off by being deformed at $N_r = 0$ due to the poor convergence of the steady-state initialisation but flattens out after a few impeller revolutions.
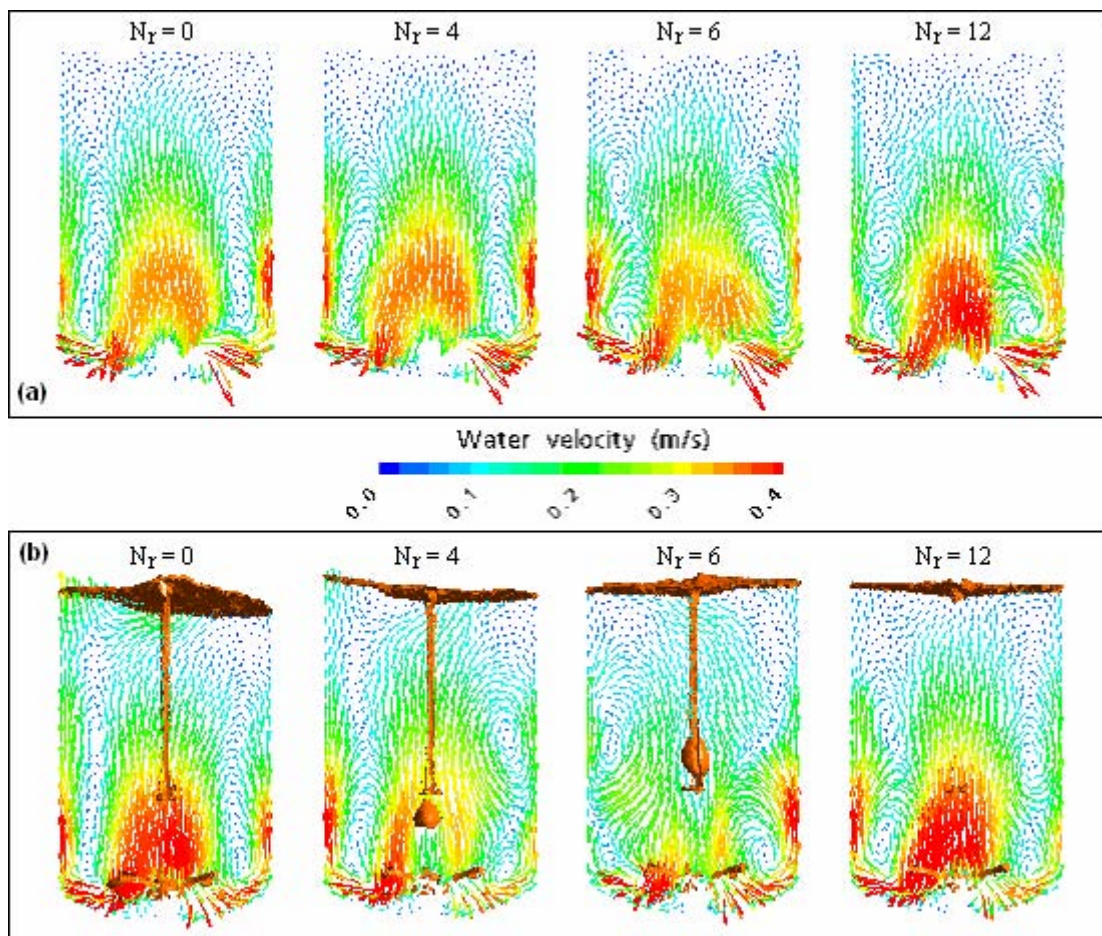
Figure 5.4. Axial-radial instantaneous velocity vectors on the vertical median plane of the two baffles obtained after steady-state ($N_r = 0$) and at the end of $N_r = 4$, 6 and 12 agitator revolutions, $N = 100$ RPM: (a) single phase simulation; (b) two phase simulation.

The predicted flat free-surface at 100 rpm is in very good agreement with the experimental observations made at this rotation speed. Figure 5.4 shows that the steady-state initialization imposes a double loop flow structure and it takes about five revolutions to break it into

multiple secondary recirculation loops. In addition, a Fast Fourier Transform (FFT) spectral analysis (Duhamel and Vetterli (1990)) of the numerical velocity data obtained from monitor points during many agitator revolutions showed a complex, periodic flow structure. The number of acquisition points compatible with this FFT analysis must be a power of two and was set to Z = 2048 and 4096 for the k-ε and SSG RSM simulations, respectively. These data were sampled numerically each iteration with a frequency, F_s, equal to 300 Hz, giving the resolution frequencies ($\Delta f = F_s/Z_{FFT}$) equal to 0.15 Hz and 0.073 Hz for the k-ε and SSG spectral analysis, respectively. The power spectra obtained at N = 100 RPM, using the k-ε and the SSG turbulence models, are presented in Figure 5.5(a) and Figure 5.5(b) for one example position respectively, (Y = 200 mm and r = 75 mm).
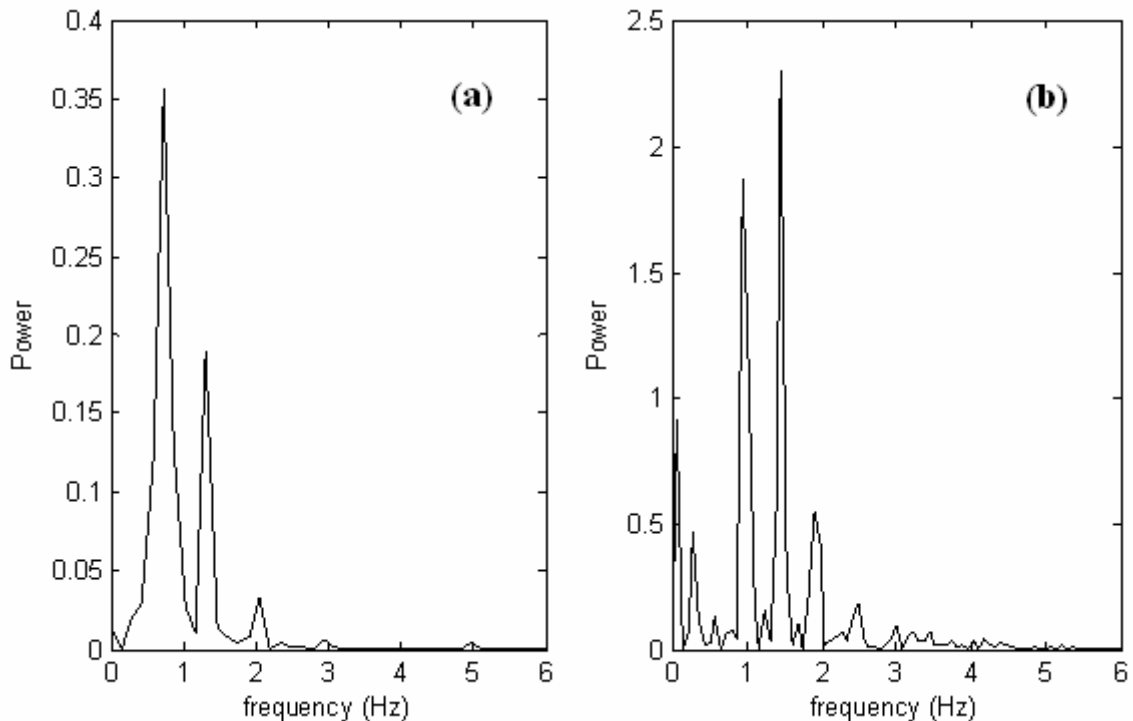
Figure 5.5. Fast Fourier Transform power spectrum of the velocity; Y = 200 mm, r = 75 mm, N = 100 RPM; (a) k-ε model, (b) SSG Reynolds Stress model.

The frequency analysis revealed comparable characteristic frequencies which are 0.73 Hz, 1.32 Hz with the k-ε model and 0.95 Hz, 1.46 Hz for the SSG model. The three-bladed agitator frequency is 5 Hz which corresponds to three times the complete revolution frequency of the agitator at 100 RPM (1.66 Hz). Thus the intrinsic period of the flow was found not to be an exact multiple of the agitator rotation rate. These periodic fluctuations of the flow can be linked to instabilities.

The investigation of macro instabilities (MIs) in stirred vessels has received much attention by numerous authors. MIs are principally caused by changes in the circulation patterns which constrains the flow to oscillate between different stable configurations, and to one (or more) precessing vortices revolving around the axis of the tank. In the investigations carried out by Hasal *et al.* (2003), Nikiforaki *et al.* (2003 and 2004), Roussinova *et al.* (2003) and more recently Ducci and Yianneskis (2007) and Paglianti (2006), the reader can find further details on the subject. In the partially-baffled stirred vessel investigated in this study, a small camera (Philips Toucam ProII) located just above the liquid surface on the vessel axis allowed tracking of the free-surface deformations. A precessing vortex, revolving around the vessel axis with an estimated frequency of 0.4 Hz, is clearly visible at 100 RPM and an actual trajectory is shown in Figure 5.6.
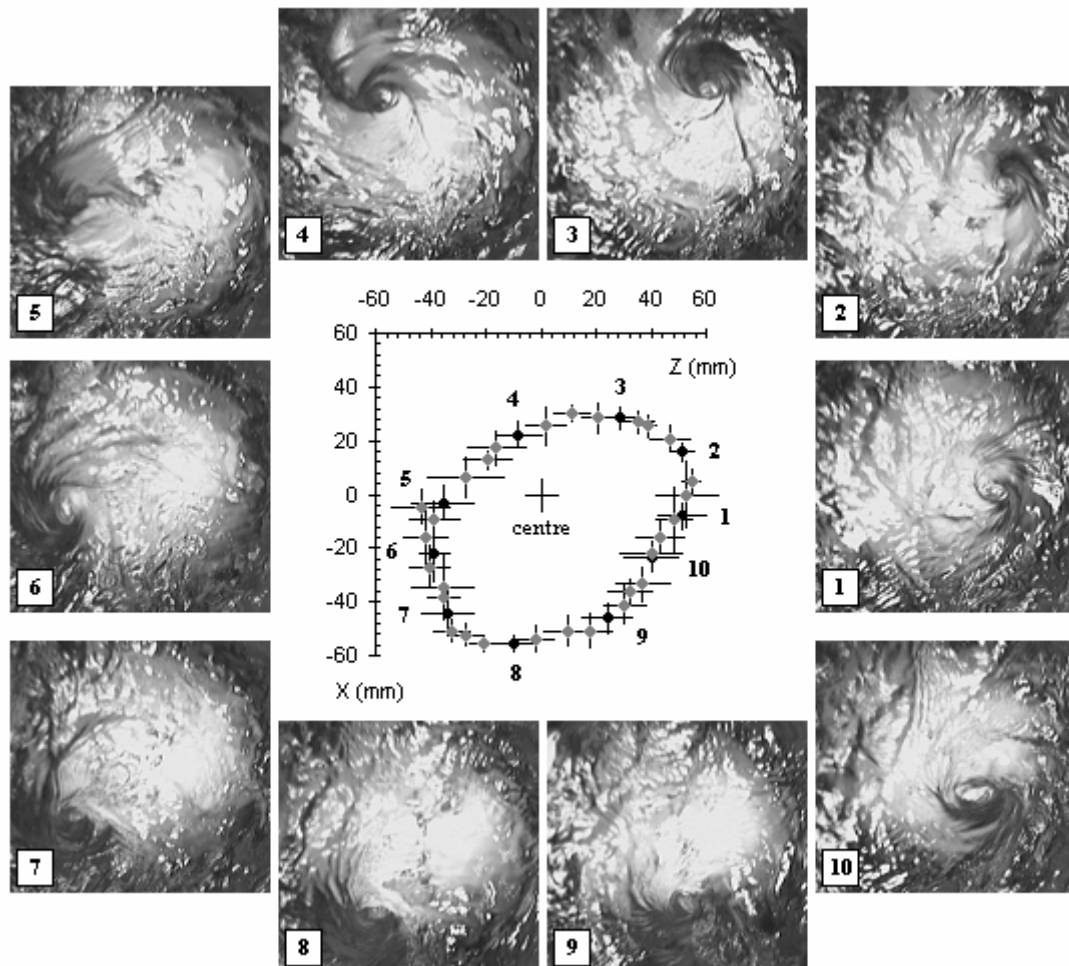
Figure 5.6. Snapshots of the precessing vortex visible on the free-surface (N = 100 RPM) and trajectory around the vessel axis; The Z direction is in the plane orthogonal to the baffles; X direction in the baffle plane; the centre is located on the vessel axis.

The flow instabilities deduced from the computational analysis cannot be linked to the precessing vortex phenomena observed experimentally because the free-surface effects are not taken into account in the single phase simulations. Nevertheless, the experimental measurements of free-surface behaviour must be pointed out for the system studied. Although we were not able to correlate the predicted frequencies to any agitator-baffles interaction, a period of around two agitator rotations appeared to be the most characteristic, as shown in an analysis of vorticity structures detailed in the next section.

5.4.2. <u>Vorticity structures</u>

Figure 5.7(a) presents the 10 s^{-1} vorticity isosurface, obtained numerically at N = 100 RPM with the single phase approach using the standard k-ε turbulence model, coloured by the water velocity to highlight the high and low velocity areas.
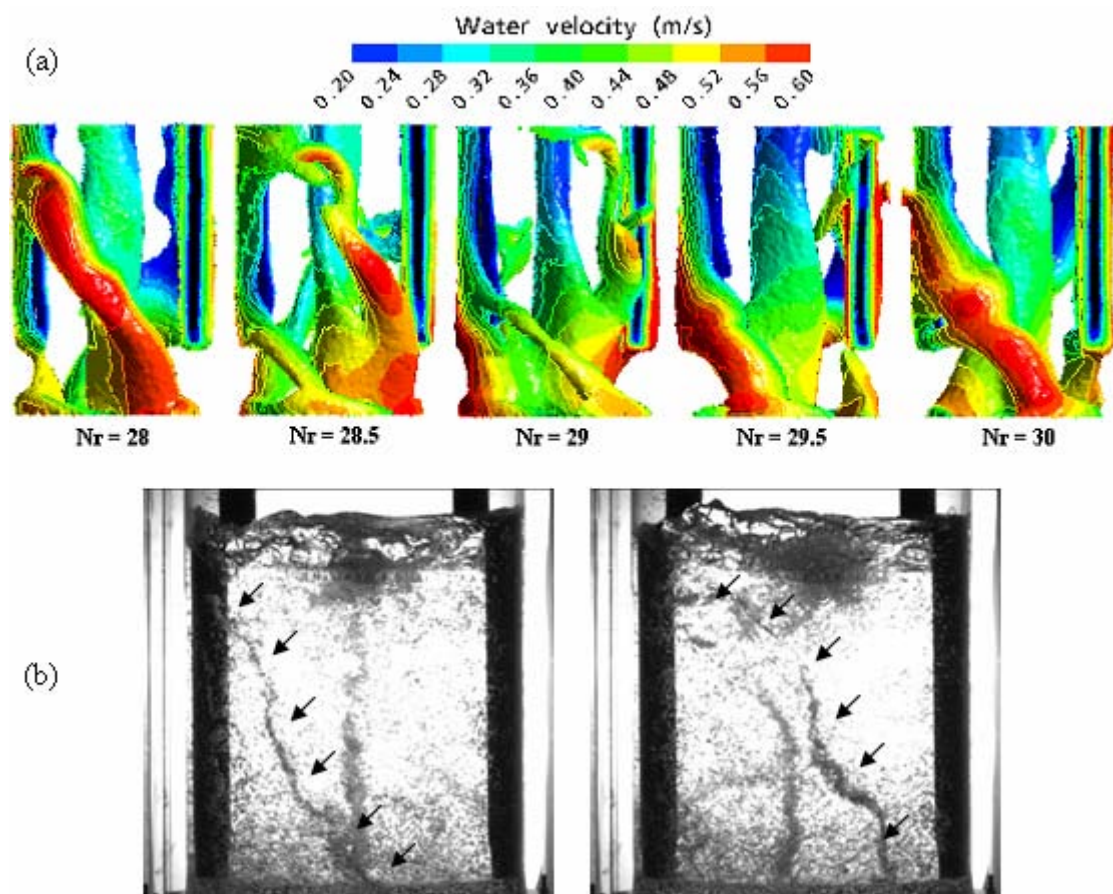
Figure 5.7. (a): Numerical isosurface of vorticity equal to 10 s^{-1} for the time period covered from the 28th to 30th agitator rotations obtained using a single-phase simulation and the k-ε turbulence model (N = 100 RPM), coloured by a contour plot of water velocity; (b) two successive experimental snapshots at N = 217 RPM.

It shows a high vorticity region in the middle of the tank extending from above the agitator to the free-surface. When the circumferential velocity is sufficiently high in this region to deform the free-surface, a central vortex is formed. The most interesting and unusual feature is the evidence of a swirling vortical structure with filamentous connections of vortices between the rear of the two baffles and the agitator region. These filaments rotate in the vessel in the same direction as the agitator but the global movement was found to have a period of about two agitator revolutions. These vortical structures cannot be observed experimentally with a camera at low rotation speed but they are highlighted at higher rotation speed because they trap and carry gas bubbles. As shown in Figure 5.7(b) at 217 RPM, a vortical filament which contains gas bubbles links the rear of the baffle and the bottom dish area then rotates in the vessel. This swirling movement which develops with a relative low frequency leads to locally high and low velocity values giving oscillations of the local velocity values, explaining the features observed in Figure 5.3. This vortical structure confirms the characteristic frequencies obtained by FFT and provides further evidence of the flow complexity which exists in this partially-baffled system.

5.4.3. <u>Numerical predictions versus experimental data</u>

For the numerical results, the data have been averaged only over the fifteenth to thirtieth revolutions from the single phase and multiphase cases for the reasons outlined earlier. These numerical predictions have been compared with experimental observations and PIV measurements at two rotations speeds (100 and 200 RPM).

5.4.3.1. Effect of the turbulence model

The single phase model has been used at low rotation speed (N = 100 RPM) with the flat free-surface hypothesis for investigating the effect of the turbulence models on the prediction of the velocity profiles. Figure 5.8 shows a comparison between experimental data and numerical predictions (N = 100 RPM) of axial and radial velocities along the entire vessel radius corresponding to three vessel heights of Y = 318, 458 and 598 mm from the bottom dish, obtained using the k-ε and the SSG Reynolds stress turbulence models.
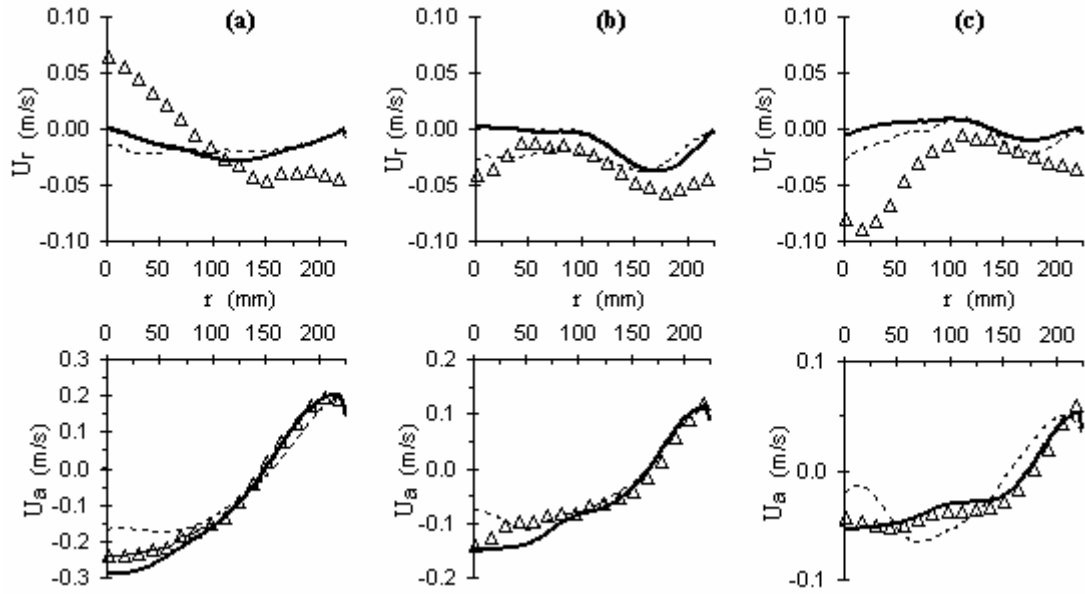
Figure 5.8. Comparisons between radial/axial velocity measurements obtained by PIV and CFD predictions at different heights (N = 100 RPM); symbols: PIV; bold line: CFD with the k-ε model; dashed line: CFD with the Reynolds Stress (SSG) model; (a) Y = 318 mm; (b) Y = 458 mm; (c) Y = 598 mm.

Firstly, it can be noted that there is good agreement for the axial velocity as shown in Figure 5.8. The k-ε turbulence model provides numerical predictions close to the experimental data and in better agreement than results obtained using the RSM-SSG model. Moderate agreement between experimental and numerical results was observed with the radial velocity component for both turbulence models tested. The reasons for the deviations observed between experimental and computational results relative to the radial velocity could be linked both to the computational method and to the experimental strategy.

On one hand, the numerical data have been averaged successively during the agitator rotations to observe how the average develops and it was noted that a stable result was never reached during the averaging process and the velocity changes because of the periodic nature of the flow. For example, the fluctuation of the averaged velocity from revolution 22 to 30 numerically estimated on the line of Y = 388 mm with the k-ε model is ± 0.015 m/s and ± 0.02 m/s for the axial and radial velocity components, respectively (the error bars corresponding to these fluctuations have been dropped from the figure for clarity). Thus, the accuracy of the prediction of the very low radial velocity component is strongly affected by the instantaneous velocity fluctuations impacting substantially on the numerical averaged result.

On the other hand, due to the small magnitude of the radial velocity compared with the axial and tangential ones, the experimental measurement of this velocity component could be affected by any small non-alignment or asymmetry of the experimental apparatus, as well as by a slight deviation of the laser plane. An asymmetry linked to the position of the laser sheet (e.g. vertical alignment, radial position different from zero) has been studied using the CFD results obtained at 100 RPM. Instead of considering the orthogonal baffle plane as the PIV plane, the numerical velocity fields have been plotted on planes inclined at ±5° and ±10° to the original plane. As shown in Figure 5.9 below, for two different heights, these do not show the same level of asymmetry on the axis as measured experimentally.
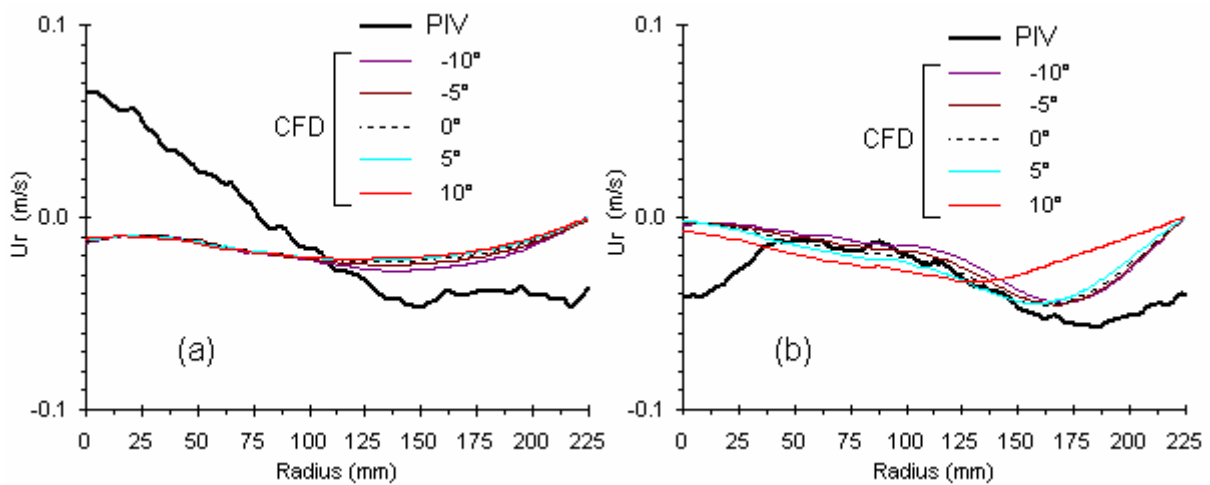
Figure 5.9. Comparison between experimental PIV data and numerical CFD predictions of the radial velocity on other planes inclined at ±5° and ±10° to the original plane: (a) Y = 318 mm; (b) Y = 458 mm.

A small intrinsic geometrical asymmetry of the vessel (small errors in the vertical alignment of the baffles, or different baffle-shell distances) or one induced by the agitator rotation (e.g. different interaction with the two suspended baffles) could be present. Unfortunately, these asymmetric effects could not be quantified experimentally.

In addition, it must be pointed out that the gas bubble disengagement, observed experimentally near the vessel axis, has a major impact on the liquid velocity in this region. The disengagement process of the gas pumped down near the axis generates radial motion of the bubbles which entrains liquid. This effect modifies the liquid flow patterns imparted by the impeller and cannot be predicted using the CFD model used here, as it is not designed to model the details of the bubble disengagement process. Finally, the motion of the precessing vortex could also affect the velocity values measured near the free-surface. The vortex core,

as shown previously, revolves in a volume which is contained inside a 100 mm diameter cylinder around the vessel axis (including the most eccentric trajectories), may explain the deviation observed in this area. This point is returned in §5.4.3.4.

More globally, the numerical time-averaged contour plots of the normalized axial velocity U_a^* (= U_a/U_{tip}), obtained at 100 RPM with the k-ε model and the SGG Reynolds stress model shown in Figures 5.10(b) and 5.10(c), are compared with PIV experimental data plotted in Figure 5.10(a). In the same way, the normalized axial-radial velocity U_{ar}^*, defined as $U_{ar}^* = (U_a^2 + U_r^2)^{0.5}/U_{tip}$ which is the projected norm of the velocity vectors on the plane orthogonal to the baffles is also presented in Figures 5.11(b) and 5.11(c) and is compared with the experimental data of Figure 5.11(a) obtained at N = 100 RPM.
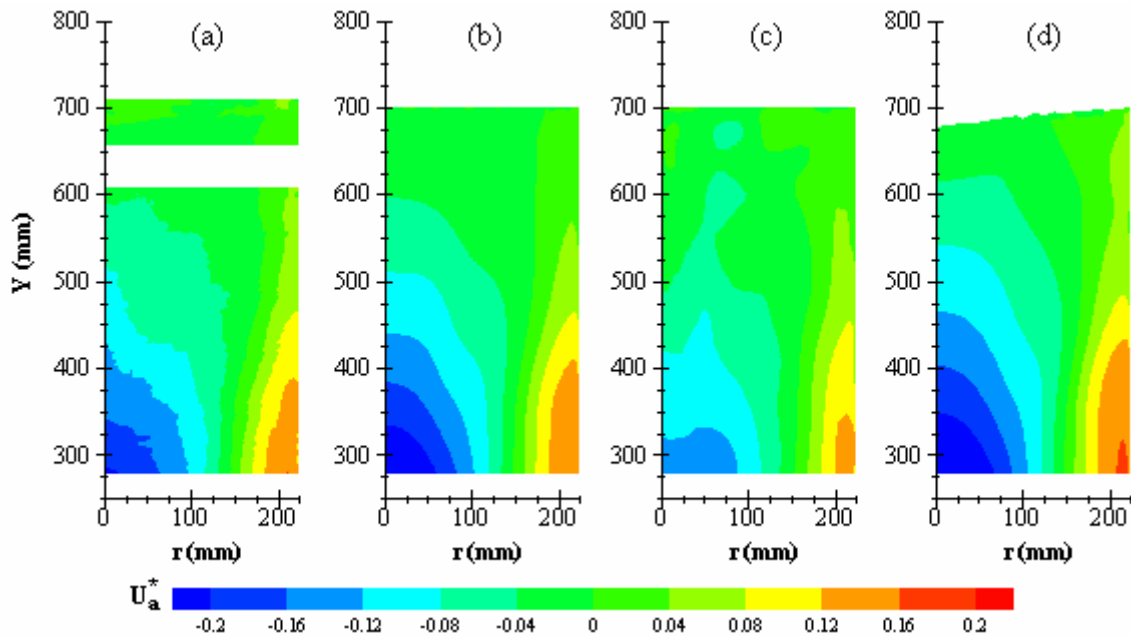
Figure 5.10. Contours plots of normalized axial velocity on the PIV plane for N = 100 RPM: (a) experimental PIV data; (b) single phase numerical data using the k-ε model; (c) single phase numerical data using the Reynolds Stress (SGG) model; (d) multiphase numerical data using the k-ε model.

Figure 5.11. Contours plots of normalized axial-radial velocity on the PIV plane for N = 100 RPM: (a) experimental PIV data; (b) single phase numerical data using the k-ε model; (c) single phase numerical data using the Reynolds Stress (SSG) model; (d) multiphase numerical data using the k-ε model.

The "onion-skin" shapes of the axial and axial-radial velocity contours, as well as their values (velocity magnitudes) are in good agreement with the PIV data for the k-ε model over the entire domain corresponding to the PIV plane. Surprisingly, the modelling using the SSG Reynolds Stress model leads to characteristic shapes of the velocity contours close to the vessel axis which differ significantly from those obtained experimentally and those predicted using the k-ε model. The predictions close to the vessel wall are in good agreement with experimental data for both the turbulence models tested. The Reynolds Stress model used, which is known to provide more accurate results for highly swirling flows such as those encountered in unbaffled vessels for example, is not superior to the standard k-ε model for our situation. Thus, the k-ε model appears to be well-adapted and to perform better than the RSM-SSG for this case and has therefore been chosen as the turbulence model for developing the multiphase approach.

5.4.3.2. Single phase versus multiphase modelling approaches

Figures 5.10(d) and 5.11(d) present contour plots of normalized axial velocity and axial-radial velocity obtained using the multiphase approach. The numerical results have been averaged

over agitator revolutions number fifteen to thirty. The results presented are the liquid phase velocities below the free-surface, characterised by an isosurface of averaged liquid volume fraction equal to 0.9. The free-surface location obtained by averaging the liquid volume fraction during fifteen agitator revolutions is predicted to have a maximum deformation of only 25 mm at the centre tank. This result is in agreement with experimental observations that give a quasi-flat free-surface at this rotation speed, although the small precessing vortex which revolves around the vessel axis was not predicted numerically. In addition, the comparisons between Figures 5.10(a) and 5.10(d), and then Figures 5.11(a) and 5.11(d), show that the axial velocity and the axial-radial velocity fields are in good agreement with both the PIV results and the single phase numerical predictions. This is an important result as it shows that taking the free-surface deformation into account in the simulations using an inhomogeneous approach does not modify the results obtained from a single phase simulation at low rotation speed. The simplest case of a flat free-surface is solved in good agreement with experimental data by the complex inhomogeneous approach.

5.4.3.3. Power consumption

The power consumption was calculated as the product of the torque T_o on the agitator and shaft, with the impeller angular velocity equal to $2\pi N$ (N in s^{-1}).

The power draw can be also expressed in turbulent flow as $P = N_p \rho N^3 D^5$, where N_p is the dimensionless power number of the impeller. For the agitator used in this study, no power number data are available from the literature. The torque has been measured from N = 60 RPM to N = 340 RPM, corresponding to Reynolds numbers from 6.7×10^4 to 3.8×10^5, respectively. Sufficient data are necessary to calculate the power number due to the torque fluctuations caused by the unsteady nature of the flow. For each rotation speed, the torque has been recorded during two minutes at 5 Hz (120 instantaneous values) to obtain the arithmetic average of the torque and its standard deviation (σ). The absolute error attached to the averaged torque is obtained by adding the measurement precision uncertainty (0.1 N m) to 2σ (to give a 95% confidence interval). Figure 5.12(a) shows an example of a torque measurement obtained at N = 100 RPM.

Figure 5.12(b) shows the evolution of the power input predicted using the inhomogeneous approach versus the number of agitator revolutions for N = 100 RPM and 200 RPM. For N = 200 RPM, the power consumption stabilises, while some fluctuations persists for N = 100 RPM after fifteen agitator rotations.
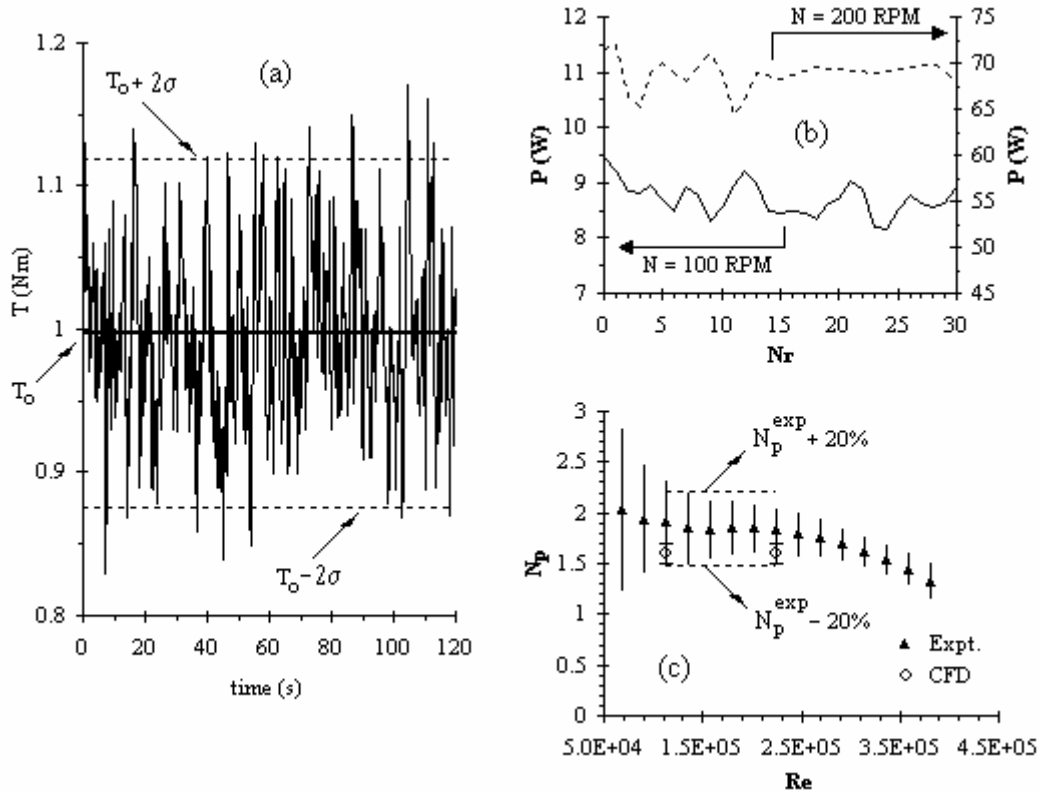
Figure 5.12. (a) Experimental measurement of the torque for N = 100 RPM; (b) Simulated power consumption versus number of agitator revolutions for N = 100 RPM and N = 200 RPM. (c) Experimental and computed power number versus Reynolds number.

These fluctuations are due to transitions in the structure of the flow field and have previously been observed in the transient simulations carried out by Campolo *et al.* (2002) in a study of a similar partially-baffled vessel. These results are consistent with the analysis of the instantaneous velocity fields made earlier in this paper, where the quasi-steady state was deemed to be reached after fifteen agitator rotations.

The experimental data for the averaged power numbers are presented in Figure 5.12 (c) versus the Reynolds number. The uncertainty of the torque measurement is very high at low velocity and the power numbers obtained for Re < $1.1{\times}10^{5}$ are not considered in the following

analysis. For Re $\geq 2.5 \times 10^5$ (N > 220 RPM), the power number decreases with increasing Reynolds number, due to the vortex formation, and the significant vessel aeration observed visually at high rotation speed. Verschuren *et al.* (2000) have reported exactly the same evolutionary behaviour of the power number versus Re and come to the same conclusions regarding the impact of the vortex at high Reynolds number (Re > 10^5). For $1.1 \times 10^5 \leq$ Re $\leq 2.2 \times 10^5$ (100 RPM $\leq$ N $\leq$ 200 RPM), the power number is stable and its averaged value N_p^{exp} is equal to 1.85 ± 0.4.

In addition, the power number has been calculated numerically using the torque values from the CFD simulations at 100 RPM and 200 RPM. The averaged value of the power number obtained from the fiftieth to the thirtieth agitator revolutions were the same for 100 and 200 RPM, which is consistent with a constant value of N_p in turbulent flow without aeration. The uncertainty has been taken to be two times the standard deviation of the power number values obtained at 100 RPM from $15 \leq$ Nr ≤ 30. The power number predicted numerically was $N_p^{CFD} = 1.6 \pm 0.1$. The numerical predictions have been compared with the experimental values in Figure 5.12(c) and fairly good agreement is shown.

5.4.3.4. Hydrodynamics with flat and deformed free-surfaces

At N = 200 RPM, a vortex is created at the free-surface and the assumption of a flat free-surface cannot be made (Chapter 4 and Torré *et al*., 2007a). Due to the presence of only two beaver-tail baffles in the vessel, the baffling effect is not sufficient to prevent the high tangential fluid motion and a vortex is formed. Its shape can be predicted numerically with the inhomogeneous approach and allows the velocity field to be captured accurately in cases with a deformed free-surface.

The numerical velocity fields are compared with PIV data through vector fields in Figures 5.13 and 5.14.
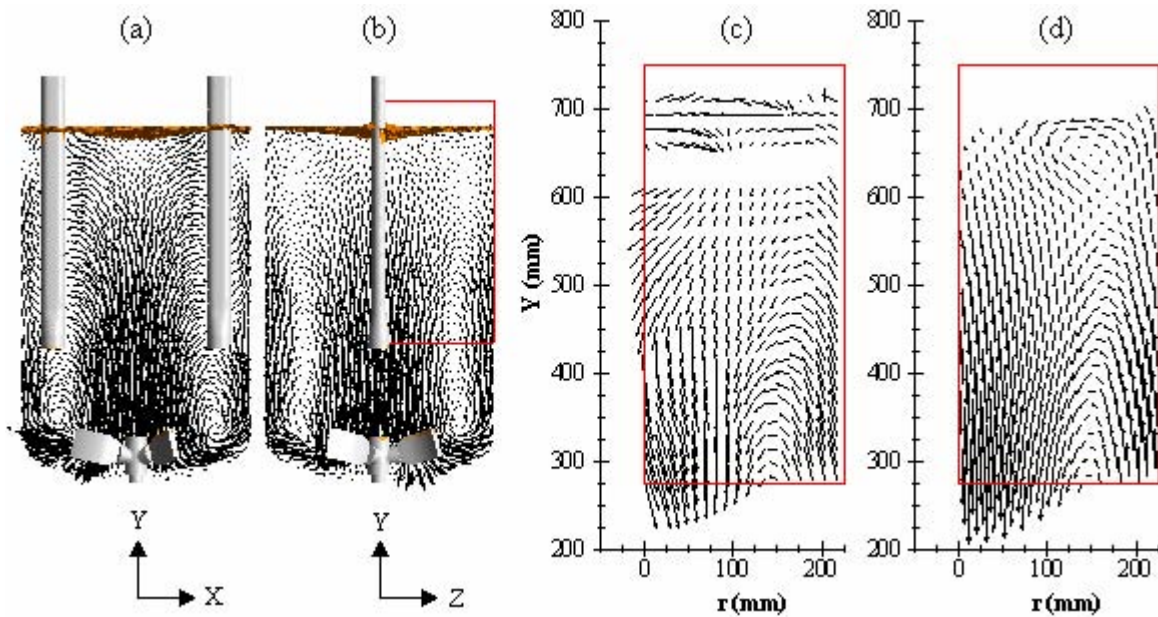
Figure 5.13. Numerical axial-radial velocity vectors for N = 100 RPM on the XY baffle plane (a) and on the YZ plane orthogonal to baffles (b); zoom of the velocity vector field on the PIV plane: (c) experimental; (d) numerical.
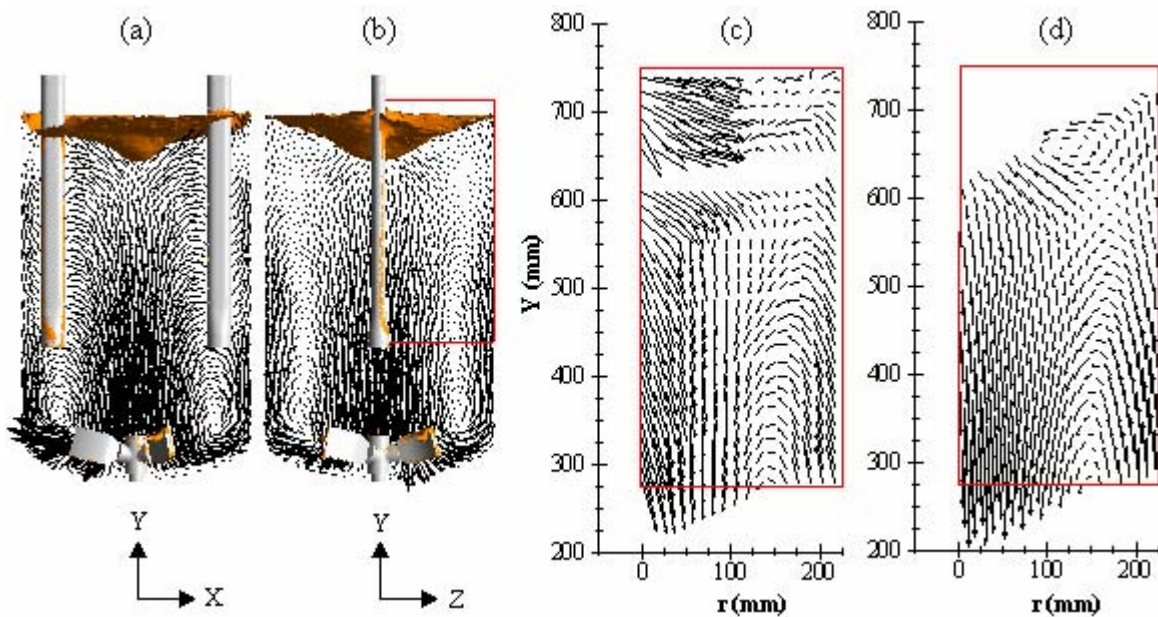
Figure 5.14. Numerical axial-radial velocity vectors for N = 200 RPM on the XY baffle plane (a) and on the YZ plane orthogonal to the baffles (b); zoom of the velocity vector field on the PIV plane: (c) experimental; (d) numerical.

As presented in Figures 5.13(a) and 5.13(b) for N =100 RPM, and in Figures 5.14(a) and 5.14(b) for N = 200 RPM, the global mixing action is based on a typical circulation consisting of a downward stream in the centre of the vessel and an upward stream at the periphery, with

a rotational flow superposed on these streams. For the two agitator speeds, the velocity vectors show that the impeller generates a radial fluid jet that is deflected by the curved dish in the upward direction and generates the upward flow. The agitation pumps the liquid axially in the centre of the vessel, causing a large circulation loop to be created between the vessel axis and the vessel wall. It should be noted that a small recirculation loop is formed below each baffle.

The non-zero value of the radial velocity measured on the vessel axis at N = 100 RPM and already pointed out in the analysis of Figure 5.8, is discussed here through the analysis of the experimental axial-radial vector field presented in Figure 5.13(c). The velocity patterns differ from those obtained at higher agitator rotation speeds by a negative radial velocity of the liquid in the area r < 100 mm and Y > 425 mm. This unusual feature of the flow is assumed to be due to the movement of the precessing vortex coupled with the disengagement of gas bubbles in this area.

At 100 RPM, the aeration point is not located at the vessel axis as observed for higher rotation speeds but follows the precessing vortex movement, which rotates around the vessel axis along a circular path with a maximum diameter of 100 mm. This assumption is corroborated by the high radial component of the vectors obtained inside the vortex core located in the top left corner of the PIV plane shown in Figure 5.14(c) for N = 200 RPM. The extreme instability of the vortex shape leads to the presence of both liquid and gas in the measurement area corresponding to the location of vortex core and leads to measurement of a liquid velocity in the vortex core. Therefore, a measurement point is sometimes in the liquid and sometimes in the gas, which leads to spurious vectors as the free-surface is deformed and unstable.

The experimental data show a non-zero radial component of the velocity vectors along and close to the vessel axis. It can be hypothesized that, at this rotation speed, the effect of air introduction at the bottom of the vortex core and the disengagement of these gas bubbles before reaching the agitator due to buoyancy, contributes to add a radial component to the velocity measured close to the vessel axis. In Figure 5.14 these vectors are present in the vortex core at 200 RPM. This is unusual when compared with the results obtained with an unbaffled vessel, where no liquid is present inside the vortex core due to the development of a stable free-surface shape that generates a vortex core composed of gas only. These velocity

vectors were kept for the analysis and not filtered as being spurious during the post processing of the raw PIV data. It should be noted in Figure 5.13 that for the quasi-flat free-surface obtained at 100 RPM, only the highest row of vectors, just above the free-surface, are spurious and are caused by small fluctuations of the interface location. The high radial velocity component close to the vessel axis was also noted for other PIV measurements carried out at a higher rotation speed with a very high free-surface deformation.

At N = 200 RPM, the significant deviation of the radial velocity component close to the axis observed in Figure 5.14 is attributed mainly to the disengagement of air bubbles. The depth of the vortex and the amount of air entrainment at the free-surface both increase with increasing agitator speed. Therefore, the perturbation of the liquid flow for high agitator speeds is due to disengagement of the air bubbles becoming more important. As evidence of this hypothesis, at 275 RPM, it was noted that the experimentally measured radial velocity component was very high near the vessel axis. At this rotation speed, the air bubbles introduced in the vessel form a gas column linking the agitator region and the free-surface and the measurements showed that the magnitude of the radial velocity is significant and the axial velocity component is close to zero, due to the very high rate of gas introduction/ disengagement at the centre of the tank, as shown in Figure 5.15.
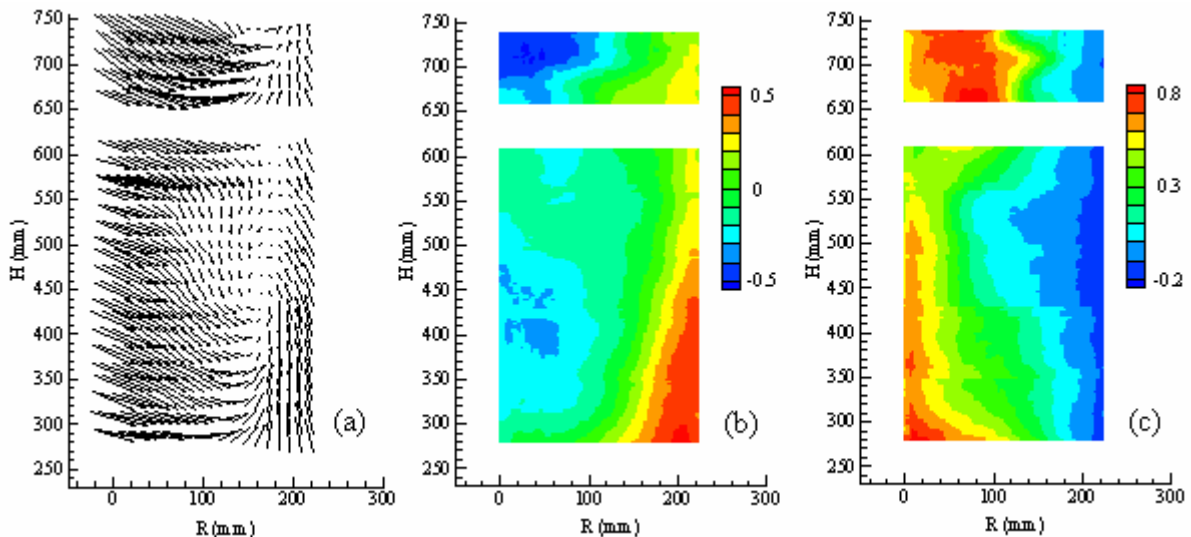
Figure 5.15. Experimental data obtained by PIV (Δt = 0.3 ms, 960 couple of frames) for N = 275 RPM on the XY baffle plane: (a) axial-radial velocity vectors; (b) contour plot of axial velocity; (c) contour plot of radial velocity.

Figure 5.16 presents normalized axial and axial-radial velocity contour plots for the 200 RPM case and shows good agreement between the experimental data and the numerical predictions.
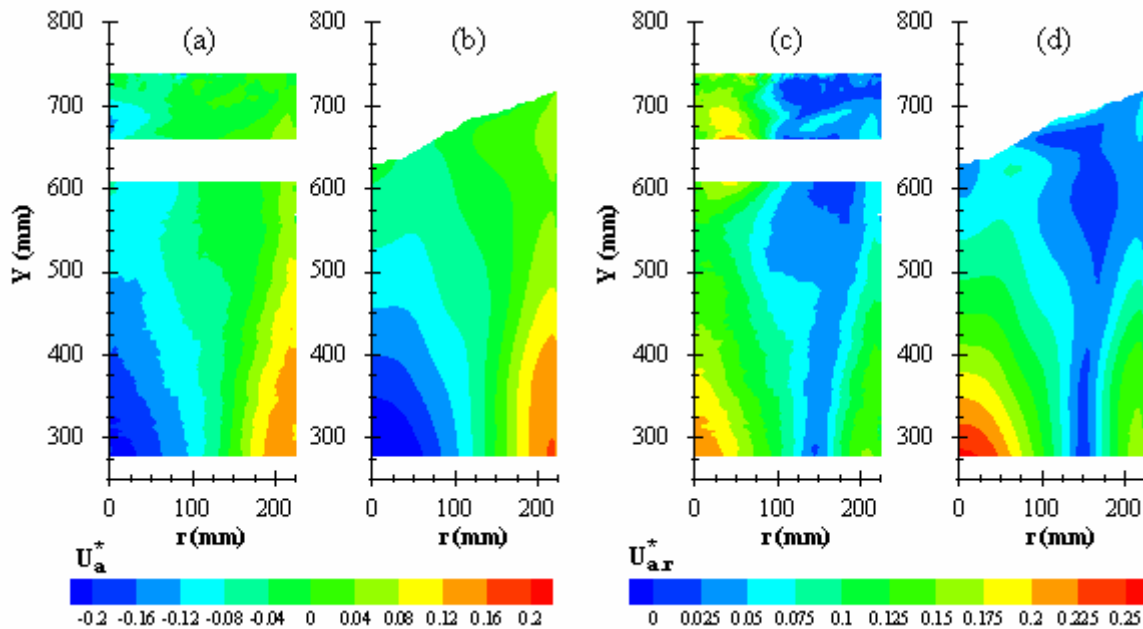
Figure 5.16. Contours plots of normalised velocity on the PIV plane for N = 200 RPM: (a) experimental axial velocity; (b) numerical axial velocity; (c) experimental axial-radial velocity; (d) numerical axial-radial velocity.

The areas of low velocity which result from the creation of trailing vortices due to the impact of the fluid in tangential motion with the baffles appears clearly in Figures 5.16(c) and 5.16(d).

5.5. CONCLUDING REMARKS

A CFD model that can be used to perform transient simulations in partially-baffled mixing vessels with free-surfaces has been described. Here it was showed that at low rotation rates a steady, multiphase simulation does not converge, but it can be used as a starting point to obtain transient-averaged data from a converged transient simulation that agree reasonably well with the experimental data. An important result is that the system requires simulation of at least five impeller rotations to break down the initial flow pattern and meaningful averaging can only begin after around fifteen revolutions. The time averages show a similar flow

structure to the steady-state results but highlight a complex vortical motion with a period of just over two impeller revolution times. The transient model also captures the free-surface behaviour well, as the steady-state model does at higher rotation speeds.

The current work compares numerical results obtained using the standard k-ε and the SSG Reynolds Stress turbulence models with experimental PIV data. The numerical predictions using the standard *k*-ε turbulence model show good agreement with experimental data. Surprisingly, the SSG Reynolds Stress model, which is known to perform better than the k-ε for high swirling flows, gave unphysical results for axial velocities in the areas close to the vessel axis. Thus, the k-ε model was preferred to the RSM-SSG model for the multiphase simulations.

The power consumption has been determined both experimentally and numerically for different agitator rotation speeds. The power number was observed to decrease with Reynolds number at high Reynolds number, with this decreases being attributed to vortex formation and vessel aeration. Good agreement was obtained between the experimental value (N_p^{exp} = 1.85 ± 0.4) and numerical predictions (N_p^{CFD} = 1.6 ± 0.1).

The inhomogeneous multiphase model gives the same good agreement with experimental data as that from single phase simulations. The free-surface was predicted to be quasi-flat at 100 RPM in agreement with experimental data. The multiphase simulations successfully reproduced the hydrodynamics and free-surface shape for a case at higher rotation speed (200 RPM), where the free-surface deformation cannot be neglected. More generally, the inhomogeneous multiphase approach used here for modelling a partially-baffled vessel with a free-surface shows promise for the computation of hydrodynamics in other stirred vessels which have non-negligible free-surface shape deformation. This method remains numerically affordable and allows the numerical assumption of a flat free-surface, often made in computational studies, to be relaxed.

The major outstanding issue from this study is the inability of RANS turbulence models to capture the details of the precessing vortices seen experimentally. Such features could be studied using traditional LES simulation, which is extremely computationally expensive if it is applied throughout the flow domain) or more likely using Detached Eddy Simulation

(DES) or Scale Adaptive Simulation (SAS) (see Chapter 12) which retain the benefits of RANS simulations in boundary layers (where these models perform well), yet capture the turbulence structure in the bulk of the tank.

Chapter 6

TRANSIENT HYDRODYNAMICS AND FREE-SURFACE CAPTURE DURING AGITATOR STOPPING

In this Chapter, the transient hydrodynamics and the free-surface shape have been numerically predicted by CFD for the partially-baffled agitated vessel during the stopping phase of the agitator, including the inertial period after the agitator has completely stopped. The introduction presents a brief literature review of CFD modeling of mixing vessels using a transient approach. The simulations presented were carried out in a fully transient manner using a gas/liquid inhomogeneous two phase flow model, coupled with a k-ε turbulence model. The time dependence of the system studied reveals that the history of the fluid evolution during the impeller slowing phase determines the instantaneous results, implying that the resulting hydrodynamics cannot be determined via a classical steady-state approach. Finally, the comparison of the numerical prediction of the free-surface shape during stopping with experimental data is shown to be good.

6.1. INTRODUCTION

It is important to be able to calculate the transient hydrodynamics with high accuracy during the stopping phase of a reactor, especially when this stopping is due to a breakdown of the process. In particular, such simulations can be very useful to design and choose operating parameters for injecting an inhibiting solution to stop the chemical reaction quickly.

In order to control a runaway reaction, the inhibiting agent (known as a "killer" or "stopper" in polymer processes) can be dosed for quenching the reaction (see Chapter 2). As these killers are very active substances, the reaction inhibition process involves the injection of a small quantity of fluid into the reactor, requiring rapid mixing in the bulk and an injection location well adapted to give a high efficiency. The mixing behaviour depends not only on geometric parameters, such as the nozzle type, the reactor and baffles, and the agitator but

also on fluid dynamic and physical properties. As detailed previously in Chapter 2, the mixing of an inhibiting agent in a stirred reactor has already been studied by various workers, e.g. Dakshinamoorthy *et al*. (2004 and 2006), Hristov and Mann (2002) or Kammel *et al*. (1996), with an agitator continuously in rotation. A particularly interesting case, which has rarely been studied, is the mixing of the killer (or stopper) during the slow down and stopping phase of the agitator. This situation is frequently encountered when an exothermic reaction is to be quenched following an unplanned power shutdown.

Much published work has studied the transient mixing in a stirred tank, such approaches becoming more feasible due to the improvement of computers. Numerical methods such as Direct Numerical Simulation (DNS) and Large Eddy Simulations (LES) can now be used. DNS resolves all turbulent length and time scales and implies that the numerical grid size has to be smaller than the Kolmogorov scale. Verzicco *et al*. (2004), and recently Sbrizzai *et al*. (2006) who coupled DNS with Lagrangian tracking particles, have investigated unbaffled stirred tank reactors. In the Large Eddy Simulation (LES) model, the continuity and momentum equations are filtered prior to being solved in a transient fashion. Simulations have predicted unstable behaviour successfully in both static mixers and stirred tanks (Paul *et al*. (2004)). This method has proved to be a powerful tool as described in Derksen (2003), Hartmann *et al*. (2004), Hartmann *et al*. (2006) and Yeoh *et al*. (2004). A detailed survey of the different numerical methods and results for the calculation of turbulent flows for single phase and multiphase problems can be found in Sommerfeld and Decker (2004). The recent review by Van den Akker (2006) gives further details and references on the LES method, including the lattice-Boltzmann solution techniques, for more advanced CFD approaches.

As shown in detail in Chapter 4, multiphase simulations are highly computationally intensive because there are roughly twice as many equations to be solved as for a single phase simulation and the convergence is slowed due to the complexity of the multiphase physics (Lane *et al*., 2000). Although the long calculation time and the significant computer resources necessary still remain prohibitive, particularly for multiphase problems, numerous authors, such as Brucato *et al*. (1998), Campolo *et al*. (2003), Joshi and Ranade (2003), or more recently Javed *et al*. (2006) have made good predictions of the complete flow field in unsteady conditions using the Sliding-Mesh (SM) approach. In addition, the results presented in Chapter 5 and in Torré *et al*. (2007c), which showed the good agreement obtained between

numerical prediction and experimental PIV data, demonstrate that this approach performs well in single phase for the system studied.

Regarding these transient simulations, they are usually performed to predict a time-dependant flow but the start-up or the stopping phase of the agitator is usually omitted. The only computational study we could find that uses a non-constant agitator speed was that of Smith (1997) who developed a fluid dynamics code for predicting the transient mixing after the start-up phase of the agitator in an unbaffled agitated vessel. A quasi-three dimensional single phase model, used with the k-ε turbulence model and Lagrangian tracer particles as an indicator of the mixing behaviour, allowed prediction of the resuspension of a slurry after the start of the agitator. The agitator speed was linearly ramped up to 100 RPM in 5 s and the free-surface at the top of the tank was assumed to be flat. In spite of a lack of experimental data for comparison, the simulations were found to agree qualitatively with mixing observations. Concerning the numerical modelling of the fluid behaviour following an agitator stopping, no results have been found in the literature.

Laboratory and pilot plant scale experiments with runaway conditions are difficult to carry out because of the hazards associated with such conditions, thus the use of Computational Fluid Dynamics (CFD) becomes very useful in this case. The commercial CFD package ANSYS CFX 10.0 is used to develop a transient model to study the hydrodynamics during impeller slowdown. This study is devoted firstly to the modelling of the agitator stopping, applied to the case of an under-baffled stirred vessel developed for industrial applications. One of the goals of this study was to simulate, using CFD, an impeller with a decreasing speed and the associated flow in the reactor, taking into account the inertia of the fluid after the agitator has stopped and the diminution of the vortex, until the final state where there is no residual movement and a flat free-surface is formed. Finally, the capability of the CFD model to predict the free-surface evolution during agitator stopping was analysed via comparison with experimental data obtained by a video imaging process. The ability to predict the vortex shape during stopping is a crucial challenge to overcome to allow modelling in future studies of industrial applications, where the inhibiting agent is injected at the free-surface of polymerisation reactors.

6.2. CFD MODELLING

6.2.1. <u>System studied</u>

The complete description of the mixing equipment used in this study and a literature review of work on unbaffled and partially-baffled vessels was given in Chapter 3. The agitation speed during the stopping period is linked to the rotational inertia of the whole agitation system which includes not only the impeller and shaft but also the rotor of the electrical motor and the gear wheels of the gear reducer. The agitator system studied was constrained by the speed controller (Leroy Somer Proxidrive®) to decelerate with a linear function of time and to stop in 6.4 s. As a first approach, the experimental settings have been used in the simulations to compare CFD predictions with experimental data.

6.2.2. <u>Simulation strategy</u>

The numerical simulations were carried out using a commercial CFD package (ANSYS CFX 10.0) to predict the flow field and the free-surface shape by resolution of the Reynolds Averaged Navier-Stokes equations, by using an Eulerian-Eulerian multiphase model in a fully transient manner. The fluids used were water and air at 25°C. To model the free-surface deformation, an inhomogeneous model (in which a separate velocity field is determined for the gas and liquid phases) was chosen to allow phase separation. The interfacial momentum transfer between the two phases was modelled using a disperse phase model in which the liquid phase is continuous and the gas phase is dispersed. This model, characterized by the solution of an individual set of continuity and momentum equations for each phase, was coupled with a homogeneous k-ε turbulence model, which assumes that the turbulent quantities are the same for the two phases. This is clearly a significant assumption, as whilst the flow will start off being fully turbulent, as the impeller slows the turbulence generated by the agitator diminishes and ultimately the flow becomes laminar. The duration of the current simulation is such that there remains significant rotational flow at the end of the calculation. This, together with the stirring effect of gas bubbles breaking away from the impeller blades as it slows down, supports the assumption of turbulent flow. The volume fractions of the phases are tracked with the condition that the volume fractions for all phases sum to unity.

The governing equations are not detailed here as they are the same as those presented in Chapter 4 and in Torré *et al.* (2007a). A constant bubble size d_b of 3 mm and a constant drag coefficient C_D of 0.44 have been chosen for all the simulations as our previous results showed that the simplified model presented previously in Chapter 4 could capture the free-surface geometry to within experimental accuracy.

During the impeller stopping phase, the flow characteristics are highly time dependent. This time dependence has been treated using the transient rotor-stator model available in ANSYS CFX 10.0, which takes the transient impeller movement into account via a sliding mesh (SM) approach. To predict the true transient interaction between a stator and a rotor passage, a sliding interface is used to allow a smooth rotation between components allowing the interface position to be updated at each time step, as the relative position of the meshes on each side of the interface is changed. This model is robust and yields high accuracy predictions of loading but the principle disadvantage of this method is that the computer resources required are large, in terms of simulation time, disk space and quantitative post processing of the data (ANSYS-CFX 10.0 User's guide, 2006).

The no slip condition was applied at all solid/liquid interfaces. At the top of the vessel, a free-slip condition was set, but as the vessel lid was well removed from the region of interest this played no role in the simulation results. This last condition prevents any flow through the surface and the normal gradients for all other quantities have been set to zero. A maximum number of 15 coefficient loops per time step was adequate to resolve the strong non-linearities present in the multiphase flow equations. The transient simulations were started from a converged steady state result run at the same impeller rotation speed (275 RPM) using a multiple reference frame approach. Both simulations assumed an initial liquid height of 700 mm, with 100 mm of gas above it.

The transient scheme allows modelling of the deceleration phase of the agitator by defining an impeller speed as a decreasing function of time. The impeller speed was modelled in a first approach by the linear function N(t) which varied from N_m = 275 RPM to 0 RPM, as expressed in Eq. (6.1), in agreement with the decreasing speed function measured on the pilot reactor.

$$
\begin{cases}
N(t) = N_m & \text{for } t_0 \leq t < t_1 \\[2mm]
N(t) = \dfrac{N_m}{t_2 - t_1}(t_2 - t) & \text{for } t_1 \leq t < t_2 \\[2mm]
N(t) = 0 & \text{for } t_2 \leq t < t_f
\end{cases}
\tag{6.1}
$$

with t_o the initial time, t_1 and t_2 respectively the beginning and the end of the agitator stopping phase and t_f the final time, when the simulation is stopped.

The time step has been set to ensure a constant angle rotation of 2° per time step. This small rotation angle was found to give good convergence in less than 15 coefficient loops per timestep. As the impeller rotation speed is decreasing while the agitator is stopping, the time step has been modified to give a constant rotation angle of 2° by a time step function depending on the rotation speed as expressed in Eq. (6.2), which gives a maximum time step of 0.01 s.

$$
\text{time step} = \frac{1}{\text{Max}(3N, 100)}
\tag{6.2}
$$

An unstructured grid composed of 208,000 nodes was used in the transient simulations. The density of cells was optimised by sensitivity studies to be fine enough to capture the flow without being excessive, as shown previously. Inflation meshing was used at all walls to ensure boundary layers are captured correctly. Figure 6.1 shows the computational grid resolution, the inflation mesh at the walls and the surface mesh on the agitator and baffles.

The rotating part of the vessel was set to be the bottom dish, which includes the agitator. A second order bounded scheme was used for the convective terms in the momentum and volume fraction equations and a first order upwind scheme was used for the turbulence equations. Similarly, the transient terms were represented via a second order Euler scheme for the momentum and volume fraction equations and a first order scheme for the turbulence equations. The convergence criterion adopted for the simulation at each time step is based on the RMS (Root Mean Square) normalized values of the equations residuals. The convergence at each time step was such that the residuals for the mass, momentum and turbulence equations were below 10^{-4} and that for the volume fraction equations was below 10^{-3}. The simulation was carried out on a dual-processor Xeon 2.8 GHz computer with 2 Gbytes RAM and required 68 days of CPU time.
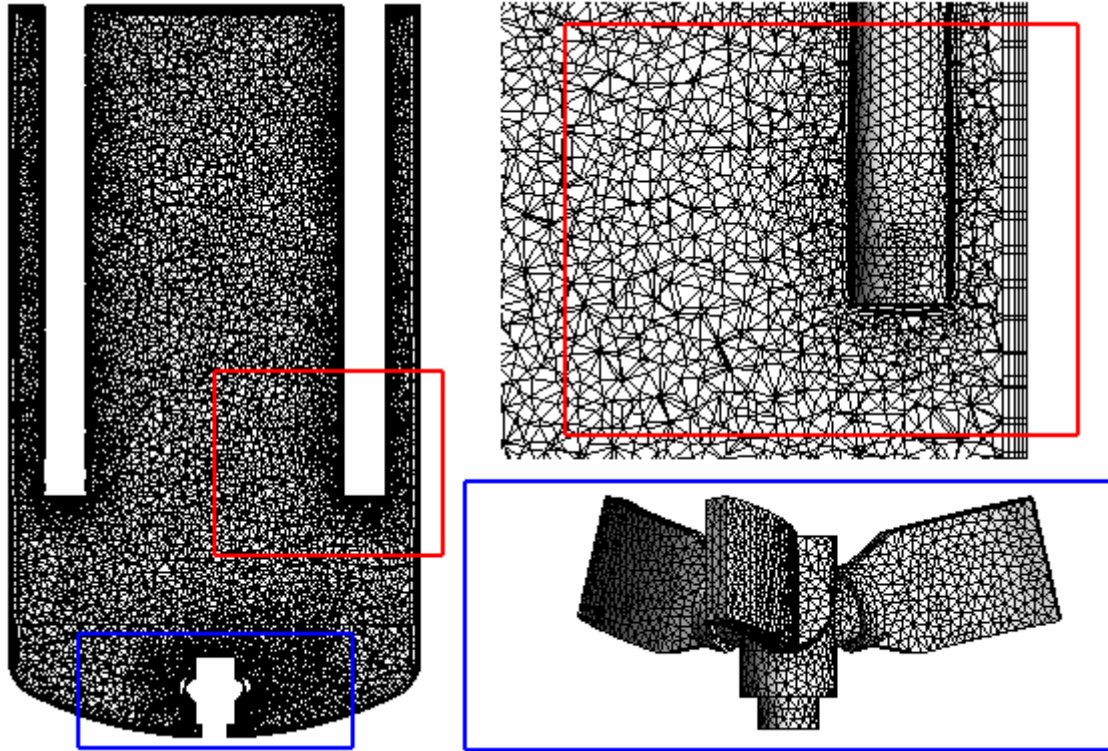
Figure 6.1. Details of the computational grid used in the simulation.

6.3. EXPERIMENTAL FREE-SURFACE CAPTURE

The free-surface shape which develops in the vessel studied is highly unsteady, so an instantaneous picture of the vortex cannot give a correct description of the free-surface boundaries except in the case where the free-surface is flat. The development of an experimental method of free-surface capture required an imaging process technique based on a superimposition of images. When the vortex is formed and more generally when air bubbles are dispersed in water, the gas/liquid interface provides a dark area which contrasts against the transparent water medium. These contrasted areas were used to fix the boundaries of the free-surface by superimposition of instantaneous pictures. When a sufficient number of pictures were superimposed, the free-surface contour was highlighted. As detailed in Chapter 4, the same imaging process was successfully used to capture the free-surface shapes obtained at constant rotation speeds varying from 200 RPM to 350 RPM.

The acquisition of numerous images is relatively easy for the case of constant rotation speed, but this experimental strategy is more complex to carry out during the stopping period of the agitator. For the case of non-constant agitator rotation speed, the method requires superimposing images obtained exactly at the same time during the stopping sequence. Due to the complexity of the acquisition and image post-processing, only sixty experiments were made. The camera used was a high resolution CMOS camera (HCC-1000 model from VDS Vosskühler) monitored by the NV1000 software from New Vision Technologies. The camera was located 1110 mm away from and normal to the vessel jacket sidewall, and was equipped with a telephoto lens Nikon – Nikkor 50mm/1.2. The frame rate, exposure time and total recording time were 10 frames/s, 2.2 ms and 10 s, respectively and the image resolution was 1024×1024 pixels². These settings remained fixed for all the captures.

The agitator speed was set at the initial speed of 275 RPM. The agitator stopping order was manually given to the speed controller at the same time the video camera was started. Ten seconds of recording time was sufficient to capture the complete evolution of the free-surface from the initial state to a final flat state obtained after the agitator has completely stopped. For the sixty videos recorded, each was decomposed in 100 frames and only the frames which correspond to the times 0, 1, 2, 3, 4, 5, 6 and 7 seconds were kept. The frames correspond to the times marked as experimental points on Figure 6.2, were superimposed to give averaged pictures made by superimposition of sixty frames. This number of frames was sufficient to capture the free-surface evolution during agitator stopping.
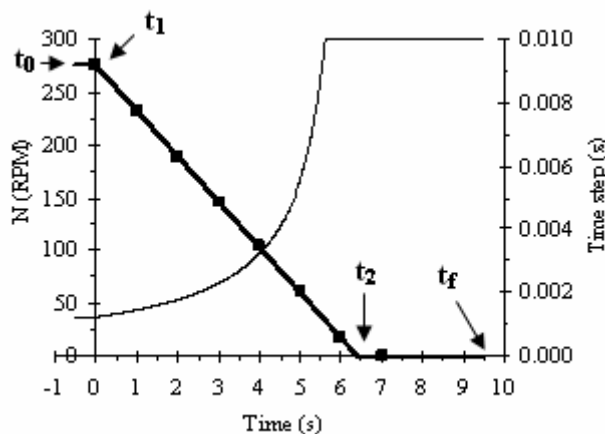
Figure 6.2. Agitator speed (bold line) and time-step (normal line) used in the simulations for modelling the agitator stopping. (■): experimental points for the free-surface shape comparison.

6.4. RESULTS AND DISCUSSION

The transient simulation was run with the following parameters: t_o = -0.5 s, t_1 = 0 s, t_2 = 6.4 s and t_f = 9.5 s, with an impeller rotation speed decreasing from 275 to 0 RPM. The negative value of t_o represents the fact that the simulation has been run with a transient scheme with a constant rotation speed of 275 RPM during 0.5 s after initialization with a steady-state result and before starting the stopping phase at t_1. This allows the simulation to settle down in transient mode before the ramp is applied. Figure 6.2 in §6.3 shows the linear ramp of deceleration of the agitator speed and the time-step versus time.

6.4.1. <u>Analysis of the free-surface dynamics</u>

Figure 6.3 presents the numerical prediction of the free-surface shape from 0 to 9.5 s. In Chapter 4, a Multiple Reference Frame (MRF) approach and a steady-state were assumed. The numerical predictions were also compared with experimental data with very good agreement obtained by considering an isosurface of water volume fraction equal to 0.9 for the air/water interface to represent the free-surface. Therfore, the same volume fraction threshold was used here.

The agitator stopping phase is represented by Figure 6.3(a) to Figure 6.3(n) and the inertial period which follows the complete stopping of the agitator is shown in Figure 6.3(o) and Figure 6.3(p). The baffle effect provided by the two beaver-tail baffles is not sufficient to prevent the highly swirling fluid movement, with a particularly unstable and deep vortex being created at a rotation speed of 275 RPM. The vortex shape shown in Figure 6.3(a) is characteristic of the under-baffled agitated vessel used in this study. The same vortex shape was predicted numerically, as presented in Chapter 4, for different impeller rotation speeds using a steady-state approach. At the bottom of the central vortex bulb, the simulation predicts a column of gas linking the vortex core to the agitator. This gas aspiration is hypothesized to be one of the causes responsible for the high gas dispersion observed experimentally at this rotation speed.
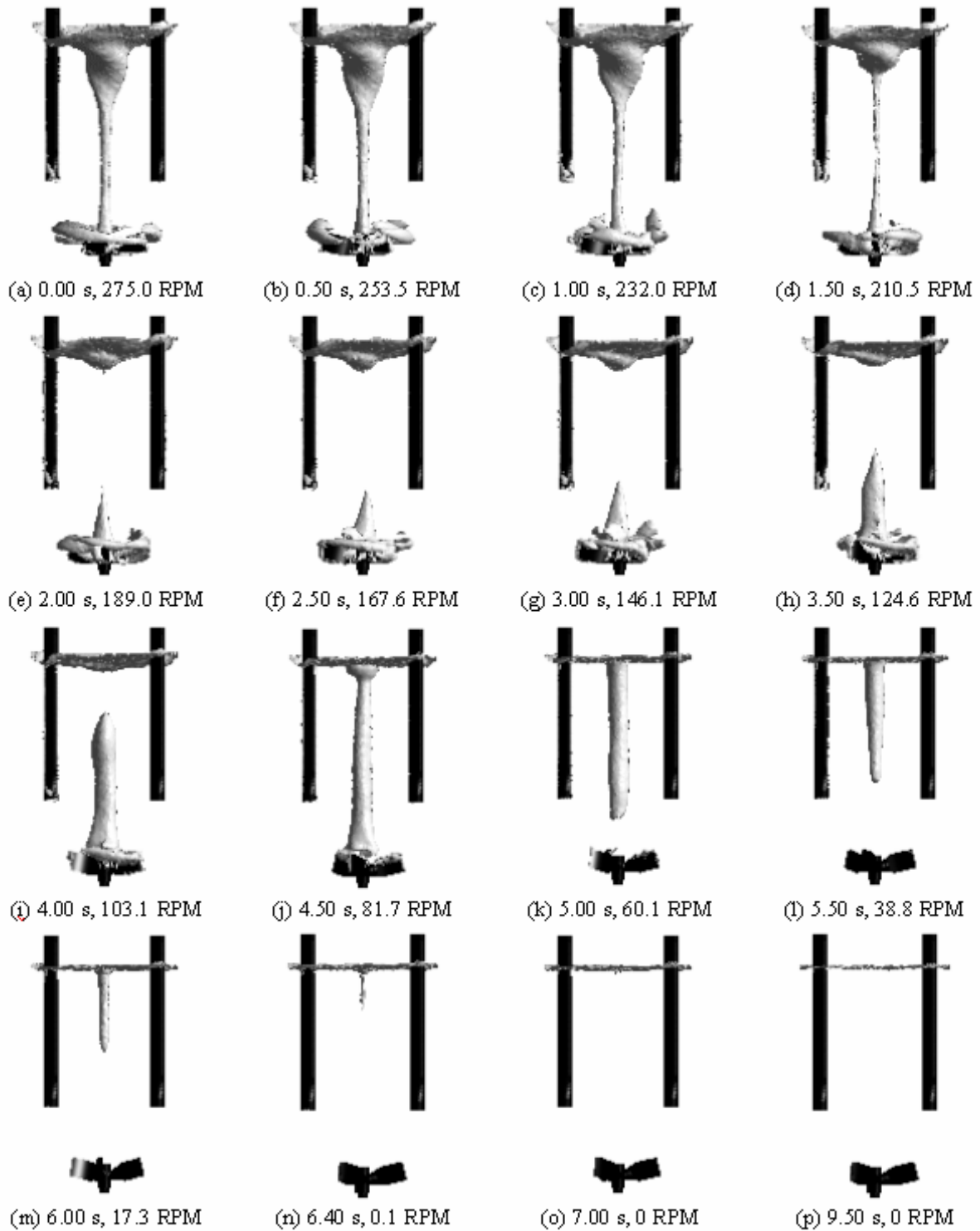
Figure 6.3. Evolution of the free-surface during impeller slowdown and stopping. Each caption gives the simulation time from the start of the impeller slowdown and the impeller rotation rate.

The depth of the vortex core and the diameter of the gas column decrease rapidly. It is observed that 1.5 seconds after stopping the impeller (Figure 6.3(d)) that the gas column breaks. Thus, the initial continuous region of gas separates into two regions: one comprising

the vortex core and the top vessel part and one located close to the impeller. The free-surface becomes flat first and then the gas located in the impeller region rises before the impeller stops completely. The free-surface becomes flat roughly 2 seconds before the agitator stops completely (6.4 s), as shown in Figure 6.3(j). As shown in Figure 6.3(o) and Figure 6.3(p), the free-surface remains flat during the inertial period after the agitator stops. It can be assumed that the air bubbles in the impeller region are trapped due to low pressure in the regions of high turbulence and the vortices created by the impeller and that the gas rises when the buoyancy force becomes dominant. This gas rise phenomenon cannot be observed in a steady-state simulation because the high gas volume fraction in the impeller region observed with a low rotation speed (as shown in Figure 6.3(i) with 103.1 RPM) is linked to the transient evolution history. Such a transient simulation allows the study of the hydrodynamics during the agitator stopping phase.

6.4.2. **Flow patterns and velocity profile analysis**

Figure 6.4 presents the liquid velocities on the vertical baffle plane for two simulation times at the same relative location of the agitator blades.
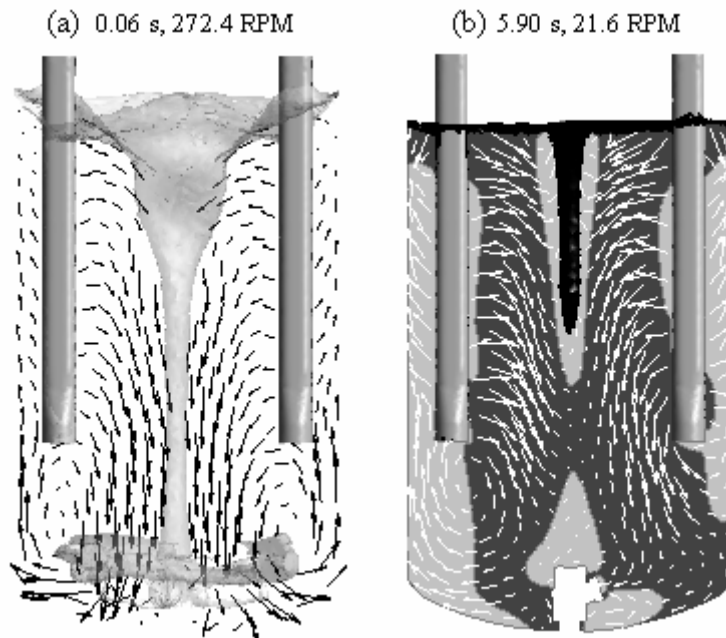
Figure 6.4. Radial-axial vector plots and the free-surface profile for two times from the start of the impeller slowdown; (a) black velocity vectors, free-surface in light grey; (b) white velocity vectors, axial velocity contour plot with positive values in light grey and negative values in dark grey, free-surface in black.

As shown in Figure 6.4, the rotation speed magnitude has a significant effect on the velocity patterns which develop in the vessel. Two circulation loops are clearly visible in Figure 6.4(a) for a high rotation speed but only one remains at lower speed (Figure 6.4(b)). At the beginning of the agitator stopping phase, the rotation speed is sufficient to maintain two circulation loops below the baffles during a complete rotation (360°) of the agitator, as shown in Figure 6.4(a). In contrast, the circulation loops are alternatively formed below each baffle during one 360° agitator rotation during the stopping phase. This observation confirms the high unsteadiness of the time-dependant phenomena observed during this agitator stopping phase. Positive values of the axial velocity of the liquid surrounding the central gas zone are observed in Figure 6.4(b) due to the entrainment of the liquid by the rising gas. The distributions of liquid volume which is associated with a particular liquid speed range have been determined during the transient simulation, the liquid speed being defined as $U_{ijk} = (u^2 + v^2 + w^2)^{0.5}$ with u, v, w being the Cartesian components of the liquid velocity. The liquid speed normalized by the tip speed is denoted U^*_{ijk} and is defined as U_{ijk}/U_{tip}, with $U_{tip} = \pi ND$. For different simulation times, a curve fitted to the liquid speed histogram and the liquid speed distributions normalized with the tip speed are presented in Figure 6.5(a) and Figure 6.5(b), respectively.
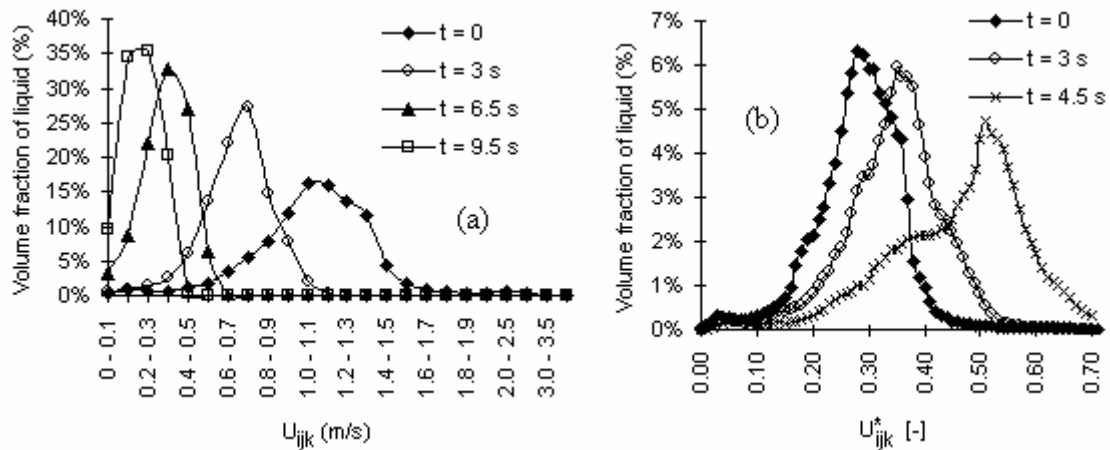
Figure 6.5. The distribution of liquid volumes associated with liquid velocity ranges for different simulation times; (a) volume fraction of liquid versus liquid speed, (b) volume fraction of liquid versus liquid speed normalized by the tip speed.

The decrease of the agitator rotation speed during the slowing phase implies that the velocity distribution shifts from the high to the low velocity magnitudes, as can be observed in Figure 6.5(a). The velocity distributions normalized with the tip speed at times of 0, 3 and

4.5 s are presented in Figure 6.5(b). As the impeller slows down there are regions of flow that continue to rotate and these have a higher spread relative to the current tip speed, so the distributions cannot be superimposed. The history of the fluid evolution determines the instantaneous transient result by adding high velocity components that were generated earlier in time when the impeller was moving faster.

6.4.3. <u>Volume-averaged velocity and agitation index</u>

The volume-averaged velocity $\langle U \rangle$ and the agitation index I_G were first proposed by Mavros and Baudou in 1997 as a measure of the agitation quality in a stirred vessel. They evaluated the performance of various impellers using the agitation index. In the same way, Fangary *et al.* (2000) compared the effectiveness of different impellers applied with a non-newtonian liquid and Alliet-Gaubert *et al.* (2006) used this index coupled with CFD simulations to provide an analysis for laminar or transient-laminar single phase flow in a multi-stage stirred vessel.

The agitation index of Mavros and Baudou (1997), developed and used initially for single phase mixing experiments, can be used easily in computational studies but the original formulation had to be modified for treating our numerical multiphase problem. To define the volume-averaged velocity $\langle U \rangle$ expressed in Eq. (6.3), it is postulated that each velocity U_{ijk} correspond to a volume of liquid V_{ijk}, which is related to the vessel dimension and the grid point coordinate i, j, k. To take into account the changing zones of liquid and gas resulting from the flattening of the free-surface during the agitator stopping phase, the speed U_{ijk} calculated in each cell must be filtered by a function depending on the liquid volume fraction. This function, denoted $\xi(x)$ and defined in Eq. (6.4), allows consideration of only the cells where the liquid volume fraction $\alpha_{l,ijk}$ is above the liquid volume fraction threshold ($\alpha_l^t = 0.9$) used to define the free-surface.

$$\langle U \rangle = \frac{\sum_i \sum_j \sum_k U_{ijk} V_{ijk} \xi(\alpha_{l,ijk})}{\sum_i \sum_j \sum_k V_{ijk} \xi(\alpha_{l,ijk})} \qquad (6.3)$$

with the liquid speed U_{ijk} expressed as $U_{ijk} = (u^2 + v^2 + w^2)^{0.5}$

$$\xi(\alpha_{l,ijk}) = H(\alpha_{l,ijk} - \alpha_l^t) \tag{6.4}$$

with $\alpha_l^t = 0.9$ and where H(x) is the Heaviside function (step function).

The original formulation of the agitation index, I_G, was also modified. Mavros and Baudou (1997) defined this index as the ratio of the volume-averaged velocity, $\langle U \rangle$, and the agitator tip speed, U_{tip}. In the case studied here, the tip velocity cannot be used as the denominator as it becomes zero when the agitator stops. Thus, the mixing quality is compared through a percentage giving the ratio of the liquid volume-averaged velocity between the initial and the final states. The modified agitation index is expressed in Eq. (6.5).

$$I_G = 100 \frac{\langle U \rangle}{\langle U_O \rangle} \tag{6.5}$$

The agitation index has been calculated during the agitator stopping phase and is plotted against time in Figure 6.6. In the same figure, the dashed line shows the theoretical lower limit of the agitation index calculated for the linear agitation speed decreasing function used in this study.
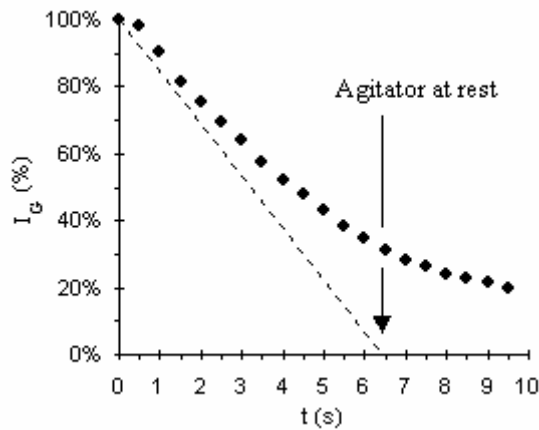
Figure 6.6. The agitation index versus time during the agitator stopping phase and the inertial period.

The gap between the symbols and the dashed line is due to the impact of the fluid inertia during the stopping phase. This inertial effect was already observed in Figure 6.5(b) and discussed earlier in this Chapter. This agitation index analysis could be very useful as an integral quantity to describe the transient process when the agitator slows down. Particularly, it can be used to investigate the influence of different sets of parameters, to clarify the impact

of the initial conditions on the dynamics of the free-surface and to quantify the mixing quality during the stopping phase. Unfortunately, we have not yet been able to perform multiple simulations to test this due to the very long calculation times required.

6.4.4. <u>CFD predictions versus experimental data</u>

The comparison of the numerical predictions and experimental free-surface profiles are presented in Figure 6.7. The numerical results represent the projection of the isosurface of water volume fraction equal to 0.9 onto the vertical baffle plane. This value has proved to give good agreement at 275 RPM with experimental averaged pictures made by superimposition of 300 frames as demonstrated previously in Chapter 4. The high value of 0.9 of the volume fraction threshold was attributed to the presence of the dynamical equilibrium zone of intense gas/liquid exchanges which occurs around the free-surface. The experimental method appeared to be very sensitive to the gas dispersed in the vessel and particularly if the number of frames superimposed is less than 200. In this case, a dark area can be observed on the final averaged picture even if a small percentage of gas is present.

The fact that only sixty frames have been superimposed to obtain Figure 6.7 yields a wide area of gas/liquid exchange near the free-surface boundaries on the average picture. It may explain why the experimental vortex appears larger than the numerical prediction. Nevertheless, this uncommon vortex shape obtained experimentally at 275 RPM, which is so distinctive with its central bulb, is in agreement with the numerical result. The liquid elevation, the bulb and the gas column at the vortex bottom are well predicted. In contrast, the gas dispersion visible in the bottom experimental picture of Figure 6.7(a) is not obtained numerically. This is because the current simulation does not model the bubble production process of shear-induced stripping at the gas-liquid interface.

As shown in Figure 6.7(c) and Figure 6.7(d), the model predicts separated gas regions located at the top of the vessel and in the agitator area (also visible in Figures 6.3(e) to 6.3(g)), with a significant vortex depth decrease, and a free-surface which has flattened compared with the initial state. Experimentally, the averaged picture at these times reveals a free-surface bulb shape close to the initial state and no distinct gas segregation was observed. The free-surface flattens in agreement with numerical predictions. When the free-surface becomes

almost flat, good agreement between the experimental data and numerical predictions is observed, as shown in Figures 6.7(e) to 6.7(h).
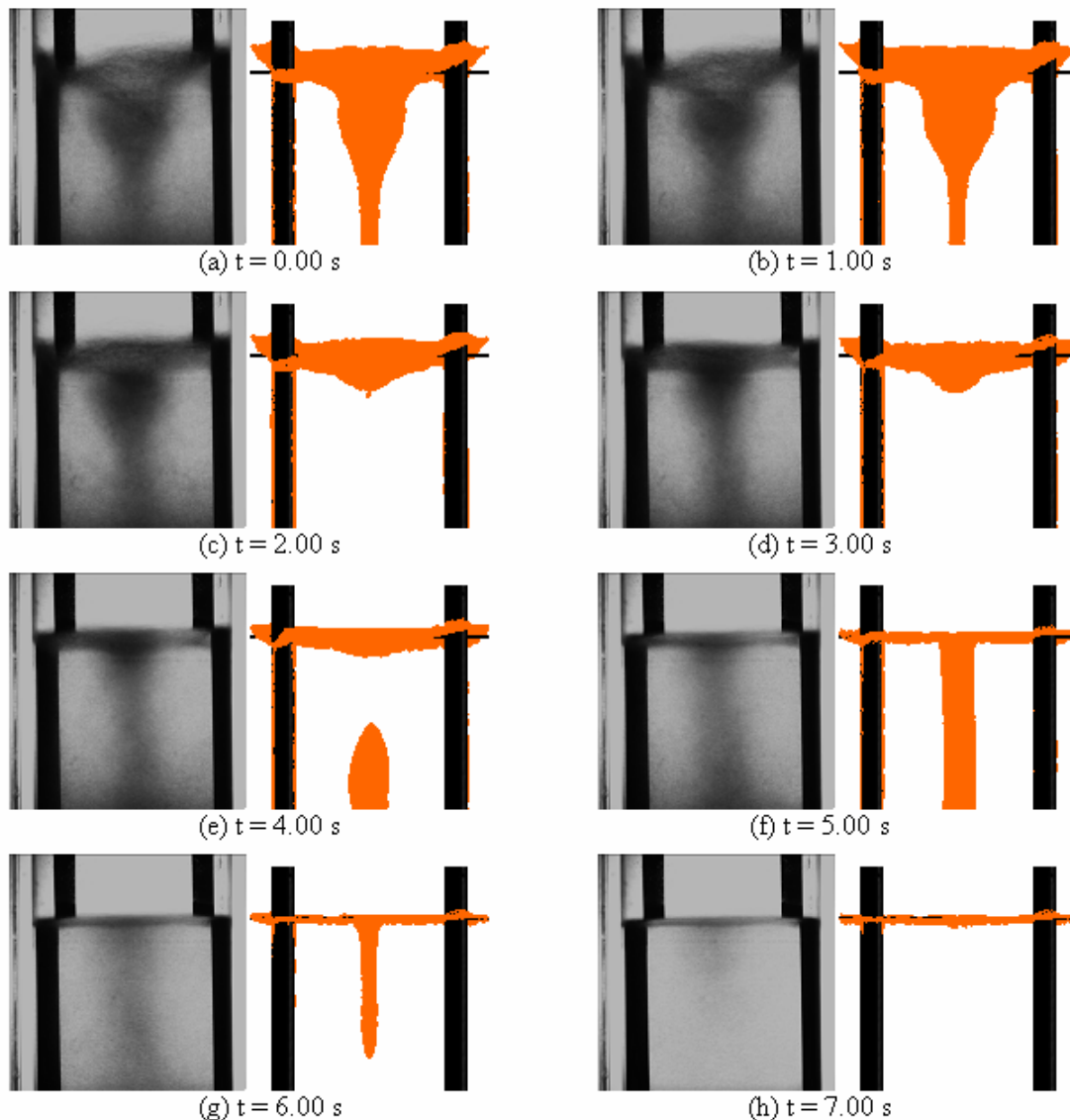
Figure 6.7. Comparison between experimental data and numerical predictions of the free-surface shape profile during agitator stopping. For each time: left: experimental; right: numerical.

The author noted that the predicted free-surface evolution could be highly dependent on the time at which the agitator speed is reduced. In Chapter 5 and in Torré *et al.* (2007c), the simulation of the same vessel with only water and a flat free-surface at 100 RPM during thirty five agitator revolutions revealed very complex flow and vortical structures associated with low frequency instabilities linked to the under-baffled configuration. Thus, running in transient mode for several agitator rotations at constant speed and then stopping the agitator may lead to different free-surface shape profiles depending on the flow structure just before

the point of stopping. In the sixty experiments carried out, it was clearly visible that the free-surface shape profile can be different from one run to another. Averaging the free-surface profiles appears to be a good way of avoiding the high dependence of the initial conditions. Thus, the discrepancies observed between experimental data and numerical predictions during agitator stopping are highly linked to the initial state. The numerical shape evolution presented in this study has to be considered as one of the possible solutions amongst all of the various possibilities.

This analysis shows that the discrepancies that exist between the modelling and the experimental data could also come from either the modelling hypothesis or from the experimental strategy of free-surface capture. The complex physical phenomena that develop in the dynamical equilibrium zone of intense gas/liquid exchanges cannot be fully taken into account in the modelling. Inclusion of only drag forces may not represent fully the physics of the problem, particularly when the global system is highly unsteady, as in the under-baffled case studied here. The interfacial forces acting on the gas bubbles should also contain virtual mass, lift forces, turbulent dispersion, etc. but the modeling of such forces remains a major challenge. Nevertheless, the global features of the free-surface shape evolution during the stopping phase are well predicted. The initial and final states and the global dynamics of the free-surface flattening phenomenon observed numerically are in good agreement with physical considerations and experimental data. In addition, the numerical prediction of gas disengagement located in the impeller region is observed experimentally during the stopping phase. Thus, although the model was used with simplified physics, the inhomogeneous approach appears a good solution for modelling free-surface profiles and transient hydrodynamics, even in conditions with gas disengagement and decreasing agitator speed.

6.5. CONCLUSION

CFD simulations, using a gas/liquid inhomogeneous model, coupled with a homogenous turbulence model in a full transient scheme, have been run to predict the vortex shape and the flow field in an under-baffled agitated vessel during stopping. Qualitative and quantitative numerical and experimental data have been extracted to visualize the dynamics of the free-surface and to describe the time dependant phenomenon occurring during the impeller

slowing phase, including the inertial period after the agitator has completely stopped. The CFD results obtained are in accordance with physical considerations and the free-surface shape evolution tendency predicted numerically is in good agreement with experimental data. The study of the hydrodynamics of the stirred tank during the stopping phase, together with an estimation of the mixing behaviour based on the agitation index during the transient process, has revealed that the history of the fluid evolution and the effect of the fluid inertia during the impeller slowing phase determine the instantaneous results. Therefore the flow field at any given time during the stopping phase cannot be determined via a classical steady-state approach. Modelling free-surface profiles by using a gas/liquid inhomogeneous approach appears a good solution even with simplified physics, as shown by the results obtained previously with an MRF approach and a steady state assumption (see Chapter 4) and here in a full transient manner. Nevertheless, the inertial period has to be considered carefully and the criterion for switching between turbulent and laminar flow has to be investigated in depth if the simulations are to be continued to the point at which the fluid comes to rest.

Chapter 7

CONSTRUCTION AND USE OF DESIGN OF EXPERIMENTS FOR MIXING TIME MODELLING

In this Chapter, the mixing process of a fluid jet injected into the partially-agitated pilot reactor was investigated by mixing time experiments with a colouring/decolouring technique using iodine and thiosulphate. After a brief review of the mixing time definitions and measuring techniques, the first part presents mixing time results for experiments carried out at different agitator speeds, at atmospheric pressure, with a single injection position and pipe diameter. These experimental data allowed determination of the dimensionless mixing time law for these conditions. In the second part, the influence of the agitation speed was complemented by the effect of the injection pressure, injection pipe diameter and the injection position, using a Design of Experiments (DoE) approach. The DoE, used with an analysis of variance, allowed construction of a mixing time model which included all the factors studied. This correlation satisfied the statistical assumptions of the model and the predictions were in good agreement with new experimental data.

7.1. MIXING TIME

The mixing process is usually characterized conveniently by the mixing time. This quantity was one of the most crucial parameters that required fundamental and industrial research work to quantify single-phase homogeneous liquid mixing.

To determine the mixing time experimentally, a tracer is introduced at some location in the stirred vessel and the tracer concentration is measured as a function of time by a suitable method. Then, this tracer distributes throughout the vessel and mixes until reaching a uniform concentration. The mixing time is defined as the time required to achieve a certain degree of uniformity after a perturbation (Nere *et al.*, 2003). The tracer can be a chemical species (inert or reactive), an electrolyte or a fluid with a different temperature. Various techniques have

been developed to measure it, such as: conductivity methods (Kramers *et al.* (1953), Lundén *et al.* (1995), Raghav Rao and Joshi, (1988), Sano and Usui (1985)), thermal methods (Hoogendoorn and Hartog, 1967), spectroscopic methods (Févotte and Puel (2003), Pineault and Cloutier (1972)), colorimetry (single or dual indicators) and coloration/discoloration methods (Baudou *et al.* (1997), Cabaret *et al.* (2007), Fox and Gex (1956), Melton *et al.* (2002)), Laser Induced Fluorescence – LIF – (Gaskey *et al.* (1990), Muhr *et al.* (1999)), Planar Laser Induced Fluorescence – PLIF – (Fall *et al.*, (2001), Houcine *et al.* (1996), Mahouast (1993)), liquid crystal thermography (Hackl and Wurian (1979), Lee and Yianneskis (1997)) and electrical impedance/resistance tomography (Holden *et al.* (1998), Kim *et al.* (2006), Williams *et al.* (1993)). In the case of large and non-transparent reactors, a radioactive tracer can be injected (Roustand *et al.*, 1997); however, the method is too costly for laboratory experiments and this method was judged not sufficiently accurate for small stirring devices (Hackl and Wurian, 1979). For further technical details, the reader is referred to the corresponding reference listed above and to Nere *et al.* (2003) for general descriptions of these methods.

These techniques can be classified in two categories: local and global methods, depending on the volume of fluid necessary for the measurement to obtain the mixing time. The local methods, which can use one or several local intrusive probe(s), give information at one or multiples locations in the vessel. These methods work by recording a physical property (e.g. conductivity, temperature, etc) at the given location(s) and the mixing time is the time taken to reach a certain value or a stabilisation of the physical parameter measured. Although these methods are accurate and usable in non-transparent industrial equipment, it has been shown (Yeoh *et al.*, 2005) that the mixing time obtained using these techniques depends on the probe resolution – determined by both its size and its frequency response – (Rielly and Britter, 1985), probe location (Ruszkowki and Muskett (1985), Jaworski *et al.* (2000)), inert or reactive tracer (Mana, 1997), feed pipe location (Guillard and Trägårdh (2003), Patil *et al.* (2001)), etc.

For this study, it was chosen to carry out mixing time experiments using a visual method which offers many advantages. These methods are non-intrusive and do not disturb the flow in the vessel, they are also very easy to perform with no particular instrumentation needed if the determination is done with the naked eye, and they offer many useful and instructive features, such as the capability to identify and very often quantify the unmixed zones (Cabaret

et al., 2007). However, the vessel must be transparent and the fluid must not be opaque, these conditions being the case for our study, as the pilot reactor is made of glass and filled with water. One of the main limitations of this technique is the subjectivity of the measurement made with the naked eye and it must be the same person who carries out all of the measurements.

Amongst all of the visual techniques which can be carried out using the naked eye, the colouring/decolouring method has been chosen as it is much easier to detect small coloured regions in a discoloured mass of fluid than the inverse. Hiby (1985), who compares the colourization with the decolourization methods through a mathematical analysis, declared that, if dead zones are present, the value of the mixing time is different depending on which method is used. Two important conclusions were: (i) the prolongation of mixing time by dead zones can be detected and measured only by the decolouring method, (ii) the mixing time measured with a chemical indicator are valid also for inert mixing components. Therefore, we chose the colouring/decolouring method for all our experiments.

The mixing time, T_m, is obtained by the colouration/decolouring method using iodine and thiosulphate. Both reactants are chosen to undergo an instantaneous redox reaction. The colouring and the discolouring agents are the iodine (which colours the stirred liquid brown/orange) and the sodium thiosulphate, respectively. When the reaction with the thiosulphate is complete, the stirred liquid changes from a brown/orange to a colourless solution, as presented in Figure 7.1, and according to the following chemical redox reaction:

$$I_2 + 2S_2O_3^{2-} \quad \rightarrow \quad 2I^- + S_4O_6^{2-} \quad ^{(*)}$$
$$\text{(brown-orange)} \qquad \text{(colourless)}$$
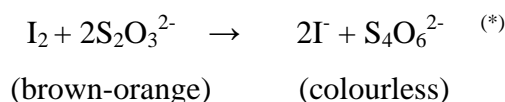
$^{(*)}$ *oxidation-reduction pair: I_2 / I^- (iodine / iodide) and $S_4O_6^{2-} / S_2O_3^{2-}$ (tetrathionate / thiosulphate)*
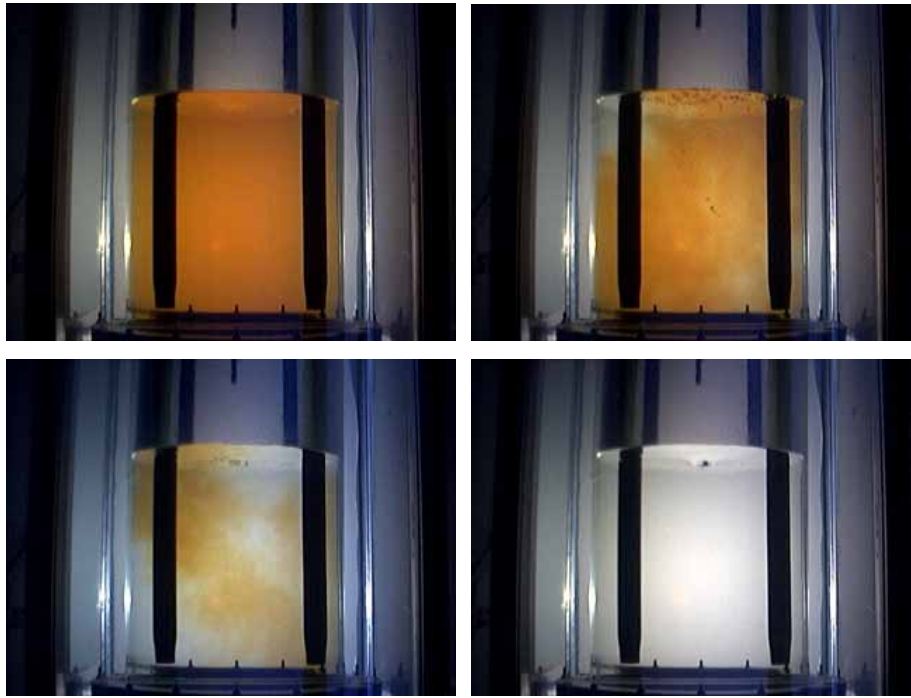
Figure 7.1. Example images of a colouring/decolouring experiment.

Thus, the mixing time is a measurement of the time necessary to detect visually the disappearance of the last wisp of colour.

The complete experimental apparatus is detailed in Chapter 3 and the reader is referred to there for technical details. For all the mixing-time experiments carried out here, the stirred vessel was filled with 109 litres of tap water. A volume of 10 ml of iodine solution at 1 mol/l was introduced at the free-surface and mixed under agitation (N = 100 RPM) during at least one minute. The volume of the decolouring agent (thiosulphate solution) was calculated by scaling-down the volume of stopper introduced in the real industrial conditions. Therefore, a volume of 533 ml of thiosulphate solution was always introduced in the killer vessel of the pilot reactor in all the experiments carried out. The detailed protocol to make the reactant solutions is detailed in Appendix A.

For the experiments carried out at atmospheric pressure, the manual valve of the feeding funnel was opened, leaving the killer vessel open to atmosphere. In pressurized conditions, the killer vessel was pressurized to the desired pressure using 8 bar air and a pressure control valve. After the pressure stabilised, the agitation speed was set at the desired value and maintained for around one minute to ensure the flow had developed and was not in the transient phase that occurs at agitator start-up. Finally, the automatic draining valve was

opened to inject the decolouring agent into the vessel, while simultaneously the stop-watch was started. The stop watch was stopped when the whole tank was completely decoloured, giving the value of the mixing time. Finally, the stirred tank was drained to the sewer and the vessel was cleaned with tap water before starting a new experiment.

A set of preliminary experiments were carried out to test the method of colouration/decolouration. As a systematic determination of the mixing time by using a computerized technique has proved to perform well, as shown in Cabaret *et al.* (2007), we tried to develop an image processing technique based on the analysis of the grey levels, by monitoring the experiments with a camera and analysing the video using Visual Basic macros. Due to the presence of dark areas coming from the vortex formation and the vessel aeration, no satisfactory result were obtained and the determination of the mixing time with the naked eye was found to be more accurate and reproducible. Therefore, the development of an elaborated image processing tool for this application was outside of the scope of this study, the use of the naked eye method was prefered. Nevertheless, this remains a very interesting possibility for future work.

Thirty two experiments were carried out with injections primarily at atmospheric pressure and with a single pipe diameter equal to 17.8 mm. For 50 RPM ≤ N ≤ 250 RPM, Figure 7.2 and Figure 7.3 show the mixing time evolution versus the agitation rotation speed and versus the reciprocal of the agitator speed, respectively.
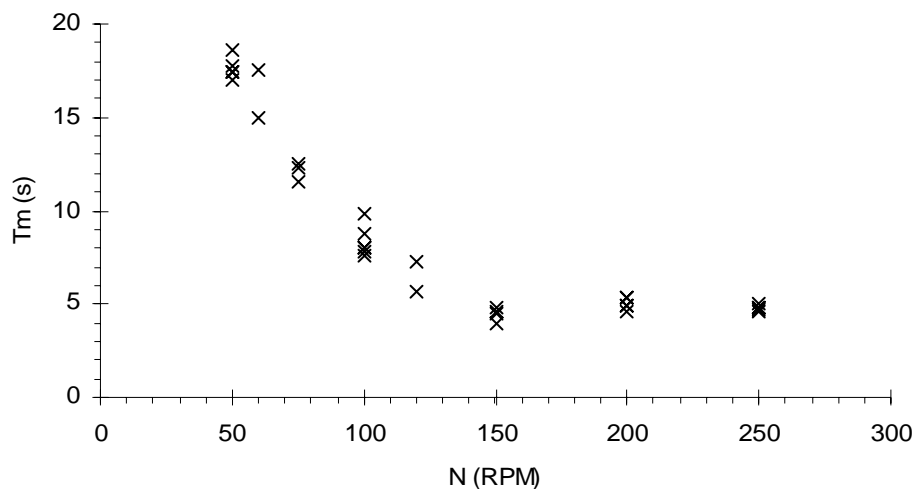
Figure 7.2. Experimental plot of mixing time versus agitator speed. The injection conditions were atmospheric pressure and an injection pipe diameter of 17.8 mm.

In addition to the evolution with N of the mixing time, Figure 7.2 shows the variability of the mixing time measurements. For example, in the six experiments carried out at N = 100 RPM, the mixing time varies from 7.6 s to 9.8 s giving a standard deviation of 0.86 s. Although measuring the mixing time with the naked eye is subjective, this variability is not attributed entirely to this cause. This variability is mainly attributed to the low frequency macro-instabilities (MIs) which develop in this partially-baffled stirred vessel. These MIs have been observed both experimentally and predicted numerically, as explained previously in Chapter 5 and in Torré *et al.* (2007c). The dispersion of the reactant would have a very different behaviour if the jet passes through or misses one of the filamentous vorticity structures, which link the baffle and the agitation regions and rotates at low frequency in the vessel. In addition, if the injected liquid falls close to, or worse into, the precessing vortex which revolves on the free-surface around the vessel axis (at 100 RPM, a typical trajectory is shown in Figure 5.6 of Chapter 5), the dispersion of the reactant will be very different to an injection at 180° to this perturbation. This highlighted the necessity to carry out a *sufficient number* of experiments to capture the significant intrinsic variability of the system studied.
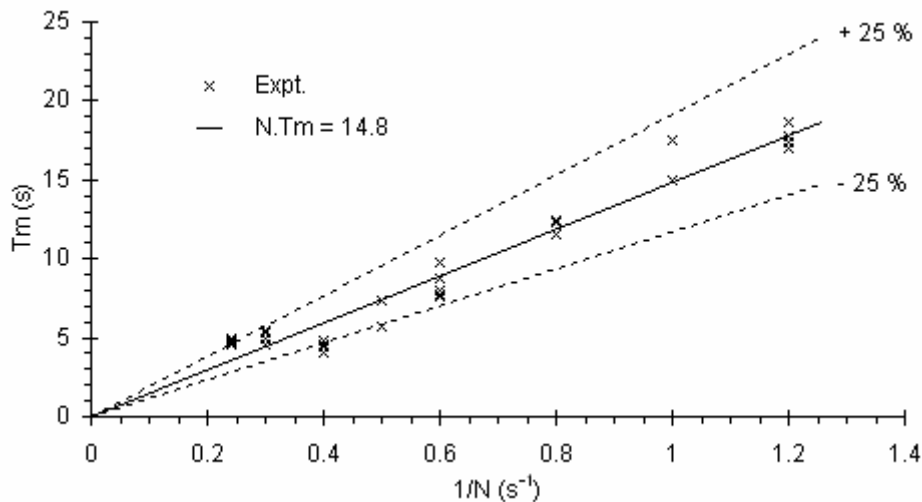
Figure 7.3. Experimental plot of mixing time versus the reciprocal of agitator speed. The injection conditions were atmospheric pressure and an injection pipe diameter of 17.8 mm.

As shown in Figure 7.3, the experimental data for $T_m = f(1/N)$ were found to be fitted well by a straight line passing through the origin. The linear fit and the determination of the fitting parameter (constant equal to 14.8) has been done using the software Statgraphics Centurion XV using an optimisation technique based on a least-squares method (Marquardt-Euler algorithm). The R^2 statistic gave 95.4 % for the fit, meaning that this model explains 95.4 %

of the variability of the mixing time. Surprisingly, since the vessel configuration is not fully-baffled and is relatively far from the standard conditions (see §2.3.2.), this result is in agreement with the well-known law of the dimensionless mixing time, expressed in Eq. (7.1):

$$N.T_m = K \qquad\qquad\qquad (7.1)$$

with the constant K equal to $14.8 \pm 25\%$ (only valid for the present configuration).

However, two remarks must be made concerning the establishment of this type of law. On one hand, this law is usually determined with the tracer introduced as a pulse in the vessel. In our case, the draining time for injecting 533 ml with a 17.8 mm pipe at atmospheric pressure was around one second and was not "instantaneous", causing the mixing process to begin before all the injected fluid was in the vessel. On the other hand, the fluid is injected into the vessel as a jet. This type of injection modifies the bulk hydrodynamics because of two reasons: it is a momentum source which can modify the turbulence levels locally and it is a coherent jet which introduces numerous gas bubbles into the bulk due to the impact on the free-surface. These two aspects are discussed later in Chapter 8.

Although the data fit a dimensionless mixing time law in the region of rotation speed from 50 to 250 RPM, it was highlighted that with a rotation speed above 200 RPM, the gas aeration of the mixing vessel begins to be very important, as shown in the snapshots of Figure 7.4.
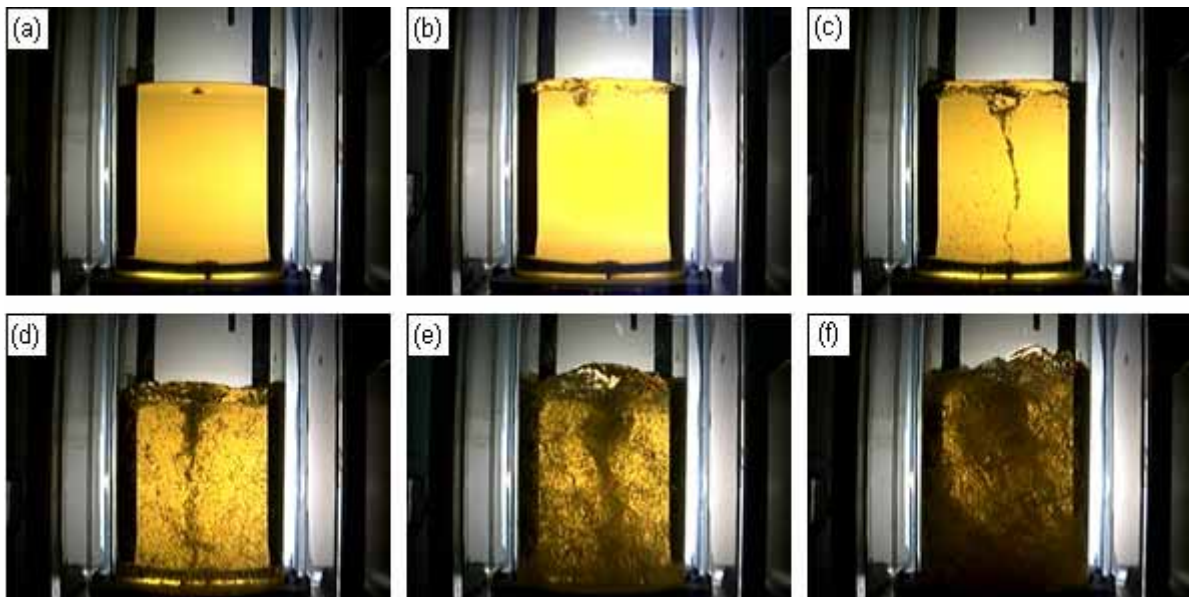
Figure 7.4. Visualization of the mixing vessel aeration for different agitator rotation speeds: (a) 50 RPM, (b) 100 RPM, (c) 150 RPM, (d) 200 RPM, (e) 250 RPM, (f) 400 RPM.

The introduction of air bubbles via the vortex modifies both the loading of the impeller and the structure of the flow. This vessel aeration could have a great influence on the mixing time and the mixing time law may not be valid for higher rotation speeds (e.g. 400 RPM as shown in Figure 7.4(f)). As noted by Guillard and Trägårdh (2003), the effect of a gas phase on the mixing process in aerated stirred tanks reactors has rarely been investigated and the conclusions linked to the mixing time in aerated conditions can vary from one author to another. For example, some authors observed that the mixing time was always longer in aerated vessels than for those obtained in single phase liquid with similar energy input (Ju and Chase, 1992), others exactly the inverse (Pedersen *at al.*, 1994) and others that the mixing time increased and decreased, depending on the aeration rate and turbine agitation speed (Vasconcelos *et al.*, 1998). In our case, the measurement uncertainties linked to the mixing time determination become too large when the rotation velocity is above 250 RPM. The gas/liquid interface makes the bulk so dark that it is very difficult to measure the discolouration time with any accuracy. Note that the use of a computerized method or a direct imaging process for measuring the mixing time would also be useless in these aerated conditions due to the presence of too many dark areas. Thus, it can be noted that the effects of significant aeration seems to be unfavourable for enhanced mixing.

The constant K of Eq. (7.1), being specific to the dataset obtained with the given vessel configuration tested, is not usable if the injection conditions are modified (e.g. injection point, injection pressure). The construction of a mixing time law that includes the numerous factors involved in this problem (agitation speed, injection pressure, pipe diameter, injection position, etc.) could not be done by a one-per-one parameter strategy. The number of experiments to carry this out, regarding the variability of the response and the number of variables to be investigated, led to investigation of a global approach which would minimize the number of experiments without decreasing the precision of the results significantly. This strategy is the Design of Experiments presented in §7.2.

7.2. DESIGN OF EXPERIMENTS (DoE)

7.2.1. <u>Presentation and notations</u>

Design of Experiments (DoE) is widely used in research and development, where a large proportion of the resources are devoted to optimization problems. This method was first developed in the 1920s and 1930, by the renowned mathematician and geneticist Sir Ronald Aylmer Fisher for application to agriculture experiments in the agronomic station of Rothamstead (Fisher, 1949). It has not really diffused into the industrial community in spite of the work of numerous scientists (Plaquett and Burmann (1946), Box and Behnken (1960) Reschtschaffner (1967), Doehlert (1970), and others), this approach was simplified and generalized in the 80s by the Doctor Genichi Taguchi, who proposed lists of design of experiments tables (Taguchi and Konishi, 1987) to allow popularisation of this tool in Europe.

In numerous situations, the researcher or the engineer needs to understand how a system reacts as a function of different factors susceptible to modify it. A Design of Experiment is a structured, organized method that is used to determine the relationship between the different factors affecting a process and the output of that process. It is not easy to establish such relations between the different responses and factors, particularly if interactions exist between these factors. Design of Experiment involves designing a set of experiments in which all relevant factors are varied systematically. When the results of these experiments are analysed, they help to identify optimal conditions, the factors that most influence the results, and those that do not, as well as details such as the existence of interactions between factors.

To be able to study the influence of a factor on the response whatever the level of the other factors, a "mesh" must be built in the domain of validity of the factors and an experiment is performed at each point of the mesh. The principle of the method of Design of Experiments consists in building well-structured data matrices and to not study all the points of the mesh but only some chosen for their characteristic of orthogonality. The principal advantages of this method are a reduction in the number of experiments, the possibility to study a large number of factors, the detection of the eventual interactions between the factors, and the determination of the results with good precision. However, the resulting model is a

mathematical model and always requires the judgement of the experimenter to check if the results are physically acceptable or not.

Building a design means carefully choosing a number of experiments that are to be performed under controlled conditions and which give a better definition of the problem.

There are four interrelated steps in building the design:
- define an objective for the investigation, e.g. better understand or sort out important variables;
- define the variables that will be controlled during the experiment (design variables), and their levels or ranges of variation;
- define the variables that will be measured to describe the outcome of the experimental runs (response variables);
- amongst the available standard designs, choose the one that is compatible with the objective, the number of design variables and the precision of measurements, and has a reasonable cost.

Standard designs are well-known classes of experimental designs. They can be generated automatically as soon as the objective has been decided, the number and nature of design variables, the nature of the responses and the number of experimental runs. Therefore, the statistical software STAGRAPHICS Centurion XV was used to build the Design of Experiments presented here. For further details of this subject the reader is advised to consult the published papers and books of Aggarwal *et al.* (1997), Alexis (1995), Goupy (1999, 2005), Louvet and Delplanque (2005), Pillet (1997), Souvay (1995) and Vigier (1988), which have been used to understand and use the concepts and the methods presented in this Chapter.

Throughout the rest of this Chapter, a standard notation is used which represents the factors to be manipulated by the letter *X* and the response variables by the letter *Y* (Statgraphics Centurion XV 15.0.10, user's guide). In designing an experiment, we construct a set of *n* experimental runs in order to fit a statistical model of the general form of Eq. (7.2):

$$Y = f(X_1, X_2, X_3, \dots X_k) + \varepsilon \qquad\qquad (7.2)$$

This model represents the manner in which a selected response variable is affected by a set of *k* experimental factors, while ε represents the noise or experimental error. In particular:

Y_i = response observed on the i-th experimental run, i = 1, 2,…, n

X_{ij} = the level of the j-th experimental factor on the i-th experimental run, j = 1, 2,…, k

ε_i = experimental error on the i-th experimental run

n = number of experimental runs

k = number of experimental factors

Then we have Eq. (7.3):

$$Y_i = f(X_{i1}, X_{i2}, X_{i3}, \ldots X_{ik}) + \varepsilon_i \qquad (7.3)$$

where the function f( ) represents the mean or expected value of the response as a function of the experimental factors. The experimental error ε is typically assumed to follow a normal distribution with mean 0 and standard deviation σ.

A statistical model of the above form is constructed for each of the response variables being studied. Since when analysing the results of an experiment, each response is modelled separately, it is sufficient to write the model in terms of a single response.

7.2.2. <u>The design adopted</u>

The understanding and then the optimization of the mixing of the reactant contained initially in the killer vessel into the partially-baffled, agitated vessel has required a preliminary analysis of the parameters which could play a significant role in this mixing process, while keeping in mind the industrial constraints. For this study, it was decided to maintain the vessel geometry, the baffle type and their number, the impeller model and its position in the vessel constant. The industrial bulk volume (constant filling ratio) as well as the injected killer volume were also scaled-down and are not changed in any of the experiments. Finally, it was decided to use only water as the working fluid. Changing the physical properties of the fluids was considered to be unwise before having a solid knowledge of this problem. Therefore, the design was built with 5 factors and 3 levels per factor as presented in Table 7.1 and in Figure 7.5.

Table 7.1 Factors and level of factors for the design of experiments.

Factor	Symbol	Unit	Low level	Central level	High level
Agitation speed	N	RPM	50	100	150
Pressure	P	bar relative	0	1	2
Injection pipe diameter	d	mm	7.2	12.5	17.8
X position	X	mm	0	47	94
Y position	Y	mm	0	64.7	129.4
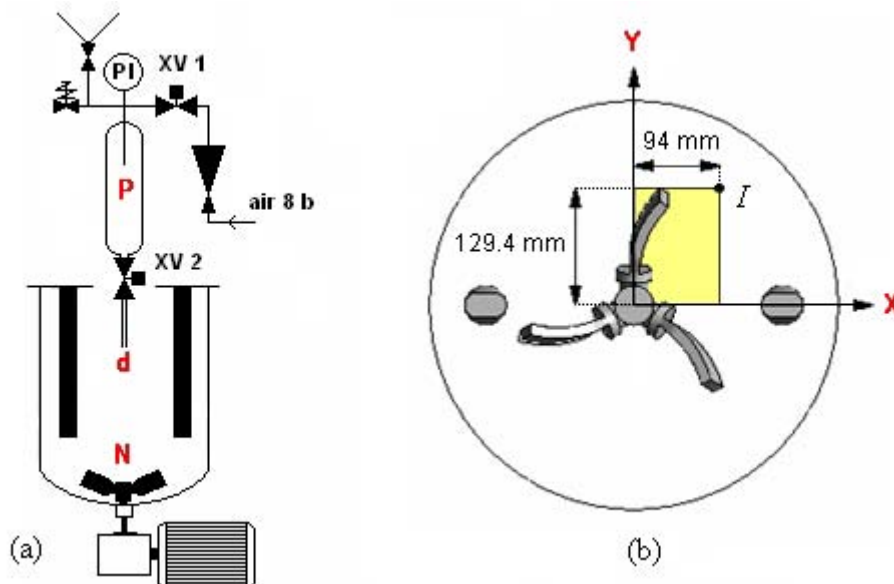
Figure 7.5. Schematic of the pilot reactor and localisation of the factors. (a) lateral view, factors P, d and N; (b) top view, factor X and Y.

The Design of Experiments presented is a Response Surface design, intended to select the optimal settings of a set of experimental factors. These designs involve at least three levels of the experimental factors, which must be quantitative. Each effect was supposed, *à priori*, to have a quadratic effect on the response.

The Design of Experiments chosen for this analysis was primarily based on a Box-Behnken design (Box and Behnken, 1960) with 46 experiments. Box-Behnken designs (BBD) are a class of rotatable or nearly rotatable second-order designs based on three-level incomplete factorial designs (Ferreira *et al.*, 2007). This first design corresponds to the first 46 rows of the experimental matrix presented in Appendix B. The experimental points are all located at an equal distance from the centre of the experimental domain, located in the centre of the 40 elementary cubes which build the global 5-cube. For three factors ($X1$, $X2$, $X3$), the graphical representation can be seen more easily in the form of a cube that consists of the central point and the middle points of the edges as shown in the Figure 7.6. For additional

information, a review of Box-Behnken designs is presented in Ferreira *et al.*, (2007) and an example of the use of the response surface methodology with this design is given by Aslan and Cebeci (2007).
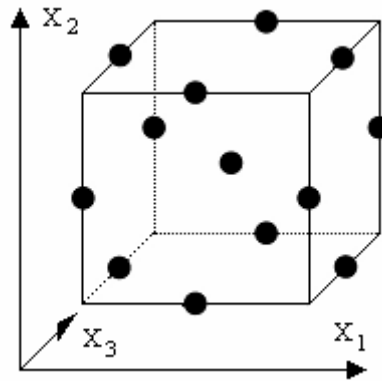
Figure 7.6. Graphical representation of BBD with three factors.

This initial design was augmented by 17 points to reinforce the prediction around the injection point located at X = 94 mm, Y = 129.4 mm, which corresponds to the real stopper injection location in the industrial case (transformed using the scale-down rules).

Note that if all the possible combinations between the factors had been studied (called a complete Design of Experiments), with five factors with three levels per factor, the number of experiments to be carried out would have been equal to $3^5 = 243$ (instead of 63). This type of design is of course unrealistic, justifying the use of well-known geometries allowing reduction of the number of experiments.

7.2.3. <u>Analysis of Variance (ANOVA) and the adjusted model</u>

The relative magnitude of the effect and the significance of the different factors can be obtained by the decomposition of the variance, called ANOVA. The ANOVA partitions the variance of the response into several components: one for each main effect, one for each interaction, and one for the experimental error. To have a good understanding of the ANOVA tables presented in this paragraph requires explanation of some definitions (based on Polhemus, 1999):

- **The sum of squares** measures the increase in the variance of the experimental error which would occur if each term were separately removed from the model. The sums of squares for the total error is also included, where:

$$S_{error} = \sum_{i=1}^{n} e_i^2 = \sum_{i=1}^{n} (y_i - \hat{y}_i)^2 \qquad (7.4)$$

with e_i the i-th residual, measuring the difference between the observed response for run *i* and the value predicted by the fitted model;

- The **degrees of freedom** (df) associated with each term;

- The **mean square** (MS) associated with each term, obtained by dividing the associated sum of squares by its degrees of freedom;

- The Fisher ratio, named F-ratio, which divides the mean square of an effect by the mean squared error, are used to determine the statistical significance of each effect:

$$F = \frac{MS_{effect}}{MSE} \qquad (7.5)$$

where the MSE estimates the variance of the experimental error:

$$MSE = \frac{S_{error}}{df_{error}} \qquad (7.6)$$

- The **P-value** associated with testing the null hypothesis that the coefficient for a selected effect equals 0, implying that the effect is not present. P-values below a critical level, such as 0.15 (15%), indicate that the corresponding effect is statistically significant at that significance level.

- The **R²** value ranges from 0% to 100% and measures how well the model fits the observed response data. The percentage of the variability in the response variable which has been represented by the fitted model, is calculated by:

$$R^2(\%) = 100 \left(1 - \frac{S_{error}}{S_{total}}\right) \qquad (7.7)$$

- The **error of estimation** is the estimated standard deviation of the experimental error given by :

$$\hat{\sigma} = \sqrt{\mathrm{MSE}} \qquad\qquad\qquad (7.8)$$

The ANOVA of the results concerning the initial mixing time model is detailed in Table 7.2.

Table 7.2. ANOVA table for the initial model at the significance level of 15%.

Source	Sum of squares	df	Mean square	F-ratio	P-value
A:N	230.707	1	230.707	78.91	0.0000
B:P	*1.20326*	*1*	*1.20326*	*0.41*	*0.5247*
C:d	8.7209	1	8.7209	2.98	0.0915
D:X	10.9357	1	10.9357	3.74	0.0599
E:Y	9.41191	1	9.41191	3.22	0.0800
AA	27.5276	1	27.5276	9.42	0.0038
AB	*3.77378*	*1*	*3.77378*	*1.29*	*0.2623*
AC	*3.16502*	*1*	*3.16502*	*1.08*	*0.3041*
AD	*3.15483*	*1*	*3.15483*	*1.08*	*0.3048*
AE	8.89765	1	8.89765	3.04	0.0884
BB	8.44667	1	8.44667	2.89	0.0966
BC	*3.29774*	*1*	*3.29774*	*1.13*	*0.2943*
BD	*5.1617*	*1*	*5.1617*	*1.77*	*0.1911*
BE	*2.17675*	*1*	*2.17675*	*0.74*	*0.3931*
CC	*2.46901*	*1*	*2.46901*	*0.84*	*0.3634*
CD	*1.42712*	*1*	*1.42712*	*0.49*	*0.4886*
CE	*2.22965*	*1*	*2.22965*	*0.76*	*0.3875*
DD	*1.3737*	*1*	*1.3737*	*0.47*	*0.4968*
DE	*0.608026*	*1*	*0.608026*	*0.21*	*0.6507*
EE	*4.60467*	*1*	*4.60467*	*1.58*	*0.2164*
Total error	122.791	42	2.92359		
Total (corr.)	793.211	62			

$R^2 = 84.5$ %
Error of estimation = 1.71

Since the P-value of each effect is not below 0.15, the considered effect is not significant at the significance level specified (15%). As shown in the last column of Table 7.2, the model could be simplified (adjustment of the model) to eliminate the factors included in the experimental error. As these effects are included in the experimental error (noise), all the terms of the initial model are not relevant. The simple effect of the pressure (B) is not significant but it was conserved in the model because the effect of the pressure is expressed through its quadratic term BB and its interaction with the X position (BD). After simplification of the initial model, the ANOVA of the final model obtained is presented in Table 7.3.

Table 7.3. Analysis of variance for the final model at the significance level of 15%.

Source	Sum of squares	DF	Mean square	F- ratio	P-value
A:N	241.336	1	241.336	86.89	0.0000
B:P	*3.89408*	*1*	*3.89408*	*1.40*	*0.2420*
C:d	9.25677	1	9.25677	3.33	0.0739
D:X	11.1563	1	11.1563	4.02	0.0505
E:Y	6.14028	1	6.14028	2.21	0.1433
AA	40.958	1	40.958	14.75	0.0003
AD	6.24227	1	6.24227	2.25	0.1401
AE	14.0222	1	14.0222	5.05	0.0291
BB	13.2506	1	13.2506	4.77	0.0337
BD	14.2105	1	14.2105	5.12	0.0281
CC	6.78403	1	6.78403	2.44	0.1244
EE	9.18901	1	9.18901	3.31	0.0749
Total error	138.869	50	2.77739		
Total (corr.)	793.211	62			

R-squared = 82.5 %
Error of estimation = 1.67

The statistical significance of the R-squared (R^2 = 82.5 %) means that this adjusted model can explain 82.5 % of the variability of the mixing time experiments. The results of Table 7.3 are plotted on a standardized Pareto chart, as is shown in Figure 7.7, where the horizontal axis displays the standardized effects, defined by Eq (7.7):

$$\text{Std. effect} = \frac{\text{effect}}{\text{std. error for the effect}} \qquad (7.7)$$
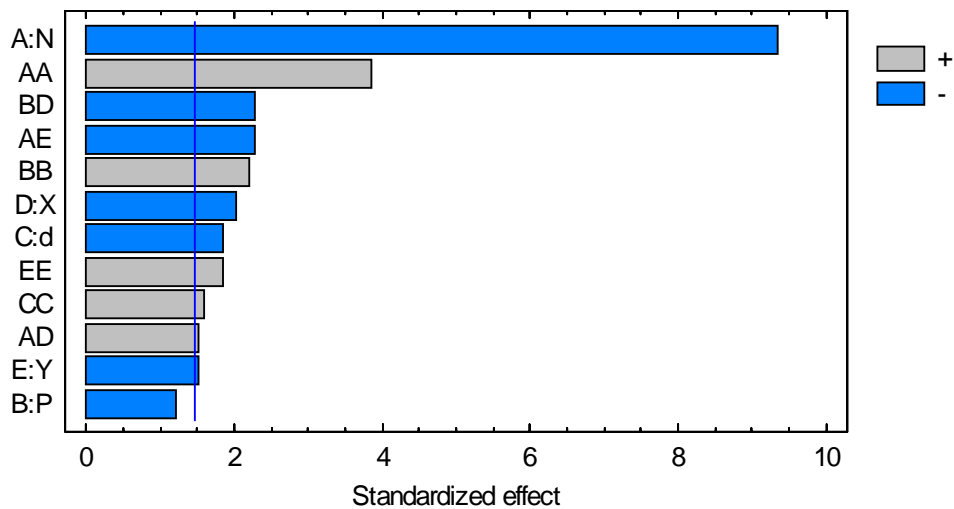
Figure 7.7. Standardized Pareto chart for the initial model.

The length of each bar is proportional to the value of a t-statistic calculated for the corresponding effect and these standardized effects may be used to test the statistical significance of the effects. Any standardized effect to the right of the vertical line indicates that it is statistically significant at the specified significance level (15 %).

In the current case, the main effects, namely the agitation speed (A), the pipe diameter (C), the X position (D) and the Y position (E) are statistically significant at the 15% significance level, with four quadratic contributions for the agitation speed (AA), the pressure (BB), the pipe diameter (CC) and the Y position (EE). There are also three significant interactions between the pressure and the X position (BD), the agitation speed and the Y position (AD), and the agitation speed and the X position (AD).

7.2.4. <u>Tests of the adjusted model</u>

Before using the mixing time model obtained by this DOE, the adjusted model must be tested both by diagnostics plots and by comparing the predictions of the model with new experimental data (validation experiments).

7.2.4.1. Diagnostic plots

Figure 7.8 plots the observed response Y_i versus the fitted values $\hat{Y}_i$, together with a diagonal line.
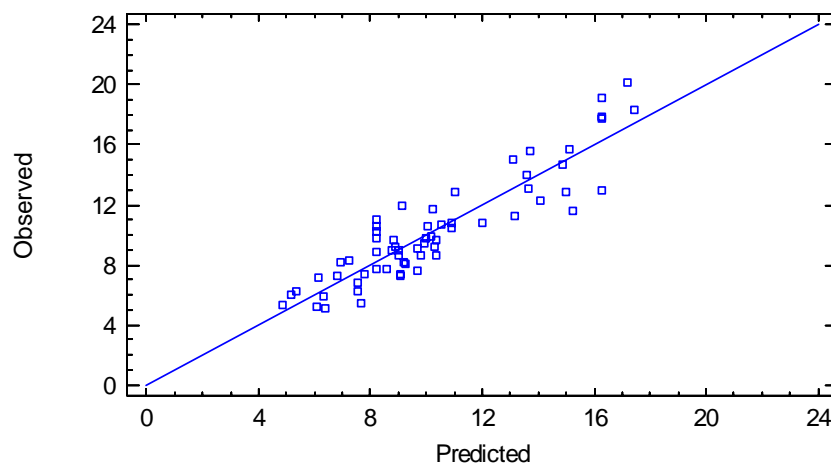
Figure 7.8. Observed response versus fitted values with the adjusted model.

If the model fits well, the values should lie close to the line. It is clear that the predicted value fits the experimental observations with reasonably good agreement.

Figure 7.9 plots the residuals ε_i versus run number i, with a horizontal line at zero.
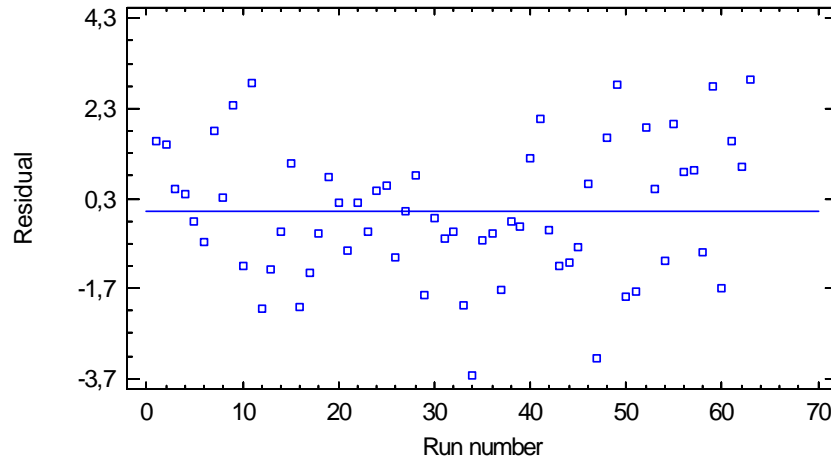
Figure 7.9. Residual versus run number for the adjusted model.

Any non-random pattern may indicate a time-dependent trend or other effect. It is not the case here and the residuals vary randomly around the line, thus an external factor is not superimposed on the observations.

Figure 7.10 plots the residuals ε_i against quantiles of a normal distribution, with a fitted line as a reference.
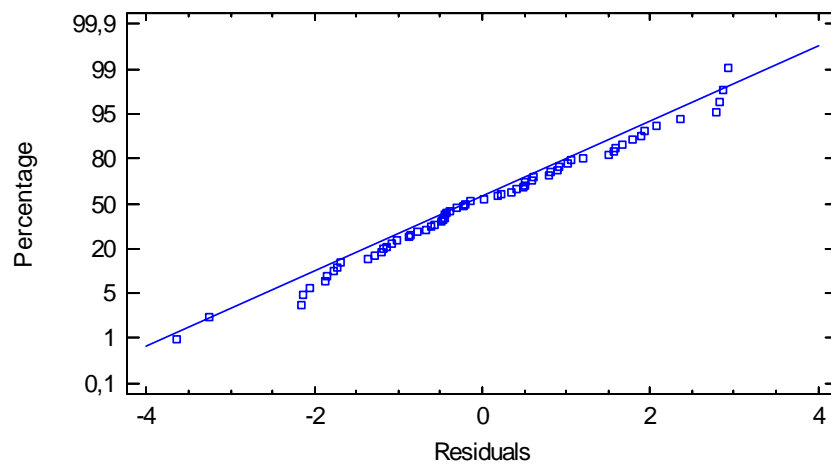
Figure 7.10. Residual plotted against quantiles of a normal distribution.

The points lie along a straight line so the experimental error follows a normal distribution. This is an important hypothesis of the Design of Experiments method which is validated here because the experimental error, ε, is typically assumed to follow a normal distribution with mean 0 and standard deviation σ.

7.2.4.2. Regression model

The coefficients used in the polynomial model for the prediction of the mixing time are listed in Table 7.4.

Table 7.4. Fitting coefficients for the mixing time model.

Coefficient	Estimation	Coefficient	Estimation
constant	29.0382	AD	0.000365391
A:N	-0.19895	AE	-0.000423499
B:P	-1.29704	BB	0.97726
C: d	-0.733801	BD	-0.0232703
D:X	-0.0285584	CC	0.0247845
E:Y	0.00732769	EE	0.000204299
AA	0.00068076		

The DOE model equation which gives T_m (in seconds) is expressed in Eq. (7.9) with the agitation speed N in RPM, the injection pressure P in bars, and the pipe diameter d and the injection position X and Y in mm. The precision of the model is $\pm \sigma_{mod} = \pm 0.85$ s.

$$T_m \text{ (s)} = 29.0382 - 0.19895(N) - 1.29704(P) - 0.733801(d) - 0.0285584(X) + 0.00732769(Y) + 0.00068076(N^2) + 0.000365391(N.X) - 0.000423499(N.Y) + 0.97726(P^2) - 0.0232703(P.X) + 0.0247845(d^2) + 0.000204299(Y^2)$$

$$(7.9)$$

7.2.4.3. Model predictions versus new experiment results

The regression model forms a predictive equation which can be used to predict values of the response variable at various combinations of the experimental factors. Before exercising the model, it must be ensured that the model fits the data well.

New experiments have been carried out with intermediate values of the factors to test the DoE model on points located between the initial points of the mesh. Table 7.5 shows the parameters chosen for these validation experiments (denoted *V1*, *V2* and *V3*) and the mixing time results. Note that the pipe diameters have been chosen based on the standard pipe diameters available in the lab (10 mm and 15 mm). Two other important points have been tested: the initial injection point (denoted *I*) and the centre point of the experimental domain (denoted *C*). The experimental standard deviations (σ_{exp}) are based on the experimental results and the standard deviation for the DoE model (σ_{mod}) is the error of estimation coming from the ANOVA analysis available in Table 7.3.

Table 7.5. Comparison between model predictions, new experiments results, centre point and the initial injection point.

	number of experiments	N (RPM)	P (bar)	d (mm)	X (mm)	Y (mm)	Tm_{exp} (s)	σ_{exp} (s)	Tm_{mod} (s)	σ_{mod} (s)
V1	3	125	0.5	15	23.5	97.05	7.1	0.8	6.6	1.7
V2	3	75	1.25	10	70.5	32.35	10.5	1.4	10.3	1.7
V3	3	75	0.25	7.2	82.25	113.23	13.1	1.5	13	1.7
I[*]	4	50	0	17.8	94	129.4	16.9	2.7	16.2	1.7
C[**]	6	100	1	12.5	47	64.7	9.7	1.2	8.2	1.7

[*] : initial injection point
[**]: centre point

As shown in Figure 7.11, the DoE predictions and the experimental results are in very good agreement. The trends are well predicted, as well as the values of the mixing time.
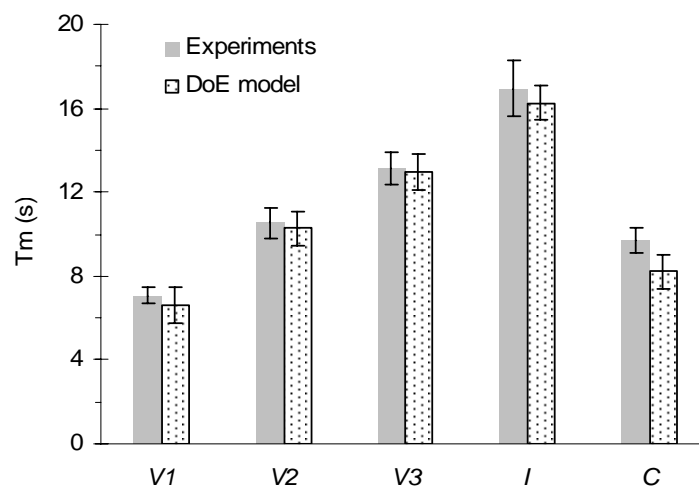
Figure 7.11. Comparison between experimental data and the DOE model predictions (errors bars correspond to $\pm$ $\sigma_{mod}/2$).

It has already been confirmed using the diagnostic plots presented in §7.2.4.1 that the statistical hypothesis made for the design was valid. Here, the accuracy of the model predictions is demonstrated over the entire experimental domain. In addition, the mixing time data prediction via the DoE model can be superimposed on the data of Figure 7.3 to verify if the DoE model is compatible with Eq (7.1). Note that the data set considered in §7.1 is independent of the mixing time data which enables the DoE model to be built, as shown in Figure 7.12.
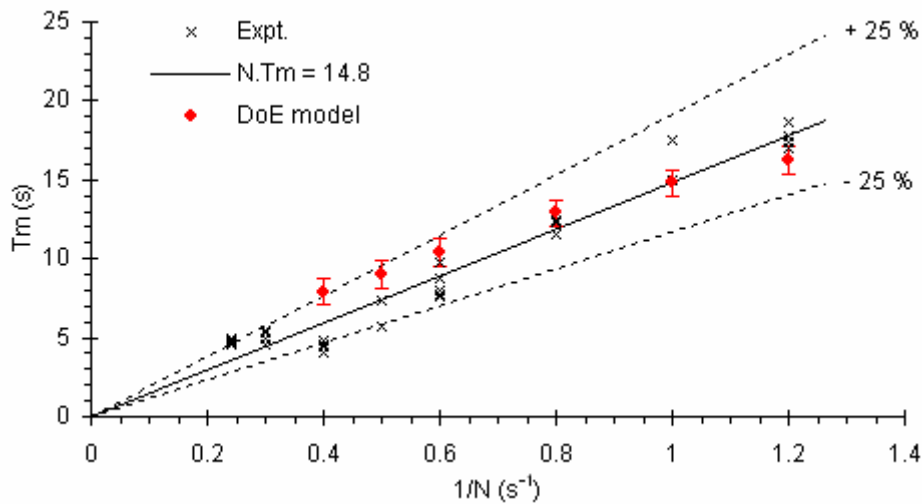
Figure 7.12. Comparison between the experimental data from §7.1 and DoE model predictions of the mixing time versus the reciprocal of the agitator speed. The injection conditions were atmospheric pressure and an injection pipe diameter of 17.8 mm. The error bars of the DoE predictions are set equal to $\pm\sigma_{mod}/2$).

In spite of two different form of law concerning the variation of the mixing time with N (hyperbolic for the dimensionless mixing time ($T_m = K/N$) and a quadratic polynomial for the DOE model), the predictions of the DoE model are in good agreement with the data of §7.1. Therefore, the DoE model can replace Eq. (7.1) and be used as a more general predictive tool covering the domain of the operating conditions of the DoE.

7.3. RESULTS

7.3.1. <u>Main effects</u>

Figure 7.13 shows how the predicted response $\hat{Y}$ varies when each of the factors in the model is changed from its low level to its high level, with all other factors held at the centre of the experimental region (midway between the low level and the high level).
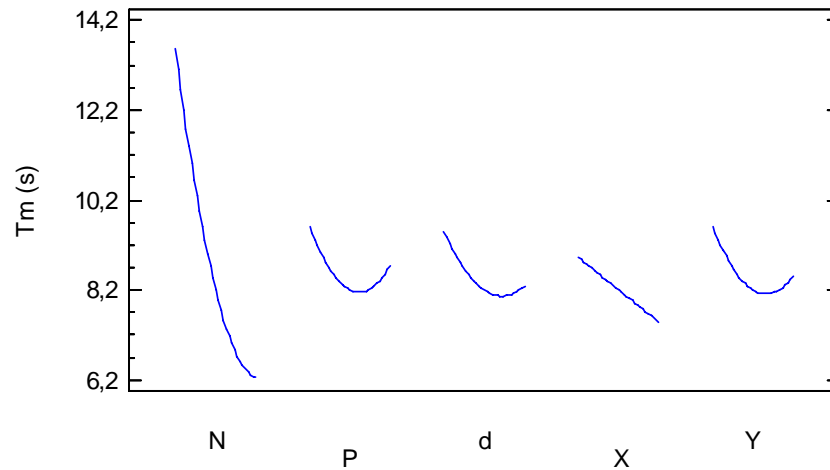
Figure 7.13. Main effects plot for each of the factors in the model (for each factor considered, all other factors remain at the centre of the experimental region).

The agitator rotation speed (N) has the largest impact on the mixing time. It is noted that there is a non-linear contribution to the mixing time curves corresponding to agitation speed (N), the injection pressure (P), the pipe diameter (d) and the Y position (Y). As shown, the behaviour is non-linear for all of the effects except for the X position, and the choice of three levels per factor is justified. Note that the curve $T_m = f(N)$ was shown to perform well in §7.2.4.3.

7.3.2. <u>Interaction plots</u>

When significant interactions exist amongst the experimental factors, the main effects plots do not tell the whole story about the factors which interact and they can even be misleading. In such cases, an interaction plot is produced for each pair of factors. The interaction plot shows how the predicted response varies when a selected factor is changed from its low level to its high level, separately for the low and high levels of a second factor. If two factors do not interact, the effect of one factor will not depend upon the level of the other and the two lines in the interaction plot will be approximately parallel. If the factors interact, the lines will not be parallel and may even cross. In our case, only three interactions are relevant at the

significance level of 15%: the interaction between the rotation speed and the X position, the interaction between the agitation speed and the Y position and the interaction between the pressure and the X position. Figures 7.14 and 7.15 plot in a different manner each interaction. For example, for the interaction AD (or DA), Figure 7.14 gives the variation of T_m from N= 50 to 150 RPM (factor A) with X (factor D) maintained either at its higher level (X = 94 mm, denoted +) or its lower level (X = 0 mm, denoted -); Figure 7.15 gives the variation of T_m from X = 0 to 94 mm with N maintained either at its higher level (N = 150 RPM, denoted +) or its lower level (N = 50 RPM, denoted -).
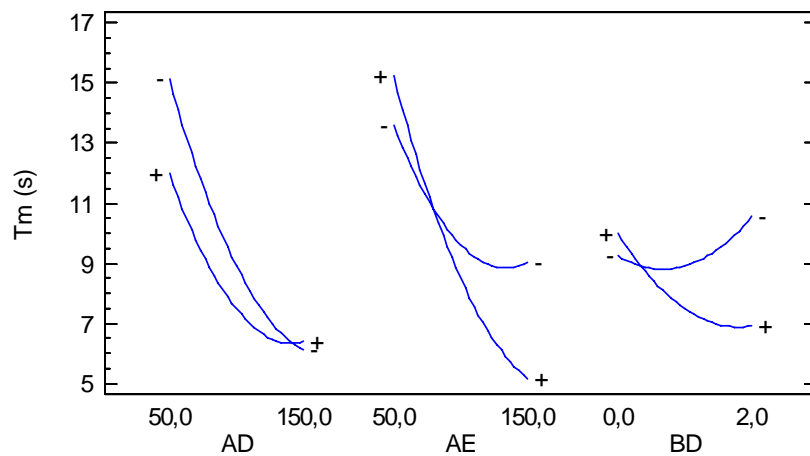
Figure 7.14. AD, AE and BD interaction plots. Abscissa shows the variation of the first letter of the plotted interaction. (+): higher level of the factor; (-): lower level of the factor.
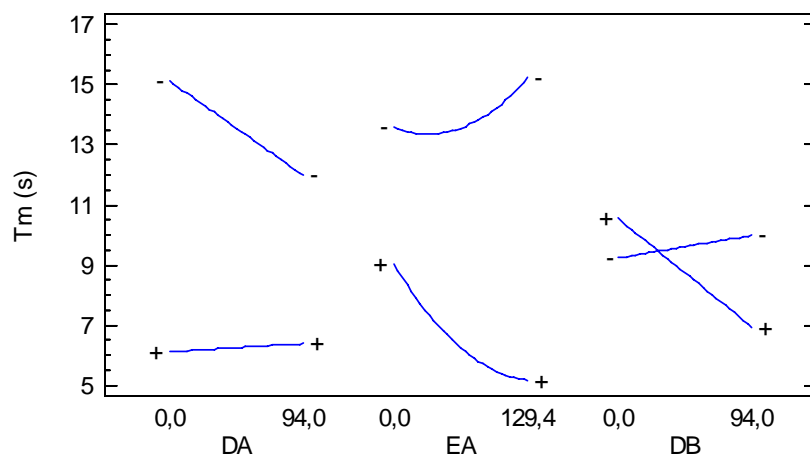
Figure 7.15. DA, EA and DB interaction plots. Abscissa shows the variation of the first letter of the plotted interaction. (+): higher level of the factor; (-): lower level of the factor.

AD and DA interactions: the effect of the position X on the mixing time is more important at low rotation speed. An increase of the value of X from 0 to 94 mm is favourable at 50 RPM but has almost no influence at 150 RPM.

AE and EA interactions: the effect of the position Y on the mixing time has a different influence at low rotation and high rotation speeds. An increase of the value of Y from 0 to 129.4 mm is favourable at 150 RPM mm and is unfavourable at 50 RPM.

BD and DB interactions: at X = 0, the minimum mixing time is obtained for an intermediate pressure between 0 and 2 bars. When the jet is introduced using a high pressure, the thiosulphate is injected directly to the bottom of the tank and the reactant has difficulties in flowing upwards, with the last areas to be decolourized being observed experimentally in the upper parts of the tank. In contrast, a jet injected at atmospheric pressure does not have enough momentum to penetrate into the base of the vessel. An intermediate value seems to be the optimum.

7.3.3. <u>Response surfaces and contour plots</u>

Once a suitable model has been fitted and checked, the results must be displayed in a manner that is easily understandable. Since it is often difficult to gain insights by looking at a mathematical equation, the results are presented by surface plots and contour plots for displaying the fitted model. The surface plot displays the predicted response as a function of any two of the experimental factors, with the other factors held at selected values. The height of the surface represents the predicted value, $\hat{Y}$, which is plotted over the range of the experimental factors. The contour plots show regions at selected values of the predicted response. In the cases presented here, the plot divides the range of the predicted values for the mixing time into 15 regions extending from 4 to 19 s.

The influence of the injection location point is analysed with response surfaces presented in Figure 7.16 calculated with the intermediate pipe diameter (d = 12.5 mm). Whatever the rotation speed and the injection pressure, an injection into the vortex core (X, Y) = (0, 0) appeared never to be favourable. This result is in agreement with the conclusion of the interaction plot figures analysed in §7.3.2. The more favourable injection locations are variable and depend on the injection pressure and the agitator rotation speeds: at low rotation speed (N = 50 RPM) and whatever the injection pressure value, the best position is around (X, Y) = (94 mm, 0). At high rotation speed (N = 150 RPM), the optimum injection location is

moved from (X, Y) = (0, 129.4 mm) to (X, Y) = (94, 129.4 mm) if the (relative) injection pressure is varied from 0 to 2 bar.
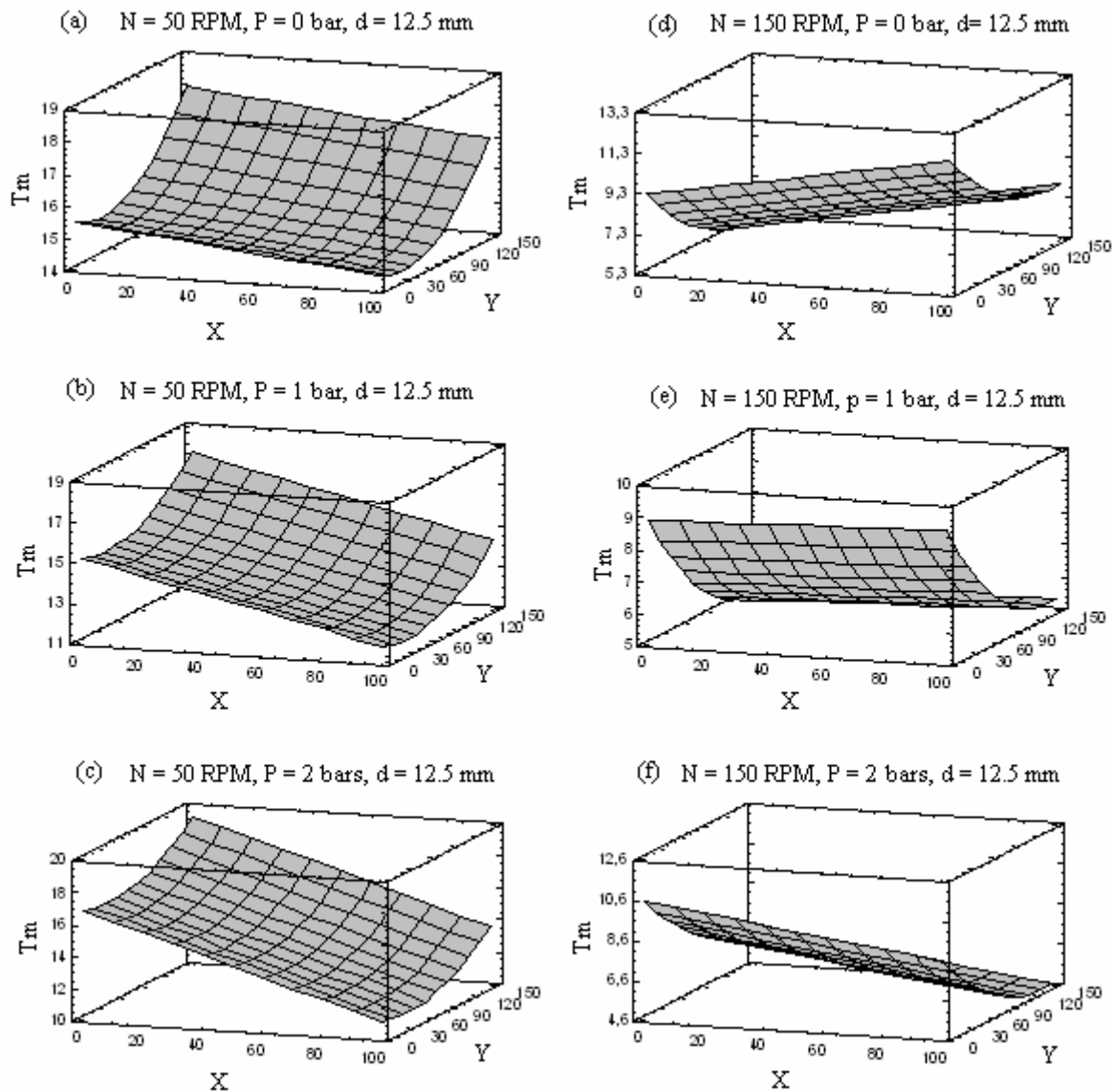
Figure 7.16. Surface plots showing the influence of the injection location for the intermediate pipe diameter (d = 12.5 mm).

These observations could be explained by the hydrodynamics of the tank and could be linked to the vortices created due to the interaction of the rotating liquid on the baffles. Such an interaction is characterised by ribbons of high vorticity and shear strain. As the agitator rotation speed is increased, this ribbon becomes larger and stronger, and therefore injection into these high vorticity areas could enhance the mixing and reduce the mixing time. At low rotation speed (50 RPM), the effect of the ribbons is closer to the baffle position and therefore closer to the position X = 94 mm, Y = 0. At higher rotation speeds, the impact of the baffle

becomes more important, the ribbon could pass the initial position (94 mm, 129.4 mm). Therefore, the initial injection point appeared not to be the optimal injection area but is a good solution if the rotation speed and the injection pressure are *sufficiently high* (a more precise conclusion at this stage is not possible). The contour plot of Figure 7.17 shows that the combined factor of pipe diameter - injection pressure is very important.
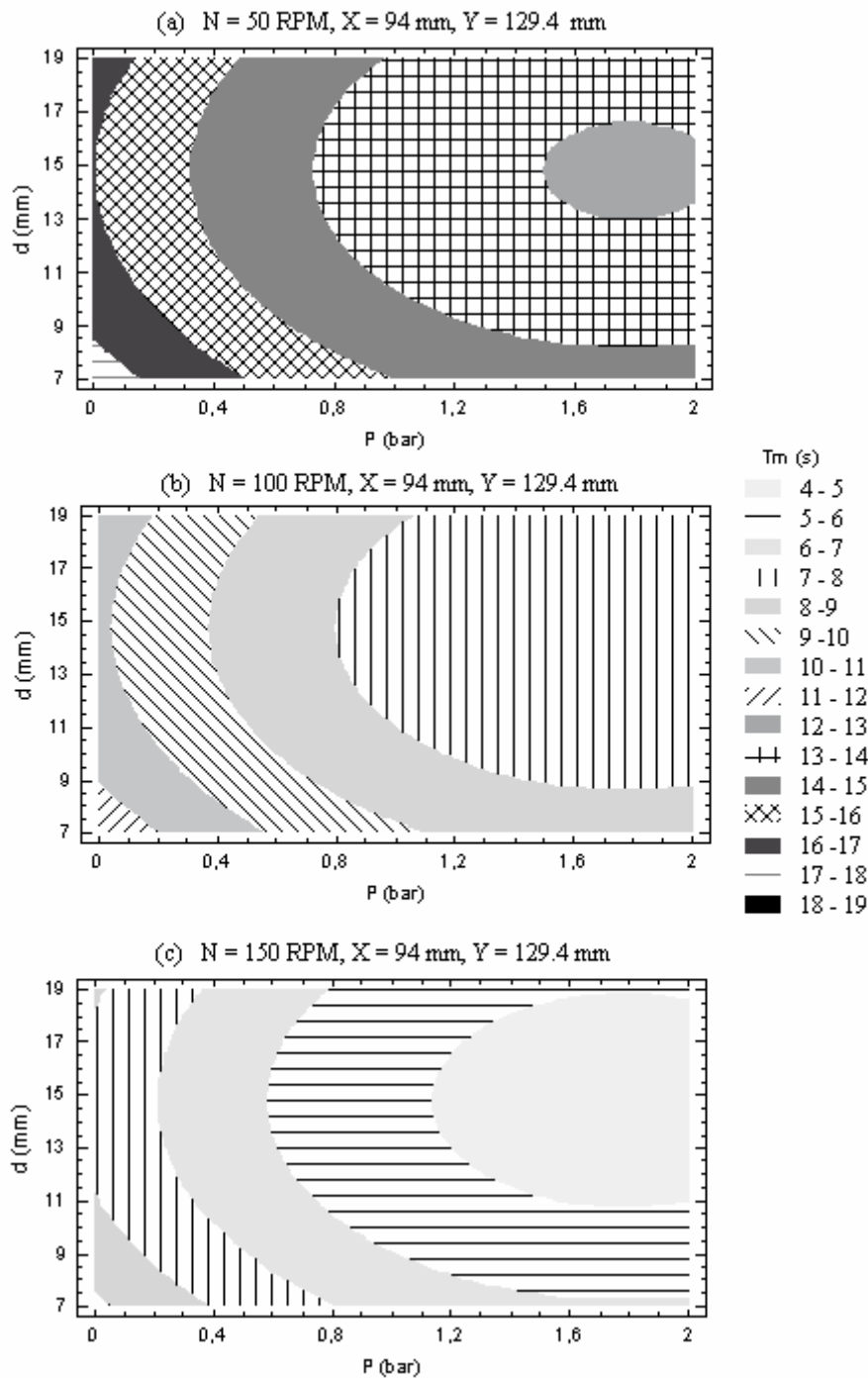
Figure 7.17. Influence of the injection pressure and the pipe diameter at the initial point.

The mixing time is reduced with a large diameter pipe and a high injection pressure. It must be noted the significant non-linear effects observed by the curvature of the lines and particularly in Figure 7.17(a) which suggests that the optimal mixing time would not be obtained for the higher values of the pipe diameter and injection pressure. This confirms the conclusion, already obtained from the BD and DB interaction plot analyse, that an optimum of (diameter – injection pressure) should exist to minimize the mixing time.

7.4. CONCLUSIONS

A Design of Experiments has been carried out to study the mixing time in the pilot reactor. The experimental conditions were set in agreement with the scale-down procedure calculated for the industrial reactor. Five parameters have been studied with 3 levels for each factor for the factors listed below:

- the agitation speed (50 RPM, 100, RPM, 150 RPM)
- the pressure in the killer vessel (0 bar (atm), 1 bar, 2 bars)
- the injection pipe diameter (7.2 mm, 12.5 mm, 17.8 mm)
- the X position (0 mm (centre), 47 mm, 94 mm)
- the Y position (0 mm (centre), 64.7 mm, 129.4 mm)

The analysis of the variance (ANOVA) carried out on the DoE results lead to a simplification of the model which has been reduced to the most significant factors considering a level of significance of 15%. This model can explain 82.5 % of the variability of the experimental data for the mixing time. In the adjusted model, the terms that remain are:

- the simple effects : A(= N), B(= P), C(= d), D(= X) and E(= Y)
- 4 quadratic contributions: AA, BB, CC, EE
- 3 interactions of order 2: AD (agitation speed – position X), AE (agitation speed – position Y), and BD (injection pressure – position X).

The hypothesis of the model has been validated using the diagnostic plots. The validation tests of the model, carried out with intermediate factor levels gave very good agreement between the experimental data and the model predictions. In addition, the predictions of the DoE model have proved to be in good agreement with a different data set used previously to

obtain a specific dimensionless mixing time law (atmospheric pressure, initial injection location and largest pipe diameter).

Finally, the use of the DoE model gave the following conclusions over the range of parameters tested:

- The agitation speed is the most important factor. It means that this mixing process is controlled mainly by the agitation speed. At high rotation speed, the effects of the other factors have a limited impact; therefore the mixing time is influenced by the other factors mainly at low rotation speed.

- At low rotation speed, the XY optimal injection location was found to be in the region behind the baffle (X = 94 mm) and this region moves towards the initial point (X = 94 mm, Y = 129.4 mm) when the injection pressure is increased. Injection into the vortex core appeared never to be favourable and the explanation for this was that the reactant is carried very quickly into the reactor bottom and has difficulty to rise leading to zones in the upper parts of the tank that are slow to react. The initial injection point appears to be a good solution if the stopper is introduced with relative high pressure (a better location being between the actual position and the baffle). In addition, changing the injection position is the most difficult for industrial optimization because the number of flanges is very limited on the upper reactor dome. Therefore, changing the injection location is not investigated in the following sections. The following studies are restricted to the optimization of the injection parameters keeping the injection position $(X, Y)_o = (94$ mm, 129.4 mm) constant.

- The pipe diameter and the injection pressure are two fundamental parameters which influence the mixing time strongly. The mixing time was reduced by both increasing the injection pressure and the pipe diameter, except for the lowest agitator speed, where the optimum was reached before the highest level of the two factors. The effects of the jet being preponderant at low agitator speed, the quadratic effects observed suggested that the highest values of the injection pressure and pipe diameter would not be the optimal settings to yield a minimum value of the mixing time. This is one of the major conclusions of this experimental work.

Instead of the injection pressure, it is be more useful to use the jet velocity which is more easily related to a physical analysis of the phenomena involved in this mixing process. This approach is followed up using CFD in the following Chapters of this thesis.

Chapter 8

LIQUID JET INJECTION STUDIES FOR REACTOR QUENCHING

The CFD study, complemented by experimental investigation, presented in this Chapter examines fluid injection via a jet on a flat free-surface of the partially-baffled stirred vessel described in Chapter 3. CFD and experimental hydrodynamics studies, together with numerical predictions of the free-surface shape, have been carried out for this vessel without considering jet injection in Chapters 4, 5 and 6. A single phase flow model, in which the inhibiting agent is represented as a fluid with the same density and viscosity as the fluid in the tank, that tracks the injected fluid via its concentration is developed. In addition, neutrally buoyant particles are released at the jet inlet to allow visualisation of the jet trajectory in a Lagrangian manner. This modelling approach takes into account the modification of the hydrodynamics of the bulk during the inhibitor injection via the momentum of the injected jet. Simulations covering various jet cross-sections and jet velocities allow the quantification of the jet trajectory following injection. The predicted jet profiles are compared with experimental data for the penetration of the fluid into the bulk. Then, the concept of a global mixing criterion is defined to quantify the mixing quality and to assess the influence of the jet trajectory on the quenching efficiency.

8.1. EXPERIMENTAL APPARATUS

The experiments carried out for this study have been conducted in the pilot mixing vessel used with the liquid injection system. The complete apparatus is shown and described in Chapter 3. The filling ratio of the mixing vessel is maintained constant in all the experiments and the height of water at ambient temperature is fixed at 700 mm. The liquid volume present initially in the killer vessel is introduced into the stirred vessel at $X_j = - 94$ mm and $Z_j = 129.4$ mm from the reactor central axis, as shown in Figure 8.1.
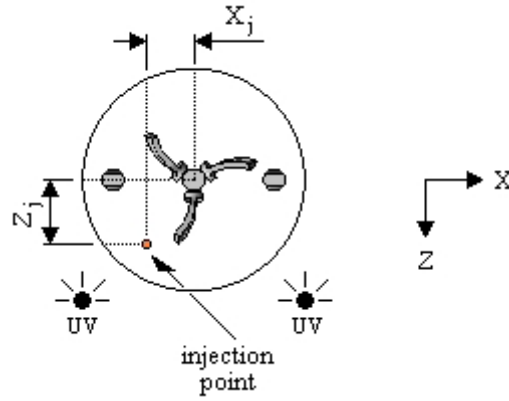
Figure 8.1. Top view of the mixing vessel showing the position of the UV light and the jet injection point

The tracking of the liquid jet during its penetration into the agitated liquid after impact with the free-surface required the use of the high speed HCC-1000 camera equipped with the tele-zoom lens (Rainbow S6X11) described in Chapter 3 (§3.2.2), UV lighting and Fluorescein. The frame rate, exposure time and picture resolution are 51 frames per seconds, 15.2 milliseconds and 1024×1024 pixels², respectively, and these settings remained the same for all of the experiments. The UV light used to illuminate the jet trajectory is produced by two "blacklight" tubes (Philips TL-D, 120 mm length, 26 mm diameter, $\lambda_{max} = 355$ nm) of 36 W each. The UV tubes were mounted vertically in front of the vessel to cover the entire height of the transparent vessel shell, as shown in Figure 8.1. The Fluorescein (formula: $C_{20}H_{10}O_5Na_2$, molecular weight: 376.28 g/mol) used for preparing the aqueous solutions of the injected liquid is a disodium anhydrous salt of general purpose grade provided by Fisher Scientific. This molecule is a commonly used fluorofore which has absorption and emission maxima at 494 nm and 521 nm (in water), respectively.

8.2. CFD MODEL

The numerical simulations were performed using ANSYS-CFX 11.0. In addition to the governing equations detailed previously in Chapter 5, an additional scalar transport equation was added. The transport equation for the scalar ϕ is given in Eq. (8.1):

$$\frac{\partial(\rho\phi)}{\partial t} + \nabla \cdot (\rho \mathbf{u} \phi) = \nabla \cdot \left[\rho\left(D_{\phi}^{lam} + D^{turb}\right)\nabla\phi\right] \tag{8.1}$$

where D_ϕ^{lam} is the kinematic diffusivity of the scalar and D^{turb} is the turbulent diffusivity expressed in Eq. (8.2) as:

$$D^{turb} = \frac{\mu^{turb}}{\rho Sc^{turb}}$$

(8.2)

with the turbulent Schmidt number, Sc^{turb}, set to 0.9.

An unstructured mesh composed of prismatic, tetrahedral and pyramidal elements was used and the boundary layer resolution was increased by using inflation meshing at all walls. A region of fine mesh below the jet injection point and descending to 500 mm below the inlet surface was used to ensure the accurate capture of the jet trajectory. The final grid used for this modelling, presented in Figure 8.2 was composed of 293,000 nodes (1,313,000 elements). The refinements of the grid in the jet injection region were made to the grid used in the previous Chapters, where the density of cells was optimised previously to resolve the flow in the vessel.
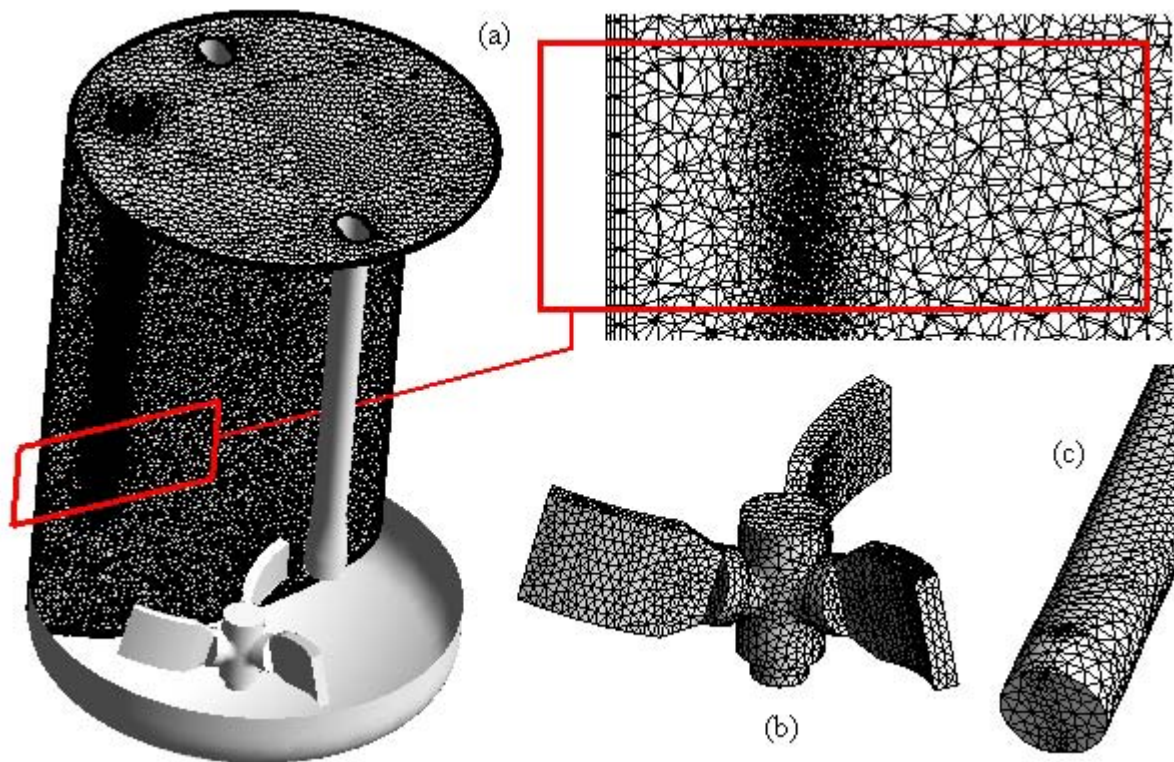
Figure 8.2. The mesh used for the CFD simulations; (a) vertical plane passing through the centre of the injection surface; (b) details of the mesh on the agitator and (c) on a baffle.

The mixing of the jet in the stirred vessel is investigated via transient simulations using the Eulerian and Lagrangian approaches simultaneously. Two different approaches were used to avoid numerical diffusion errors in tracking the path of the jet, for which Lagrangian particle tracking is well-suited, and a scalar concentration was injected to look at the global mixing behaviour because it is impractical to inject enough particles to generate a smooth concentration field that can be used in a meaningful way to compare different injection conditions. The agitated fluid is water at 25°C (ρ = 997 kg m^3 and μ = 8.9×10^{-4} Pa.s) and the inhibiting agent is represented as a fluid with the same density and viscosity as the fluid in the tank. The concentration of the injected fluid is tracked by solving an additional non-reacting scalar transport equation. The mass fraction of the passive scalar at injection was set to one. A non-reacting scalar is used as the process of interest is mixing-limited rather than being controlled by the availability of the added fluid because the mass of "stopper" injected is more than sufficient to quench the reaction throughout the tank. It is recognised that when simulations of an industrial system are made for a specific process a reactive scalar should be used.

In parallel, neutrally-buoyant particles were released at random locations from the inlet in order to visualize the jet trajectory during the injection time. These marker particles were given a small diameter (10 microns) and the Schiller Naumann drag law was used so that they would follow the mean flow of the injected fluid. A turbulent dispersion force, derived from an eddy interaction model, was added to model the turbulent fluctuations which affect the tracer particle trajectory when the ratio of the eddy viscosity to the dynamic fluid viscosity is above five (ANSYS-CFX 11.0, 2007). As the particles do not affect the flow field, the fluid-particle interaction is treated via one-way coupling, so that the particle path was updated at the end of each time-step. Lagrangian particles were released from two different randomly located positions on the inlet per timestep, and the timestep was set to 1 ms for all runs. The injection rate of particles was based on an assessment of the number needed to properly visualise the jet trajectory without adding so many that the computations became two slow and demanding in memory. The timestep value was chosen such that convergence of the residuals was achieved in less than five coefficient loops.

The agitator rotation speed was maintained at a constant value of 100 RPM in the base case simulations (giving a Reynolds number of 1.3×10^5) and was subsequently varied between 50-150 RPM. At these rotation speeds, the experiments and CFD modelling using an

inhomogeneous multiphase model have shown that the free-surface is quasi-flat with a small precessing vortex which rotates on the free-surface around the vessel axis as discussed in Chapter 5. The injected volume (always equal to 533 ml) leads to an increase of the water level of less than 4 mm which is negligible compared with the 700 mm of the initial water height and therefore the increase of the free-surface level following fluid injection was neglected. Therefore, the use of a multiphase model to predict the free-surface deformation was not necessary at the agitator rotation speeds considered here and the inlet used for jet injection was located directly on the free-surface.

The author previously used the Sliding Mesh (SM) model to study the same partially-baffled vessel used here in order to determine the complex, time-dependent hydrodynamics and transient effects, which consisted of multiple recirculation loops and macro-instabilities (see Chapter 5 and Torré *et al.*, 2007c). The need to study numerous jet injection conditions and to run the simulations for 18 seconds of real time meant that the Multiple Reference Frame (MRF) model was preferred to the SM model, which was considered to be too computationally demanding for this work. The Multiple Reference Frame model has been shown to perform well for this configuration (see Chapter 4). Therefore, a rotating reference frame is applied to the bottom dish and a stationary frame is applied to the cylindrical part of the vessel which contains the baffles, with these frames joined via a frozen rotor condition. This is clearly an important simplification but it would be extremely computationally demanding and difficult to analyse the results if we included the transient rotation of the impeller. Previous work, reported in Chapter 4, has shown that at least 15 revolutions of the impeller must be made for a transient simulation that starts from a steady-state simulation to be meaningful. As it was desired to look at many jet injection conditions the strategy of interacting the jet with a mean flow-field obtained from a frozen rotor approach, in which a transient simulation was performed but the impeller blade was not rotated, was adopted. In Chapter 5, it was noted that the time-averaged transient results show a similar flow structure to the steady-state results. In addition, the transient model captures the free-surface behaviour well, as the steady-state model does at higher rotation speeds. Based on these observations it was felt that use of the frozen rotor approach was justified.

A no-slip boundary condition is imposed on the agitator, the baffles, the bottom dish and the vessel shell. An inlet boundary condition is specified for the jet injection surface with a specified mass flow of injected liquid. This allows a fixed volume (533 ml) of liquid, which

enters the stirred vessel with a known momentum flux, to be applied only during the injection time. The jet momentum flux, denoted by M, is defined as the product of the liquid jet density, the jet cross-sectional area and the square of the jet velocity. The entire top surface of the vessel, excluding the injection area, is set as a free-slip surface with a mass sink applied at the surface to remove the same volume of fluid as injected at the inlet, thus maintaining the liquid level constant.

The choice of the turbulence model was determined previously in Chapter 5 and in Torré *et al.* (2007c) through comparisons between experimental PIV data and numerical predictions. The SSG Reynolds Stress model gave unphysical results for axial velocities in the areas close to the vessel axis, whilst the standard *k*-ε turbulence model showed good agreement with experimental PIV data and captured the shape of the free-surface well. Thus, the standard *k*-ε turbulence model, together with the scalable wall function treatment available in ANSYS CFX (Grotjans and Menter (1998), Esch and Menter (2003)), were used in this study.

A second order bounded spatial differencing scheme was used to limit numerical diffusion as much as possible and second order time integration was performed. A maximum number of 10 coefficient loops per time step was sufficient to decrease the normalized RMS residuals below 10^{-4} for the mass, momentum, turbulence and the passive scalar transport equations, with this value being considered sufficient to have a converged simulation (ANSYS-CFX 11.0, 2007).

8.3. EXPERIMENTAL TRAJECTORIES OF THE LIQUID JET

8.3.1. <u>Jet velocity</u>

The jet velocity was measured experimentally on the pilot reactor for different operating conditions. With the injection system used in this study, the jet velocity is controlled by the air pressure in the steel vessel which contains the liquid to be injected. In all the experiments carried out the steel vessel was filled with 0.533 litres of tap water, leaving an air space volume of about 2.5 litres above the liquid surface under pressurized conditions. For the experiments conducted at atmospheric pressure ($\Delta P = 0$), the valve of the feeding funnel

remained open allowing an outlet to the atmosphere. For the other pressures tested ($\Delta P > 0$), the pressure reducing valve located on the air feed pipe of the steel vessel allowed a constant pressure to be maintained inside the steel vessel.

The experiments were carried out with three different injection pipe diameters, equal to 7.2mm, 10 mm and 15 mm. The pressure in the steel vessel was set from 0 to 2 bars to cover a large range of jet velocities. The shape of the free-falling liquid jet was captured using the high-speed camera with a frame rate of 463 fps and with an exposure time of 2.16 ms, and using a calibration (one pixel on a picture corresponded to a distance of 0.1446 mm). The jet velocity was deduced from the measurement of the displacement of the jet leading edge for the maximum number of frames, for which the jet leading edge was visible. Although the leading edge of the jet bulges as it descends, due to the drag effect of the air on the liquid, the jet remained coherent for all the jet diameters, velocities and liquid fall distances used in this study.

Figure 8.3(a) shows the evolution of a water jet released at atmospheric pressure into the air space above the free-surface of the stirred liquid. The rounding of the leading edge of the jet is clearly visible and the precision of the determination of the jet position was assumed to be 5 pixels. From these pictures, the leading edge of the jet travelled a distance of 109.6 mm in 0.0518 s which corresponds to a jet velocity of 2.11 ± 0.03 m s^{-1}. For each set of parameters tested, the final jet velocity (used for further calculations) was calculated as the arithmetic average of five measurements obtained during different experiments.
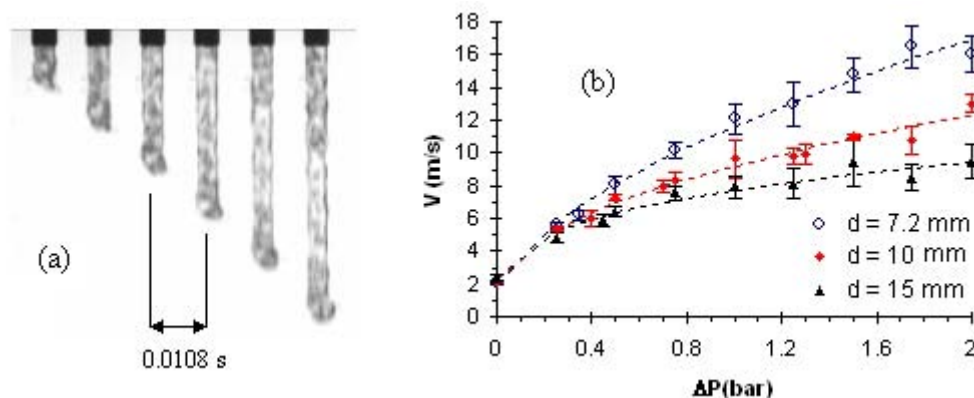
Figure 8.3. (a) Snapshots of a water jet released in air obtained with d = 10 mm and V = 2.1 m s^{-1} $\pm$ 0.1 ($\Delta P = 0$ bar); (b) jet velocities versus the pressure measured in the sampling cylinder for three injection pipe diameters (7.2, 10 and 15 mm), symbols: arithmetic average of 5 experiments, error bars: $\pm \sigma$.

The experimental results are detailed in Appendix C and shown in Figure 8.3(b), where each velocity value has been plotted versus the absolute pressure inside the steel vessel for the three pipe diameters tested. The dashed lines were determined by non-linear fitting (see Appendix C) and the errors bars are equal to the standard deviation ($\pm \sigma$) of five experimental measurements. In the analysis that follows it is assumed that the initial jet velocity is representative of the average jet velocity during the entire injection period. Using the video recording method described earlier, it was not possible to track the front of the jet at the end of the injection time due to the gas/liquid mixture expelled by the gas.

8.3.2. Experimental jet trajectories

The problem of a free-falling liquid jet which impacts a liquid surface has received considerable attention in the literature, with most studies focussed principally on the gas entrained into the quiescent liquid (Bin (1993), El Hammoumi *et al.* (2002), McKeogh (1978), McKeogh and Ervine (1981)). As concluded by Bin (1993) and reported by Chanson *et al.* (2004), the mechanism of air entrainment depends upon the jet impact velocity, the physical properties of the liquid, the nozzle design, the length of the free-falling jet and the jet turbulence level. In the experiments carried out in this study, the injection conditions were such that air was always introduced in the liquid present in the stirred vessel. Nevertheless, this study differs from classical free-falling jet studies as the main purpose is not to study the gas introduction but to quantify experimentally the liquid jet trajectory during its penetration into the bulk. Figure 8.4 shows a typical jet, captured using the black and white camera with classical daylight conditions.
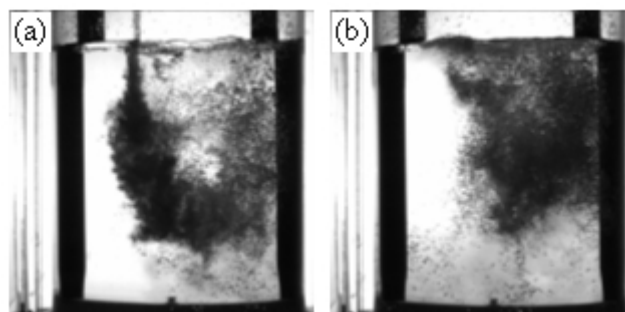
Figure 8.4. Visualisation of a water jet coloured with iodine, injected at the free-surface with classical daylight conditions (d = 10 mm, V = 6.0 ± 0.5 m s^{-1}, N = 100 RPM); (a) during injection; (b) after injection.

For this experiment a volume of 533 ml of water, added to 10 ml of iodine aqueous solution at 1 mol/L used as a dye, was injected into the partially-baffled vessel during agitation. It is obvious that the dark jet plume visible in Figure 8.4(a) during injection is a gas-liquid mixture. Air is entrained due to interfacial shear at the liquid jet interface, which drags down an air boundary layer, and due to the air entrapment process at the point of impact (Davoust *et al.*, 2002). Thus, air bubbles are entrained by the jet, then detach and finally reach the free-surface due to buoyancy, as is clearly visible in Figure 8.4(b). The air bubbles entrained with the injected liquid create a dark air-water interface, which prevents accurate visualization of the liquid jet trajectory inside the stirred vessel. Thus, this method is well adapted to visualize the gas bubbles and the gas/liquid two phase region but is not appropriate for tracking the injected liquid with any degree of accuracy.

A possible means to track the liquid jet is a method that highlights the injected liquid without showing the air bubbles. To make this possible an aqueous solution of Fluorescein with a concentration of 0.2 g/L has been used for the injected liquid. The vessel was lit by UV light and the jet injection was recorded with the same black and white camera without any other light in the room. This approach has two main advantages for the present study: (a) injection of an aqueous solution of Fluorescein is very easy to track because this appears as a bright yellow liquid under UV light, (b) the air bubbles are invisible under UV. Point (b) was demonstrated experimentally by injecting air at various flow rates below the agitator in the stirred vessel filled with tap water.

Three experiments have been carried out for each set of parameters tested. Recording each experiment with a high speed camera allowed tracking of the jet penetration trajectories from the beginning to the end of jet injection. The time at the end of injection is denoted T_{inj}, and the times equal to $0.2T_{inj}$, $0.4T_{inj}$, $0.6T_{inj}$ $0.8T_{inj}$ and T_{inj} have been considered for the jet trajectories, and for subsequent comparisons with the numerical data. Example experimental jet snapshots at time T_{inj} are presented in Figure 8.5.
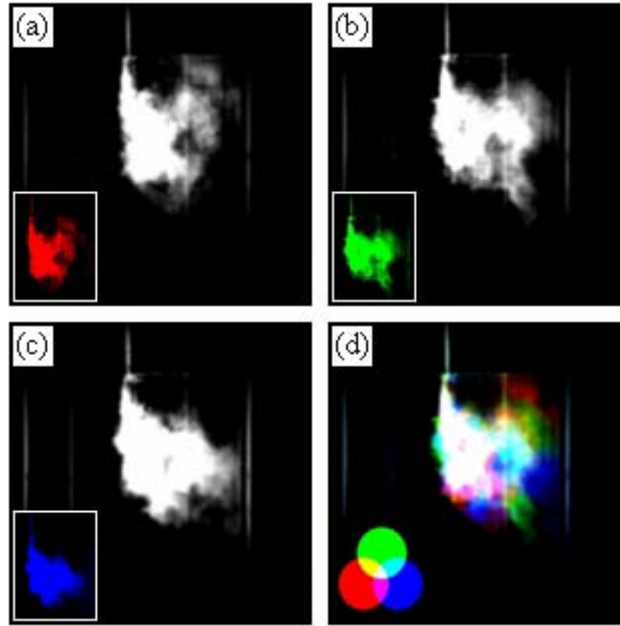
Figure 8.5. Snapshots at the end of the injection time obtained using a fluorescein aqueous solution lit with UV and their superimposition via the RGB imaging process; (a) First experiment, red component of the RGB picture; (b) Second experiment, green component of the RGB picture; (c) Third experiment, blue component of the RGB picture; (d) RGB final picture. The conditions were d = 10 mm, V = 6 m s^{-1}, N = 100 RPM.

The three raw pictures have been transformed so that each has one of the three primary colours (red, green and blue) of equal intensity, as shown in Figures 8.5(a), (b) and (c). Then, for ease of comparison with the numerical jet trajectory predicted by CFD and to quantify the reproducibility of the experiments, an RGB imaging process (additive synthesis of colours) was used to compile them into a single final picture using the software IRIS. The common area of the three different pictures is white on the final frame, as presented in Figure 8.5(d). The hydrodynamics in this partially-baffled vessel are very complex as discussed in Chapter 5. In short, the liquid circulation consists of a downward stream in the centre of the vessel and an upward stream at the periphery, with a rotational flow superposed on these streams. This partially-baffled vessel is fitted with only two beaver-tail baffles, so that the baffling effect is not sufficient to break the strong tangential motion imparted by the agitator (rotating counter-clockwise). At the same time as the jet expands its diameter radially, its velocity decreases and the jet fluid is entrained by the stirred fluid leading to the bending of the jet plume, as shown in Figure 8.5. The jet is then dispersed in the vessel due to two turbulent mechanisms: the dispersion of the plume by small eddies with a size equivalent to the size of the plume and the fluctuation of the entire plume around its mean position due to large-scale turbulent motions (Verschuren *et al.* (2002)).

A very important point that must be noted about this study concerns the introduction of air bubbles into the vessel during the injection, as shown in Figure 8.4. These bubbles enhance mixing in the vicinity of the jet, deform the jet plume and create turbulence because of the rise of the bubbles due to buoyancy. As shown in Figures 8.5(a), (b) and (c), some fluorescent tracer is entrained by the air bubbles from the jet plume to the surface. This increases the liquid jet dispersion and makes the jet plume appear larger compared with the same experiment carried out with a plunging pipe. The dynamics of disengagement of the entrained air bubbles differs from one experiment to another, depending on the flow structure which exists in the vessel during the jet injection. This chaotic phenomenon, added to the high unsteadiness of the flow (e.g. precessing vortex, macro-instabilities) which develops in the stirred vessel (see Chapter 5), makes the jet trajectory non-reproducible from one experiment to the next. The non-reproducibility is shown by the coloured areas of Figure 8.5(d), where the contribution of the air bubbles rising is clear at the edge of the visible plume. In contrast, few coloured areas are noticeable in Figure 8.5(d) near the lower limit of the jet plume, which demonstrates that the lower penetration limit is almost identical in the three experiments carried out.

Tracking the jet trajectory experimentally in an agitated vessel is very complex due to the three dimensional nature of the flow. Another difficulty is the unsteadiness of the injection which adds to the transient effects of the flow in the stirred vessel. Concerning this latter point, the problem must be considered in a different way to that of feeding studies carried out in continuous stirred tanks reactors (CSTR), such as those presented in Aubin *et al.* (2006), in which the determination of the jet trajectory is easier. The visualization of the jet mixing with only one camera located in front of the vessel does not record the real 3D movement of the injected liquid but allows analysis of the projection of this trajectory onto a plane. Therefore, CFD simulations were developed to analyse qualitatively the jet trajectory for several jet conditions (diameter and velocity) and to quantify the mixing process in the entire agitated vessel.

8.4. CFD PREDICTIONS OF THE JET TRAJECTORIES

The modelling of the trajectory of the liquid jet has been carried out for various injection conditions at a constant agitator speed (N = 100 RPM). Nine simulations were analysed, involving three jet diameters (7.2, 10 and 15 mm) and three jet velocities (2, 6 and 10 m s^{-1}), to quantify the effect of the injection parameters on the liquid jet trajectory and its penetration into the stirred vessel for N = 100 RPM. Using the physical properties of water at 25°C, these parameters gave jet Reynolds numbers which varied from 1.61×10^4 (d = 7.2 mm and V = 2 m s^{-1}) to 1.68×10^5 (d = 15 mm and V = 10 m s^{-1}) all giving fully turbulent jet conditions. All of the jet trajectories are not presented here and only two relevant examples of different jet profiles are detailed. With four different geometrical views (3D, two laterals and top), Figures 8.6 and 8.7 provide a good qualitative description of the jet behaviour in the stirred vessel.

The trajectory is shown using the tracks of the Lagrangian particles at different times during the injection, with the number of particles being proportional to the injected volume. Therefore, 60, 120, 180, 240 and 300 Lagrangian particles have been used to visualize the jet trajectory at the times $0.2T_{inj}$, $0.4T_{inj}$, $0.6T_{inj}$, $0.8T_{inj}$ and T_{inj}, respectively. Figure 8.6 shows the behaviour of a 7.2 mm liquid jet diameter, injected with a velocity of 2 m s^{-1} into the stirred vessel. As shown in Figures 8.6(b) and (c), these conditions lead to very little downward jet penetration, and the deflection of the jet plume occurs close to the free-surface. The circumferential movement of the stirred fluid is sufficient to entrain the injected fluid rapidly into the central vessel region. The region near the vessel axis is characterized by a highly swirling movement with significant streamline curvature (see Chapters 4 and 5), so that the injected liquid is pulled downwards. It is then pumped axially and expelled radially by the agitator, with the injected fluid then being deflected by the bottom curved dish and subsequently it flows upwards close to the vessel wall.

In contrast with the case presented above, Figure 8.7 shows a very different injection behaviour characterized by a higher jet velocity and a larger jet diameter. As shown in Figures 8.7(b) and (c), these injection parameters are such that the injected fluid penetrates vertically much deeper into the bulk before the jet plume becomes entrained by the tangential movement of the stirred liquid.
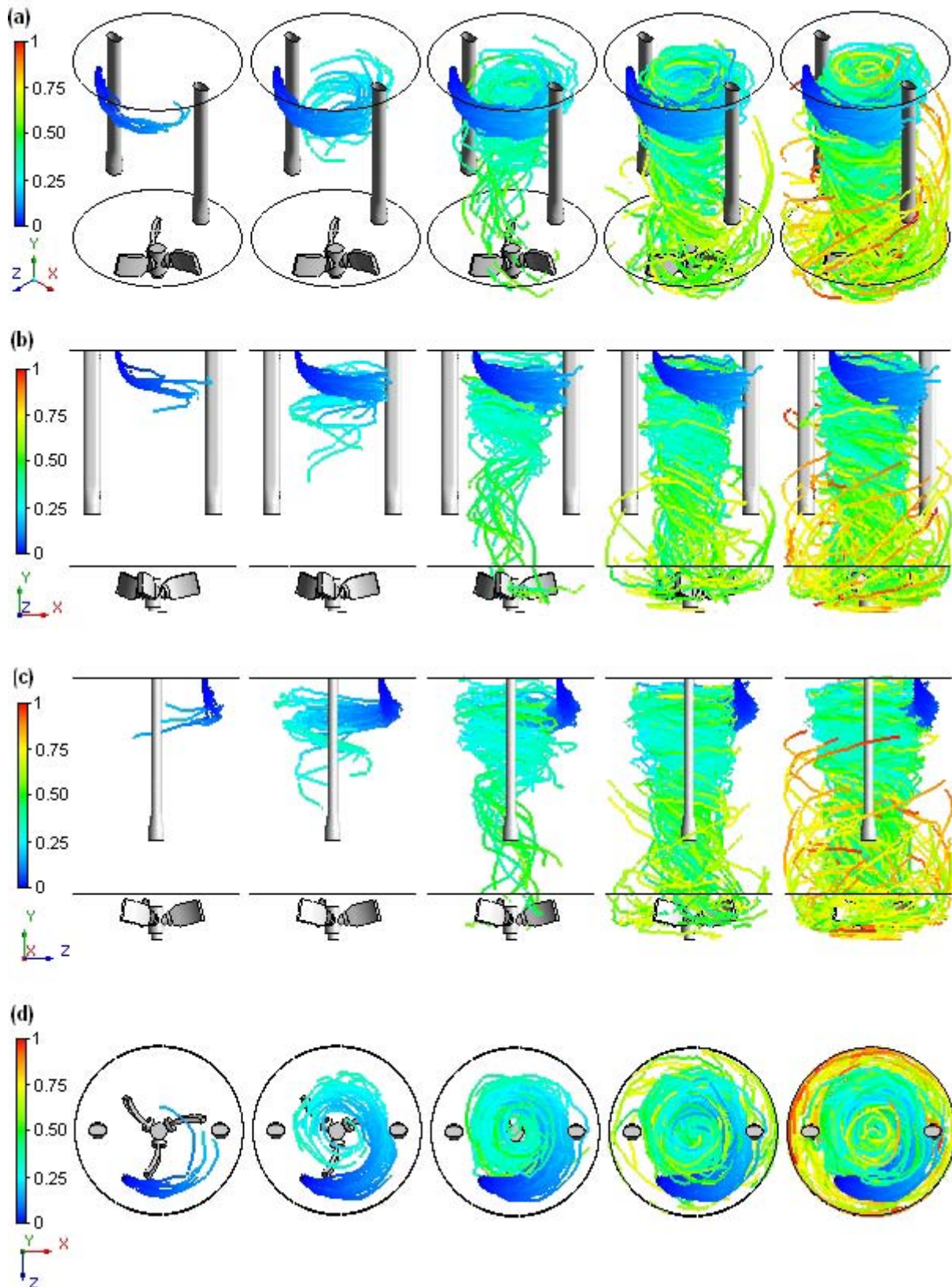
Figure 8.6. Lagrangian jet trajectories coloured by the Lagrangian particle travel time normalized by T_{inj}, for $d = 7.2$ mm, $V = 2$ m s^{-1} and $N = 100$ RPM, plotted at $0.2T_{inj}$, $0.4T_{inj}$, $0.6T_{inj}$, $0.8T_{inj}$ and T_{inj}. (a) 3D view; (b) XY lateral view; (c) YZ lateral view; (d) top view.
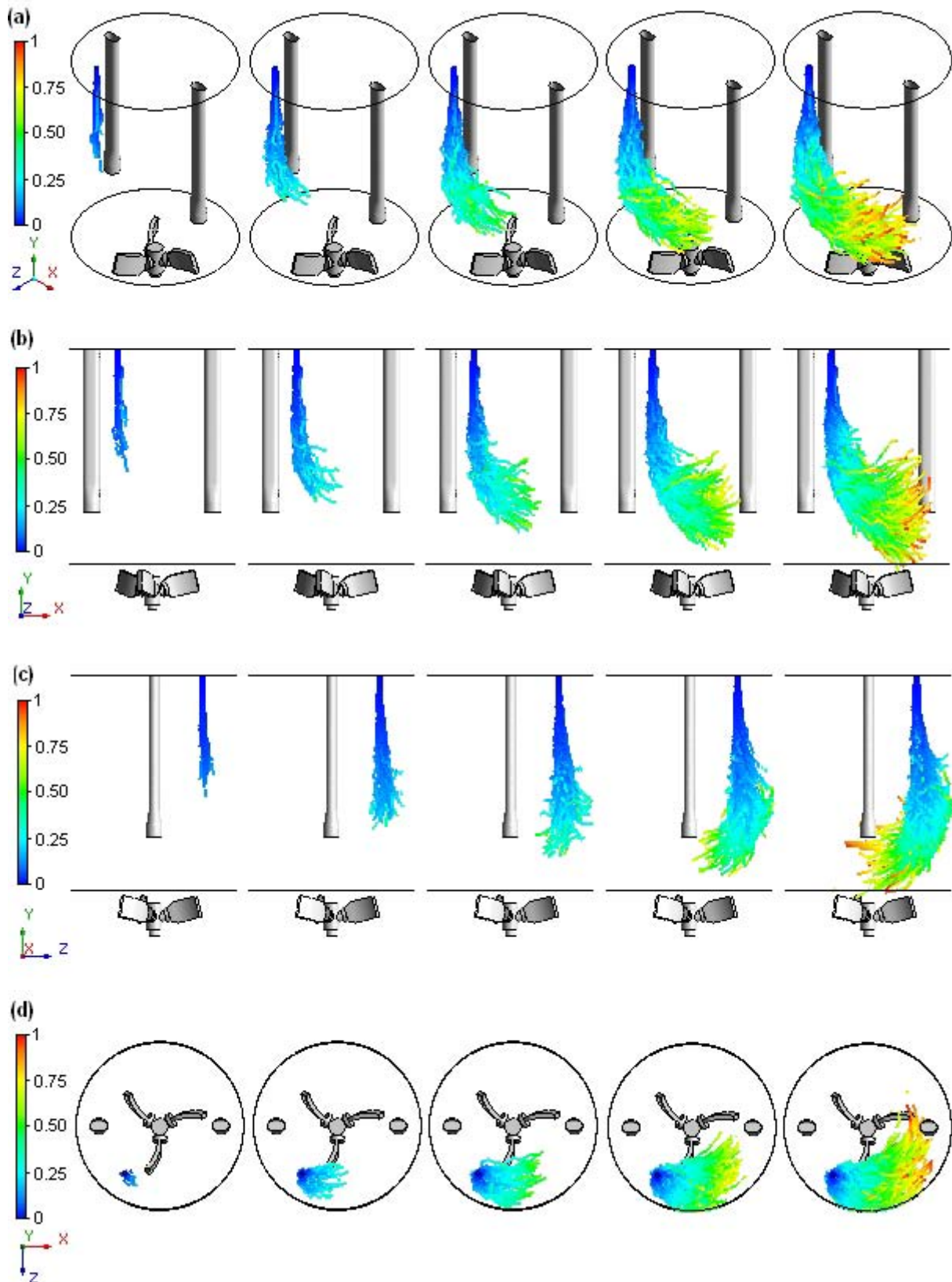
Figure 8.7. Lagrangian jet trajectories coloured by the Lagrangian particle travel time normalized by T_{inj}, for d = 10 mm, V = 10 m s^{-1} and N = 100 RPM, obtained at $0.2T_{inj}$, $0.4T_{inj}$, $0.6T_{inj}$, $0.8T_{inj}$ and T_{inj}. (a) 3D view; (b) XY lateral view; (c) YZ lateral view; (d) top view.

The analysis of the nine simulations revealed that the vertical penetration of the jet increases with both the jet diameter and the jet velocity. No correlations were found in the literature relating to the behaviour of jet trajectories penetrating into a stirred vessel, probably due to the difficulty of describing the jet movement in a three dimensional, rotating flow which have a variable axial component along the jet axis. The theoretical analysis which appeared to be the closest to the case studied here is that for liquid jets injected into a cross-flow. Studies of jet trajectories using this analogy are detailed in Chapter 11, which makes use of the results from this Chapter, as well as the results of Chapter 10 which are for the industrial scale. Four additional simulations have been carried out to determine how the jet trajectories behave at different agitator rotation speeds from 50 RPM to 150 RPM. Figure 8.8 shows the jet penetration for five agitator rotation speeds (50, 75, 100, 125 and 150 RPM) at the end of the injection time, obtained with a 10 mm jet diameter and a jet velocity of 6 m s^{-1}. This range of agitator rotation speeds has been chosen such that the assumption of a quasi-flat free-surface remained valid.
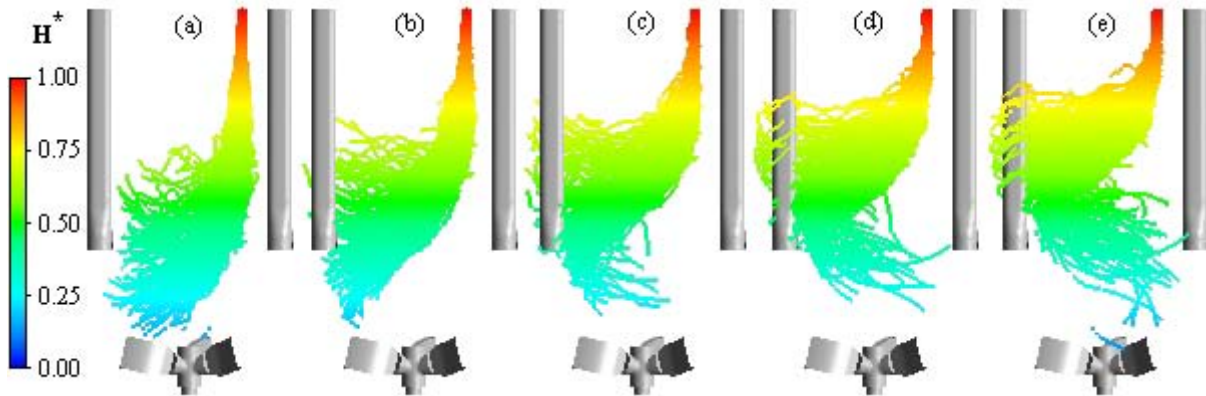
Figure 8.8. Lagrangian particle tracking (300 particles) showing the jet penetration profile (d = 10 mm, V = 6 m s^{-1}) at the end of the injection time for different agitator rotation speeds, coloured with the normalized vessel height H* (= Y/H$_{liq}$). (a) N = 50 RPM; (b) N = 75 RPM; (c) N = 100 RPM; (d) N = 125 RPM; (e) N = 150 RPM.

The tracks of 300 Lagrangian particles coloured with the normalized height H* (H* = Y/H$_{liq}$) on the XY lateral view of the vessel allowed the influence of the agitator speed on the jet penetration to be visualised. For an identical jet diameter and velocity, the CFD model gave a reduced downward jet penetration when the agitator speed was increased. Depending on the flow patterns which develop in the particular stirred vessel studied, the effect of the hydrodynamics on the jet trajectory may differ greatly from one system to another. In the partially-baffled stirred vessel studied here, the hydrodynamics in the upper part of the vessel

is characterized by a high circumferential velocity component. Thus increasing the agitator rotation speed has a direct effect on the jet plume deflection and the fluid jet penetrates downwards much less as the effect of the tangential flow becomes more important. This behaviour was also observed experimentally in the pilot reactor.

8.5. COMPARISON OF THE MODEL RESULTS WITH EXPERIMENTAL DATA

Experimental data for the liquid jet trajectories have been compared with the CFD predictions in Figure 8.9 for the 10 mm pipe diameter. As presented earlier, the use of the trichromic process requires three experiments for each jet velocity. The high frame rate of the camera used to monitor the jet injection allowed the jet trajectories to be determined for times equal to $0.2T_{inj}$, $0.4T_{inj}$, $0.6T_{inj}$, $0.8T_{inj}$ and T_{inj}. In the experiments carried out, the jet velocities were 2.1 ± 0.1, 6.0 ± 0.5 and 9.9 ± 0.6 m s^{-1} and the experimental jet trajectories have been compared with numerical predictions obtained with jet velocities of 2, 6 and 10 m s^{-1}, respectively. Five points of comparison have been taken, corresponding to the times listed above at which photographic data were available, allowing comparison with the CFD results from the beginning to the end of the injection period.

The effect of the jet velocity on penetration is shown clearly in Figure 8.9. Firstly, the jet penetration increases with the jet velocity, as discussed earlier. As shown by the significant size of the coloured areas of the Figure 8.9(a), the non-reproducibility was higher for the lowest velocity due to the dispersion of the jet plume into the bulk being more significant for a longer injection time. Nevertheless, for the lowest jet velocity, the experimental profiles do not reveal the injected liquid being entrained into the central vortex located near the vessel axis. The emission intensity of the fluorescent tracer is linked to both the UV irradiation level and the tracer concentration. With the disposition of the two UV lights shown in Figure 8.1, the liquid present in the front half of the vessel, close to the light source, is irradiated more than the liquid in the back half of the vessel. In addition, after the jet plume becomes trapped by the central vortex and the tracer has been spread throughout the vessel, the Fluorescein concentration at the centre of the vessel is not sufficient to give a fluorescence emission which could be detected by the camera.
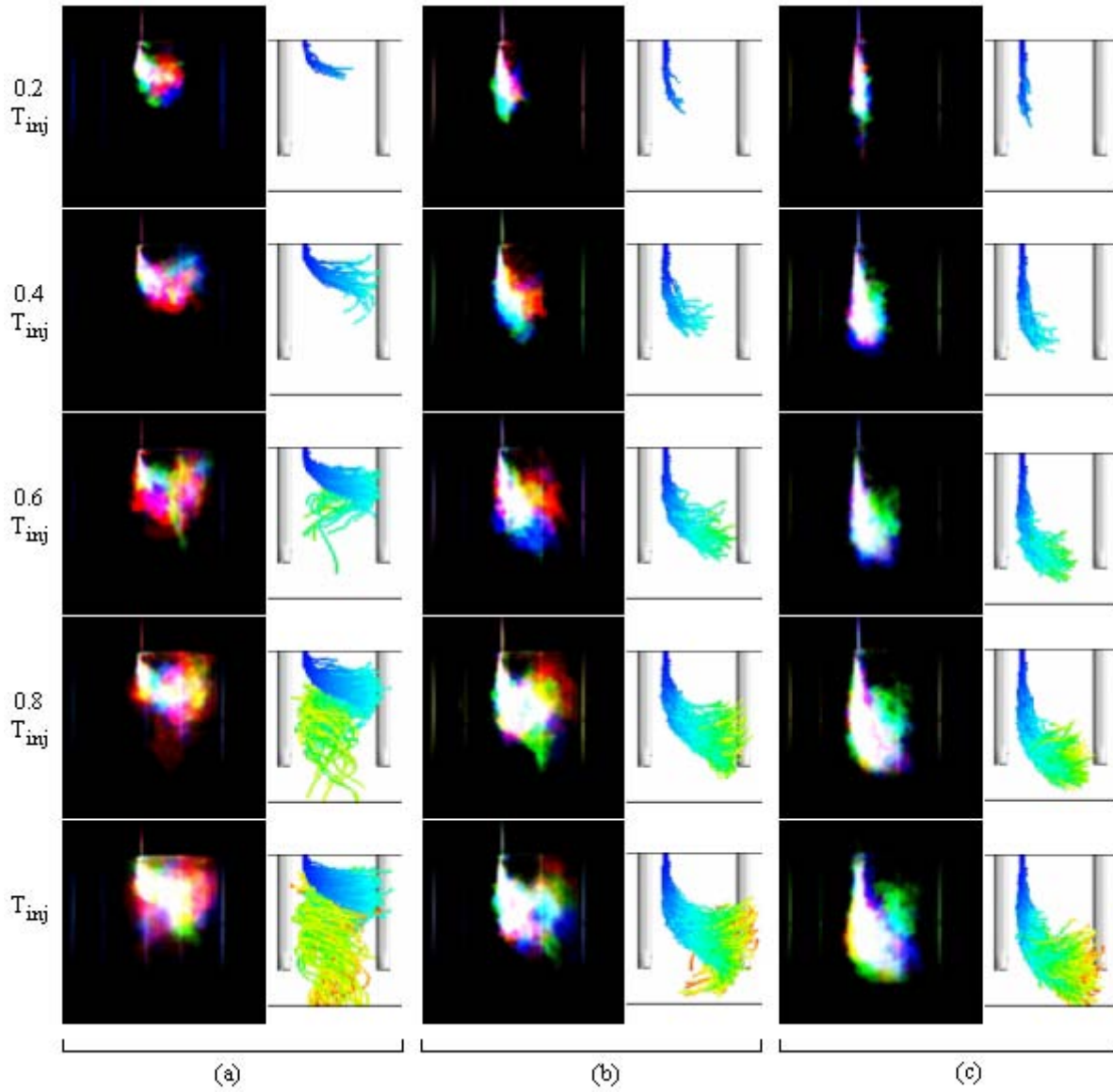
Figure 8.9. Comparison between the jet penetration trajectories (jet diameter of 10 mm and N = 100 RPM) obtained experimentally with trichromic pictures, and numerically by Lagrangian particle tracking, at times equal to $0.2T_{inj}$, $0.4T_{inj}$, $0.6T_{inj}$, $0.8T_{inj}$ and T_{inj}. (a) expt.: $V = 2.1 \pm 0.1$ m s^{-1}, num.: $V = 2$ m s^{-1}; (b) expt.: $V = 6.0 \pm 0.5$ m s^{-1}, num.: $V = 6$ m s^{-1}; (b) expt.: $V = 9.9 \pm 0.6$ m s^{-1}, num.: $V = 10$ m s^{-1}.

It must be pointed out that all of the effects arising from air introduction into the liquid bulk and the air bubble disengagement were not modelled in the CFD simulations. Firstly, the impact of the liquid jet falling through air on the liquid free-surface causes a toroidal gas cloud below the impingement point. This leads to a characteristic "mushroom" shape which appears just below the free-surface, as described in Storr and Behnia (1999) and Kersten *et al.* (2003), and observed here for the experiments carried out in daylight conditions. The use of UV, which avoids visualization of the air bubbles, means that this gas is not visible in the experimental pictures of Figure 8.9. In addition, jet impingement produces an air/water two-

phase region, described extensively in many free-falling jets studies. The air bubbles introduced in the vessel, not visible under UV light, disengaged due to buoyancy and substantially enlarged the apparent shape of the jet plume.

Secondly, the decrease of the velocity due to the jet impact on the water surface was not considered in the model. The kinetic energy loss caused by the liquid impact was assumed to be negligible compared with the kinetic energy of the jet. The author is aware that the CFD model presented in this study represents a significant simplification of the complete physics of the problem. Nevertheless, even without considering the liquid impact and the effect of the air bubbles, the numerical predictions of the jet trajectories and plume shapes show fairly good agreement with the experimental data for the three velocities tested and the different times considered from the beginning to the end of the jet injection.

8.6. MIXING CRITERIA FOR RUNAWAY REACTION QUENCHING

The mixing of two miscible liquids in turbulent conditions has been extensively studied both experimentally and numerically. The reader can find further details in Nere *et al.* (2003), where the published literature on liquid phase mixing in turbulent conditions was critically reviewed and analysed, and is therefore not repeated here. In contrast, the "mixing quality" is probably one of the most difficult concepts to define. Since the paper by Danckwerts (1952) which was the first to establish the basic concepts and the definitions of the mixing characteristics of miscible fluids, many authors have introduced various ways to define the degree of mixing in liquid mixtures. Hiby (1981) who reviewed many of these declared that the reason for the considerable scatter in mixing time data was that neither the degree of mixing which is achieved nor the measurement conditions are sufficiently well-defined, and this conclusion is still valid more than 25 years later. As was pointed out in Chapter 2, thermal runaways linked to mixing problems account for a large fraction of incidents in the chemical process industry. The mixing problem studied for safety issues is different to the classical mixing time and homogenization studies as the injected stopper must not only mix well but has to quench a chemical reaction. This means that the stopper concentration does not need to be homogeneous, but must locally reach a value high enough to quench the reaction. As the existing methods and the various indices found in the literature appeared not to be pertinent

for this case, a new simple global mixing criterion adapted for safety issues was defined. The simulations for the different jet injections carried out at N = 100 RPM were analysed using this new index to investigate the possible optimisation of mixing of the stopper in these under-baffled mixing vessels.

8.6.1. <u>Quenching curves</u>

To quench the chemical reaction completely, the stopper has to be mixed sufficiently to produce a minimum concentration throughout the entire vessel. This concentration limit depends both on the application studied and on the safety level considered for the reactor quenching, and has been calculated on the basis of real industrial data. When the liquid in the jet, which is subsequently identified via the concentration of a transported scalar variable (defined to take a value of unity in the jet), is mixed in the vessel, its concentration, C, in each numerical cell is tracked with time. The concentration values are everywhere zero before injection starts, and reach the equilibrium concentration, denoted C_{inf}, everywhere at infinite time. However, there is a large excess of stopper so it was introduced C_{min} which is the minimum quantity of stopper that must be injected to quench the reaction if it is mixed uniformly throughout the vessel. The normalised stopper concentration, C^*, is defined as C/C_{inf}. Finally, C^*_{min} is defined as the ratio of C_{min} to C_{inf} and represents the normalised minimum concentration necessary to quench the reaction throughout the vessel. The value of C^*_{min} used here is based on a real industrial system used in polymerisation reactors and equals 4.38×10^{-2}. The concentration was tracked with time in the whole vessel volume and analysis of this concentration data forms the basis of the definition of the mixing criteria presented below.

The percentage of the vessel volume which falls within a given concentration range was tracked with time. An example is presented in Figure 8.10(a) for a case with a jet diameter of 7.2 mm and a jet velocity equal to 6 m s^{-1}, at a time of 7 s after the beginning of injection. As the time increases, the spread of the histogram decreases and the data are centred on the equilibrium concentration. The exact experimental value of this final concentration C_{inf} was equal to 4.87×10^{-3}, calculated as the ratio of the injected volume (0.533 l) to the vessel volume (109.533 l). The value determined numerically, which is used in the subsequent calculations, was 4.94×10^{-3}, with the small difference being due to the removal of a small

quantity of liquid at the free-surface to keep the liquid level constant in the simulations (see section 3). A pertinent analysis of these data was the use of the cumulative curves shown in Figure 8.10(a). The curve represented with a dashed line is the classical cumulative curve obtained directly from the histogram data, and each point gives the percentage of the vessel volume with a concentration below the value given by the abscissa. The full line shows the complement of this value and represents the cumulative percentage of the quenched volume of the vessel versus the scalar concentration. Figure 8.10(b) shows the evolution over time of this curve with a 0.2 s interval.
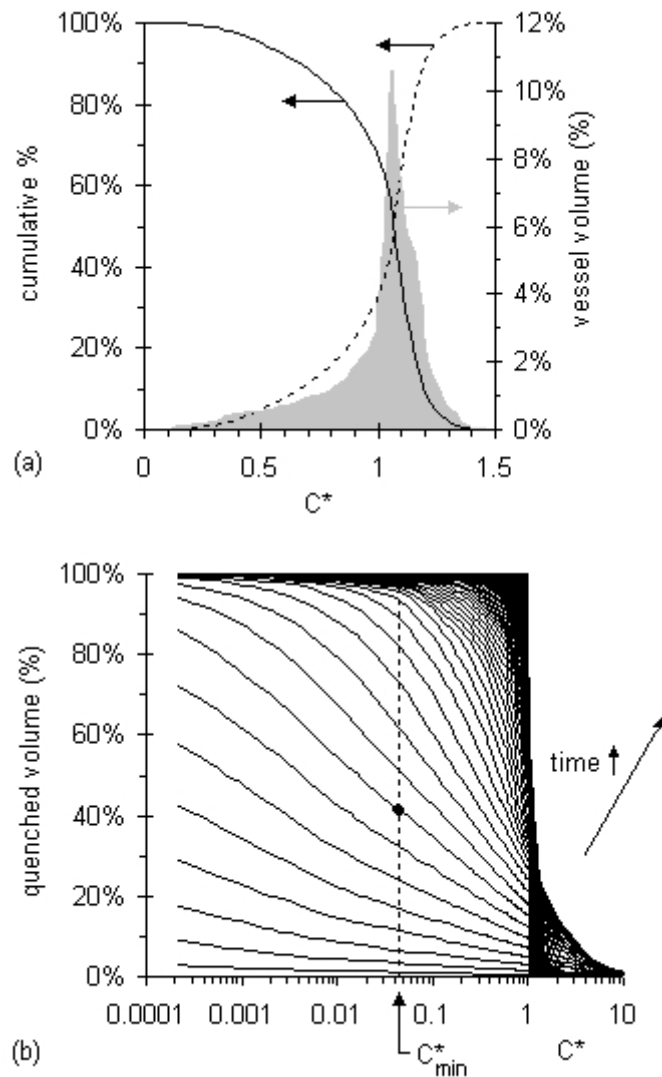
Figure 8.10. (a); Histogram of percentage (light grey filled), cumulative percentage of the vessel volume (dashed line) and cumulative percentage of the quenched volume (full line) versus normalized scalar concentration, at t = 7 s; (b) Time evolution of the cumulative curves for the quenched volume percentage versus the normalized scalar concentration; dashed line: minimum scalar concentration equal to 4.38×10^{-2}; black dot: location used for an example detailed in the text. The conditions were d = 7.2 mm, V = 6 m s^{-1}, N = 100 RPM.

For example, the black dot in Figure 8.10(b), which corresponds to a time of 1.6 s after injection started, indicates that 42% of the vessel volume has a concentration above the minimum concentration required to quench the reaction, therefore, in 42% of the vessel volume the runaway reaction would be quenched. It should be noted that we assume that there are no micro-mixing limitations and that therefore once a critical concentration is reached in a computational volume the reaction is assumed to be quenched.

If the percentage of quenched volume relative to C_{min}^* is plotted versus time (the value at the intersection of the cumulative curve and the vertical dashed line of Figure 8.10(b)), the new curve, which gives the percentage of the vessel volume quenched versus time, is named the quenching curve. This is a useful way to compare the effect of different injection conditions on the quenching efficiency. Figure 8.11 shows the quenching curves for all of the injection conditions investigated numerically at N = 100 RPM, and the jet injections conditions are summarized in Table 8.1. It is clear that, for a constant agitator speed, the quenching efficiency is affected significantly by the jet injection conditions.

The different curves of Figure 8.11 correspond to the different injection conditions and each is referenced using the short-hand notation (d [mm], V [m s^{-1}]). Although the cases (15 mm, 2 m s^{-1}) and (10 mm, 4.5 m s^{-1}) have the same jet flow rate, their quenching curves are not coincident. In addition, when the quenched volume is below 60%, it is noted that the time to quench the same volume is shorter for the (7.2 mm, 6 m s^{-1}) case than the (15 mm, 2 m s^{-1}) case which have flow rates equal to 14.86 and 21.21 l min^{-1}, respectively. Thus, the evolution of the curves cannot be explained by considering the jet flow rate alone. In contrast when the quenched volume is below 60 % all of the curves in Figure 8.11 shift from the right to the left as the jet momentum flux increases. Therefore, although the effect of the liquid jet density was not investigated in this study, the quenching efficiency was found to depend on the jet momentum flux if the quenched volume is below 60% but not directly on the jet flow rate. For a quenched volume between 60% and 100%, the conclusions and the dependence on the momentum flux are not so clear. Nevertheless, the results showed an optimum jet momentum flux, based on quenching a high percentage of the vessel volume, as the cases (7.2 mm, 6 m s^{-1}) and (10 mm, 4.5 m s^{-1}) led to the shortest quenching time for 90% of the vessel compared with higher momentum flux cases.
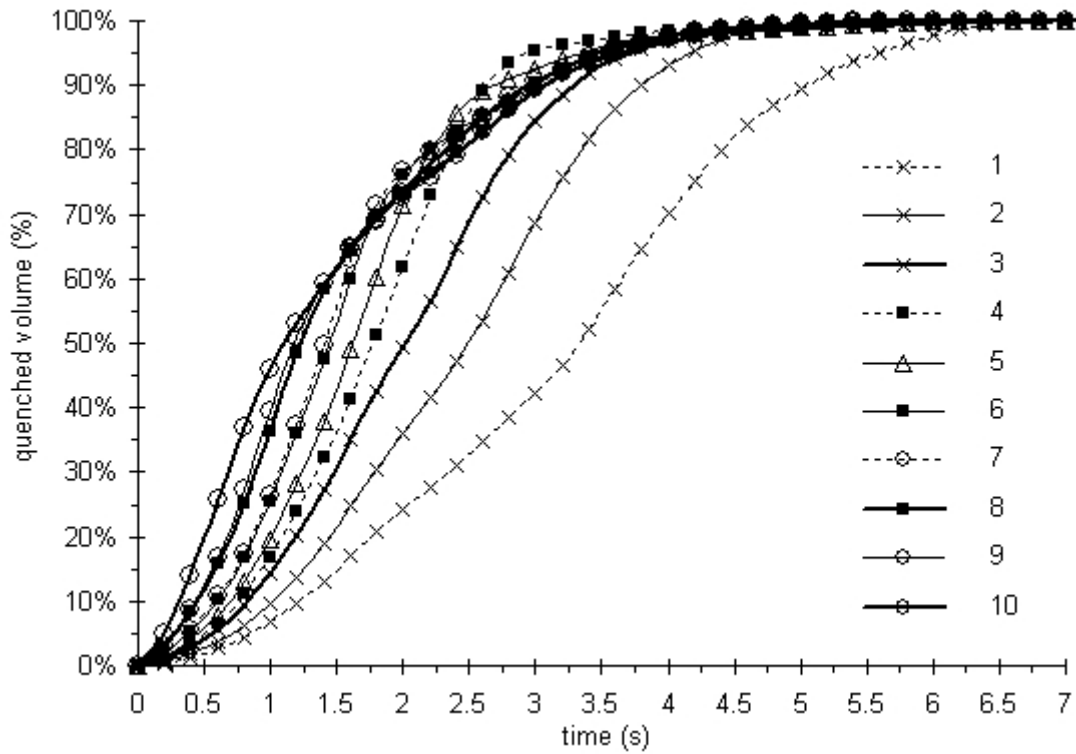
Figure 8.11. Cumulative curves of the percentage of quenched volume versus time for various jet inlet conditions. The description of each case is given in Table 8.1.

Table 8.1. Jet injection parameters: jet diameter, jet velocity, jet momentum flux, jet flow rate and the corresponding curve numbers of Figure 8.11.

d (mm)	V (m s^{-1})	M (kg m s^{-2})	Q (l min^{-1})	Curve # (Fig. 8.11)
7.2	2	0.162	4.89	1
10	2	0.313	9.42	2
15	2	0.705	21.21	3
7.2	6	1.461	14.66	4
10	4.5	1.586	21.21	5
10	6	2.819	28.27	6
7.2	10	4.059	24.43	7
15	6	6.343	63.62	8
10	10	7.830	47.12	9
15	10	17.618	106.03	10

8.6.2. <u>Mixing criteria: t_{50} and t_{90}</u>

The times t_{50} and t_{90}, which represent the time required to quench 50% and 90% of vessel volume, respectively, have also been determined and are used to quantify the optimum injection conditions at N = 100 RPM. The value of t_{50} decreases as the jet momentum flux increases, as shown in Figure 8.12(a), and was found to depend linearly on the inverse of the momentum flux to the power 0.5, as shown in Figure 8.12(b).
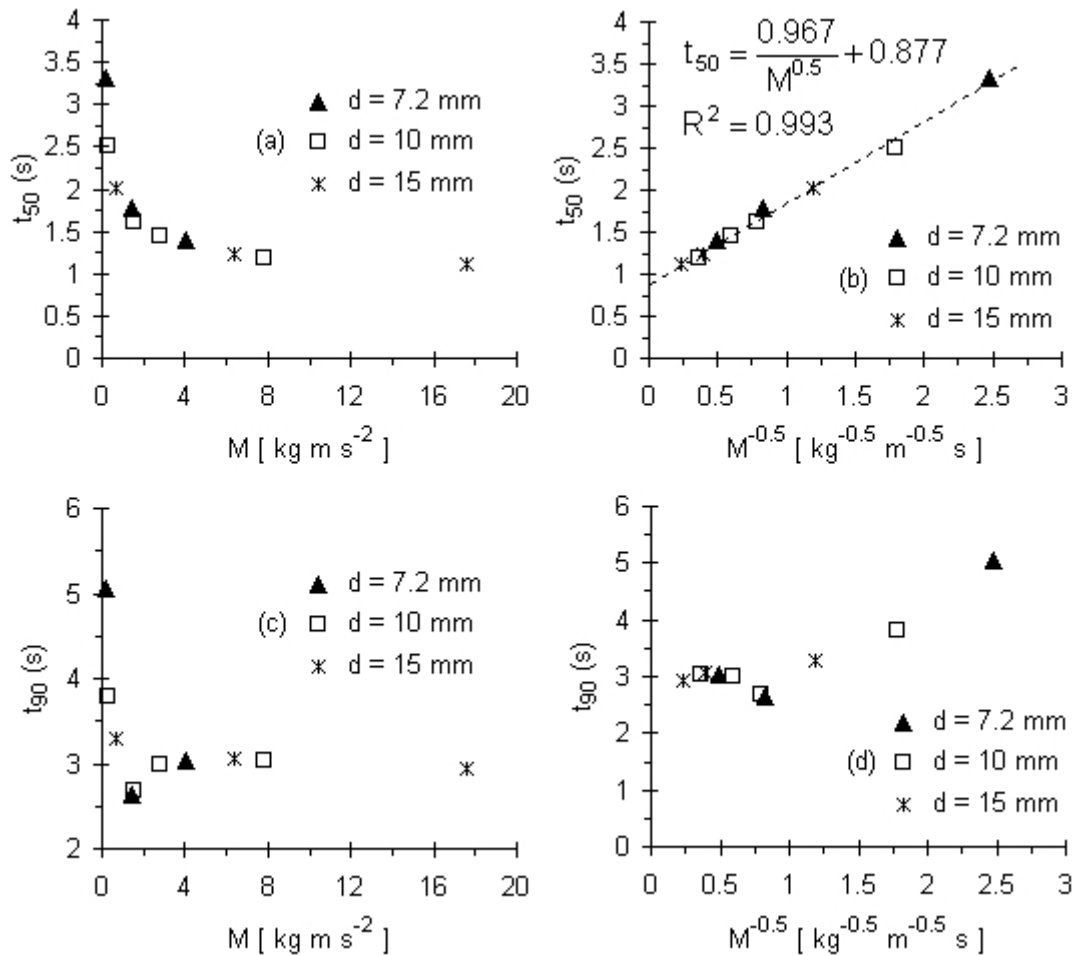
Figure 8.12. Evolutions of the various mixing criteria versus jet momentum flux and jet momentum flux to the power -0.5, at N = 100 RPM; (a) t_{50} versus M; (b) t_{50} versus $M^{-0.5}$; (a) t_{90} versus M; (b) t_{90} versus $M^{-0.5}$.

A power law between t_{90} and M was not observed as a minimum was obtained for the cases (7.2 mm, 6 m s^{-1}) and (10mm, 4.5 m s^{-1}) as shown in Figure 8.12(c), whilst the optimum jet momentum flux was clearly observed as being $M_{opt} \approx 1.5$ kg m s^{-2}. A higher jet momentum flux gave a constant value of t_{90}, as shown in Figure 8.12(d), which means that, at this rotation

speed, it is not necessary to increase M to M_{opt} to have a better quenching of 90% of the vessel volume.

8.7. IMPROVING REACTOR QUENCHING

This section is devoted to the study of the influence of the jet trajectory on reactor quenching. As it has already been demonstrated that the injection parameters influence the jet trajectory significantly, Figure 8.13 is used to show the evolution of the quenched volume with time for four different jet injection conditions. The quenched volume is represented by the isovolume where $C^* > C^*_{min}$, as this represents the region where the reaction is quenched. The conclusions obtained from this analysis of the evolution of the quenched volume versus time are affected by the fact that a full transient simulation was not made in which a sliding mesh modelled the rotation of the impeller blades, and therefore the transport by blade motion of the fluid already quenched to regions where the fluid is not quenched is not included. This is clearly a significant assumption, imposed by computational constraints but the case analysed here corresponds to the worse case scenario.

As shown previously, the minimum value of t_{90} was characterized by an optimum jet momentum flux close to 1.5 kg m s^{-2}. This optimal jet momentum condition is presented in Figure 8.13(b) and (c), while Figure 8.13(a) and (d) show the cases where $M < M_{opt}$ and $M > M_{opt}$, respectively. As shown in Figure 8.13(a), the fluid injected with the weakest momentum flux leads to a jet trajectory that causes quenching of the top part of the vessel first, then the region close to the vessel axis, and finally the vessel periphery. In contrast, the highest jet momentum flux leads to the quasi-instantaneous transport of the fluid to the bottom of the tank, as shown in Figure 8.13(d). Although this condition leads to the lowest value of t_{50}, it was not the optimal condition to quench 90% of vessel volume. The fluid, once it arrives in the bottom part of the vessel, has difficulty reaching the top part of the vessel because the mixing process is limited by the macro-mixing. In spite of the turbulence created by the high velocity jets which should enhance mixing, these conditions were not optimal for an agitator rotation speed of 100 RPM.
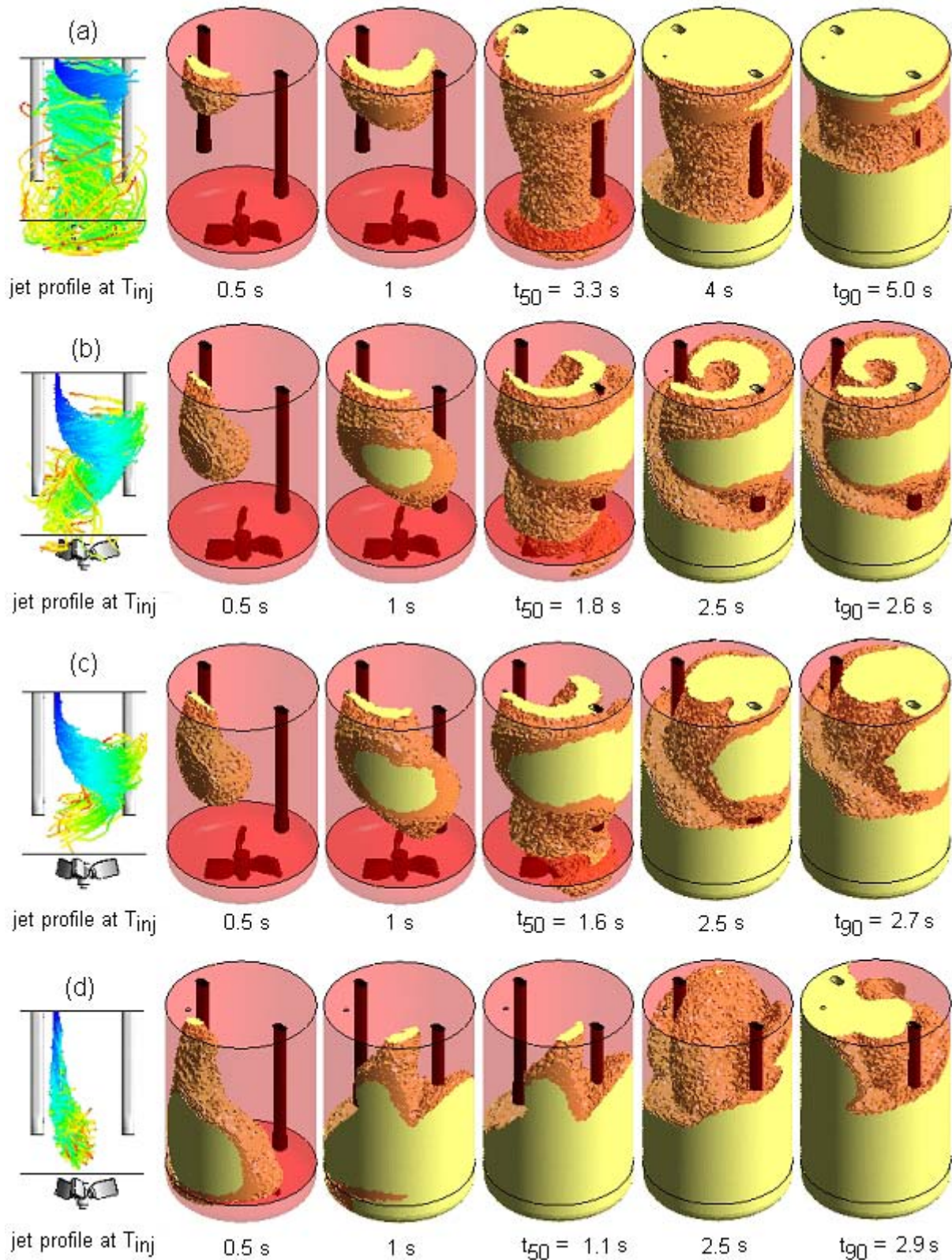
Figure 8.13. Isovolumes of scalar concentration greater than C_{min}^{*} versus time (yellow: quenched; red: not quenched), and jet profiles at T_{inj} (300 Lagrangian particles coloured by the Lagrangian particle travel time normalized by T_{inj}). (a): (7.2 mm, 2 m s^{-1}), M = 0.162 kg m s^{-2}; (b): (7.2 mm, 6 m s^{-1}), M = 1.461 kg m s^{-2}; (c): (10 mm, 4.5 m s^{-1}), M = 1.586 kg m s^{-2}; (d): (15 mm, 10 m s^{-1}), M = 17.618 kg m s^{-2}. N = 100 RPM.

In spite of the differences in the jet diameters and jet velocities, the cases presented in Figures 8.13(b) and (c) gave rise to the lowest values of t_{90} and good quenching conditions were obtained for very similar jet trajectories. Figures 8.13(b) and (c) show an efficient way to mix the fluid jet. The jet trajectories are such that the injected fluid is able to flow in several directions: one towards the top which transported the jet fluid into the upper part of the vessel, one laterally toward the middle of the tank allowing quenching of the central portion of the vessel and with this fluid getting mixed into the bottom of the vessel due to the agitator pumping effect, and one part towards the vessel periphery. The consequence is that the jet fluid is transported via the bulk flow to different locations and this has a really positive effect if 90% of the volume is to be quenched. This produces the same effect as having multiple feed locations, a situation which is well-known to reduce the mixing of an additive in batch or semi-batch reactors. Therefore, it is clear that the quenching efficiency depends on the jet trajectory. As the jet trajectory has been found to depend directly on the jet momentum flux, the jet trajectory may be controlled via its momentum flux and it is not the jet with the greatest penetration (as usually suggested) but one that produced the correct penetration to maximize the benefits of the bulk flow pattern that is optimal.

8.8. CONCLUSIONS

The fluid injection via a jet at the flat free-surface of a partially-baffled agitated vessel has been studied both experimentally and numerically to improve the understanding of the fluid mechanics of a model system related to the quenching of runaway reactions in batch industrial polymerization reactors. The experiments and the simulations have been carried out using water for both the stirred and injected fluids, using various jet cross-sections, injection velocities and agitator rotation speeds.

Experimentally, the jet trajectories have been visualized using UV fluorescence to limit the uncertainties associated with the entrainment of air bubbles by the free-falling jet, as the focus this study is the liquid injection. This method was shown to perform well, and allowed the liquid jet penetration behaviour into the bulk during the injection period to be visualised. It was shown that the jet trajectory depends on the jet momentum flux and its relative

magnitude compared with tangential velocity of the bulk flow in the vessel which develops in the top part of this under-baffled stirred vessel.

Numerically, an Eulerian-Lagrangian approach which used a single-phase flow model in which the modification of the bulk hydrodynamics by the jet momentum was taken into account has been developed to investigate the effect of the jet injection parameters on the jet trajectory. The analysis of Lagrangian particles trajectories showed very clearly in three dimensions how the jet penetrates and then mixes into the bulk. Comparison of the experimental data obtained for a single jet diameter with these CFD predictions showed very good agreement. At the same time, the transport of a passive scalar was used in order to correlate the influence of the jet trajectory with the quenching efficiency, by analysing the scalar concentration distribution versus time. By considering that in each vessel elementary volume the reaction was quenched when the scalar concentration exceeded a minimum required value, the definition of the global mixing criteria t_{50} and t_{90}, (corresponding to 50 and 90% of the vessel volume quenched, respectively) were found to be useful to quantify the effect of the injection parameters on the quenching rate.

At the rotation speed of 100 RPM, the jet momentum flux was found to be correlated with the jet trajectory and the analysis of the passive scalar concentration in the vessel revealed that the quenching efficiency depended on this jet trajectory. The main conclusions can be summarised as follows:

(i)   a low jet momentum flux lead to weak downward jet penetration. This was caused by a deflection of the jet plume very close to the free-surface due to the high tangential bulk fluid movement which exists in the upper part of this under-baffled stirred vessel. The injected fluid is trapped by the central vortices and therefore does not mix efficiently in the whole vessel.

(ii)   a jet momentum flux of around 1.5 kg m s^{-2} lead to the lowest time to quench 90% of the vessel volume and this value was deemed to be the optimal jet momentum flux at N = 100 RPM. The analysis of the jet trajectories obtained in this case revealed that the injected fluid was transported optimally in the vessel by maximizing the benefits of the bulk flow pattern.

(iii)   a high jet momentum flux lead the injected fluid to reach the bottom of the vessel very quickly, and to be poorly dispersed. As the transport of this fluid is linked to macro-mixing limitations, this condition was not optimal in the vessel studied, where the flow is mainly tangential in the upper vessel. These limitations would have a stronger effect if the agitator velocity were decreased.

Therefore, it was demonstrated that this simplified CFD modelling provides a valuable qualitative description of the trajectory of a liquid jet, having the same physical properties as the stirred liquid, injected at the flat free-surface of a partially-baffled agitated vessel. The numerical method used with the global mixing criteria t_{50} and t_{90} is useful for process safety purposes in order to quantify the influence of the injection parameters on the quenching efficiency. The numerical methods developed in this Chapter are used in Chapter 10 to study the case of jet injections in real industrial reactors. The challenging problem of the study of jet injection at higher agitator rotation speeds, where the effect of the free-surface shape deformation cannot be neglected, is presented in Chapter 12 as interesting perspective of this work.

Chapter 9

APPLICATION TO S-PVC SYNTHESIS REACTORS – PART 1:

HYDRODYNAMICS, VORTEX SHAPE, POWER INPUT AND PUMPING CAPACITY

The know-how learnt in the CFD modelling at the pilot scale was used to model the industrial vessels of two PVC production plants of Tessenderlo Group: the Mazingarbe plant located in the north of France and the Beek plant in The Netherlands. The two plants have different reactors, with different geometries, agitator and baffles. One of the main advantages of using CFD is the possibility to simulate directly the mixing vessels at the full scale, avoiding the well-known uncertainties associated with scale-up. To carry out this task with a maximum confidence level, most of the CFD methods and tools used in this Chapter were previously developed and validated with experimental data from the pilot reactor, which is in exact geometrical similarity with one of the industrial reactors.

The first part of this Chapter is devoted to the study of the hydrodynamics of the industrial vessels and to the prediction of the vortex shape, as the vessels used are partially-baffled mixing vessels. In the second part, the power input is predicted using CFD for each industrial vessel, the predictions are compared with experimental data, with good agreement being found and the agitator power numbers were determined. Finally, the pumping capacity of each agitator was investigated to determine the pumping number for each industrial agitator.

9.1. THE INDUSTRIAL GEOMETRIES

The two mixing vessels are both equipped with only two baffles suspended from the top vessel head, with a bottom entering agitator system and stirred by a "Pfaudler-type" impeller. Nevertheless, important differences exist between the geometries of the two types of synthesis reactors. The agitators are not of the same models and the baffles geometries are very different.

The development of radial flow impellers of "Pfaudler-type" began in the 1960's originally for corrosion resistance but they have become widely used in the polymerization market. During the early days of PVC manufacture, the PVC tended to be sticky in nature and stuck to most metallic tanks. Its adhesion to glass was found to be less pronounced than to stainless tanks and therefore glass tanks and impellers were used. The formulation of PVC manufacture changed in the 1950's, producing PVC with greatly reduced adhesion characteristics. Therefore, stainless tanks and mixers slowly replaced the glass-coated equipment (Oldshue *et al.*, 1982). However, the Pfaudler-type glass-coated impellers are still used widely, more because of historic usage than because of its mixing efficiency (Mixing Equipment Co., 1981). There exist different models of "Pfaudler-type" impellers (called Retreat Blade Impeller, Retreat Curve Impeller, Crowfoot Impeller) deriving from the same initial concept: a three bladed impeller, with the blades inclined from the horizontal by a retreat angle, and the blades retreating backward somewhat like a spiral backswept impeller. Less research has been conducted on these impellers compared with, for example, the Rushton turbine. This is the case even though there may be more industrial mixing vessels that are equipped with curved blade impellers than with Rushton turbines.

All the geometries were modelled using ANSYS DesignModeler (versions 9.0 to 11.0). These models were based on paper drawings provided by the plant personnel or equipment suppliers and verified with photographs of the two production plants. The reference numbers of the drawings used in the modelling are listed in Table 9.1.

Table 9.1. Drawing numbers used to model the industrial S-PVC reactors

Plant	Designations	Drawing number
MZG	Face, top and bottom views of the vessel Agitator and baffles positions	Sogem, # 2855
MZG	Details of the agitator	Pfaudler, # 394 880C Drawings from Pfaudler with no ref.
MZG	Details of the baffles	Pfaudler, # 399 906 B
BEEK	Face, top and bottom views of the vessel Agitator and baffles positions	Pfaudler, # 305 703 K, 321 319 D
BEEK	Details of the agitator	Pfaudler, # 322 128 B, 322 128 D, 322129 C, 332 752 A, 316 561 C
BEEK	Details of the baffles	EHW Thale, # 535 5120

Industrial reactors of the Mazingarbe plant were taken as the reference for the scale-down from the industrial scale to the lab scale. The pilot reactor, previously detailed in Chapter 3, is an exact geometrical copy of these vessels. The hand-made agitator for the pilot vessel was an exact copy made in steel of the one installed in this industrial reactor. The industrial model differs only by the glass coating which make its contours smoother. To model this small difference, the exact glassed shape has been taken into account for the industrial modelling. This task was much more difficult compared with the modelling of the pilot agitator model because the glassed model has numerous surface details and all the edges had to be chamfered to make the shape as rounded as the original model. Figures 9.1(a) and (b) show the impeller geometry. Figures 9.1(c) and (d) compare the modelling to a picture of the real agitator taken inside the industrial vessel (that is why it is dark around the blade show in Figure 9.1(d)). Almost perfect agreement is shown.
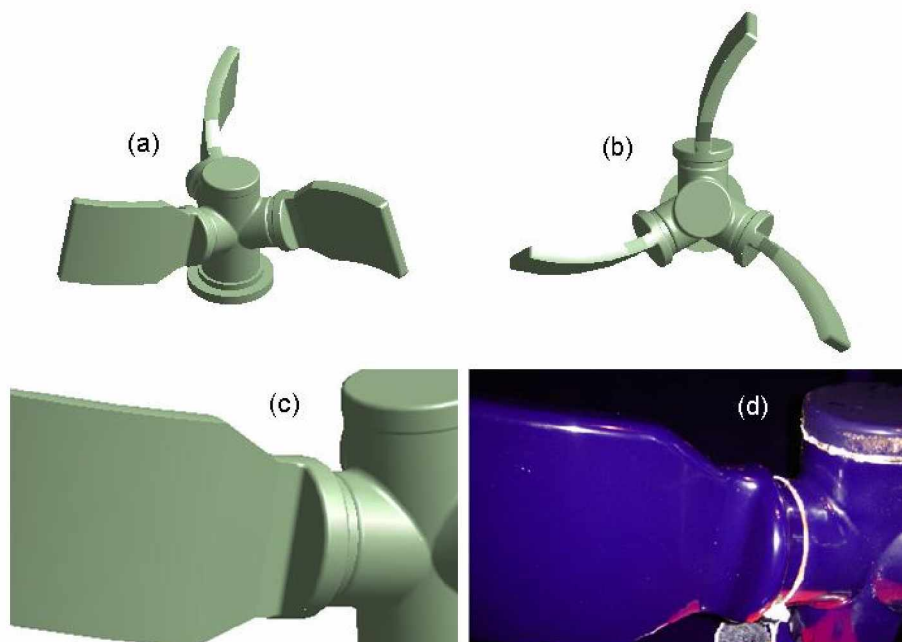
Figures 9.1. The modelled impeller of the MZG agitator: (a) 3D view; (b) top view; (c) lateral view; (d) picture of the real agitator (lateral view).

The "Pfaudler-type" agitator installed in the Beek reactors is also glass-coated and therefore required the same construction process as for the Mazingarbe impeller to model the glassed geometry accurately. This impeller is shown in Figure 9.2 and is also compared with pictures in Figures 9.2(c) and (d). These again show very good agreement.
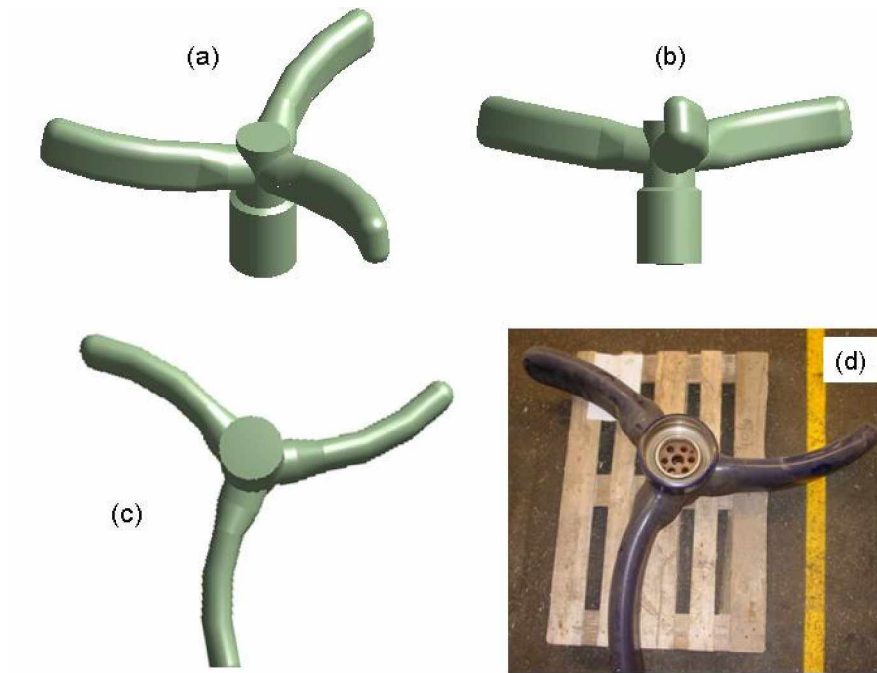
Figures 9.2. Geometry modelling of the Beek agitator: (a) 3D view; (b) lateral view; (c) bottom view; (d) picture of the real agitator (bottom view).

The synthesis reactors from Beek plant (named Beek reactors) are equipped with D-baffles. Figure 9.3 shows the model of the D-baffle geometry and a comparison with a picture of those used at the Beek plant.
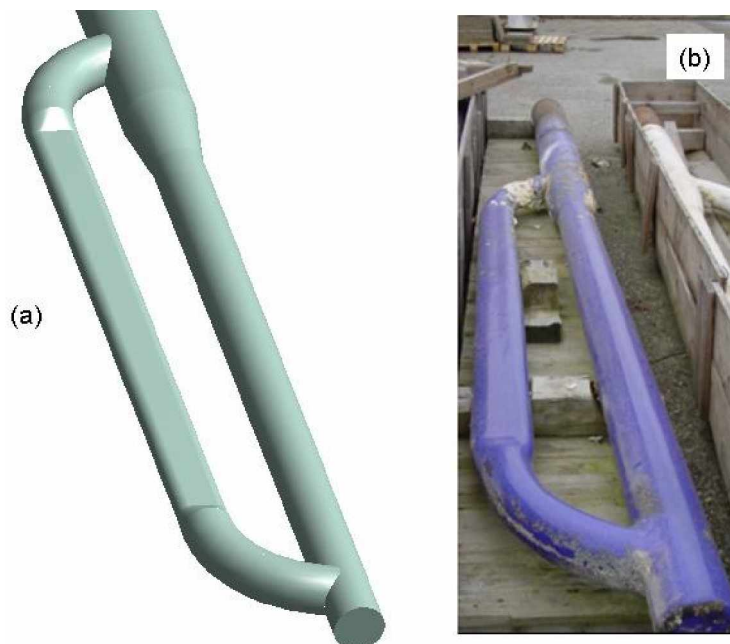
Figures 9.3. Geometry model of the D-baffles: (a) 3D view; (b) picture of real baffle.

A D-baffle would be technically very difficult to build for the laboratory scale. In contrast, a beaver-tail baffle, which is basically just a flattened pipe, was much easier to make. This is one of the major reasons that the Mazingarbe reactor was chosen as the reference geometry for the scale-down.

Figure 9.4 and 9.5 shows the 3D geometries of the Mazingarbe and Beek mixing vessels, respectively.
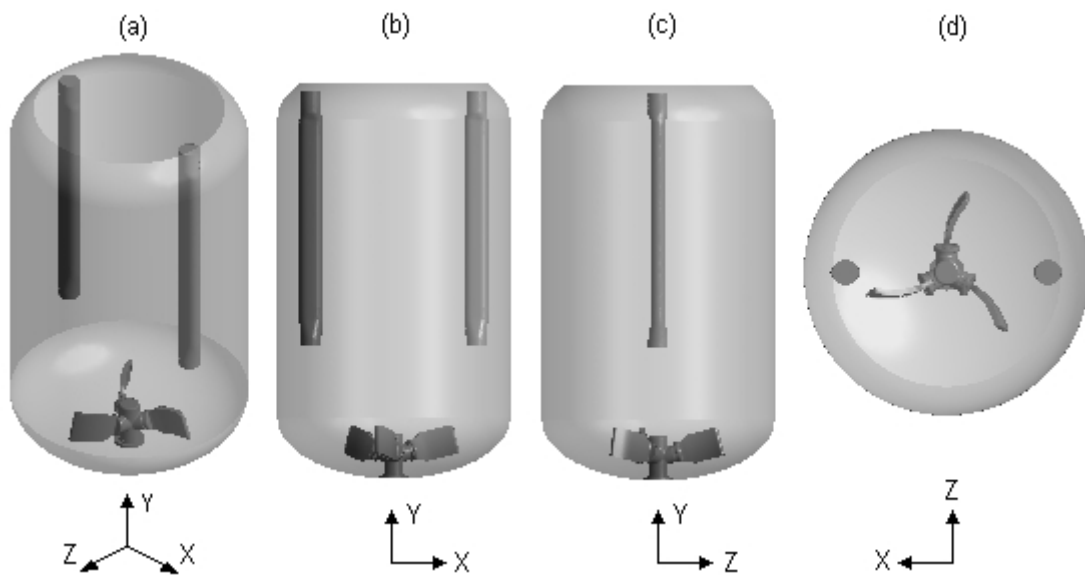
Figure 9.4. Geometry of the Mazingarbe reactor with the standard baffling configuration. (a) 3D view, (b) lateral XY view; (c) lateral YZ view; (d) top view
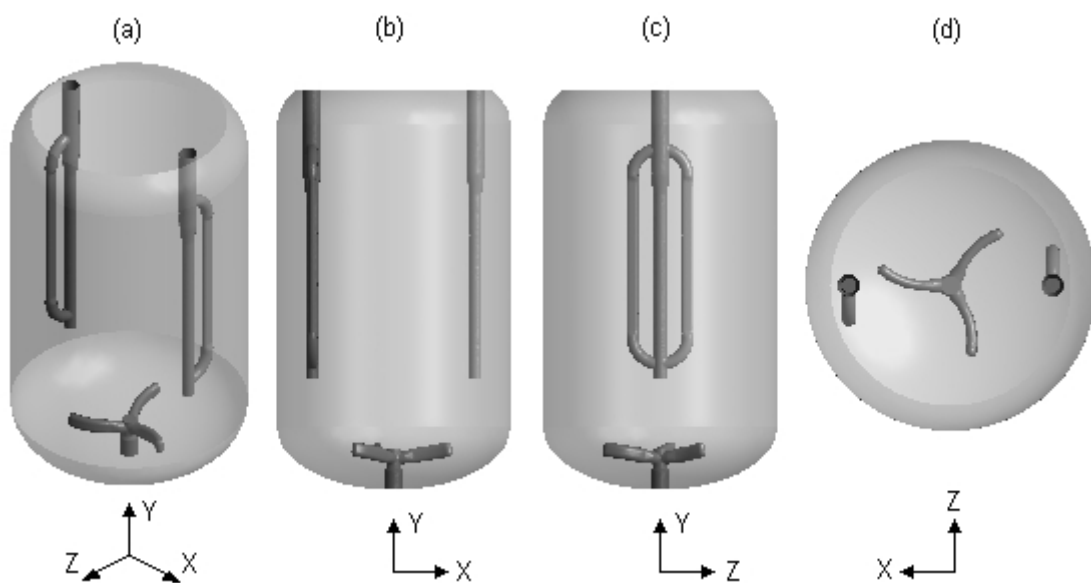
Figure 9.5. Geometry of the Beek reactor. (a) 3D view, (b) lateral XY view; (c) lateral YZ view; (d) top view

The vessels are presented equipped with their top head. The geometries presented in these figures are the standard geometries modelled for the studies presented in this Chapter. The use of the top vessel head were only necessary for the simulation including the vortex in order to take into account the interaction of fluid with the top of the head. Note that for the determination of the power and pumping numbers of the impellers, the numerical studies do not require modeling the vessel head, and therefore the CFD simulations were performed without this.

9.2. MESHING THE INDUSTRIAL REACTORS

Using a mesh of adequate quality is important for minimizing the discretization error and controls in part the quality and the efficiency of the solver convergence. Several measures of mesh quality are available in ANSYS CFX Mesh, such as measures of mesh orthogonality, expansion and aspect ratio (see the ANSYS CFX 11 user guide). Building an adequate mesh for the industrial reactors proved to be difficult. The main reason was due to unacceptable values of the mesh aspect ratio, which relates to the degree that mesh elements are stretched (largest ratio of maximum to minimum integration point surface areas for all elements adjacent to a node). Values outside of the suggested acceptable range lead to discretization errors and are often a cause of bad convergence. The difficulties in meshing the industrial reactors were not encountered for the smaller scale pilot reactor. This occurred for two main reasons. Firstly, the smoothing process used in the construction of the agitator and baffles made the meshing more difficult, as a smaller mesh size compatible with the surface details was required. Secondly, the total number of mesh elements must not be too high due to computer requirement and the finite size of memory available. Therefore, numerous tests had to be carried out with varying mesh sizes in order to produce an acceptable mesh for the two industrial vessels. Simulations were carried out for each industrial vessel to verify that the solution was grid independent. The three components of the fluid velocity (water) calculated on a horizontal line going through the agitator region, shown in Figure 9.6, where large gradient in the flow exists were used for comparison purposes. The results are shown in Figure 9.7 for three different grids, referred to as fine, medium and coarse, comprising the total number of elements listed in Table 9.2 for each vessel.
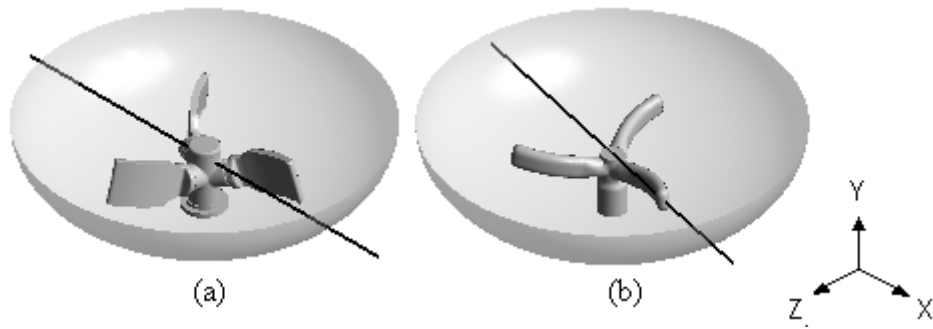
Figure 9.6. Lines where the velocity data was extracted for grid independency tests: (a) Mazingarbe reactor, Y_{line} = 400 mm; (b) Beek reactor, Y_{line} = 350 mm.
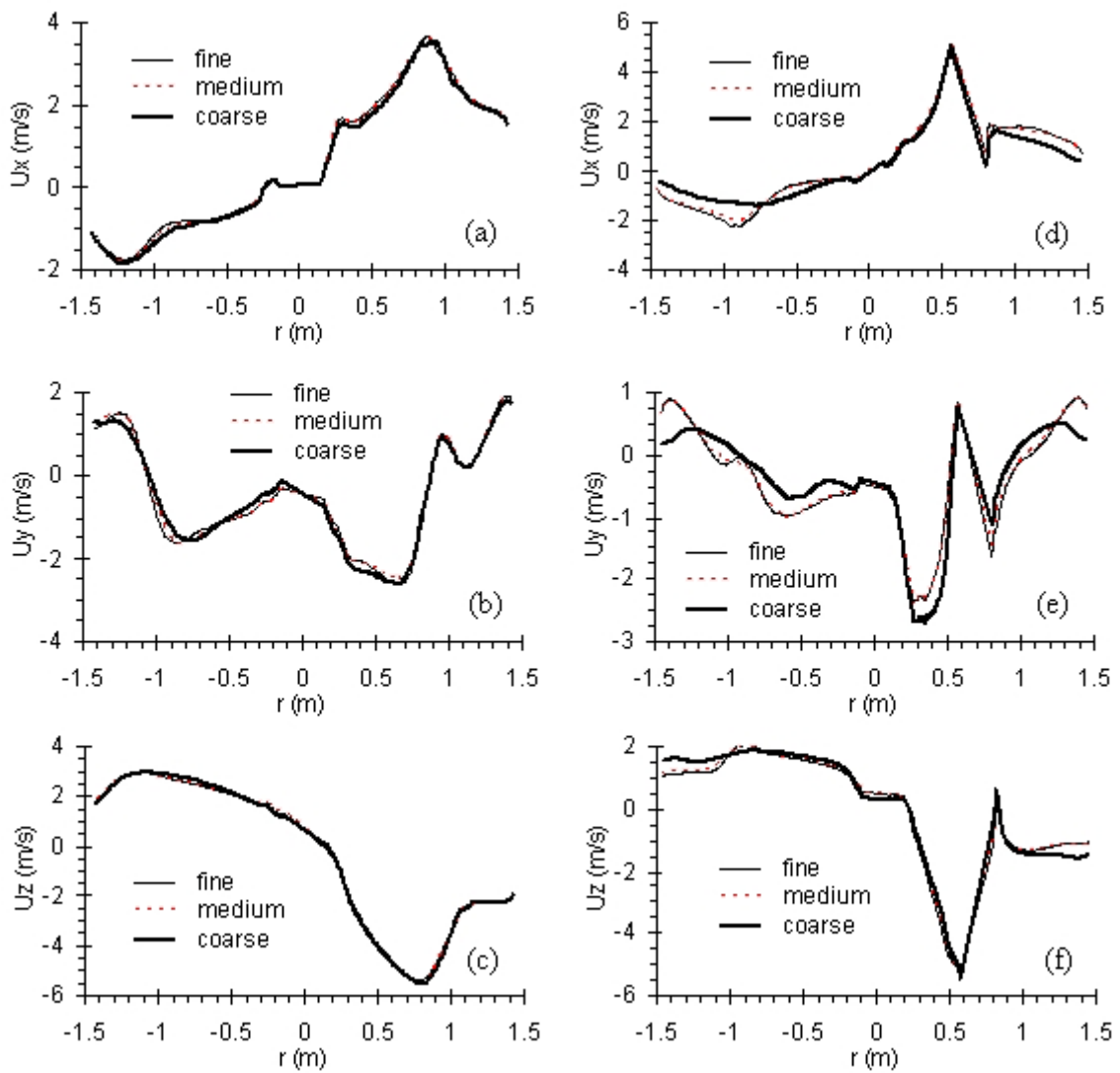
Figure 9.7. Tests of grid independence for the industrial reactors. The figure shows the effect of the grid size on the velocity components U_x, U_y and U_z. (a), (b), (c): Mazingarbe reactor; (d), (e), (f): Beek reactor

Table 9.2. Grid sizes and information relative to the grid independence tests (without the top head)

Reactor	Grid	Max grid size	Total number of elements
MZG	fine	60 mm	1 860 909
MZG	medium	80 mm	1 129 031
MZG	coarse	110 mm	736 041
Beek	fine	60 mm	2 234 417
Beek	medium	80 mm	1 501 249
Beek	coarse	200 mm	982 936

It can be seen that the three grids tested gave similar velocity profiles, but that the results obtained using the coarse grid differ slightly from those obtained with the two finer grids, as shown in Figures 9.5(b), (d), (e) and (f). In addition, using the medium size grid allowed a reduction of the total number of mesh elements by 65% and 49% for the Mazingarbe and Beek reactors, respectively, as shown in Table 9.2. Since the differences between the results obtained using the fine and medium grid are minor for the two reactors tested, the medium grid was employed in the simulations performed in this Chapter. The final mesh is shown in Figure 9.8. Note that inflation meshing was used at all walls to provide good boundary layer resolution.
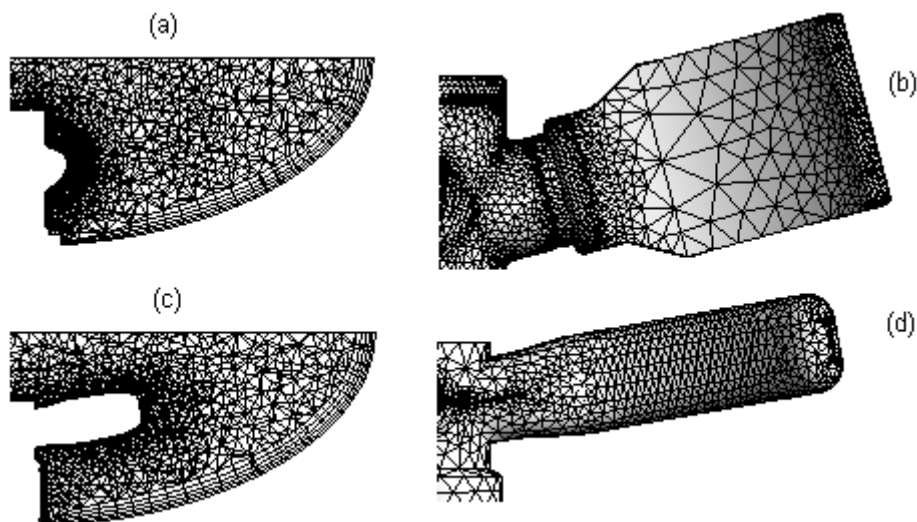
Figures 9.8. Details of the mesh used for the CFD simulations: (a) half of the bottom dish of the Mazingarbe reactor; (b) an agitator blade of the Mazingarbe reactor; (c) half of the bottom dish of the Beek reactor, (d) an agitator blade of the Beek reactor.

9.3. SIMULATION STRATEGY

In this paragraph, the results of hydrodynamics of the industrial mixing vessels are investigated using the CFD knowledge and background learnt during the previous numerical studies carried out for the pilot reactor. The analysis of the values of the parameter $\Phi_B = n_B(B_w/T)$ which quantifies the baffling effect resulting from the presence of n_B plate baffles of width B_w (see Chapter 4 and Sano and Usui (1987)) gives useful preliminary information about the baffling effect provided in these vessels (the fully-baffled condition occurs for $\Phi_B > 0.4$). Concerning the beaver-tail baffle, its width may be directly introduced in the Φ_B calculation formula, as this type of baffle, which is a flattened pipe, looks like a thick plate in cross-section. In contrast, this method may not work well for the Φ_B calculation of a D-baffle, as shown in Figure 9.5. As a matter of fact, if the simple baffle width is taken as B_W in the calculation of Φ_B, the rear part of the D-baffle is not taken into account and the baffling effect may be under-estimated.

Very few results were found in the literature concerning the estimation of the equivalent baffle width if the baffles used are not common plates. Dickey *et al.* (2004) reported data of Koen (1977) who have defined the equivalent baffle width as a percentage of the effective area to projected area for a finger baffle. As this method is not validated for D-baffles mounted in the configuration of Figure 9.5, it was preferred to use information provided by the manufacturer of the baffles to quantify the baffling condition. The baffling effect corresponding to the industrial vessel configurations were given by Pfaudler in the form of baffling factors equals to 0.50 and 0.75 for the Mazingarbe and Beek reactor, respectively (a baffling factor equal to zero corresponds to no baffle and the value of one corresponds to the fully-baffled condition). The D-baffles present a larger surface area to the rotating fluid, so the Beek configuration provides much greater baffling than that for the Mazingarbe configuration. These values have not been verified, as they were used only to qualify the industrial vessels as partially-baffled systems. Therefore, due to the fact these vessels are partially-baffled systems, a vortex is created and the free-surface deformation must be taken into account in the CFD modelling.

As already discussed in Chapter 4, the CFD predictions of both the hydrodynamics in the mixing vessel and the real free-surface shape, require the use of a multiphase model. The

inhomogeneous approach, developed previously in this thesis, has proved to perform very well in the cases which were tested for the pilot reactor: (i) in steady state (Chapter 4); (ii) in transient conditions (Chapter 5); (iii) with non-constant agitator rotation speed and gas disengagement (Chapter 6). In all of these cases, the numerical predictions were in good agreement with experimental data. Therefore, the hydrodynamics of the industrial vessels including the prediction of the vortex shape have been studied using the inhomogeneous approach and the same simplified physics as used in the pilot reactor: a single air bubble diameter (d_b = 3 mm) and a constant drag coefficient (C_D = 0.44).

The simulations of industrial reactors were much more difficult to perform compared with the simulation carried out for the mixing vessel at pilot scale due to convergence difficulties. The convergence criterion adopted here was values of the normalized residuals below 10^{-4}, as used previously for the pilot reactor (ANSYS-CFX 11.0 user's guide). Multiphase simulations were performed with water and air at 25°C. The rotating domain was set to be the entire bottom dish, which includes the agitator, and the connecting interface between the rotating and the stationary domains was represented by the horizontal surface which connects the cylindrical part of the vessel and the bottom dish. The boundary conditions were a no-slip condition at all walls, except at the very top surface of the vessel where the free-slip condition was set. In addition, the simulations were initialized with a hydrostatic pressure profile in the liquid phase.

Several simulation strategies, geometries and mesh refinements were tested to obtain the desired convergence level for the different configurations tested. All calculations were performed using a dual-processor Xeon 2.8 GHz computer with 2 Gbytes RAM. Preliminary simulations of this vessel were carried out with the reactor provided with its entire top head. This geometry did not result in an acceptable level of convergence. The best convergence was obtained with the vessel top head truncated to reduce the gas volume above the initial liquid level set at initialization. Nevertheless, the height of gas was sufficient to enable the water to rise up the vessel walls (due to the vortex generation).

9.3.1. <u>Simulation of the Mazingarbe industrial reactor</u>

The Multiple Reference Frame (MRF) model (steady-state), previously detailed in Chapter 4 for predicting the vortex shapes with the pilot reactor, gave good convergence, and was therefore chosen for studying the hydrodynamics and the free-surface shape in the Mazingarbe industrial reactor. The Reynolds number relative to the agitator was 5.0×10^6, giving fully turbulent conditions. The only way to reach good convergence levels with this vessel configuration was to keep a small space between the top of the baffles and the top surface of the vessel, as shown in Figures 9.4(b).

9.3.1.1. Baffle configuration giving the maximum baffling effect

The two beaver-tail baffles were located in the vessel with the wider part of each baffle being opposed to the tangential bulk flow, as shown in Figure 9.9(a). This configuration is that commonly uses for this type of baffles and is that currently used in the industrial vessels (named standard configuration). The optimum convergence levels and CPU time were obtained by using a timestep equal to 0.05 s for the momentum, mass and turbulence equations, and a timestep equal to 0.01 s for the volume fractions equations. The total CPU time was about 3 days with the MPICH local parallel solver used with four partitions. The normalized residuals of the momentum and mass, turbulence quantities (k and ε), and volume fractions equations are shown in Figure 9.9(b).

Figure 9.9. CFD simulation of the Mazingarbe reactor with the baffles giving the maximal perturbation (Re = 5.0×10^6): (a) geometry; (b) normalized residuals versus iteration number for the momentum and mass, turbulence quantities, and volume fraction equations

9.3.1.2. Baffle configuration giving the minimum baffling effect

Since the model used has been validated previously, one of the advantages of the CFD simulations is the possibility to test new configurations. As the beaver-tail baffles are suspended from the top reactor head, it is easy to rotate them through a 90° angle to obtain the minimum flow interaction. In addition to the analysis of the hydrodynamics and vortex shape obtained in this case and the comparison with the standard case (§9.3.1.1.), this configuration has been tested industrially to determine the influence of the power input on the final product. It is well-known that less baffling is synonymous with lower power input into the bulk due to a decrease of the agitator power number. The power input analysis relative to this configuration is detailed in §9.5.

The simulation strategy was identical to that for the simulation carried out with the baffles having the maximum influence (MRF steady-state, same boundary conditions, Re = 5.0×10^6). The mesh was built with the same mesh dimensions as defined in §9.2 and the total number of elements was 1,174,000. The total CPU time to run the simulation was 2 days and 11h. Figure 9.10(a) shows the geometry modelled. The normalized residuals for the momentum and mass, turbulence quantities (k and ε), and volume fractions equations resulting from the simulation are presented in Figure 9.10(b).
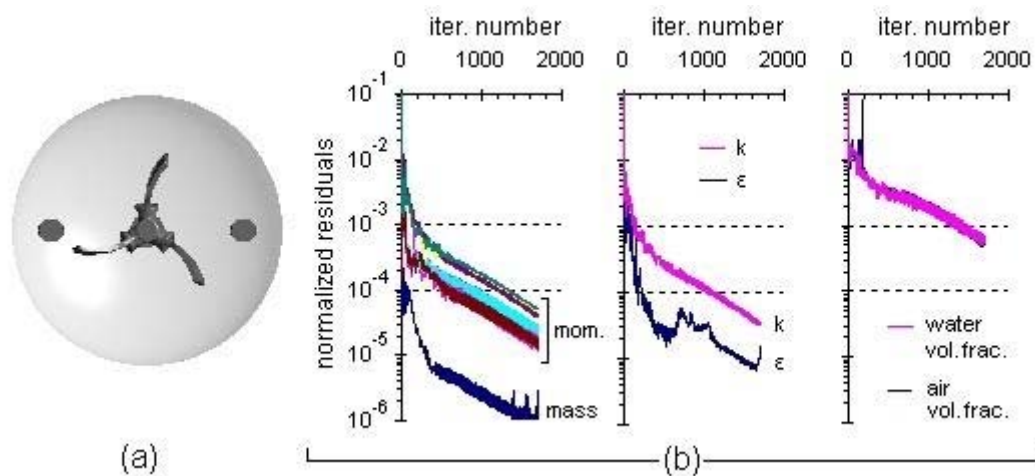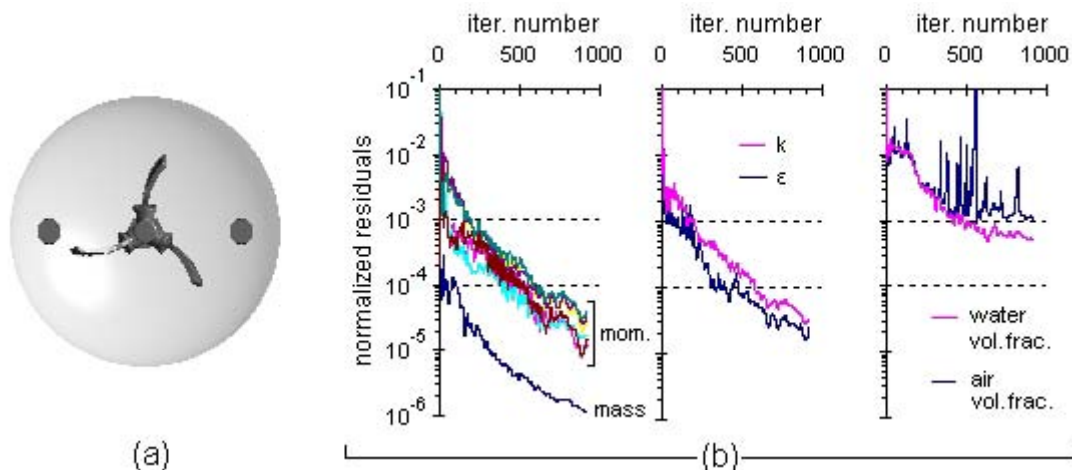

Figure 9.10. CFD simulation of the Mazingarbe reactor with the baffles providing the least perturbation (Re = 5.0×10^6): (a) geometry; (b) normalized residuals versus iteration number for the momentum and mass, turbulence quantities, and volume fraction equations.

9.3.2. <u>Simulation of the Beek industrial reactor</u>

The simulation of hydrodynamics, including free-surface modelling with this reactor equipped with a "Pfaudler type" impeller and two D-baffles, was much harder to perform compared with the Mazingarbe reactor. The steady-state approach was not able to provide a satisfactory level of convergence for the vessel used with a full top head, a truncated head, and with a small space between the baffle top and the top vessel surface. The normalized residuals, obtained using the Multiple Reference Frame (MRF) approach in steady-state, were close to the acceptable value of 10^{-4} but the simulation was not considered to be well-enough converged for reliable analysis of the results. These convergence difficulties with the steady-state approach may be due to an important transient component of the flow, created by strong interactions between the flow and the D-baffles.

Thus, the simulation was performed using the transient approach developed and tested for the pilot reactor in Chapter 5, using the sliding mesh approach with the transient rotor-stator model available in ANSYS CFX 10. The time-step was set to allow a 2° rotation angle of the agitator per time-step. In addition, as was pointed out previously in Chapter 5: (i) running this type of transient simulation requires a minimum number of agitator rotations (N_{r1}) to reach the quasi-steady state and start statistics; (ii) the use of statistics to obtain averaged variables (such as velocity, water volume fraction, etc) requires also a minimum number of agitator rotations (N_{r2}). N_{r1} and N_{r2} were found to both be equal to 15 for the pilot reactor if the transient simulation is initialized with a converged steady-state result. As already discussed in Chapter 5, the number of agitator revolutions needed to reach a quasi-steady state for the simulations at pilot scale was of the same order of magnitude as the number of revolutions needed by others, such as Li *et al.* (2004, 2005), to reach a quasi-steady state. In addition, Li. *et al.* (2005), who used CFD to model the scale-up of geometrically similar partially-baffled agitated vessels equipped with RCI and a single beaver-tail baffle at different scales (0.5 litre, 2 litres and 20 litres), have shown that the same number of impeller revolutions to be sufficient whatever the scale of the vessel (10 agitator revolutions were necessary for their study). However, we are aware of the danger of making such an assumption with non-geometrical similar vessels. The previous conclusions and the results of Li *et al.* (2005) for scale-up were taken as a guide and it was assumed that $N_{r1} = N_{r2} = 15$ was also valid for the Beek reactor. The simulation was initialized from the steady-state result (quasi-converged), then 15 agitator rotations were made before the transient statistics were started, and a further

15 agitator rotations were simulated to obtain the final result. The total CPU time for the whole simulation was about 16 days. Figure 9.11(a) shows the geometry modelled. The normalized residuals of the momentum and mass, turbulence quantities (k and ε), and volume fractions equations resulting from the transient simulation are presented in Figure 9.11(b). Note that, using this approach, all the residuals were below 10^{-4} due to the simulation being properly converged at each time-step.
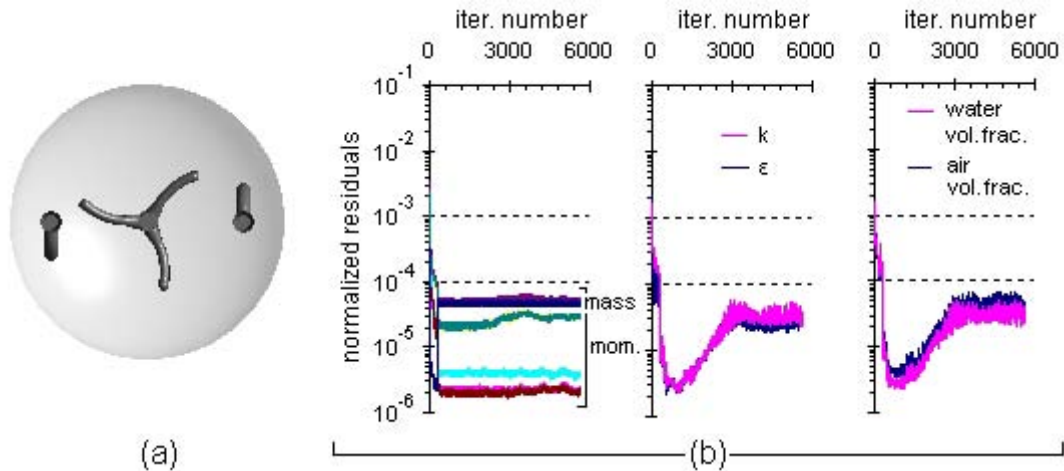
Figure 9.11. CFD simulation of the Beek reactor (Re = 6.6×10^6): (a) geometry; (b) normalized residuals versus iteration number for the momentum and mass, turbulence quantities, and volume fraction equations

9.4. HYDRODYNAMICS AND VORTEX SHAPE

This paragraph is devoted to the comparison of the hydrodynamics and the free-surface shapes which develop in the Mazingarbe reactor with the two different baffling configurations, and in the Beek reactor. The liquid zone is defined to be that with a water volume fraction above 0.9. The threshold value of 0.9 was set for the volume fraction as it was shown to define the vortex shape well and to give good agreement with experimental data at the pilot-scale (see Chapter 4). The results are presented using contour plots and axial-radial vector fields of liquid speed U_{ijk}, and are shown at the same scale with the same range of velocities to make comparisons easier between the different mixing vessels.

Figures 9.12 and 9.13 show results for the Mazingarbe reactor obtained from a steady-state simulation (see §9.3.1) for the baffles providing the maximum and minimum

perturbation to the flow, respectively. Figure 9.14 shows the results obtained for the Beek reactor, which are the result of an averaging of instantaneous velocities data made during 15 agitator rotations (see §9.3.2). Figure 9.15 compares the different vortex shapes obtained.
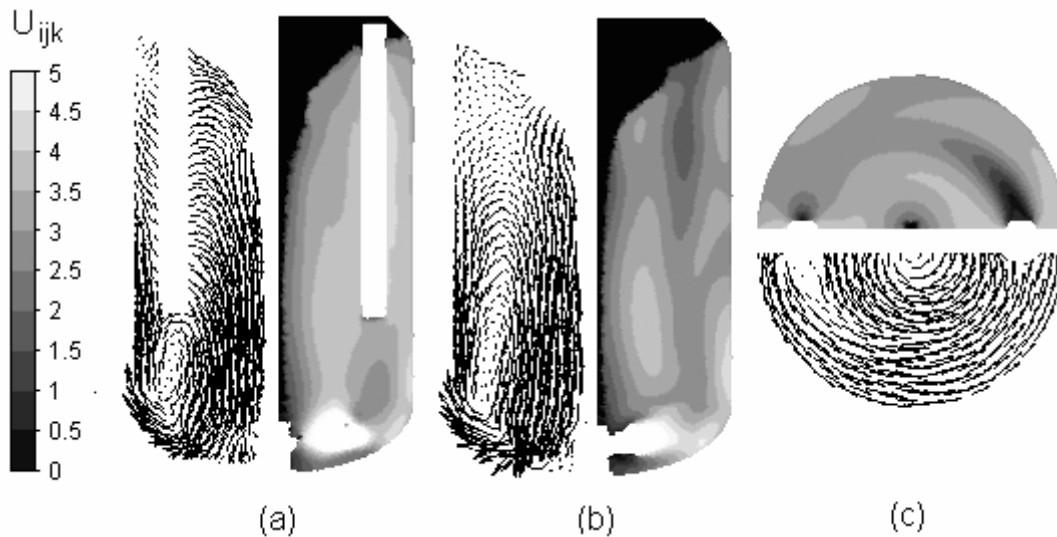
Figure 9.12. Hydrodynamics on the Mazingarbe industrial reactor with the baffles providing the maximum perturbation (Re = 5.0×10^6): (a) XY baffles plane; (b) YZ orthogonal baffle plane; (c) ZH horizontal plane at Y = $H_{liq}/2$; ($\alpha_l > 0.9$).
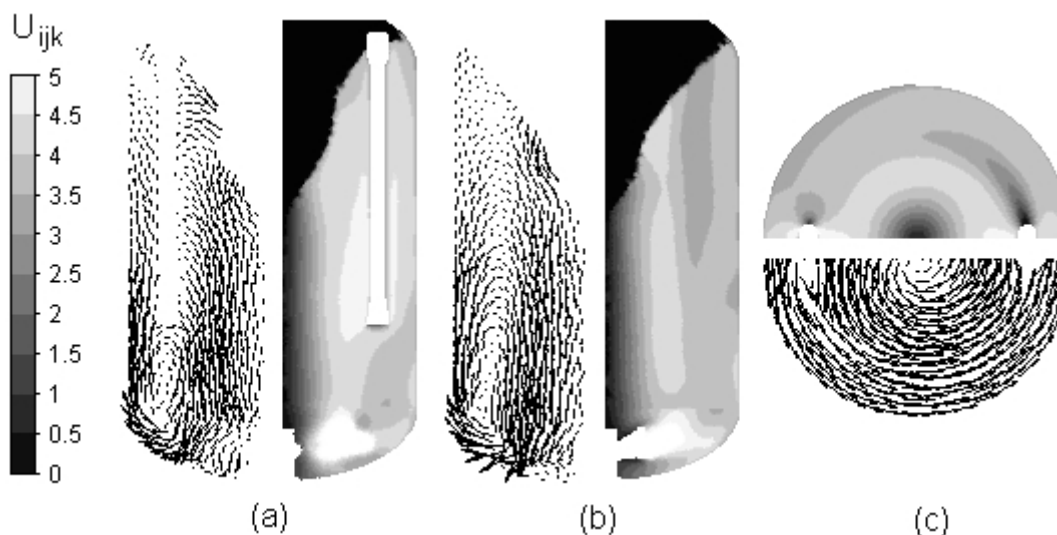
Figure 9.13. Hydrodynamics on the Mazingarbe industrial reactor with the baffles providing the minimum perturbation (Re = 5.0×10^6): (a) XY baffles plane; (b) YZ orthogonal baffle plane; (c) ZH horizontal plane at Y = $H_{liq}/2$.
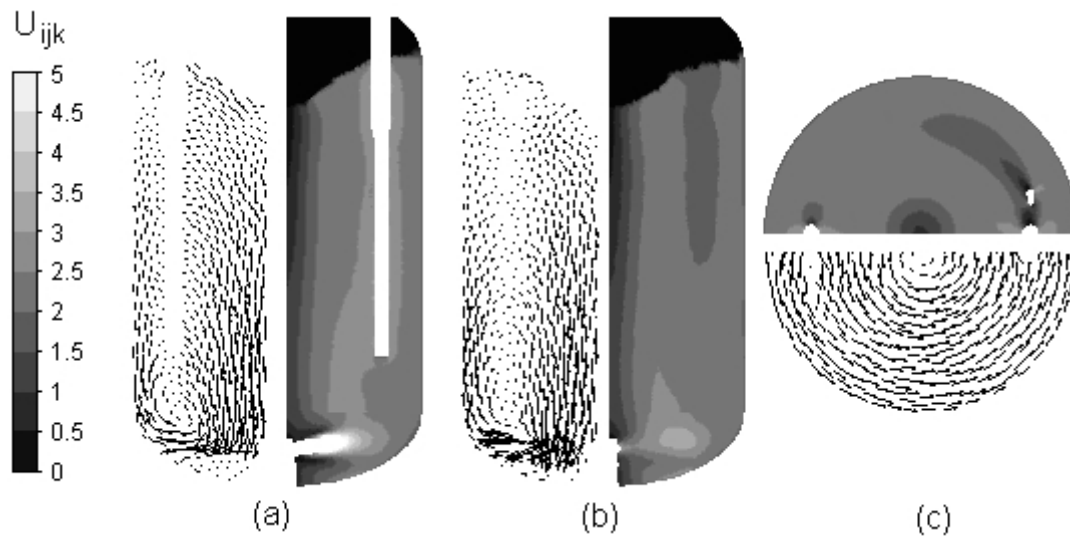
Figure 9.14. Hydrodynamics on the Beek industrial reactor (Re = 6.6×10^6): (a) XY baffles plane; (b) YZ orthogonal baffle plane; (c) ZH horizontal plane at Y = H$_{liq}$/2.
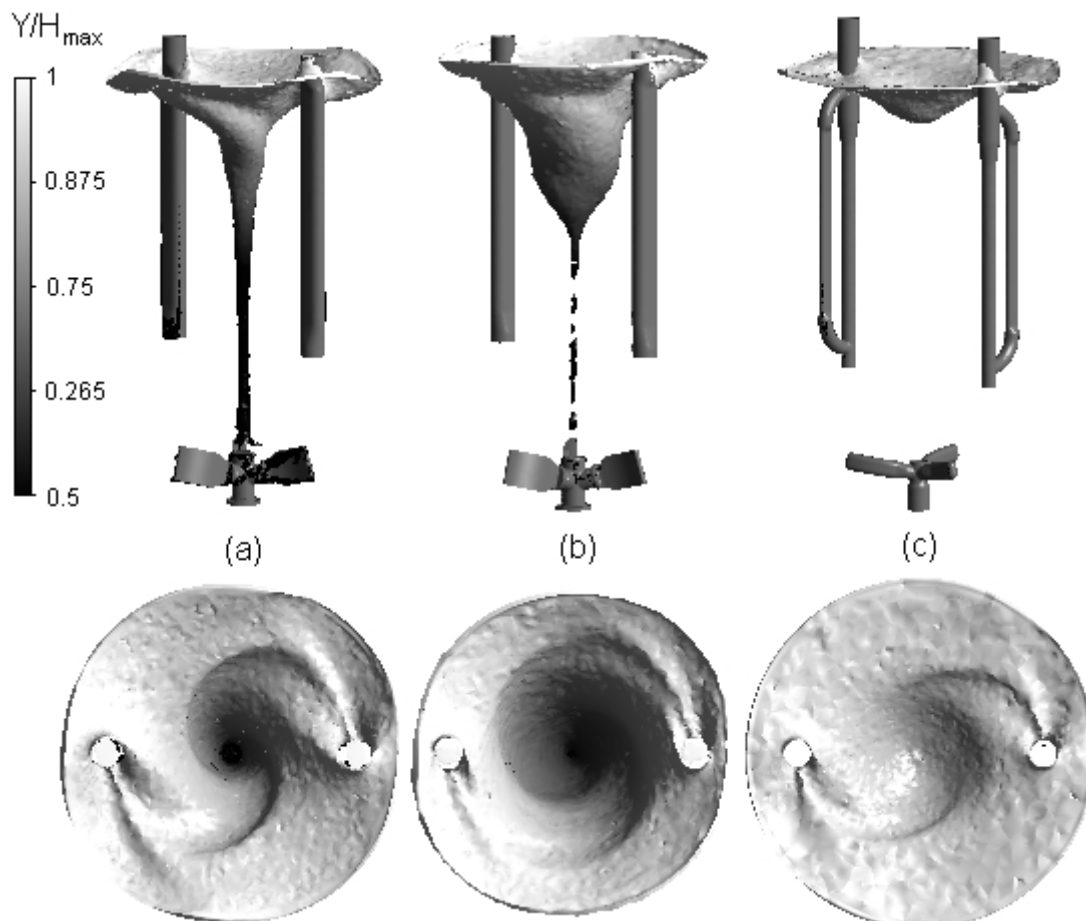
Figure 9.15. Top view of the different vortex shapes obtained. Isosurface of water volume fraction equal to 0.9 (gray scales from 0.5 to 1 with the free-surface height normalized by the maximum reactor height): (a) Mazingarbe reactor with baffles giving the maximum perturbation (Re = 5.0×10^6); (b) Mazingarbe reactor with the baffles the minimum perturbation (Re = 5.0×10^6); (c) Beek reactor (Re = 6.6×10^6).

As shown in Figures 9.12, 9.13 and 9.14 the global hydrodynamics and flow patterns are almost identical for the three cases investigated. For each case, the liquid flow is composed of a down-flow movement of the fluid at the centre of the tank due to the axial pumping action of the impeller. The fluid is ejected radially from the agitator, deflected by the curved bottom dish, and then flows up close to the vessel shell. This creates a large circulation loop from the outer region to the inner region of the vessel. Whichever of the configurations tested, Figures 9.12(c), 9.13(c) and 9.14(c) show that the fluid has a strong tangential flow motion, this swirl resulting from the partially-baffled condition. When the rotating fluid impacts the baffles, and this is shown very clearly in the views of the top of the free-surface of Figure 9.15, high shear strain zones, low velocity areas and vorticity trails are created behind the baffles. These follow the tangential movement of the fluid, and enhance mixing in this area. That may be the reason why the actual injection position of the killer in the Mazingarbe reactor, which is located above one of these trails, has been found to be an appropriate injection position, as previously demonstrated in Chapter 7. Nevertheless, differences exist between the three mixing vessel configurations.

Figures 9.12 and 9.13 show how a different baffling configuration in the Mazingarbe reactor (with the same agitator rotation speed) can influence the vortex shape. As shown in Figures 9.12(a), 9.12(b) and 9.15(a) for the baffles providing the maximum effect, the vortex has the same characteristic shape as that previously observed at the pilot reactor. The vortex has a central bulb in the baffle plane (Figure 9.12(a)) and a flatter shape in the orthogonal baffle plane (Figure 9.12(b)). The presence of only two baffles, located at 180° from each other, creates an asymmetry in the velocity field and results is a free-surface deformed differently in the baffle plane and the plane orthogonal to the baffles. As is well-known, a lower baffling effect is synonymous with higher tangential velocities in the vessel, more swirl and a stronger vortex. As shown in Figures 9.13(a), 9.13(b) and 9.15(b) the effect of the baffle orientation has an important influence on the vortex shape. The vortex in the minimum perturbation case is much wider and slightly deeper, with a different shape in the baffle plane and in the orthogonal baffle plane than for the baffles providing the maximum perturbation.

The most baffled vessel is the Beek reactor. Due to the relative importance of the baffling effects compared with the two previous cases, the vortex in this vessel was expected to be the weakest. This was confirmed, as shown in Figure 9.14. All the numerical results agree well with this well-known result: "the more baffled the vessel, the shallower the vortex".

Finally, the magnitude of the velocity in this reactor was found to be lower than in the Mazingarbe reactor, as shown in the contour plots of Figures 9.12 and 9.10.

9.5. POWER INPUT AND THE POWER NUMBER OF THE AGITATORS

The effect of agitation on suspension polymerization reactors has been studied extensively in the literature to correlate the mean particle diameter of PVC resin (d_{50}) with the agitation characteristics. Numerous correlations reported in the literature give the d_{50} value as being directly proportional to the energy consumption rate per unit volume (Saeki and Emura, 2002). In addition, the necessity to build scale-up rules for PVC suspension polymerization reactors has promoted significant research work on agitation to describe and correlate results obtained from the same size reactors with different agitation conditions, and results obtained from different size reactors. Saeki and Emura (2002), who have performed studies of results obtained from 2 m^3 pilot plant reactor up to commercial-scale reactors of 150 m^3, found a d_{50} correlation very close to the one found by Ozkaya *et al.* (1993) obtained for 27 m^3 reactors. They concluded three important rules for scale-up of S-PVC reactors: (i) the power consumption per unit volume must be kept constant; (ii) the pumping capacity per unit volume must also be kept constant; (iii) as a result, a relatively larger blade (D/T) is needed for large reactors.

As stated above, the power input is a fundamental quantity in suspension polymerization reactors. As power input is one of the main parameters which controls the structure and stability of the dispersions and therefore the particle size, it must be predicted with accuracy in the industrial vessels of this study.

9.5.1. <u>Power input in the Mazingarbe reactor</u>

The section is devoted to experimental measurements carried out for the industrial reactors of Mazingarbe and Beek, and CFD predictions made in order to predict the power drawn in these mixing vessels.

9.5.1.1. Experimental data on power consumption

Power measurements have been carried out on two industrial reactors at the Mazingarbe plant specifically for this study to evaluate the power drawn (Leclercq, 2005). The target was to carry out power measurements with the agitator rotating in an empty reactor to evaluate the total power losses: internal motor mechanical friction, friction within the bottom gland packing, stator losses, etc. Then, measurements were carried out during a complete polymerisation cycle. Finally, by subtracting the losses from the total power, the power input was estimated. More information is given in Table 9.3.

Table 9.3. Information relative to the experimental power measurements made on the industrial mixing S-PVC reactors of Mazingarbe.

	Details
Date	18/19/20 December 2005
Tested motors	« old motor » M 1201 « new motor » M 1205
Target	power measurements with reactor empty power measurements during a complete polymerization
Available data	mean power (beginning and end of a poly. cycle), power losses motor efficiency
Results	comparison between the two motors power drawn by the fluid

For example, the general profile of a power curve of an agitator motor obtained during a suspension polymerization reaction is shown in Figure 9.16 for the Mazingrabe reactor. The real power curves used for this analysis are available in Leclercq (2005).
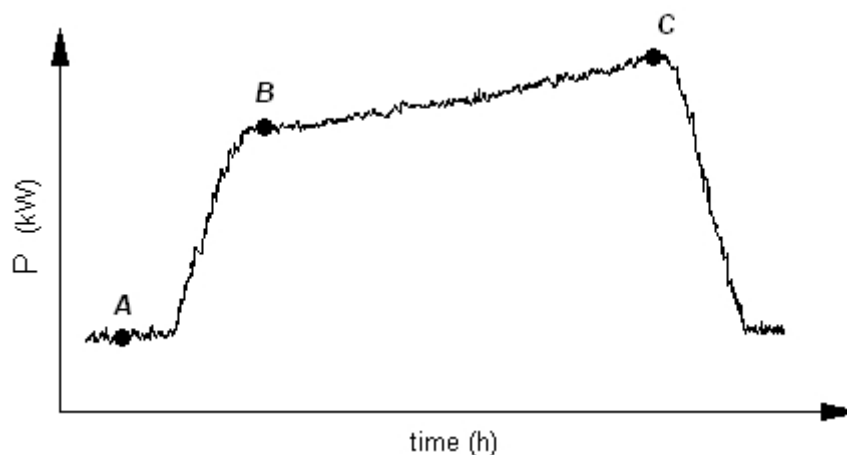
Figure 9.16. General profile of a power curve of an agitator motor obtained during a complete S-PVC polymerization: *A*: reactor empty; *B*: start of polymerization; *C*: end of polymerization.

In Figure 9.16, at point *A* the agitator is rotating in an empty vessel. The polymerization reaction is a batch operation, which is started by feeding raw material into the reactor and this leads to an increase in the motor power consumption from *A* to *B*. At point *B*, the reactor contains water and VCM with a mass ratio of 50/50 at temperature *T*. From points *B* to *C*, the increase in the power is due to the increase of the bulk density due to the formation of PVC in the monomer droplets during polymerization. The power consumption being directly proportional to the stirred fluid density means that the power consumption increases with monomer conversion. At point *C* the polymerization is finished and the PVC slurry is discharged from the reactor. Table 9.4 shows the results of power measurements for the two motors obtained with an empty reactor (point *A*) and those obtained at point *B*.

Table 9.4. Results of the power measurements for the Mazingarbe reactor (Re = 5.0×10^6).

	Old motor M1201	New motor M1205
Point *A*	$P_A = 8$ kW $\cos \varphi_A = 0.11$	$P_A = 5$ kW $\cos \varphi_A = 0.10$
Point *B*	$P_B = 74$ kW $\cos \varphi_B = 0.72$ $\eta_B = 0.891$	$P_B = 67$ kW $\cos \varphi_B = 0.75$ $\eta_B = 0.925$
$\Delta P_B \, (= P_B - P_A)$	$\Delta P_B = 74 - 8 = 66$ kW	$\Delta P_B = 67 - 5 = 62$ kW

The conclusion of the experimental measurements is that the power drawn by the system at point *B* is in the range 62 kW < P < 66 kW.

9.5.1.2. CFD predictions of the Mazingarbe agitator power number

The power input can be calculated as the product of the torque T_o acting on the agitator and shaft, with the impeller angular velocity equal to $2\pi N$ (N in s^{-1}). For eight different rotation speed from 30 RPM from 100 RPM (Re > 10^6), the impeller torque has been predicted using CFD with a single phase model. The power input can also be expressed in turbulent flow as $P = N_p \rho N^3 D^5$, where N_p is the dimensionless power number of the impeller. The calculated power using torque predictions is plotted versus $\rho N^3 D^5$ in Figure 9.17.
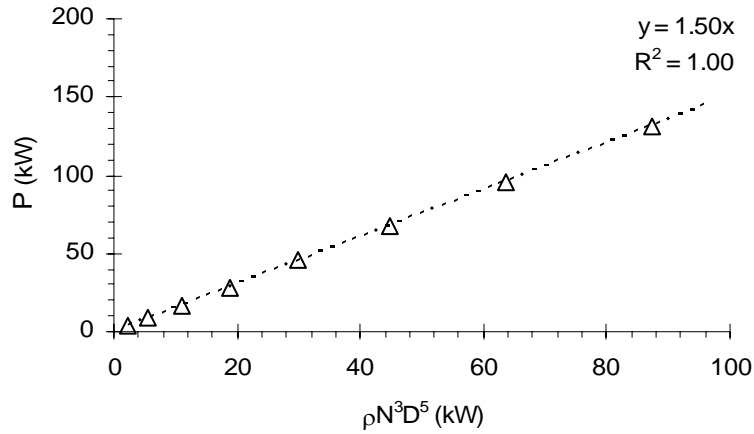
Figure 9.17. Prediction of the power input via the torque calculation for eight rotation speeds (30 RPM < N < 100 RPM) for the industrial Mazingarbe reactor.

The results are fitted perfectly by a straight line passing through zero. The slope of the fitting line of Figure 9.17 corresponds to the agitator power number and its value is predicted numerically to be $\underline{N_p^{MZG} = 1.50}$.

9.5.1.3. CFD predictions versus experimental data

The predicted power number of 1.50 was used to calculate the theoretical power input at the beginning of the polymerization cycle (point *B* in the Figure 9.16). At this point, the density of the bulk (ρ) was estimated at temperature *T* (PVC-grade 6706), with $50\%_m$ of VCM in water. The calculation was made using the software *Prophy Plus*, considering ideal liquid mixing, the NRTL thermodynamic model, a pressure of 10 bars and a mass fraction of VCM equal to 0.5. The density was estimated to be 906 kg m^{-3}. Thus, the power input predicted using the power number $N_p^{MZG} = 1.50$ is equal to $P_{CFD}^{MZG} = N_p^{MZG}\rho N^3 D^5 = 65$ kW.

The experimental data obtained in §9.5.1.1 gave $\Delta P_B = 66$ kW for the old motor and $\Delta P_B = 62$ kW for the new one. The CFD prediction of $P_{CFD}^{MZG} = 65$ kW is thus in very good agreement with the experimental measurements. As no published information is available for this impeller, the value of the power number for the Mazingarbe reactor is validated to be $N_p^{MZG} = 1.50$.

The industrial results can be compared with those obtained in Chapter 5 for the pilot reactor (same agitator model without glass coating). In the pilot reactor, N_p^{exp} was found to be

equal to 1.85 ± 0.4 and the power number predicted numerically was equal to 1.6 ± 0.1, compared with 1.50 for the industrial Mazingarbe agitator (the slightly lower value obtained for the industrial vessel might be due to the glass coating of the industrial impeller, however the precision of the measurement method is not sufficient to conclude this definitively).

9.5.1.4. Influence of the baffling configuration on the power input

As the CFD model has been validated, it can be used to predict the power input and the power number of the impeller if the baffling configuration is modified. The baffling configuration where the baffles provide the minimal perturbation was studied in terms of power input. The simulation used single phase flow and no top head. The results obtained are presented in Table 9.5 and are compared with those obtained for the baffles providing the maximum perturbation.

Table 9.5. Power input in the Mazingarbe reactor for baffles in the maximum and minimum perturbation configurations (Re = 5.0×10^6)

	Maximum configuration	Minimum configuration
Torque (N.m)	8373	6206
Power (W)	71904	53298
N_p^{CFD}	1.50	1.11

The power input is reduced by about 26% by changing the configuration of the baffles from the maximal to the minimal perturbation.

Industrial experimental data on mean motor current (the instantaneous value averaged over 400 minutes after the beginning of the polymerization), obtained for 31 polymerizations carried out in the same reactor from the 1/03/04 to the 4/04/04 with the two different baffle configurations, were analyzed using the software Statgraphics Centurion XV. For these experiments, 22 were carried out with the baffles providing the maximum effect and 9 for the minimum effect. The results obtained are shown in Figure 9.18.
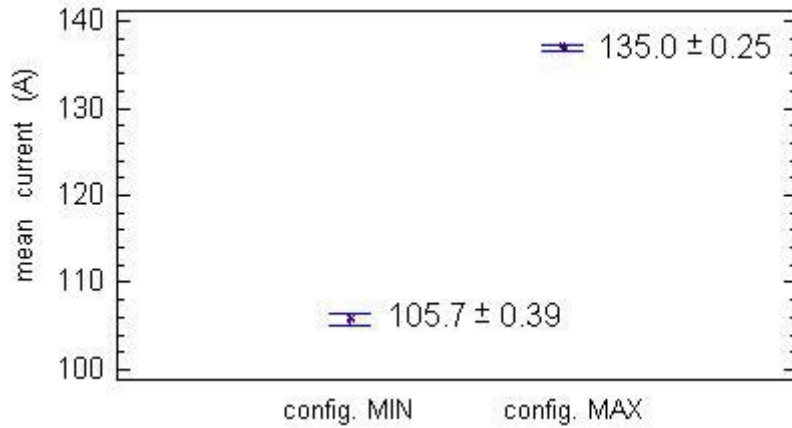
Figure 9.18. Industrial data of mean current (averaging during on 400 min) during 31 polymerizations in the Mazingarbe reactor (Re = 5.0×10^{6}): 9 in config. MIN and 22 in config. MAX.

Figure 9.18 shows a significant reduction of the mean current of the agitator motor when the baffles are rotated from the maximum perturbation position to the minimum perturbation position. Although direct use of the motor current must not be made to calculate the power input in mixing vessels due to the power losses and unknown motor power characteristics, the ratio of intensity between two different configurations in the same vessel can be compared with the predicted power number ratio obtained for these two configurations.

With the assumption of power losses << power input (here about 10% of power input in the normal configuration as shown in Table 9.4), we have the relation (9.1):

$$\frac{P^{MAX}}{P^{MIN}} \approx \frac{I^{MAX}}{I^{MIN}} \approx \frac{N_p^{MAX}}{N_p^{MIN}} \qquad (9.1)$$

The results of Table 9.5 give $\dfrac{N_p^{MAX}}{N_p^{MIN}} = \dfrac{1.50}{1.11} = 1.35$

while the results of Figure 9.16 give $\dfrac{I^{MAX}}{I^{MIN}} = \dfrac{137.1}{105.7} = 1.30$

The experimental data of $N_p^{MAX}/N_p^{MIN} = 1.35$ and the numerical CFD predictions of $I^{MAX}/I^{MIN} = 1.30$ are in good agreement.

9.5.2. <u>Power input into the Beek reactor</u>

9.5.2.1. Experimental data on power consumption

Experimental measurements have been carried out on two different reactors for two different agitation velocities (N_1 and N_2). Figure 9.19 shows the general evolution of the motor power during a polymerization carried out in the Beek reactor (Steffin, 2005). The actual power curves used for this analysis are available in Steffin (2005). The point *A* gives the power measure with the reactor empty allowing estimation of the power losses. The point *B* corresponds to a vessel full of water only. The results are presented in Table 9.6.
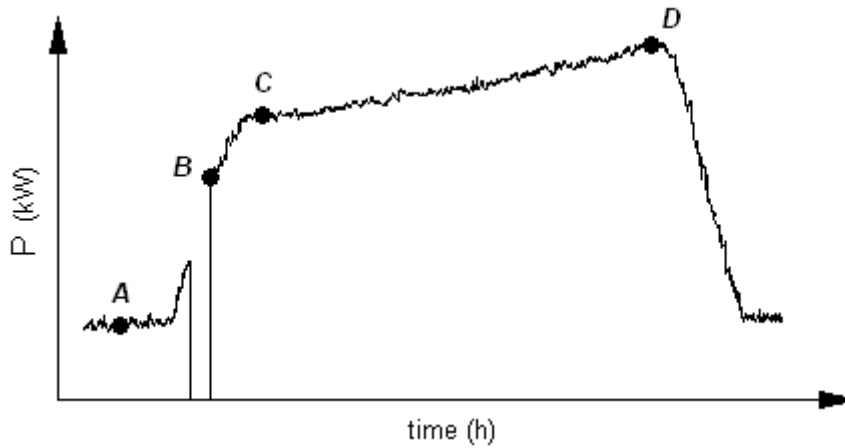
Figure 9.19. General profile of a power curve of an agitator motor obtained during a complete S-PVC polymerization in the Beek reactor: *A*: reactor empty; *B*: reactor filled with only water; *C*: start of polymerization; *D*: end of polymerization. Note that the agitator was stopped for a period between *A* and *B* leading to zero power.

Table 9.6. Results of the power measurements for the Mazingarbe reactor. Subscript 1 and 2 for the agitator velocity N_1 and N_2, respectively.

	Agitator speed N_1 (Re = 5.9×10^6)	Agitator speed N_2 (Re = 6.6×10^6)
Points A_1 and A_2	$P_{A1} = 7$ kW	$P_{A2} = 7$ kW
Points B_1 and B_2	$P_{B1} = 34 \pm 3$ kW	$P_{B2} = 40 \pm 3$ kW
$\Delta P \ (= P_B - P_A)$	$\Delta P_1 = 34 - 7 = 27 \pm 3$ kW	$\Delta P_2 = 40 - 7 = 33 \pm 3$ kW

The conclusion of the experimental measurements is that the power drawn by the fluid mixing at point B_1 is 27 kW ± 3 kW at the agitator speed N_1 and 40 kW ± 3 kW at the agitator speed N_2.

9.5.2.2. CFD predictions of the Beek agitator power number

The calculation of the Beek agitator power number was made using the same method detailed previously for the Mazingarbe reactor in §9.5.1.2. Eleven simulations have been performed from N = 30 RPM to N = 130 RPM (Re > 10^6) where the impeller torque has been predicted using the CFD model using a single phase model. The calculated power using torque predictions is plotted versus $\rho N^3 D^5$ in Figure 9.20.
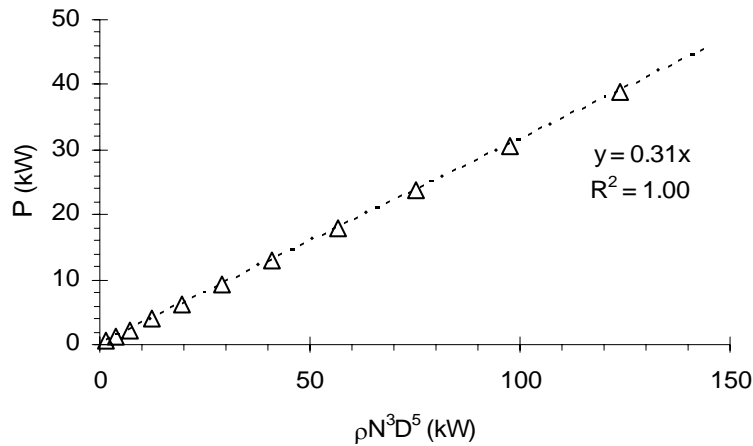
Figure 9.20. Prediction of the power input via the torque calculation for eleven rotation speeds (30 RPM < N < 130 RPM) for the industrial Beek reactor.

The results are fitted perfectly by a straight line passing through zero. The slope of the fitted line in Figure 9.20 corresponds to the agitator power number and its value is predicted numerically to be $\underline{N_p^{BEEK} = 0.31}$.

9.5.2.3. CFD predictions versus literature data

The power number value, relative to "Pfaudler type" impellers, vary over a wide range in the literature from one author to another, and this is mainly due to the different impeller models used, impeller geometries and baffling conditions. The literature results are summarized in Table 9.7.

Table 9.7. Literature survey of power numbers for Pfaudler-type impellers

Author(s)	D/T	w_b/D	θ	n_B	Baffle type	Re	N_p
Nagata (1975)	0.5	0.10	80 °	0	--	$\sim 10^5$	0.37
Nagata (1975)	0.5	0.10	80°	2	wall baffles	$\sim 10^5$	0.73
Koen (1977), reported in Dickey et al. (2004)	?	?	?	?	various partially baffling conditions	10^7	0.05 to 0.4
Pfaudler (1992)	0.72	0.15	--	0	--	10^5	~ 0.3
Verschuren *et al.* (2000)	0.6	0.29	10 °	1	?	1.4×10^4 - 10^5	0.64
Campolo and Soldati (2002)	0.57	0.125	--	2	beaver-tail	$2.4\ 10^6$	0.76
Campolo *et al.* (2002)	0.58	0.116	--	2	beaver-tail	$> 10^4$	0.697
Li et al. (2005)	0.59	0.195	15°	1	cylindrical	$> 10^4$	1.07
Reilly *et al.* (2007)	0.62	0.2	30°	4 1 1	wall baffles [*] wall baffle[*] beaver-tail[*] (*) flat base vessel	4×10^4 - 2×10^5	0.93 0.56 0.42
Our results	**0.51**	**0.121**	**15°**	**2**	**D-baffle**	**$> 10^6$**	**0.31**

The analysis of Table 9.7 reveals a wide range of turbulent power numbers for the Pfaudler type impellers from N_p = 0.05 (Dickey, 2004) to N_p = 1.07 for Li *et al.* (2005), due to various impeller geometry and baffling conditions with many unknown parameters. It must be noted that in the work of Li *et al.* (2005) the single baffle used was located much closer to the agitator than in our case, which may explain the high N_p value found by these authors. In contrast, the equipment used by Campolo *et al.* (2002) was closer to our industrial configuration. Although the ratio D/T was higher in their case and the retreat angle was not defined, the power number found was twice that of our result. The baffling effect provided by two D-baffles is assumed to be greater then for two beaver-tail baffles, so it would be expected to give a higher power number than our results. The low value found in our results may be linked to the special configuration of the vessel studied. The bottom of the baffles is located relatively high up in the tank from the impeller. The baffling conditions "observed by the impeller" in the bottom tank may be comparable with unbaffled conditions, leading to a low value of the power number. Dickey et al. (2004), who have studied a mixing vessel equipped with a retreat curve impeller and a single h-type baffle, both experimentally by PIV and numerically using CFD. Their PIV results showed that, in the impeller region, there is almost no difference in fluid velocities by using one or no baffle. The results showed only a significant direction change above the level of the lower tip of the baffle. Finally, they conclude that "at a level slightly above the impeller and below the baffles, the velocities with and without a baffle are so similar that they are indistinguishable". Dickey's results and observations could explain why the power number found in our study is relatively low.

9.5.2.4. CFD predictions versus experimental data

The power input predicted using the Beek agitator power number ($P = N_p^{BEEK}\rho N^3 D^5$) was compared with the experimental data of Table 9.6 for the two agitator rotation speeds. The results of the comparison are shown in Table 9.8.

Table 9.8. Comparison between experimental and numerical power input for the Beek industrial reactor.

	Agitator speed N_1 ($Re = 5.9 \times 10^6$)	Agitator speed N_2 ($Re = 6.6 \times 10^6$)
Experimental	$\Delta P_1 = 34 - 7 = 27 \pm 3$ kW	$\Delta P_2 = 40 - 7 = 33 \pm 3$ kW
CFD	$P_{CFD}^{BEEK}(N_1) = 27.3$ kW	$P_{CFD}^{BEEK}(N_2) = 38.4$ kW

The CFD predictions agree very well with the experimental power input. As a difference of 6% is observed for the higher velocity, it is assumed that the method is reliable with a precision of less than 10%.

9.6. PUMPING CAPACITY AND PUMPING NUMBER OF THE AGITATORS

The pumping capacity is a measure of the flow rate that crosses the impeller plane and this is a crucial variable in evaluation the circulation in the stirred vessel. Such data are fundamental for numerous applications (e.g. solid suspension, homogenization, etc.) and scale-up.

The dimensionless pumping number N_q of the impeller is defined as Eq. (9.2):

$$N_q = \frac{Q_p}{ND^3} \tag{9.2}$$

To calculate this characteristic number for each industrial impeller, the pumping flow rate was estimated using CFD. The reactor model without the top head was used, together with a single phase flow model, the Multiple Reference Frame approach and steady-state conditions were assumed. The pumping flow rate has been calculated in a control volume built surrounding the agitator. Figures 9.21(a) and (b) show the control volume used for the Mazingarbe reactor.
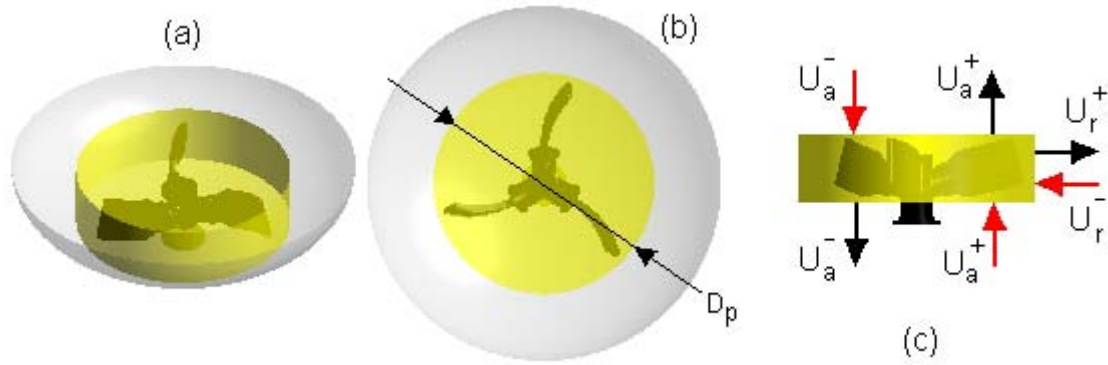
Figure 9.21 Surfaces used in the calculation of the pumping number for the Mazingarbe reactor: (a) 3D view; (b) top view; (c) flow details for the calculation of the pumping flow rate (inflow: red arrows, outflow: black arrows).

Three surfaces have been considered for the control volume used to estimate the pumping flow rate: the top of the disk, the bottom of the disk and the lateral circumferential surface. The calculation of each elementary flow rate has been done by a surface integration of the axial velocity component for the horizontal surfaces and the radial velocity component for the lateral surface as expressed in Eq. (9.3) and Eq. (9.4). For our calculations, the maximum deviation between the total inflow and the outflow was 0.6%. Whilst this difference is extremely small, the pumping flow rate was calculated using the arithmetic average of the two fluxes through the surfaces as expressed in Eq. (9.5).

$$Q_p^{in} = \int_A U_a^+ dA_{bottom} + \int_A U_a^- dA_{top} + \int_A U_r^+ dA_{lat} \tag{9.3}$$

$$Q_p^{out} = \int_A U_a^- dA_{bottom} + \int_A U_a^+ dA_{top} + \int_A U_r^- dA_{lat} \tag{9.4}$$

$$Q_p = \frac{Q_p^{in} + Q_p^{out}}{2} \tag{9.5}$$

The calculation has been performed for 8 agitator rotation speeds for the Mazingarbe reactor (from 30 to 100 RPM) and for 11 rotation speeds for the Beek reactor (form 30 to 130 RPM). Figure 9.20 shows our results plotted as $Q_p = f(ND^3)$, D being the diameter of the agitator and N the agitator speed.
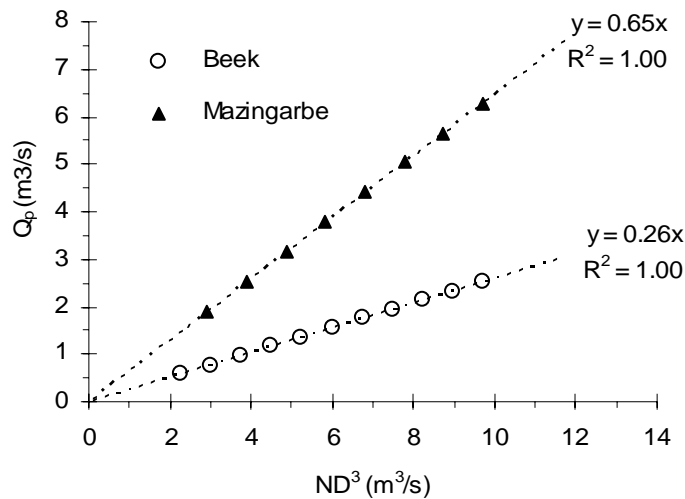
Figure 9.20. Numerical predictions of the pumping flow rate versus ND^3 for the industrial reactors of Mazingarbe and Beek.

The results are fitted perfectly by a straight lines passing through zero for the two industrial agitators. The slope of the fitted lines corresponds to the agitator pumping number N_q. The value is predicted numerically to be $N_q^{MZG} = 0.65$ and $N_q^{BEEK} = 0.26$. Concerning the agitator at Mazingarbe, no data have been published to date. Concerning the Beek reactor, the various configurations and impeller models named as "Paudler-type impellers" used in various research work make the comparison difficult (already discussed in §9.5.2.3). For example, Nagata (1975) found values of N_q equal to 0.23 and 0.29 with no baffles and with two plates baffles respectively (note than the Nagata's power number for the same impeller disagreed with our previous results of N_p, as discussed in §9.5.2.3); Li *et al.* (2005) predicted 0.55, 0.53 and 0.44 for this impeller-type in vessels of volume 0.5, 2 and 20 litres, respectively (for details, see Table 9.7). Therefore, it is very difficult to compare our value of the agitator pumping number (or power numbers) with the literature data, since important differences exist between our case and those tested by others.

9.7. CONCLUSIONS

Hydrodynamic studies were carried out using CFD for the industrial S-PVC reactors of Mazingarbe and Beek. For the Mazingarbe reactor, two different beaver-tail baffle configurations were studied (giving the maximum and minimum perturbation to the flow). For

the Beek reactor, the baffling configuration was two D-baffles used in the minimum perturbation configuration. The general flow patterns were found to be comparable with the three configurations tested. In contrast, due to different baffling conditions, the vortex shapes were found to be relatively different. The Mazingarbe reactor, with the baffles giving the maximum perturbation develops a bulb-shape asymmetrical vortex shape close to that observed in the pilot reactor. With the baffles in the minimum perturbation, the vortex was found to be wider, deeper, more symmetric and closer to the usual vortex shape classically observed for unbaffled vessels. Finally, the free-surface deformation predicted for the Beek reactor is the weakest due to the significant baffling effect of the D-baffles.

The numerically predicted power numbers for the industrial reactor at Mazingarbe are in good agreement with the experimental data obtained from the plant and with those obtained previously for the pilot reactor. This good agreement of our results provides confidence in the value of the power numbers of the industrial agitator at Mazingarbe. For the Beek reactor, although no data were available at the pilot scale, the CFD predictions of the power input were in good agreement (precision 10%) with experimental data obtained at two different rotation speeds. Agitator pumping numbers were determined using CFD for the two standard reactors configurations as laboratory studies (e.g. PIV) were not possible. Very few literature data concerning the "Pfaudler-type" impellers are available compared with other impellers and these data are very difficult to use for comparison due to important differences which exist, such as the exact impeller models used and the baffling conditions. Our results for N_p and N_q values are summarized in Table 9.9 for the industrial reactors of Mazingarbe and Beek.

Table 9.9. Summary of power numbers of industrial agitators

Reactor	Baffling conditions	N_p	N_q
Mazingarbe	2 beaver-tail in max. perturbation configuration	$N_p^{MZG, MAX} = 1.50$	$N_q^{MZG} = 0.65$
Mazingarbe	2 beaver-tail in min. perturbation configuration	$N_p^{MZG, MIN} = 1.11$	---
Beek	2 D-baffles	$N_p^{BEEK} = 0.31$	$N_q^{BEEK} = 0.26$

Chapter 10

APPLICATION TO S-PVC SYNTHESIS REACTORS - PART 2:

JET INJECTION, QUENCHING STUDIES AND SCALE-UP

The highest level of process safety has to be reached in chemical plants to guarantee the protection of people, the environment and to avoid equipment damage. The question addressed here is: how can we achieve better quenching of the industrial S-PVC synthesis reactors of Tessenderlo Group? This Chapter follows the hydrodynamic study of these reactors presented in Chapter 9 which has given a solid basis and the fundamental elements to begin jet injection and quenching studies. The CFD strategy developed for the pilot reactor in Chapter 8 and in Torré *et al.* (2008) (Lagrangian jet tracking, passive scaler mixing and quenching curves) is used here to analyse and quantify the current jet injection conditions for the Mazingarbe industrial reactors. Several jet injection conditions are investigated with two different rotation speeds to analyse the quenching efficiency and to determine the best injection conditions regarding the parameters tested (named optimized jet velocity). Finally, a scale-up strategy is proposed to predict the optimized jet velocity based on the results obtained in the pilot reactor.

10.1. INDUSTRIAL KILLER SYSTEM

10.1.1. Industrial system

The system used to quench runaway conditions fitted to the Mazingarbe industrial S-PVC synthesis reactors, is named the "killer system" and is presented in Figure 10.1(a). The "killer" agent is contained in a "killer vessel" mounted on the top head of the synthesis reactor and is isolated from the reactor by a rupture disk. Note that plunging pipes are never used in PVC synthesis reactors due to the risks of pipe clogging associated with the polymerization of VCM monomer into the pipes. 90% of the volume of the killer vessel is filled by the killer agent and its top head is open to a Nitrogen line used for pressurization. This line, in normal

synthesis conditions, is shut by the automatic valve XV. Upstream of this valve a nitrogen bottle and an intermediate vessel are set to have a pressure of nitrogen of around 80 bars (the equilibrium pressure resulting from linking a new nitrogen bottle and an intermediate vessel at atmospheric pressure).
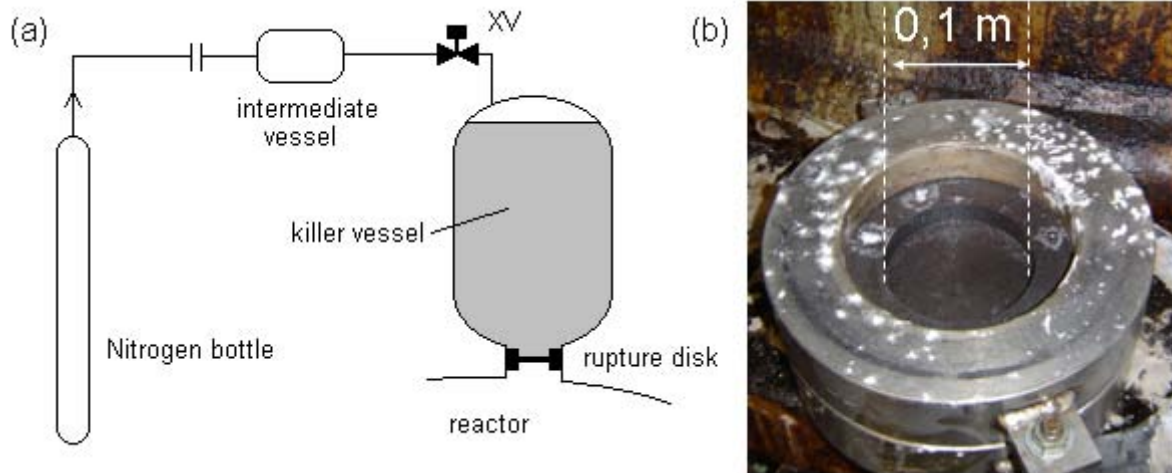
Figure 10.1. Industrial killer system for Mazingarbe reactors. (a) schematic of the installation; (b) picture of the carbon rupture disk.

When the runaway reaction has to be quenched, the automatic valve XV is opened, allowing the nitrogen to flow into the killer vessel and thus increase the pressure inside it. When the pressure acting on the rupture disk located at the bottom of killer vessel becomes higher than its bursting pressure, the rupture disk bursts and the killer agent is drained into the reactor. The intermediate vessel allows sufficient pressure energy to develop to burst the rupture disk within a second after the automatic valve opens. The rupture disk is a carbon model with total fragmentation allowing a clean and direct passage of 0.1 m diameter for the killer agent, as shown in Figure 10.1(b).

On one hand, experiments have demonstrated that the inside of the synthesis reactor is in contact with the killer agent quasi-instantaneously as the rupture disk bursts immediately (< 1 s) after the killer vessel is pressurised. In contrast, some important questions remained open as concerning how the killer is mixed, how much time it needs to achieve a *sufficient degree of mixing*, how deep is the killer jet penetration?

10.1.2. **Current injections conditions**

Experiments have been carried out on an industrial reactor at the Mazingarbe plant to estimate the current killer jet velocity, and to know if it is worth improving the actual killer system. The killer vessel was filled with water instead of the killer agent and the reactor was pressurised with nitrogen to be closer to real quenching conditions. Two safety-glass windows mounted on flanges on the top of the industrial reactor head allowed installation of a video-camera and a light source in order to: (i) visualize the shape of the jet; and (ii) to measure the draining time. A video of the experiment was made to allow further analysis. The jet has clearly been shown not to be a spray and looked like a round coherent jet for up to half of the total reactor height. The draining time, measured directly by watching the video by two different people with a stop watch, was defined to be the time from the rupture disk bursting to the instant when the liquid draining finished. Details of the experiment and results are summarized in Table 10.1.

Table 10.1. Details of the experiment performed to determine the current jet velocity for the Mazingarbe industrial reactors.

Description	Information
date	15/01/05
location	Mazingarbe
reactor	# 15
reactor pressure	8.7 bars
N_2 equilibrium pressure in the intermediate vessel	86.7 bars
time to burst the rupture disk	< 1 s
drainage time	15 s

The mean velocity, V_o, is calculated as the ratio of the initial killer volume to the product of the draining time multiplied by the rupture disk surface area. This calculation leads to consideration of the case of a constant velocity during the draining. For 0.183 m^3 of water introduced in the killer vessel and an effective rupture disk surface of 7.85×10^{-3} m² (rupture disk effective diameter of 0.1 m, as shown in Figure 10.1(b)), the calculation gave a mean jet velocity equal to 1.55 m/s.

The maximum jet velocity is obtained just after the bursting of the rupture disk due to the highest pressure and the maximum water height inside the killer vessel (even if the water height has a small influence compared with the pressure). If the system function is ideal, the

nitrogen flow must be sufficient to compensate for the decrease of pressure resulting from the decrease of the liquid level in the killer vessel. Otherwise, the pressure difference between the top head of the killer vessel and the reactor may decrease during the draining period and the jet velocity is also lower. Therefore, it is clearly a significant assumption to consider a constant jet velocity for this industrial experiment. Nevertheless, this estimation obtained in pressurised conditions close to the real quenching conditions (both the killer system and the reactor), was the best could be achieved. The theoretical calculation of the outlet jet velocity was considered to be outside of the scope of this study, regarding the complexity of modelling the entire hydraulic system. Therefore, in the following calculations and analysis it was set:

$$V_o = 1.55 \text{ m s}^{-1}$$

10.2. CFD STUDY

The geometry of the Mazingarbe reactor, equipped with baffles resulting in large flow perturbations, used in these jet studies was described previously in §9.1 of Chapter 9. The modelling of the jet injection in the industrial reactor was performed with exactly the same CFD method as that described in §8.2 of Chapter 8 for the pilot agitated vessel. Therefore, the details of the geometry, the governing equations, and the jet simulation strategy are not repeated here.

The injection point was maintained at the current industrial injection location. The main reasons are: (i) this injection point has proved to be a good location as explained in Chapter 7; (ii) in this type of reactors, the space on the top reactor head is very limited (reinforcements of the baffles, feeding pipes and vessels or raw materials). The coordinates of the injection point are $X_j = -658$ mm and $Z_j = 906$ mm and this injection point is in exact geometrical similarity with the injection point in the pilot reactor named "Initial" in Chapter 7. The mesh was refined in a region below the jet injection point descending to 3.5 m below the inlet surface to ensure the accurate capture of the jet trajectory. The value of 3.5 m corresponds to the length of the line control set in the pilot reactor multiplied by the scale-up factor. The unstructured grid used, which comprised of a total number of elements equal to 1,615,900, is shown in Figure 10.2.
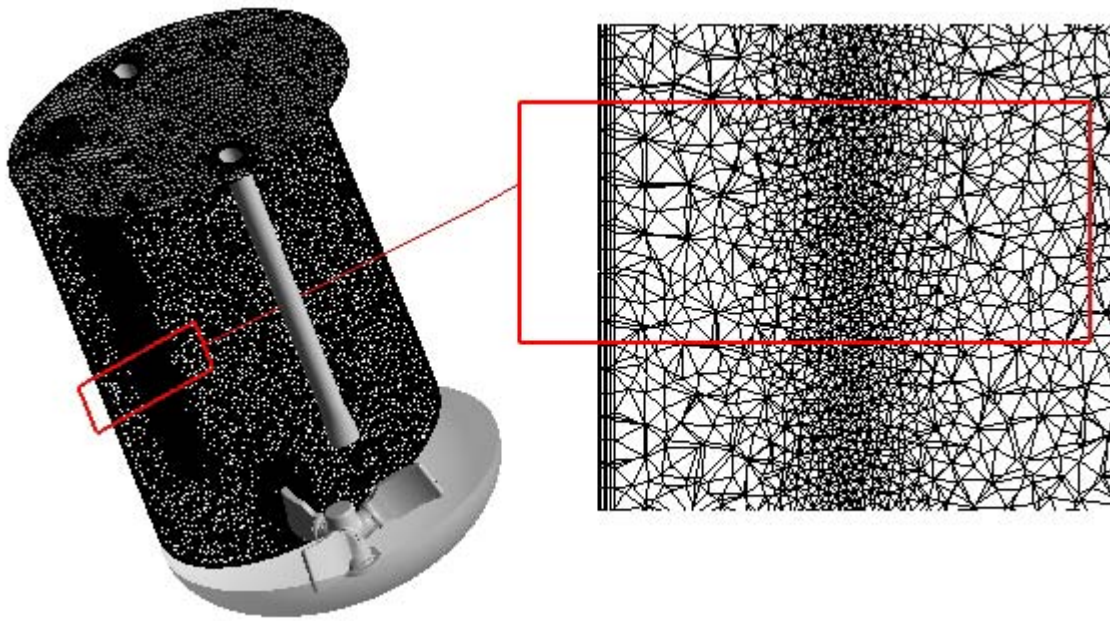
Figure 10.2. Details of the mesh used for the CFD simulations of the Mazingarbe industrial reactor on a vertical plane passing through the centre of the injection surface

For the pilot jet injections studies, the agitator rotation speeds were set such that the free-surface was quasi-flat. In contrast, the simulation of the industrial case implied setting the agitator speed to that used in the PVC process. To carry out the jet injection studies for the industrial vessel, we were constrained to consider the top free-surface as flat because, as to the best of our knowledge of this problem, the way to inject a momentum-driven jet onto a deformed free-surface was not operational at time this work was performed. A new way of thinking about the simulation of mixing vessels with a deformed free-surface has been developed and is presented briefly as a perspective to this work in Chapter 12. The author is aware of the significant assumption made since it was demonstrated previously in Chapter 9 that the free-surface shape is strongly deformed at the agitator speed set in normal process conditions giving $Re = 5.0 \times 10^6$ (nominal agitator speed). Therefore, in addition to the studies carried out with the nominal agitator speed, a case-study with half of the nominal speed was investigated ($Re = 2.5 \times 10^6$). This last condition may represent what would happen when the killer has to be introduced after the agitator begins to slow down due to a breakdown of the process (e.g. power failure). As discussed previously in Chapter 6, the analogy is not perfect, due to the inertial effects during the agitator stopping phase. Nevertheless, the agitator velocity which would corresponds to a constant Froude number ($Fr = ND^2/g$), equal to 8.57×10^{-2}, lead to an agitator velocity of 108 RPM, a value which has been shown to give a

quasi-flat free-surface. If, in the first approach, we consider that a comparable free-surface shape is obtained for the same Froude number, we can justify the assumption of flat free-surface when the industrial agitator speed is set to half the nominal value.

The different jet velocities investigated are chosen as multiples of the current injection velocity V_o. Thus, four jet velocities ($V = V_o$, $5V_o$, $10V_o$ and $20V_o$) have been tested for each agitator speed giving a total of eight simulations for this study. The properties of the agitated fluid and the injected killer were kept at the same values as used in previous studies with the pilot reactor (water at 25°C with $\rho = 997$ kg m^3 and $\mu = 8.9 \times 10^{-4}$ Pa.s).

10.3. JET INJECTION PROFILES AND REACTOR QUENCHING

Figures 10.3, 10.4, 10.5 and 10.6 shows the path of the jets obtained from the simulation of the industrial reactor of Mazingarbe for half of the nominal agitator speed and for jet velocities equal to V_o (current injections conditions), $5V_o$, $10V_o$ and $20V_o$, respectively. The other jet profiles obtained for the nominal agitator speed are presented in Appendix D.

The jet trajectories are shown using the tracks of the Lagrangian particles at different times during the injection. Therefore, 120, 240, 360, 480 and 600 Lagrangian particles have been used to visualize the jet trajectory at the times $0.2T_{inj}$, $0.4T_{inj}$, $0.6T_{inj}$, $0.8T_{inj}$ and T_{inj}, respectively. In addition, the killer mixing was followed via the tracking of a concentration of a transported scalar variable C, as defined previously in Chapter 8 for the pilot reactor. The values of the equilibrium concentration C_{inf}, and of the minimum concentration C_{min} necessary to quench the reaction are the same than those used in Chapter 8, as the values used previously were based on the real industrial data presented here. The minimum concentration results from the mixing of 8 litres of killer agent in the whole vessel volume. This quantity has proved to be sufficient to stop a polymerization in normal agitation conditions. Figure 10.7 shows the evolution with time of the reactor quenching volume which results from the different jet injections conditions. The reader is reminded that the t_{50} and the t_{90} are the times necessary to quench 50% and 90% of the reactor volume, respectively.
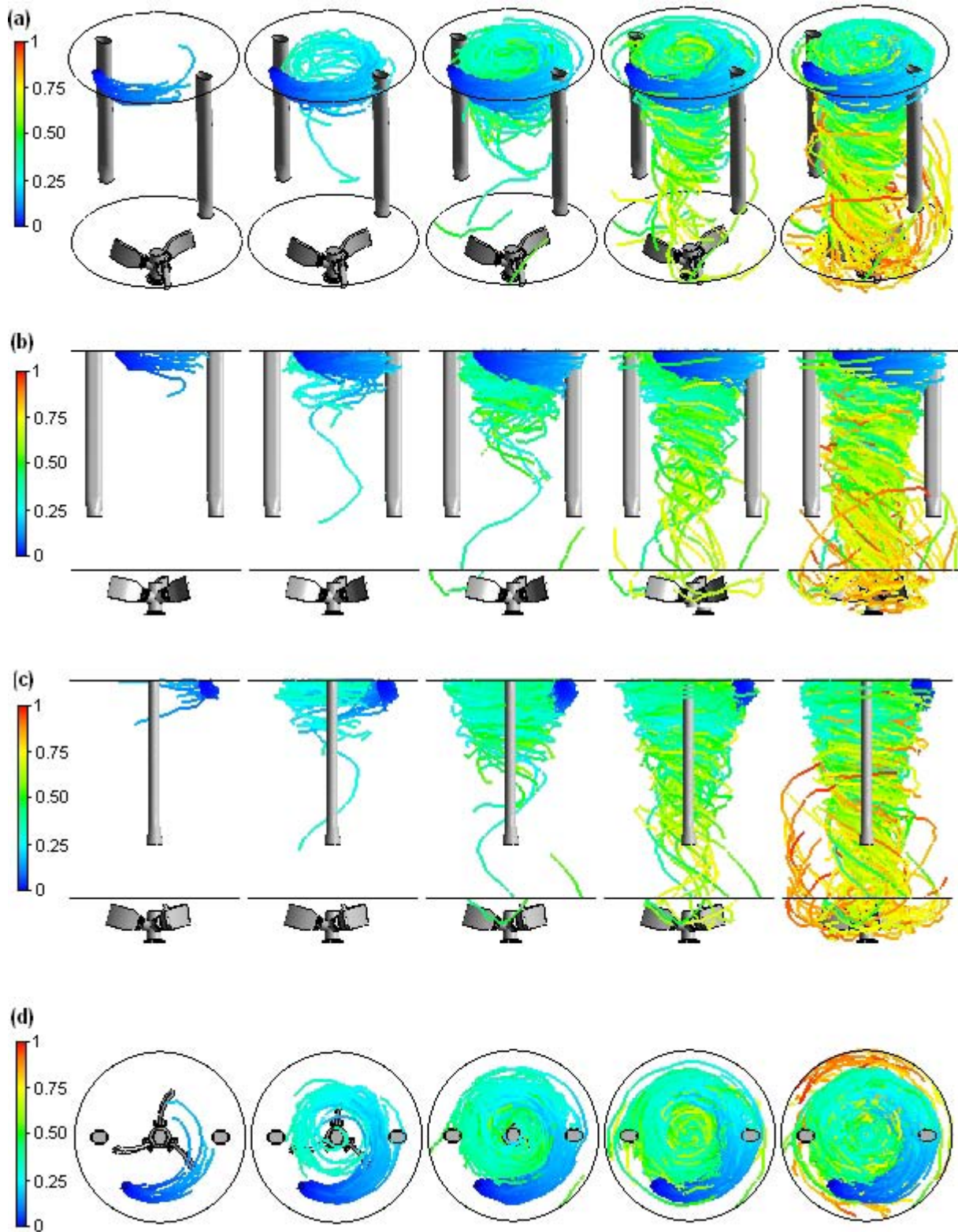
Figure 10.3. Lagrangian jet trajectories coloured by the Lagrangian particle travel time normalized by T_{inj}, for d = 0.1 m, $V = V_o = 1.55$ m s^{-1} (current injection conditions) and Re = 2.5×10^6, plotted at $0.2T_{inj}$, $0.4T_{inj}$, $0.6T_{inj}$, $0.8T_{inj}$ and T_{inj}. (a) 3D view; (b) XY lateral view; (c) YZ lateral view; (d) top view.
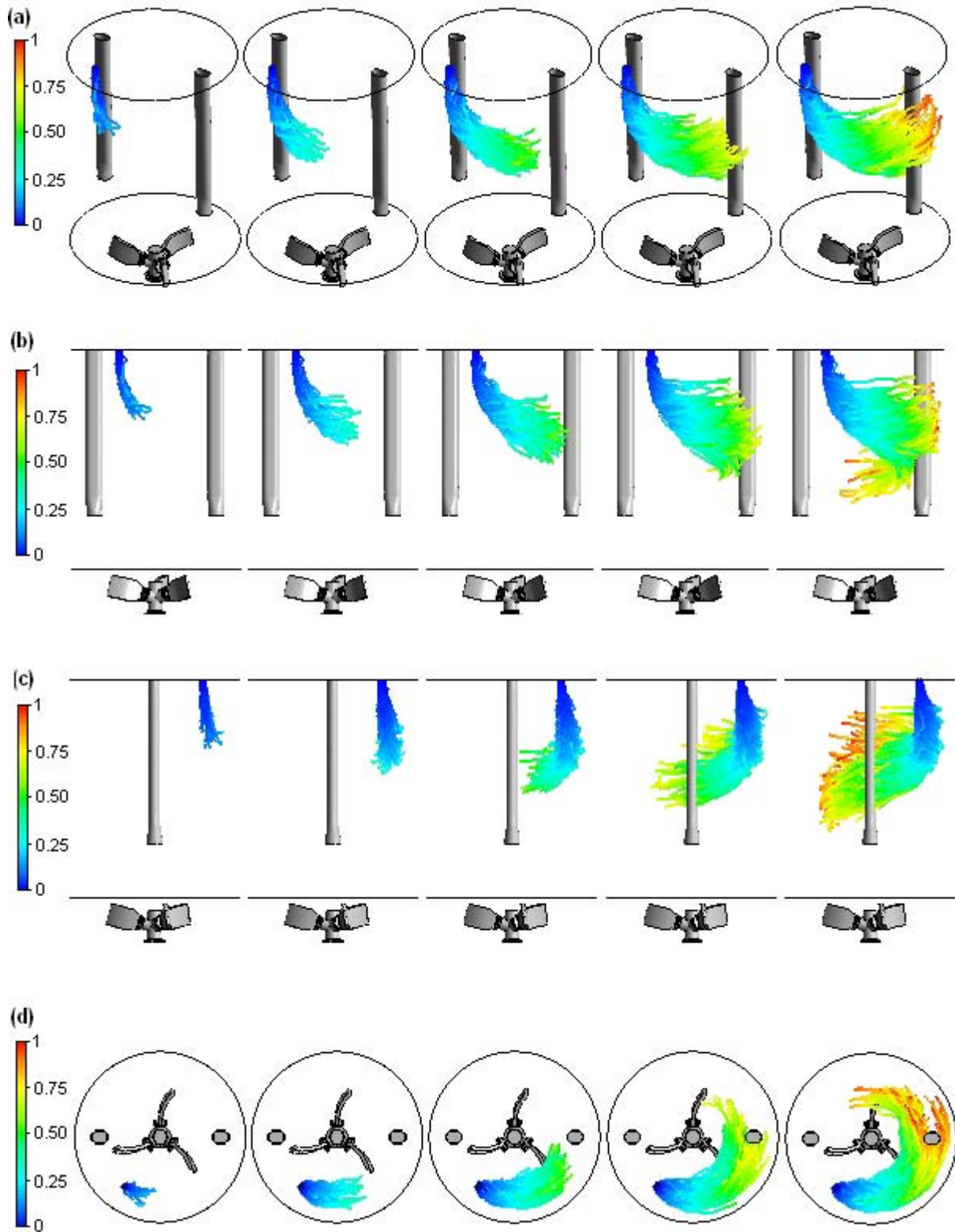
Figure 10.4. Lagrangian jet trajectories coloured by the Lagrangian particle travel time normalized by T_{inj}, for d = 0.1 m, V = $5V_o$ = 7.75 m s^{-1} and Re = 2.5×10^6, plotted at $0.2T_{inj}$, $0.4T_{inj}$, $0.6T_{inj}$, $0.8T_{inj}$ and T_{inj}. (a) 3D view; (b) XY lateral view; (c) YZ lateral view; (d) top view.
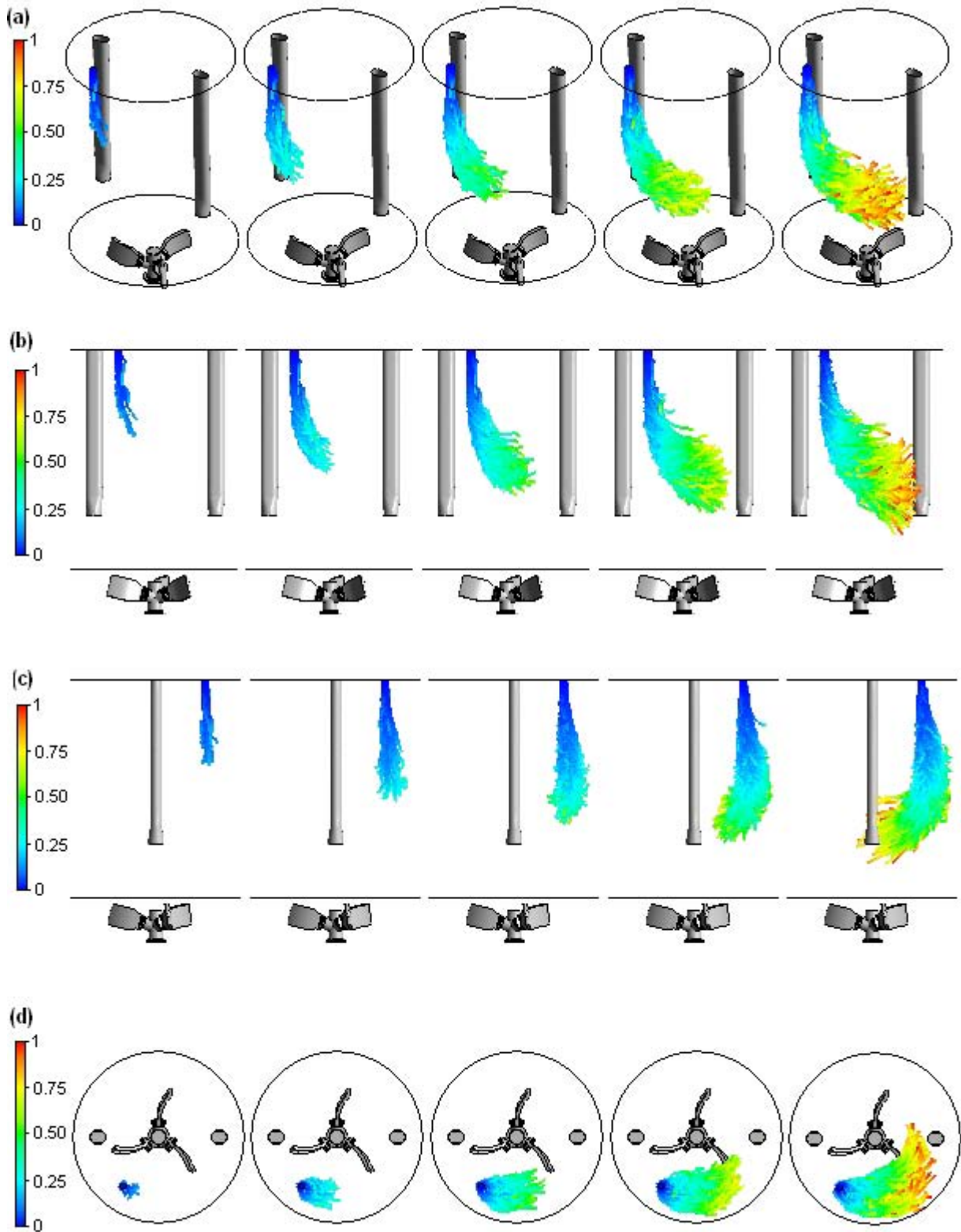
Figure 10.5. Lagrangian jet trajectories coloured by the Lagrangian particle travel time normalized by T_{inj}, for d = 0.1 m, V = $10V_o$ = 15.5 m s^{-1} and Re = 2.5×10^6, plotted at $0.2T_{inj}$, $0.4T_{inj}$, $0.6T_{inj}$, $0.8T_{inj}$ and T_{inj}. (a) 3D view; (b) XY lateral view; (c) YZ lateral view; (d) top view.
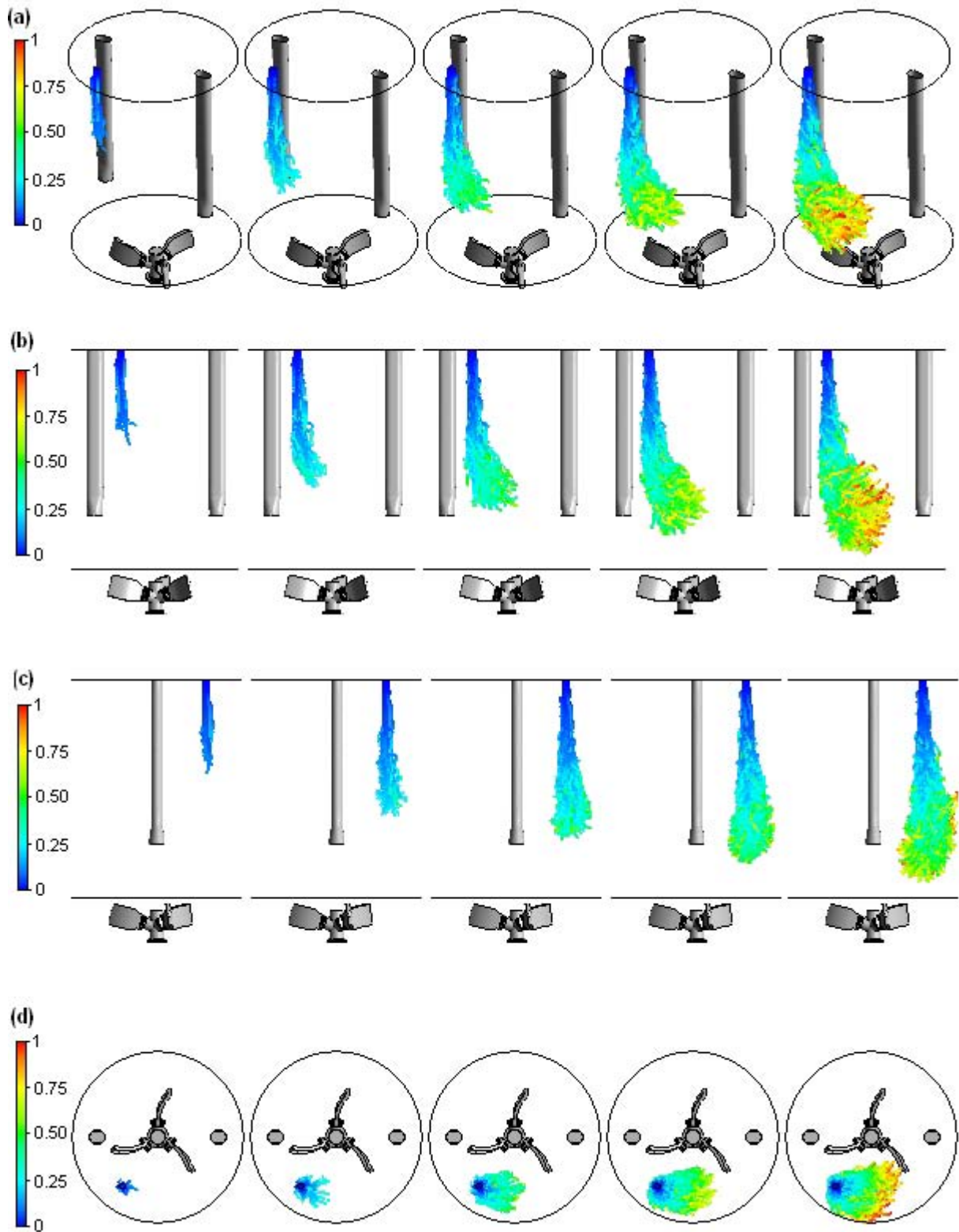
Figure 10.6. Lagrangian jet trajectories coloured by the Lagrangian particle travel time normalized by T_{inj}, for d = 0.1 m, V = 20V$_o$ = 31 m s^{-1} and Re = 2.5×10^6, plotted at 0.2T_{inj}, 0.4T_{inj}, 0.6T_{inj}, 0.8T_{inj} and T_{inj}. (a) 3D view; (b) XY lateral view; (c) YZ lateral view; (d) top view.
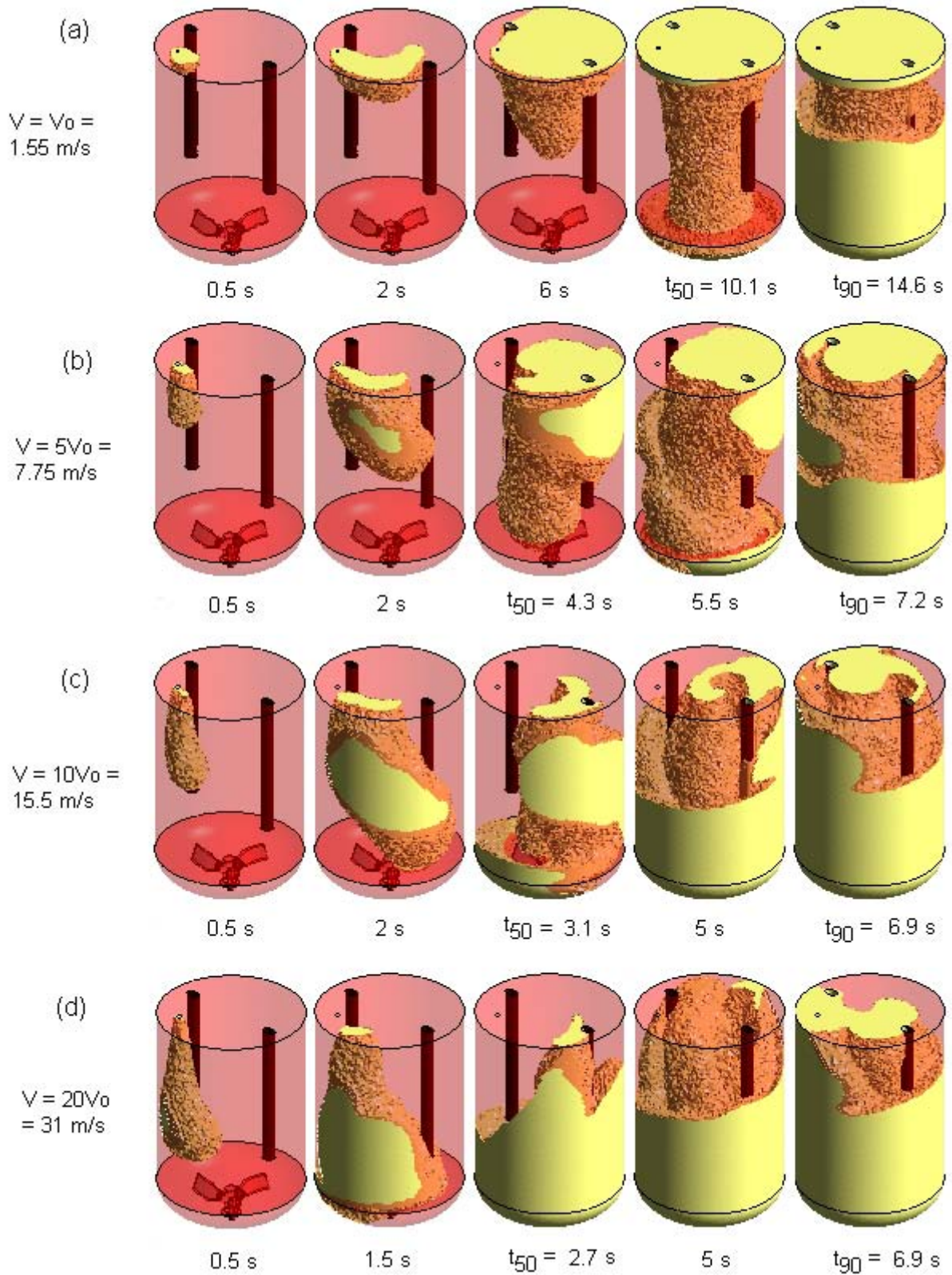
Figure 10.7. Evolution of the reactor quenched volume versus time with different jet injection velocities for half of the nominal agitator speed: (a) $V_o = 1.55$ m s^{-1}; (b) $V = 7.75$ m s^{-1}; (c) $V = 15.5$ m s^{-1}; (d) $V = 31$ m s^{-1}.

Figure 10.3 shows very clearly how the jet penetrates the bulk using the current injection conditions. A very weak downward jet penetration is predicted, leading to an immediate bending of the jet plume and that is very close to the free-surface due to the combined effects of the high tangential movement of the stirred fluid in this region and the weak jet momentum flux. From these injection conditions, the injected fluid is constrained to follow the tangential bulk flow, leading to very rapid entrapment by the central vessel swirling region. It was previously discussed in Chapter 8 that this type of injection is not favourable for efficient mixing. When the injected fluid is trapped by the central swirling flow, it flows downward in the centre of the vessel following the high streamline curvature which develops near the vessel axis. This swirling movement has proved to be one of the worse situations to mix the killer efficiently in the reactor. The reactor quenching which results from the current injection conditions is presented in Figure 10.7(a). It is shown that the top of the reactor is the first to be quenched, after the region close to the vessel axis is quenched, and finally the stopper is pulled out radially from the agitator and flows upwards in the region close to the vessel shell.

The jet profiles resulting from the injection conditions shown in Figures 10.4 and 10.5 gave a more efficient killer mixing into the reactor as shown very clearly in Figures 10.7(b) and (c). The initial killer jet separates itself into an upward flow which can quench the upper part of the reactor and a downward flow which follows the central fluid motion which goes though the agitator and quenches the lower part of the reactor. Thus, the killer is distributed in the entire vessel in an efficient way.

Figure 10.6 shows the jet resulting from the highest injection velocity tested. This condition lead to very good jet penetration into the vessel but lead also to the entire killer volume being injected into the vessel bottom. This type of injection has proved previously not to be efficient because the top part of the vessel takes a long time to be quenched. Therefore, as already pointed out in Chapter 8, the better injection conditions are not synonymous with the highest jet velocity and the system can be optimized to maximize the benefits of the flow pattern present in the vessel. The term "optimized" has not to be understood as the result of a real optimization problem, where a multi-variable analysis allows maximization or minimization of a response depending on several possible factors. In the industrial application presented in this Chapter, the injection location and the jet diameter were fixed, and the optimization refers only to the jet velocity. The result of this analysis was named the optimized jet velocity. The quenching curves (percentage of quenched reactor volume versus

time) are given in Figures 10.8(a) and (b) for the four jet velocities tested at the two agitator speeds. The data for t_{50} and t_{90} are summarized in Tables 10.2 and 10.3, for half of the nominal agitator speed and for the nominal speed, respectively.
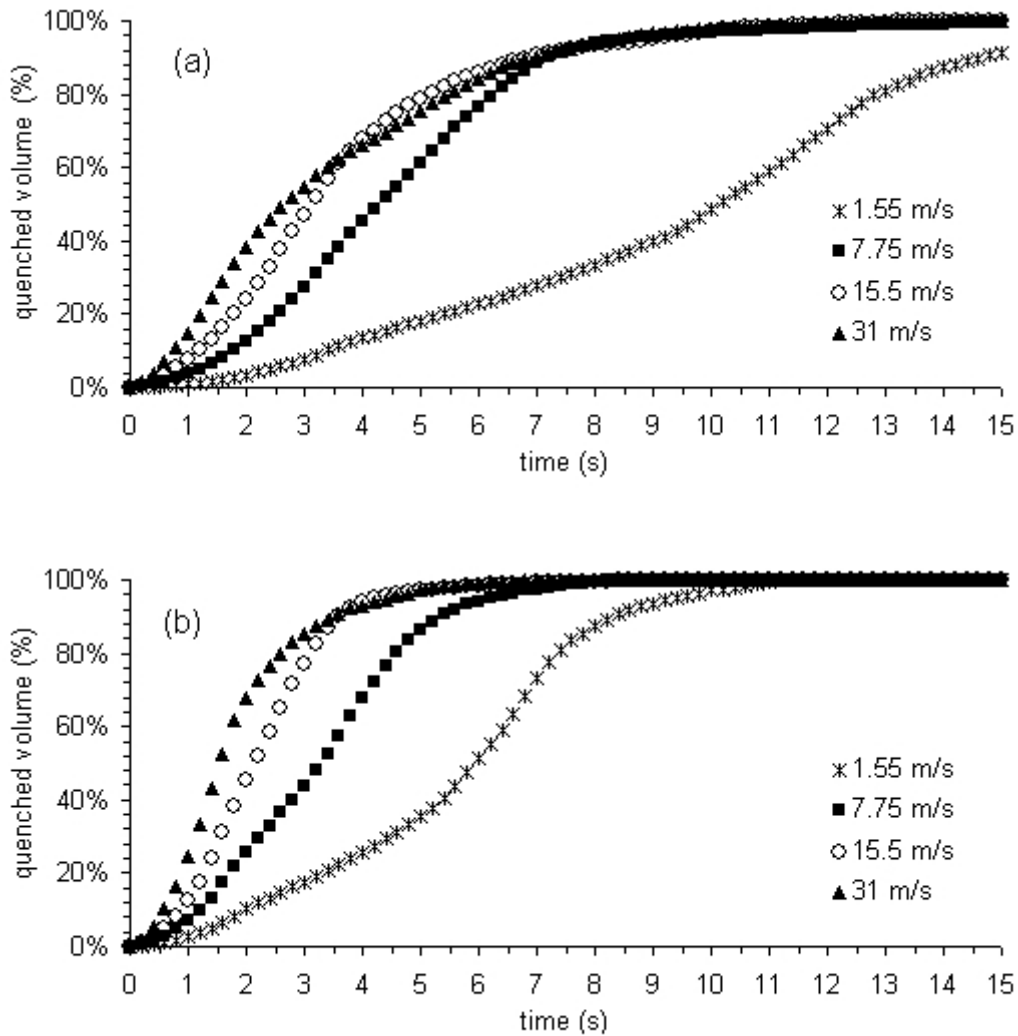
Figure 10.8. Quenching curves from the modelling of the industrial reactor at Mazingarbe for different jet velocities ($V_o = 1.55$ m/s): (a) half of the nominal agitator speed; (b) nominal agitator speed.

Table 10.2. t_{50} and t_{90} for half of the nominal agitator speed.

V (m/s)	V/V$_o$	t_{50} (s)	t_{90} (s)	t_{50}/t_{50o}	t_{90}/t_{90o}
1.55	1	10.14	14.65	1.00	1.00
7.75	5	4.29	7.22	0.42	0.49
15.5	10	3.12	6.88	0.31	0.47
31	20	2.66	6.92	0.26	0.47

Table 10.3. t_{50} and t_{90} for the nominal agitator speed.

V (m/s)	V/V$_o$	t_{50} (s)	t_{90} (s)	t_{50}/t_{50o}	t_{90}/t_{90o}
1.55	1	5.93	8.35	1.00	1.00
7.75	5	3.29	5.35	0.56	0.64
15.5	10	2.14	3.58	0.36	0.43
31	20	1.54	3.49	0.26	0.42

This quantitative analysis of the time necessary to quench a given percentage of the vessel volume confirms the conclusion deduced from the analysis of Figure 10.7. The quenching curves shown in Figure 10.8(a) obtained for half of the nominal agitator velocity shows that the time to quench 90% of the reactor volume is greatly reduced by increasing the jet velocity from V_o to $5V_o$. As detailed in Table 10.2, increasing the jet velocity by a factor 5 compared with the current conditions would reduce the time to quench 90% of the reactor volume by a factor of two.

Concerning the same analysis performed at the nominal velocity, the macro-mixing limitations are obviously lower if the agitator rotation speed is increased, and the optimized jet velocity was expected to be higher. This is confirmed by the quenching curves of Figure 10.8(b) and the data of Table 10.3. The effects of the jet velocity are more evident if compared with the previous results obtained when the agitator velocity was half of the nominal value. In this case, the optimized jet velocity was found to be $10V_o$, as a higher jet velocity does not reduce the value of t_{90}. Since increasing the current velocity by a factor of 5 lead to a reduction of the value of t_{90} by 36%, the optimized jet velocity is reached for V = $10V_o$, where the value of t_{90} is reduced by 57% compared with the current injection conditions.

Regarding the two cases tested, it is obvious that the optimized value of the jet velocity depends on the agitator rotation speed due to the macro-mixing phenomena. The higher the agitator speed, the lower the jet velocity required to reach the plateau in t_{90}. Figure 10.9 shows the gain obtained by increasing the jet injection velocity on the t_{50} and t_{90}.
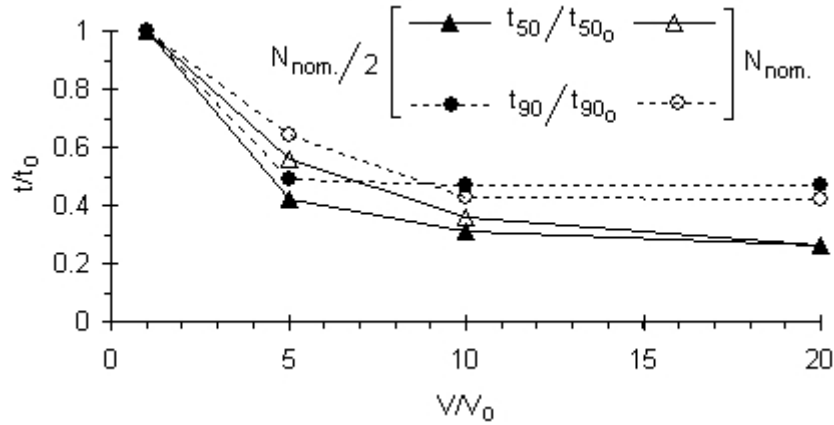
Figure 10.9. Influence of the jet velocity on t_{50} and t_{90}, for the two agitation speeds tested, and for jet velocities equal to V_o, $5V_o$, $10V_o$ and $20V_o$.

As previously discussed, the best choice to improve the industrial quenching system is to increase the jet velocity until the value of t_{90} becomes nearly constant. This condition is reached for a jet velocity equal to ten times and five times the current injection velocity, for the nominal and half of the nominal agitator speed, respectively. Based on the two cases studied, the value of the injection velocity that is ten times the current value was concluded to allow the best mixing of the killer into the reactor (jet diameter and jet injection position fixed):

$$V_{opt.} = 10V_o = 15.5 \text{ m/s.}$$

10.4. SCALE-UP OF THE OPTIMIZED INJECTION VELOCITY

In this paragraph, a scale-up criterion for t_{90} is proposed, denoted Ψ_{90}, and defined as the ratio of the tangential momentum flux, M_a, given by the agitator to the bulk fluid, and by the jet momentum flux M_j. Ψ_{90} is dimensionless.

The jet momentum flux is defined as $M_j = \rho_j A_j V^2$, where A_j is the jet cross section and V is the jet velocity.

$$\rightarrow M_j = \rho_j \left(\frac{\pi d^2}{4} \right) V^2 \text{ where d is the jet diameter} \tag{10.1}$$

The agitator tangential momentum flux can be defined as $M_a = \rho_a A_a V_{tip}^2$ where the surface A_b is the projected agitator blade surface (rectangle from the blade edge to the agitator axis), V_{tip} is the tip velocity (= $2\pi N R_a$). Figure 10.10 shows a schematic of an agitator blade and the dimensions used in the calculation of the projected agitator blade surface.
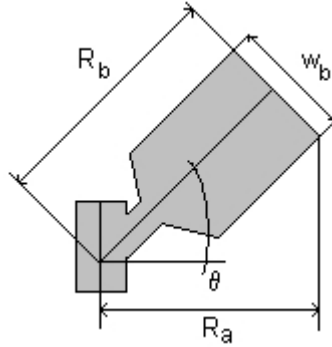
Figure 10.10. Details of an agitator blade for the calculation of A_a.

$$A_a = R_b \times w_b = \left(\frac{R_a}{\cos\theta} - \frac{w_b \tan\theta}{2} \right) w_b$$

$$M_a = \rho_a \left(\frac{R_a}{\cos\theta} - \frac{w_b \tan\theta}{2} \right) w_b \left(2\pi N R_a \right)^2$$

→   with $R_a = D/2$, we have: $M_a = \dfrac{\pi^2 \rho_a}{2} \left(\dfrac{D}{\cos\theta} - w_b \tan\theta \right) w_b D^2 N^2$ (10.2)

The ratio of Eq. (10.2) and Eq. (10.1) gives Eq. (10.3):

$$\Psi_{90} = \frac{\dfrac{\pi^2 \rho_a}{2} \left(\dfrac{D}{\cos\theta} - w_b \tan\theta \right) w_b D^2 N^2}{\rho_j \left(\dfrac{\pi d^2}{4} \right) V^2}$$ (10.3)

The pilot reactor and the industrial reactor are in perfect geometrical similarity with the scale-up factor F. Thus, each dimension L of the industrial vessel is equal to the corresponding dimension of the pilot reactor multiplied by F. If the subscripts "ind" and "lab" are used for the industrial and the pilot reactor respectively, we have:

$$L_{ind} = F \times L_{lab}$$ (10.4)

Using Eq. (10.4), Eq. (10.3) can be rewritten as $D_{ind} = F \times D_{lab}$ and $w_{b,ind} = F \times w_{b,lab}$ and finally, the scale-up criterion Ψ_{90} is given by Eq. (10.5):

$$\Psi_{90} = \frac{M_a}{M_j} = \frac{\dfrac{\pi^2 \rho_a}{2}\left(\dfrac{D_{lab}}{\cos\theta} - w_{b,lab}\tan\theta\right)w_{b,lab}D_{lab}^2 N^2 F^4}{\rho_j\left(\dfrac{\pi d^2}{4}\right)V^2} \tag{10.5}$$

The proposed method is to find the jet momentum flux for the industrial reactor ($M_{j,lab}$) by using results obtained with the pilot reactor. It was shown in Chapter 8 that the optimum jet momentum flux at N = 100 RPM is 1.5 kg m s^{-2} in the pilot reactor. For the pilot reactor, the factor F is equal to 1.

Using Eq (10.2), we have:

$$M_{a,lab} = \left(\frac{\pi^2 997}{2}\right)\left(\frac{0.26}{\cos(15°)} - (58\times10^{-3})\tan(15°)\right)(58\times10^{-3})0.26^2\left(\frac{100}{60}\right)^2 = 13.59 \text{ kg m s}^{-2}$$

Combined with the optimal momentum flux of $M_{j,lab}$ = 1.5 kg m s^{-1}, Ψ_{90} becomes:

$$\rightarrow \Psi_{90} = \frac{13.59}{1.5} = 9.06$$

Using this value it should be possible to find the optimum jet momentum flux for the industrial reactor by Eq (10.6):

$$\Psi_{90} = \frac{M_{a,lab}}{M_{j,lab}} = \frac{M_{a,ind}}{M_{j,ind}} \tag{10.6}$$

Using Eq. (10.6), the theoretical jet momentum flux have been determined for the industrial reactor for the two agitator speed investigated (nominal speed and half of the nominal speed). The theoretical results can be compared with the conclusion of the CFD quenching study relative to the optimized injection velocity, which allows the maximum reduction of t_{90} previously detailed in §10.3. The results are presented in Table 10.4.

Table 10.4. Comparison between the optimized jet velocities predicted using the theoretical scale-up method and those obtained by analysis of the quenching curves presented in §10.3.

Agitator speed	from scale-up	from quenching curves
Half of the nominal speed	8.8 m s^{-1} = 5.7 Vo	7.75 m s^{-1} = 5 Vo
Nominal speed	17.6 m s^{-1} = 11.4 Vo	15.5 m s^{-1} = 10 Vo

The jet injection velocities found using the scale-up criterion are in reasonably good agreement with the results found independently from the quenching curve analysis. The author is aware that this scale-up analysis is very simplified, but the use of the scale-up criterion Ψ_{90} gives an acceptable value of the optimized jet velocity.

10.5. CONCLUSIONS

The quenching behaviour of the industrial synthesis reactors of the Mazingarbe PVC plant has been studied using CFD. Several jet velocities have been tested with the same injection diameter (rupture disk diameter) and a fixed injection location. The quenched reactor volume was characterized by a concentration of the killer agent above the minimum concentration necessary to quench the reaction in the whole reactor volume. The Lagrangian particle tracks which allowed visualization of the jet shape and demonstrate clearly that the current injection conditions provide a jet without sufficient penetration. The current injection conditions are characterized by an immediate bending of the jet plume close to the surface and an entrapment in the swirling region close to the vessel axis. This jet path leads to poor quenching of the reactor volume. In contrast, higher jet velocities allowed a more significant penetration into the bulk and showed higher quenching efficiencies. A jet velocity of ten times the actual injection velocity (15.5 m/s instead of 1.55 m/s) has been proposed as the optimized jet velocity value. This jet velocity optimizes the penetration, maximizing the benefits of the bulk flow patterns on the mixing of the killer. Finally, a scale-up method, based on the previous results obtained for the pilot reactor, allowed prediction of the optimized jet velocity with relatively good agreement with the industrial simulation results.

Chapter 11

A MODEL FOR THE JET TRAJECTORY AND PENETRATION DEPTH

This Chapter is devoted to the analysis of the jet trajectories, obtained using CFD, at two different scales (laboratory and industrial scales). One of the goals was to be able to describe how the jet penetrates the bulk of the fluid and to build an easy to use correlation for research and industrial purposes. A model of the jet trajectory based on an analogy with a jet in a cross-flow has been used to predict the jet trajectory for the pilot and industrial scales. The correlation, built using a statistical analysis, has shown that the jet in a cross-flow model performs very well to describe the jet trajectories. A very interesting conclusion is that the correlation coefficients were found to be independent of the scale. Finally, the author proposed a definition of the penetration depth and use it in its dimensionless form to predict how the jet penetrates the bulk in the industrial vessel with the current injection conditions.

11.1. ASSUMPTIONS OF THE MODEL

The jet trajectory was predicted numerically using Lagrangian particle tracking from the start to the end of the injection time. As the injection is transient, only the trajectory during the injection time was considered and the Lagrangian particles were not followed after the end of the injection time. The jet trajectory and its behaviour have been described in detail previously in Chapter 8 for the pilot reactor and Chapter 10 for the industrial scale vessels. Due to the three dimensional and transient nature of the flow (of both the jet and the agitated fluid) significant assumptions have to be made to simplify the system studied. A three dimensional study of the jet trajectory would require a 3D function which could correlate the 3D plots represented by the Lagrangian particle tracks located in the whole vessel. This was considered to be beyond the scope of this study due to the very different 3D jet behaviours observed and the complexity of the resulting trajectory. The analysis was limited to the two dimensions X and Y because this appeared to be the best way to describe the jet trajectories and is a first step to quantifying the jet penetration. The details of the system studied and the description of the coordinate system used are presented in Figure 11.1.
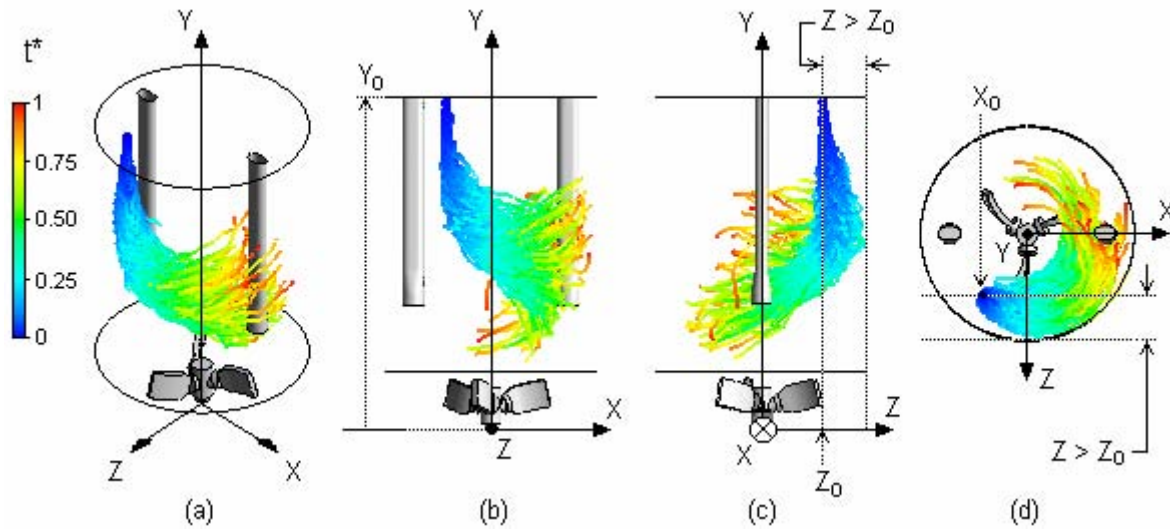
Figure 11.1. Details of the coordinate system: (a) 3D view; (b) XY lateral view; (c) YZ lateral view; (d) XZ top view.

The jet trajectories considered for the correlation analysis correspond to the projection of the Lagrangian particle tracks onto a vertical plane, named the injection plane, and are defined by the point X_o, Y_o, Z_o and the unit vector pointing in the z direction which is normal to this plane. This process transforms the 3D problem into two dimensions, and retains a good description of what is observed laterally, as shown in Figure 11.1(b). As shown in Figure 11.1(c), the jet is firstly deflected towards the vessel shell, then it passes through the injection plane before spiralling in the central part of the vessel. Only the tracks having $Z > Z_o$ have been considered to model the jet trajectory and all the data with $Z < Z_o$ were discarded.

11.2. ANALOGY WITH JET IN A CROSS-FLOW STUDIES

The theoretical analysis which appeared to be the closest to the case studied here is that for liquid jets injected into a cross-flow. As mentioned in Muppidi and Mahesh (2005), the dependency of the mean jet trajectory on the jet diameter is very well-known and the flow field of a jet in a cross-flow is believed to be influenced primarily by the effective velocity ratio R (which in this case simplifies to $R = u_j / u_{cf}$, where u_j is the jet velocity and u_{cf} is the cross-flow velocity). The reader can find further details on the subject in Margason (1993). Figure 11.2 illustrates the case of a jet in cross flow.
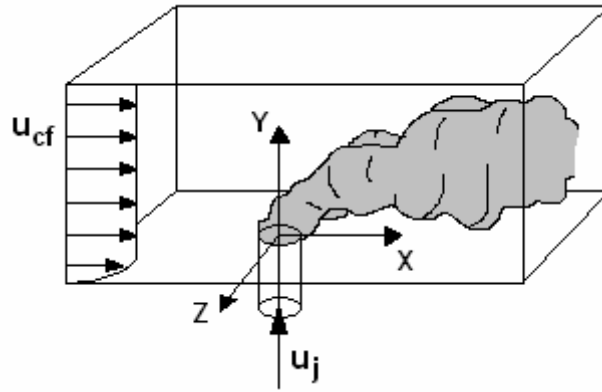
Figure 11.2. Schematic of a jet in a cross-flow.

It was assumed that the equation which describes the jet trajectory in the case studied here is similar in form to that already found in the literature for jets in cross-flows. This is clearly a significant assumption, as the velocity in the agitated vessel is not constant as usually considered for u_{cf} in jet in a cross-flow studies. The form of the equation which was chosen to model the jet trajectory in the stirred vessel was inspired by the correlations of Ivanov (1952, see Abramovich, 1963), Shandorov (1957, see Abramovich, 1963), Gordier (1959) and Patrick (1967). These very simple equations have proved to perform well in describing the trajectory of a jet injected normally into a cross flow (Rajaratnam, 1976). These jet trajectory correlations are summarized in Table 11.1.

Table 11.1. Correlations describing the penetration behaviour for circular jets injected normally into a cross-flow with $R = u_j / u_{cf}$ (Rajaratnam, 1976).

Investigators	Equations	Remarks
Ivanov (1952, see Abramovich, 1963)	$Y/d = R^{0.87}(X/d)^{0.33}$	*R* was varied from 3.5 to about 32 and Ivanov also experimented with oblique jets.
Shandorov (1957, see Abramovich, 1963)	$Y/d = R^{0.79}(X/d)^{0.39}$	*R* was varied from 1.4 to 4.7 and Shandorov also experimented with oblique jets.
Gordier (1959)	$Y/d = 1.31R^{0.74}(X/d)^{0.37}$	Gordier worked with water jets in a water tunnel – axis joins maximum total pressure points.
Patrick (1967)	$Y/d = R^{0.85}(X/d)^{n}$ $n = 0.38$ (from velocity measurements) $n = 0.34$ (from concentration measurements)	*R* varies from 6 to about 50.

To find an equivalent of the cross-flow velocity for our problem, it was decided to consider the agitator tip-speed (U_{tip}). It would be interesting to consider a more accurate value of the bulk velocity which really impacts the fluid jet when it enters the vessel (for example, the integral of the tangential component of the bulk velocity on the vertical line normal to the injection surface in the upper part of the vessel). However such a measure is impractical if a simple correlation is to be established. The agitator tip-speed, which gives the maximum velocity value in the vessel, gives an acceptable, scalable and practical parameter to use in the model.

The equations proposed in Table 11.1 use a jet injection orifice centred at $(X, Y) = (0, 0)$. The cross flow velocity and the jet velocity are directed toward O_x and O_y, respectively, as shown in Figure 11.2. For our case, the jet injection in the stirred vessel is located at the coordinates (X_o, Y_o and Z_o) where the origin of the coordinate frame is located at the bottom of the agitator (centre of the bottom dish).

A coordinate transformation is made using Eq. (11.1) for the X, Y and Z coordinates, respectively.

$$
\begin{cases}
X^* = X - X_o \\
Y^* = Y_o - Y \\
Z^* = Z - Z_o
\end{cases}
\tag{11.1}
$$

The numerical values of X_o, Y_o and Z_o are given in Table 11.2.

Table 11.2. X_o, Y_o and Z_o for the pilot and the industrial reactor.

	Pilot reactor	Industrial reactor
X_o (m)	-0.094	-0.6583
Y_o (m)	0.7	4.888
Z_o (m)	0.1294	0.9061

In agreement with the correlations listed in the Table 11.1, the jet trajectory is modelled using the form expressed in Eq. (11.2):

$$
\frac{Y^*}{d} = A_1 \left(\frac{V}{U_{tip}} \right)^{A_2} \left(\frac{X^*}{d} \right)^{B}
\tag{11.2}
$$

11.3. DETERMINATION OF THE MODEL CONSTANTS

For each case analysed, the data for the Lagrangian particle tracks have been exported for times starting at zero to the final injection time. The data set has then been transformed using the transformation expressed in Eq. (11.1). Finally, only the data corresponding to $Z^*>0$ and $X^*>0$ have been conserved for further statistical analysis. These calculations were done using the commercial software Statgraphics Centurion XV both for the partially-baffled vessel modelled at the laboratory and industrial scales.

The first analysis of the Lagrangian tracks data was performed by doing a non-linear fit of the cloud of points from the model to Eq. (11.3) using the Levenberg-Marquardt algorithm.

$$\frac{Y^*}{d} = A\left(\frac{X^*}{d}\right)^B \qquad (11.3)$$

The Levenberg-Marquardt algorithm (or LMA), first published by Levenberg (1944) and rediscovered by Marquardt (1963), provides a numerical solution to the problem of minimizing a general non-linear function. Such minimization problems arise often in least squares curve fitting and non-linear programming. The LMA interpolates between the Gauss-Newton algorithm (GNA) and the method of gradient descent. The LMA is more robust than the GNA, which means that in many cases it finds a solution even if it starts very far from the final minimum.

11.3.1. <u>Pilot reactor</u>

Thirteen simulations have been carried out with the pilot reactor. Nine of them were run with different jet diameter and the jet injection velocities but with the same agitator speed and four additional runs were devoted to the analysis of the influence of the agitator speed for a constant jet diameter and jet velocity. Figures 11.3 and 11.4 show the results of the non-linear fit to the Lagrangian particle track data. The simulation conditions and the number of the corresponding chart of Figures 11.3 or 11.4 are detailed in the Table 11.3. The parameters obtained from the non-linear fitting which corresponds to Figures 11.3 and 11.4 are given in Table 11.4.

Table 11.3. Details of the simulations for the pilot reactor and identification of the corresponding figure where the fit to the data is shown

N (RPM)	d (m)	V (m/s)	U_{tip} (m/s)	Fig. #
100	0.072	2	1.36	11.3(a)
100	0.1	2	1.36	11.3(b)
100	0.15	2	1.36	11.3(c)
100	0.072	6	1.36	11.3(d)
100	0.1	6	1.36	11.3(e)
100	0.15	6	1.36	11.3(f)
100	0.072	10	1.36	11.3(g)
100	0.1	10	1.36	11.3(h)
100	0.15	10	1.36	11.3(i)
50	0.1	6	0.68	11.4(a)
75	0.1	6	1.02	11.4(b)
100	0.1	6	1.36	11.4(c) same as 11.3(e)
125	0.1	6	1.70	11.4(d)
150	0.1	6	2.04	11.4(e)

Table 11.4. Fitted A and B constants, 95% confidence interval [*] and R-squared (R²) statistics [**] (model $(y*/d) = A(X*/d)^B$ for the pilot reactor).

Fig. 11.3	A	95% conf. int. A (lower)	95% conf. int. A (upper)	B	95% conf. int. B (lower)	95% conf. int. B (upper)	R² (%)
(a)	5.69	5.64	5.75	0.31	0.30	0.31	79.09
(b)	5.93	5.89	5.98	0.33	0.32	0.33	81.97
(c)	5.80	5.76	5.85	0.36	0.35	0.36	78.63
(d)	15.68	15.62	15.74	0.28	0.28	0.28	80.41
(e)	16.24	16.15	16.32	0.26	0.26	0.26	69.90
(f)	14.87	14.78	14.95	0.28	0.28	0.29	57.72
(g)	23.47	23.37	23.57	0.25	0.25	0.25	74.22
(h)	21.93	21.81	22.04	0.29	0.29	0.30	67.92
(i)	18.54	18.42	18.65	0.32	0.31	0.32	49.67

Fig. 11.4	A	95% conf. int. A (lower)	95% conf. int. A (upper)	B	95% conf. int. B (lower)	95% conf. int. B (upper)	R² (%)
(a)	23.43	23.31	23.55	0.27	0.26	0.27	60.08
(b)	19.77	19.69	19.86	0.27	0.26	0.27	72.49
(c)	16.24	16.15	16.32	0.26	0.26	0.26	69.90
(d)	14.25	14.19	14.31	0.28	0.27	0.28	77.18
(e)	12.07	12.01	12.12	0.29	0.29	0.29	80.82

[*] The confidence interval provides a bound when estimating a parameter for which the mean and standard deviation of the population can be estimated. From Figure 11.3(a), we can conclude with 95% confidence that the A constant value is somewhere between 5.64 and 5.75.

[**] **R²** is the percentage of the variability in Y^*/d that has been explained by the model. In this case, the non-linear regression against X^*/d explains about 79.09 % of the variability in Y^*/d. The closer it is to one, the better the model has reproduced the data.
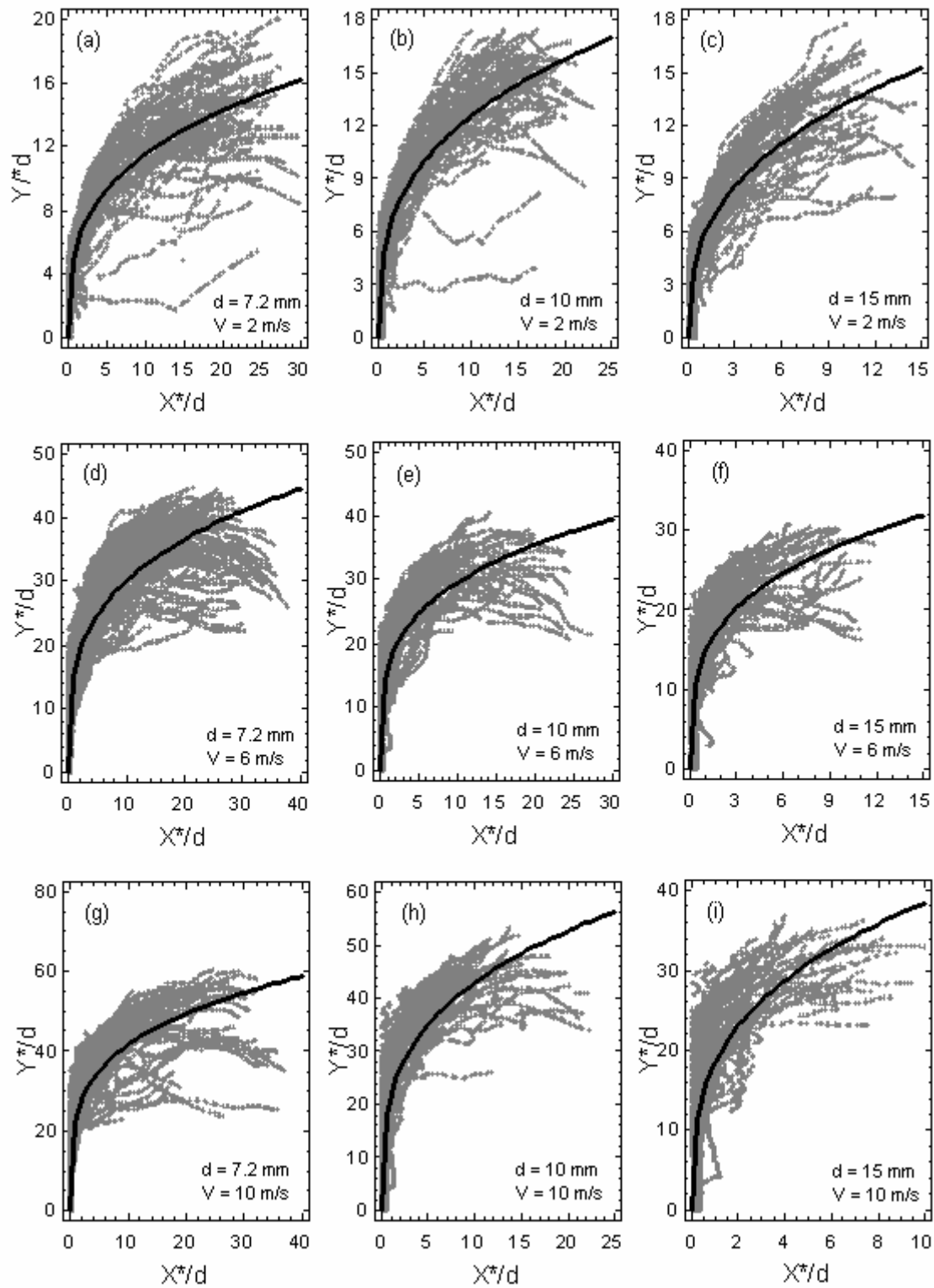
Figure 11.3. Comparison between the Lagrangian particle tracks from CFD (grey symbols) and the jet trajectory correlation (black line) at N = 100 RPM for the pilot reactor.
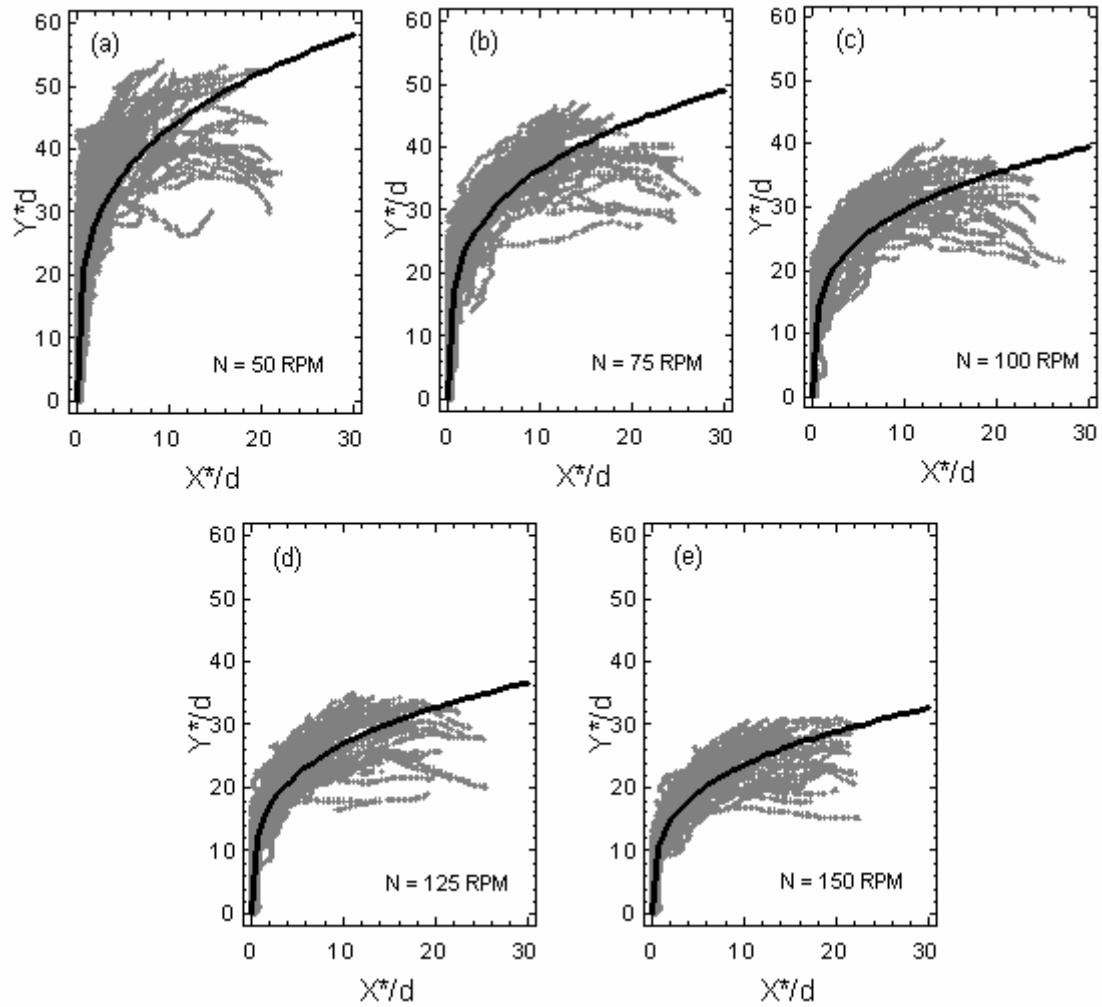
Figure 11.4. Comparison between the Lagrangian particle tracks from CFD (grey symbols) and the jet trajectory correlation (black line) with d = 10 mm and V = 6 m s^{-1} at different agitator rotation speeds for the pilot reactor.

11.3.2. <u>Industrial reactor</u>

The actual jet velocity has been measured experimentally in the industrial reactor and was equal to V_o = 1.55 m/s. Simulations have been carried out for the industrial reactor at two different agitator rotation speeds: the nominal speed (N_{nom}) and half of the nominal speed ($N_{nom}/2$). Four have been carried out for each agitator speed considering the jet diameter to remain constant and for jet velocities equal to V_o, $5V_o$, $10V_o$, and $20V_o$. Figure 11.5 shows the results of the non-linear fit to the Lagrangian particle tracks. The simulation data and the corresponding charts of Figure 11.5 are detailed in Table 11.5.

Table 11.5. Details of the simulations for the pilot reactor.

N (RPM)	d (m)	V (m/s)	U_{tip} (m/s)	Fig. number
$N_{nom}/2$	0.1	1.55	3.86	11.5(a)
$N_{nom}/2$	0.1	7.75	3.86	11.5(b)
$N_{nom}/2$	0.1	15.5	3.86	11.5(c)
$N_{nom}/2$	0.1	31	3.86	11.5(d)
N_{nom}	0.1	1.55	7.73	11.5(e)
N_{nom}	0.1	7.75	7.73	11.5(f)
N_{nom}	0.1	15.5	7.73	11.5(g)
N_{nom}	0.1	31	7.73	11.5(h)
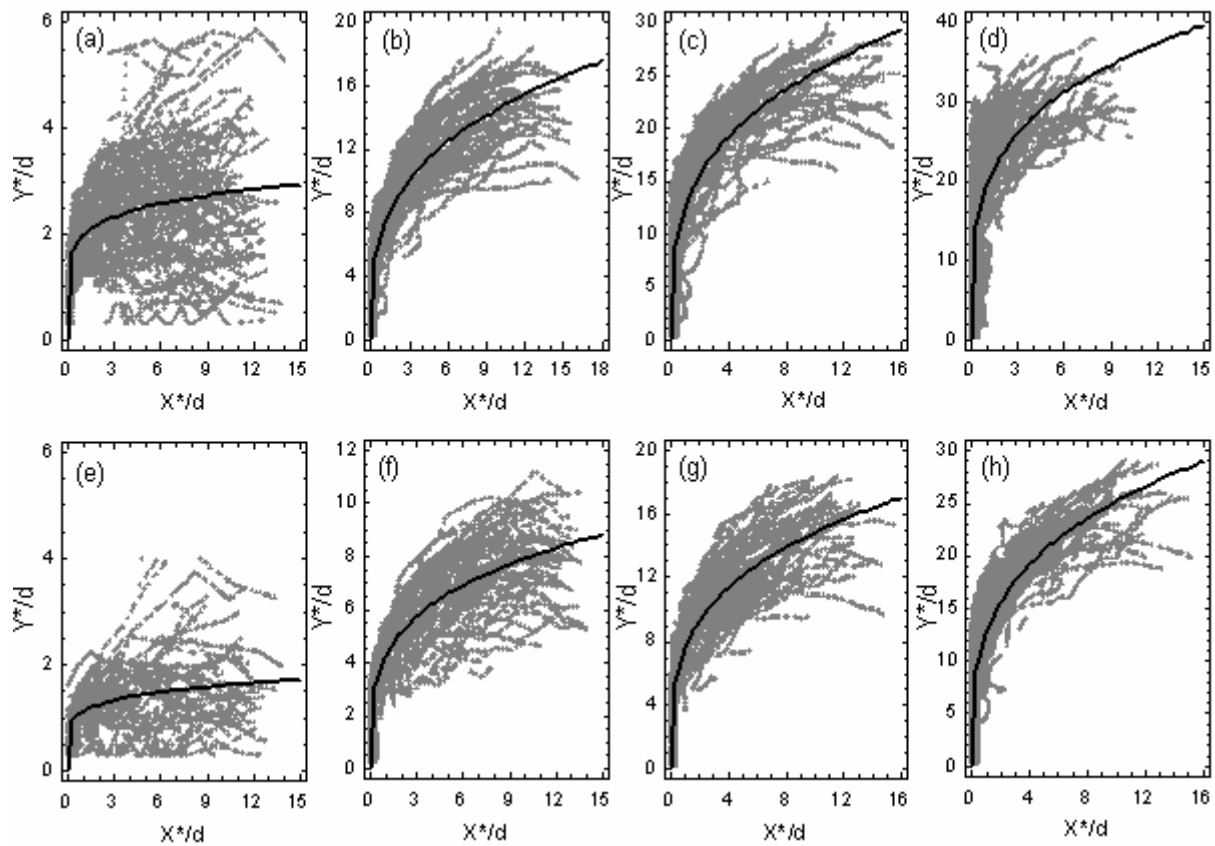
Figure 11.5. Comparison between the Lagrangian particle tracks from CFD (grey symbols) and the jet trajectory correlation (black line) with d = 0.1 m for the industrial reactor: (a) $N_{nom}/2$, V = 1.55 m s^{-1}; (b) $N_{nom}/2$, V = 7.75 m s^{-1}; (c) $N_{nom}/2$, V = 15.5 m s^{-1}; (d) $N_{nom}/2$, V = 31 m s^{-1}; (e) N_{nom}, V = 1.55 m s^{-1}; (f) N_{nom}, V = 7.75 m s^{-1}; (g) N_{nom}, V = 15.5 m s^{-1}; (h) N_{nom}, V = 31 m s^{-1}.

The results of the non-linear fit which corresponds to Figure 11.5 are given in Table 11.6.

Table 11.6. Fitted A and B constants, 95% confidence interval, and R-squared (R²) statistics (model $(Y*/d) = A(X*/d)^B$ for the industrial reactor).

Fig. 11.5	A	95% conf. int. A (lower)	95% conf. int. A (upper)	B	95% conf. int. B (lower)	95% conf. int. B (upper)	R² (%)
(a)	1.98	1.95	2.01	**0.14**	0.14	0.15	15.54
(b)	7.12	7.08	7.16	0.31	0.31	0.32	81.14
(c)	12.49	12.43	12.54	0.31	0.30	0.31	75.05
(d)	19.55	19.45	19.65	0.26	0.26	0.26	56.40
(e)	1.13	1.10	1.16	**0.15**	0.14	0.17	13.14
(f)	4.29	4.26	4.33	0.27	0.26	0.27	73.22
(g)	7.58	7.53	7.62	0.29	0.29	0.29	81.09
(h)	12.69	12.62	12.76	0.30	0.29	0.30	74.46

11.3.3. <u>Analysis of the results</u>

The form of the law used to correlate the data gives good agreement between the model and the Lagrangian particle tracks. <u>It must be noted that the constant B is of the same order of magnitude when considering either the pilot scale or the industrial scale</u> with two exceptions for Figures 11.5(a) and 11.5(e). These deviations are explained by the difficulty of fitting to data of Figures 11.5(a) and 11.5(e). Due to the low jet velocity, the "particles" accumulate very close to the free-surface and the jet shape is not well defined. The one-factor statistical analysis presented in the following paragraph give more details about this.

11.3.3.1. Determination of the constant B

The 21 observations (pilot and industrial) have been analysed and the results are represented in Figure 11.6(a) using a box-and-whiskers plot.

The box-and-whisker plot, invented by Tukey (1977), is constructed by drawing:
- a box extending from the lower quartile to the upper quartile. The middle 50% of the data values are thus covered by the box;
- a vertical line at the location of the median, which divides the data in half;
- a cross sign at the location of the mean;
- whiskers extending from the quartiles to the largest and smallest observations, unless some values are far enough from the box to be classified as "outside points", in which case the whiskers extend to the most extreme points that are not classified as "outside". "Outside"

points are points more than 1.5 times the inter-quartile range above or below the limits of the box.
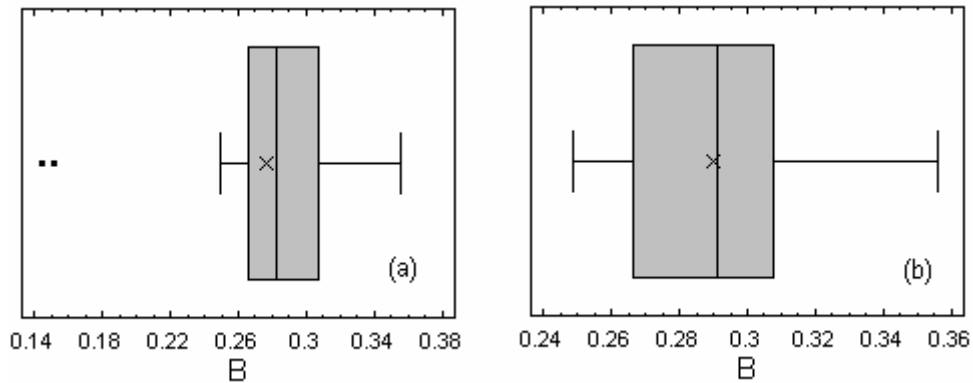
Figure 11.6. Box-and-whiskers plots of B: (a) complete data set; (b) data set without outliers.

As shown in Figure 11.6(a), the values of B around 0.15, which correspond to Figures 11.5(a) and (e), are outside the box. A substantial difference between the median and the mean indicates either the presence of an outlier or a skewed distribution. In the case of a skewed distribution, the mean would be pulled in the direction of the longer tail, which is not the case here. Thus, this confirms the two extreme points around 0.15 are outliers and must be deleted from the data set used to calculate the average value of the constant B. These deviations are explained by the bad non-linear fitting because the jet trajectory obtained with V = 1.55 m/s gave clouds of point very close to the free-surface and the optimization method does not work well for large numbers of points without a well-defined form. Figure 11.6(b) present the analysis of the data set modified and the analysis of the 19 observations gave the results presented in Table 11.7.

Table 11.7. Results of the statistical analysis of the coefficient B.

Number of observations	19
Mean	**0.29**
Standard deviation	0.03
Minimum	0.25
Maximum	0.36
Span	0.11
Standardized asymmetry	1.23
Standardized flatness	0.44

The mean value and the standard deviation of B are 0.29 and 0.03, respectively. The standardized asymmetry and flatness are between -2 and +2 which mean that the data set follows a normal law (this is useful to know when performing further statistical tests on these data as for example those concerning the standard deviation).

$$B = 0.29$$

11.3.3.2. Determination of the constant A

All the non-linear fits were re-estimated after setting the constant B to 0.29 and the results are presented in Table 11.8 and in Figures 11.7, 11.8 and 11.9.

Table 11.8. Estimation of the A constant by non-linear fittings with B = 0.29, 95% confidence interval, and R-squared (R²) statistics.

Scale	A	95% conf. int. A (lower)	95% conf. int. A (upper)	R² (%)	Fig. number
Pilot	5.90	5.88	5.93	78.92	11.7(a)
Pilot	6.32	6.29	6.34	81.30	11.7(b)
Pilot	6.28	6.25	6.31	76.48	11.7(c)
Pilot	15.47	15.44	15.51	80.37	11.7(d)
Pilot	15.64	15.58	15.71	69.13	11.7(e)
Pilot	14.81	14.73	14.89	57.67	11.7(f)
Pilot	22.02	21.94	22.09	72.47	11.7(g)
Pilot	21.97	21.88	22.07	67.91	11.7(h)
Pilot	18.57	18.45	18.69	49.32	11.7(i)
Pilot	22.96	22.86	23.07	59.63	11.8(a)
Pilot	19.21	19.14	19.28	71.99	8(b)
Pilot	15.64	15.58	15.71	69.13	11.8(c) same as 11.7(e)
Pilot	14.03	13.98	14.07	77.05	11.8(d)
Pilot	12.10	12.06	12.13	80.82	11.8(e)
Indus	1.57	1.56	1.59	5.86	11.9(a)
Indus	7.33	7.30	7.36	80.82	11.9(b)
Indus	12.67	12.62	12.71	74.83	11.9(c)
Indus	19.49	19.39	19.59	55.73	11.9(d)
Indus	0.91	0.90	0.92	6.08	11.9(e)
Indus	4.14	4.12	4.16	72.81	11.9(f)
Indus	7.59	7.56	7.62	81.09	11.9(g)
Indus	12.77	12.72	12.83	74.42	11.9(h)
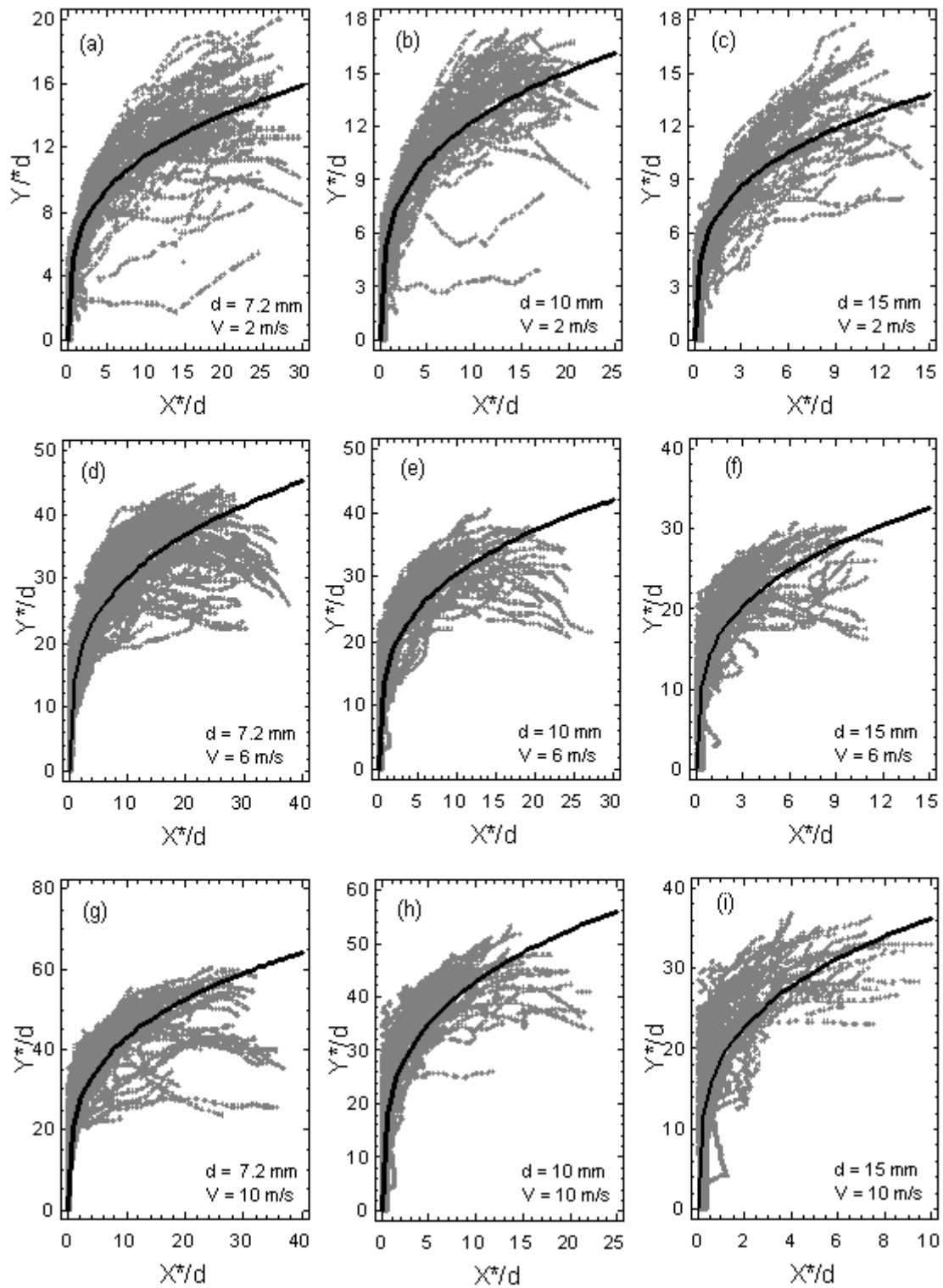
Figure 11.7. Comparison between the Lagrangian particle tracks from CFD (grey symbols) and the jet trajectory correlation (black line) at N = 100 RPM for the pilot reactor. The value of the constant B of the model is set to 0.29.

Figure 11.8. Comparison between the Lagrangian particle tracks from CFD (grey symbols) and the jet trajectory correlation (black line) with d = 10 mm and V = 6 m s^{-1} at different agitator rotation speeds for the pilot reactor. The value of the constant B of the model is set to 0.29.

Regarding the initial model proposed for the correlation, the constant A depends on the quantity (V/U$_{tip}$) with the form expressed in Eq. (11.4). The curve of ln(A) versus ln(V/U$_{tip}$) used to estimate values for the A$_1$ and A$_2$ constants of Eq. (11.4) is shown in Figure 11.10.

$$A = A_1 \left(\frac{V}{U_{tip}} \right)^{A_2}$$

(11.4)

Figure 11.9. Comparison between the Lagrangian particle tracks from CFD (grey symbols) and the jet trajectory correlation (black line) with d = 0.1 m for the industrial reactor: (a) $N_{nom}/2$, V = 1.55 m s^{-1}; (b) $N_{nom}/2$, V = 7.75 m s^{-1}; (c) $N_{nom}/2$, V = 15.5 m s^{-1}; (d) $N_{nom}/2$, V = 31 m s^{-1}; (e) N_{nom}, V = 1.55 m s^{-1}; (f) N_{nom}, V = 7.75 m s^{-1}; (g) N_{nom}, V = 15.5 m s^{-1}; (h) N_{nom}, V = 31 m s^{-1}. The value of the constant B of the model is set to 0.29.
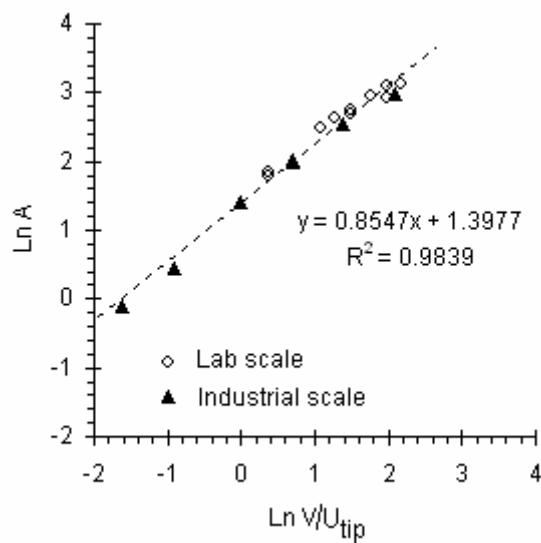
Figure 11.10. A plot of ln(A) versus ln (V/U_{tip}) for the pilot and the industrial reactor.

The data are fitted extremely well by a straight line which means that a single correlation fits the data for the two reactors and that the proposed model constants are independent of the scale factor. The slope gives $A_2 = 0.85$ and the intercept point with the ordinate axis gives $A_1 = e^{(1.3977)} = 4.05$.

Therefore Eq. (11.4) is rewritten in Eq. (11.5) as:

$$A = 4.05 \left(\frac{V}{U_{tip}} \right)^{0.85} \tag{11.5}$$

11.3.4. <u>Correlation of the jet trajectory</u>

Therefore, the correlation is expressed in Eq. (11.6) by:

$$\frac{Y^*}{d} = 4.05 \left(\frac{V}{U_{tip}} \right)^{0.85} \left(\frac{X^*}{d} \right)^{0.29} \tag{11.6}$$

with $0.072 \text{ m} \leq d \leq 0.1 \text{ m}$, $0.68 \text{ m s}^{-1} \leq U_{tip} \leq 7.73 \text{ m s}^{-1}$ and $0 \leq X^* \leq -2X_o$ ($X_o < 0$).

This correlation is independent of the reactor scale and the jet trajectory $Y = f(X)$ is expressed in Eq. (11.7) as:

$$Y = Y_o - d \left[4.05 \left(\frac{V}{U_{tip}} \right)^{0.85} \left(\frac{X - X_o}{d} \right)^{0.29} \right] \tag{11.7}$$

with $0.072 \leq d \leq 0.1$ and $0.68 \text{ m s}^{-1} \leq U_{tip} \leq 7.73$ and $X_o \leq X \leq -X_o$ ($X_o < 0$).

Eq. (11.7) is compared with the Lagrangian particle tracks in physical coordinates for the pilot and industrial reactors in Figures 11.10, 11.11 and 11.12.
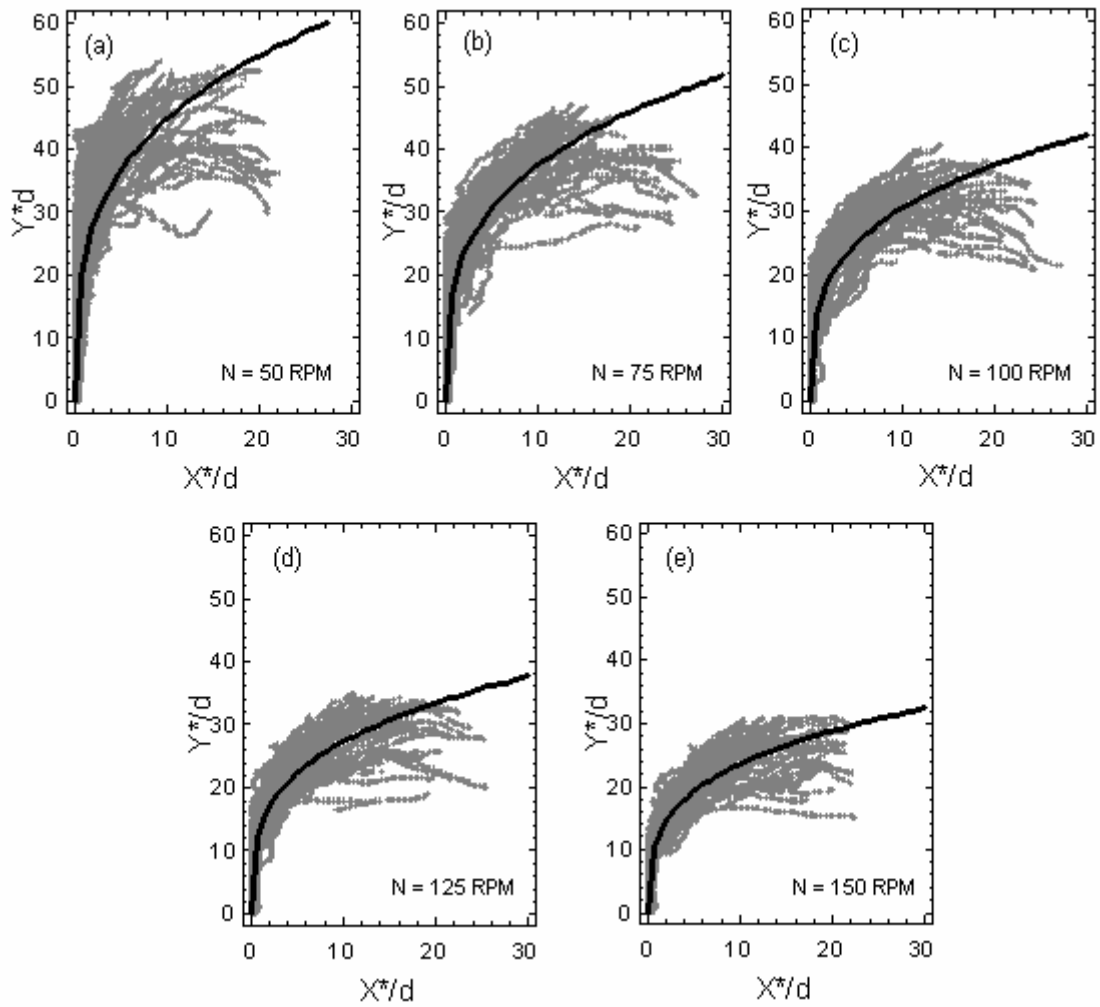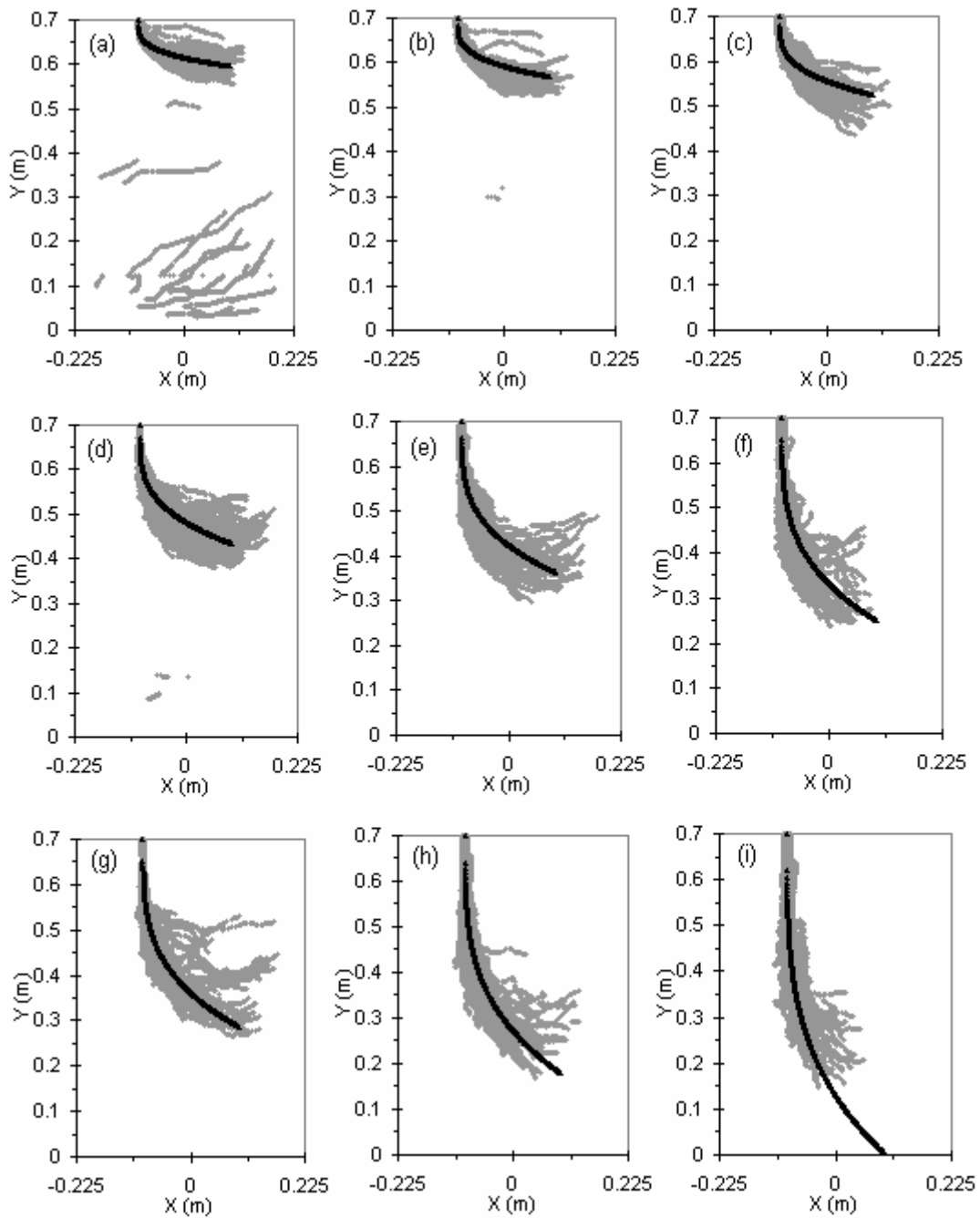
Figure 11.10. Comparison between the Lagrangian particle tracks from CFD (grey symbols) and the jet trajectory obtained by using Eq. (11.7) (black line) at N = 100 RPM for the pilot reactor: (a) d = 7.2 mm, V = 2 m s^{-1}; (b) d = 10 mm, V = 2 m s^{-1}; (c) d = 15 mm, V = 2 m s^{-1}; (d) d = 7.2 mm, V = 6 m s^{-1}; (e) d = 10 mm, V = 6 m s^{-1}; (f) d = 15 mm, V = 6 m s^{-1}; (g) d = 7.2 mm, V = 10 m s^{-1}; (h) d = 10 mm, V = 10 m s^{-1}; (i) d = 15 mm, V = 10 m s^{-1}.
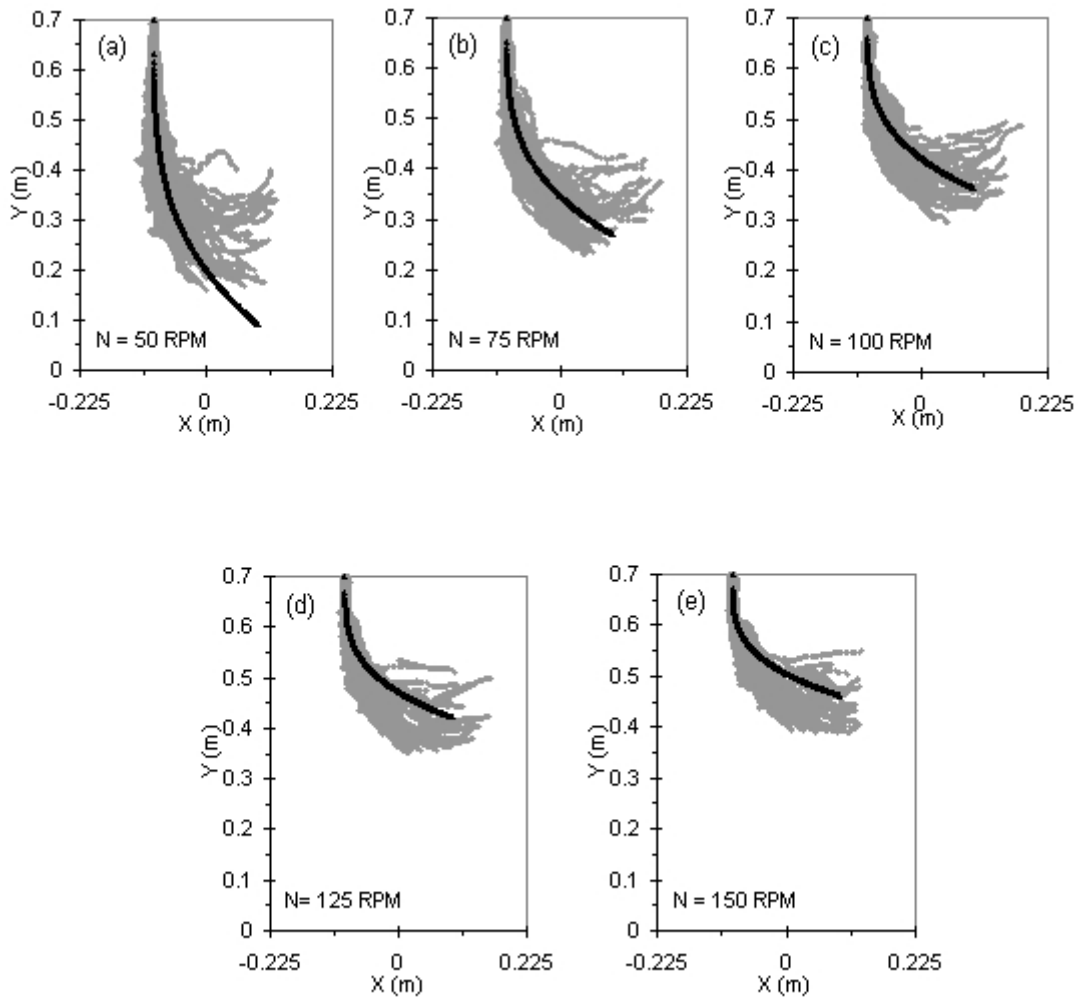
Figure 11.11. Comparison between the Lagrangian particle tracks from CFD (grey symbols) and the jet trajectory obtained by using Eq. (11.7) (black line) with d = 10 mm and V = 6 m s^{-1} for different agitator rotation speeds (pilot reactor).

The model proposed is able to describe the CFD data for the jet trajectory with very good agreement for various jet injection and agitation conditions. One of the most important results is that the correlation is found to be the same for the laboratory and the industrial scales. Surprisingly, the constants A_1 and A_2 found here for a completely different situation to that of a jet in a cross-flow are very similar to those presented in Table 11.1.
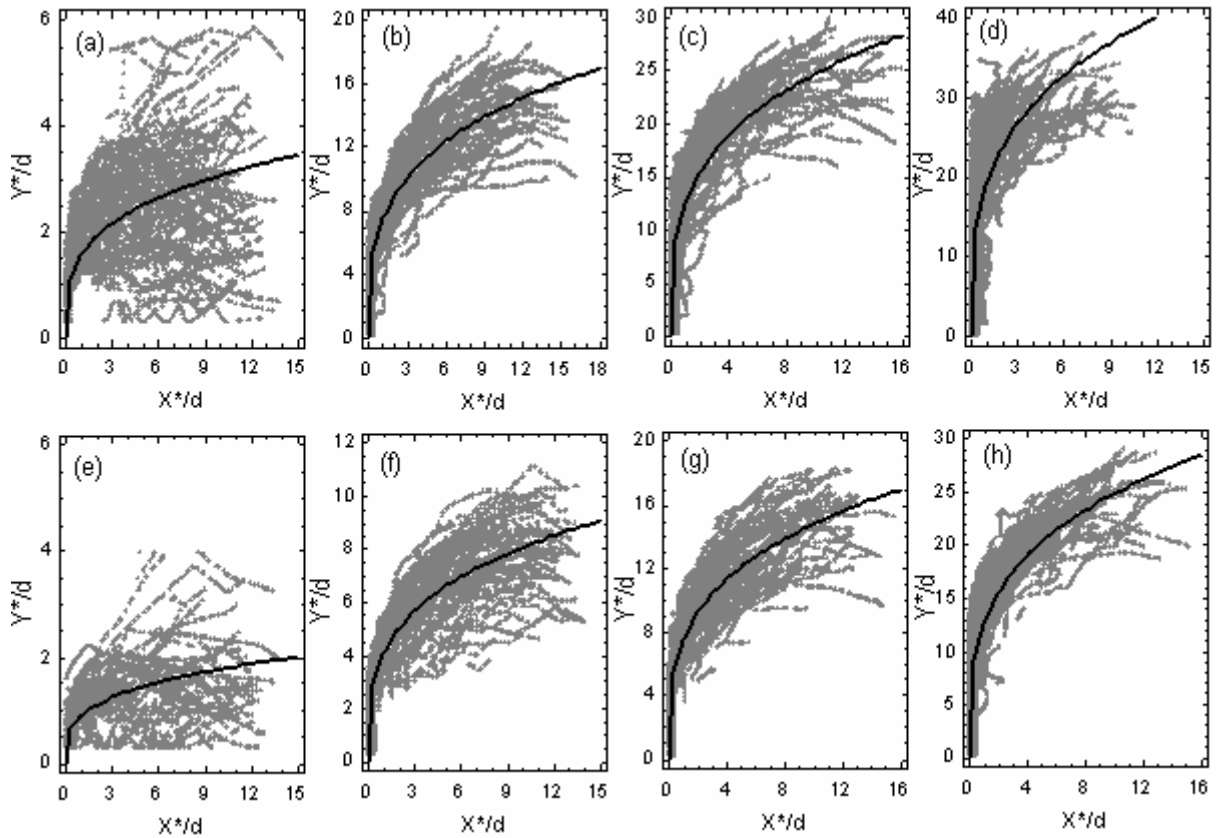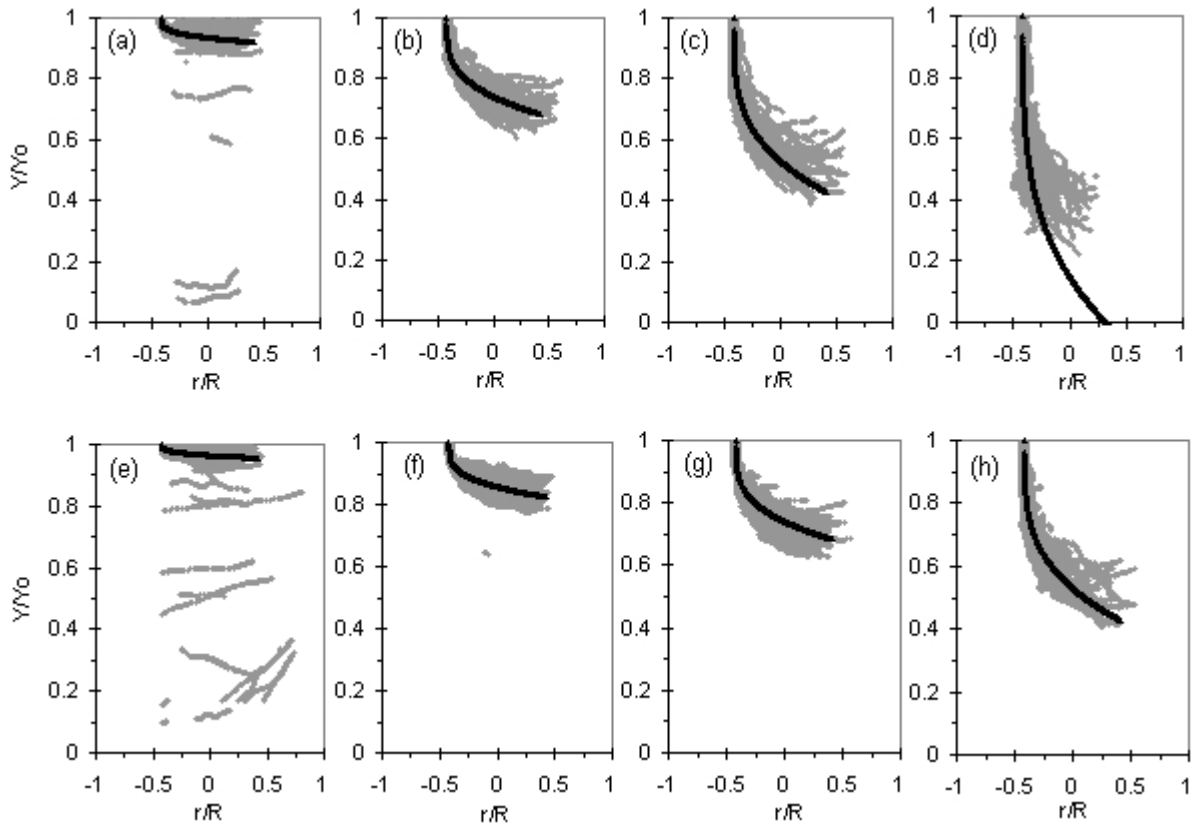
Figure 11.12. Comparison between the Lagrangian particle tracks from CFD (grey symbols) and the jet trajectory obtained by using Eq. (11.7) normalized (black line) with d = 0.1 m for the industrial reactor: (a) $N_{nom}/2$, V = 1.55 m s^{-1}; (b) $N_{nom}/2$, V = 7.75 m s^{-1}; (c) $N_{nom}/2$, V = 15.5 m s^{-1}; (d) $N_{nom}/2$, V = 31 m s^{-1}; (e) N_{nom}, V = 1.55 m s^{-1}; (f) N_{nom}, V = 7.75 m s^{-1}; (g) N_{nom}, V = 15.5 m s^{-1}; (h) N_{nom}, V = 31 m s^{-1}.

The theoretical jet trajectory obtained by using the correlation of Eqs. 11.6 and 11.7 is compared with experimental results in Figure 11.13.

Figure 11.13 was obtained using the same trichromy process that was used previously in Chapter 8 and the reader is referred to this section for further details of this technique. In this figure, good agreement is shown between the jet trajectories calculated theoretically using the correlation and the experimental data obtained with three different jet velocities at N = 100 RPM. This demonstrates clearly that the correlation describes the jet trajectory in this vessel very well in both a qualitative and quantitative sense.
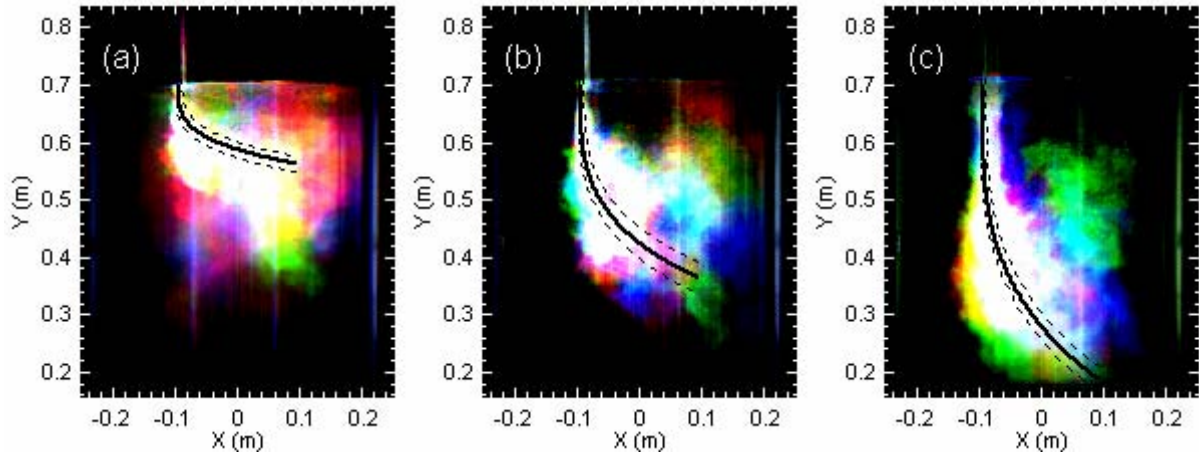
Figure 11.13. Comparison between experimental pictures of jet injections obtained using the trichromy imaging process and the theoretical jet trajectory correlation (full line) at N = 100 RPM. (a) V = 2.1 ± 0.1 m s^{-1}; (b) V = 6.0 ± 0.5 m s^{-1}; (c) V = 9.9 ± 0.6 m s^{-1}. The dotted lines show the uncertainty limits for each trajectory predicted by the correlation.

11.4. JET PENETRATION DEPTH

The author proposes to define the jet penetration depth H_p in Eq. (11.8) as the depth of the jet below the initial level of liquid at the centre of the vessel (X=0).

$$H_p = Y_o - Y\big|_{X=O} \tag{11.8}$$

$$H_p = d\left[4.05\left(\frac{V}{U_{tip}}\right)^{0.85}\left(\frac{-X_o}{d}\right)^{0.29} \right] \tag{11.9}$$

$$H_p = K\left(\frac{V}{U_{tip}}\right)^{0.85} d^{0.71} \quad \text{with} \quad K = 4.05\left(-X_o\right)^{0.29} \tag{11.10}$$

$$\rightarrow H_p \propto \left(\frac{V}{U_{tip}}\right)^{0.85} d^{0.71} \tag{11.11}$$

This expression presented in Eq. (11.11) shows that the jet penetration is proportional to the ratio (V/U_{tip}) to the power of 0.85 and to the jet diameter to the power of 0.71.

In addition, it is proposed to define the dimensionless jet penetration depth H_p^* in Eq. (11.12) as the ratio of the jet penetration depth divided by the initial liquid level:

$$H_p^* = \frac{H_p}{Y_o} = \frac{d}{Y_o}\left[4.05\left(\frac{V}{U_{tip}}\right)^{0.85}\left(\frac{-X_o}{d}\right)^{0.29}\right] \qquad (11.12)$$

$$H_p^* = K'\left(\frac{V}{U_{tip}}\right)^{0.85} d^{0.71} \quad \text{with} \quad K' = \frac{4.05(-X_o)^{0.29}}{Y_o} \qquad (11.13)$$

Eq. (11.13) is illustrated for N = 41 RPM in Figure 11.14 for three different jet diameters. The actual system with d = 0.1 m gives a jet velocity equal to V_o = 1.55 m/s.
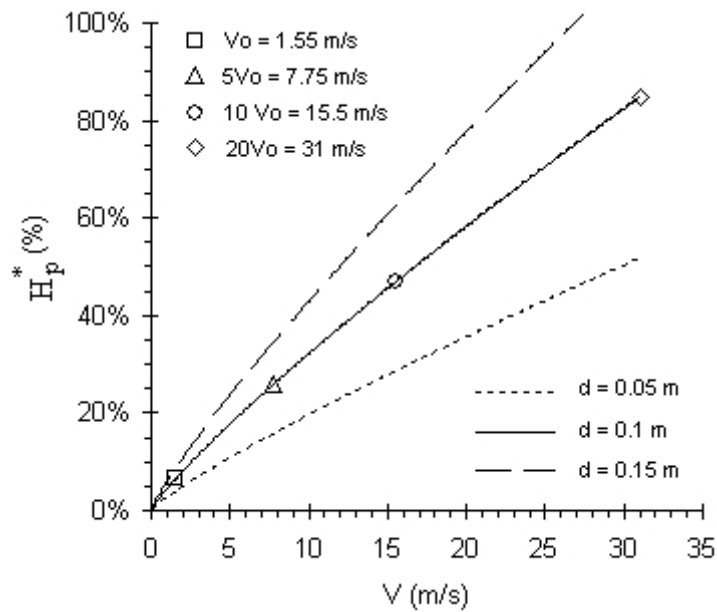
Figure 11.14. Variation of the dimensionless jet penetration depth with the jet velocity and the jet diameter for N = N_{nom}/2 (industrial reactor).

The diameter of the jet cannot be modified easily because the maximum allowable flange diameter is 0.15 m and the carbon disk currently available for a flange of nominal diameter equal to 0.15 m is only d = 0.1 m. This means that the only way to improve the jet penetration in the industrial case treated here is to increase the jet velocity.

11.5. CONCLUDING REMARKS

The Lagrangian particle tracks from 21 CFD simulations have been analysed in order to find a correlation describing the jet trajectory in the same partially-baffled vessel at two scales (laboratory and plant). The mains results are summarized as follows:

- the model, derived from jet in cross-flow studies, describes the jet trajectory very well;
- the correlation is independent of the scale;
- the predicted jet trajectory is in very good agreement with the computed Lagrangian particle tracks from various conditions of jet velocity, jet diameter and agitator rotation speed;
- the predicted jet trajectory is in good agreement with experimental data
- the proposed correlation is:

$$\frac{Y^*}{d} = 4.05 \left(\frac{V}{U_{tip}} \right)^{0.85} \left(\frac{X^*}{d} \right)^{0.29} \quad \text{with}$$

$$\begin{cases} X^* = X - X_o \\ Y^* = Y_o - Y \end{cases}$$

$0.072 \text{ m} \le d \le 0.1 \text{ m},$

$0.68 \text{ m s}^{-1} \le U_{tip} \le 7.73 \text{ m s}^{-1}$

$0 \le X^* \le -2X_o \ (X_o < 0)$

A fluid of water at 25°C

The optimal velocity, found by using the quenching curves, of $10V_o = 15.5$ m/s, gives a penetration depth of 46.8 % of the total liquid height instead of 6.5% with the actual jet velocity of 1.55 m/s. This means that the liquid jet would penetrate to a depth of 2.3 m below the free-surface instead 0.32 m at present (on the vessel axis) which is 7.2 times better than the present configuration.

Chapter 12

A STUDY OF POSSIBLE NEW SIMULATION STRATEGIES

This Chapter presents briefly two promising approaches in which only preliminary results were obtained during the course of this thesis. These are (i) a new turbulence modelling approach, and (ii) a new concept to simulate mixing vessels with a deformed free-surface. This Chapter starts by presenting a new turbulence modelling approach named Scale Adaptive Simulation (SAS). This approach can operate in RANS and LES-mode without an explicit mesh dependency, and has already proved to perform well in various cases tested by the developers of the model. This approach, which has not been tested yet for mixing vessels, has been used coupled with the Shear Stress Transport (SST) turbulence model (SST-SAS) for a single-phase model for the partially-baffled agitated vessel investigated in Chapter 5. Comparisons with experimental PIV data and the other turbulence models (k-ε, RSM-SSG) tested previously are presented. Finally, the author presents a new way to undertake the simulation of agitated vessels with deformed free-surfaces, named the free-surface cut strategy. Although only a few simulations were performed at the very end of the thesis, the results presented here illustrate the capability of this new approach.

12.1. SST-SAS: A PROMISING TURBULENCE MODELLING APPROACH

12.1.1. <u>Why test another approach to model turbulence?</u>

The simulation of unsteady flows represents a continuously increasing demand in all areas of CFD (aerodynamics, combustion, chemical engineering, etc). One of the most popular approaches, as used previously in this study, is based upon use of the Reynolds Averaged Navier-Stokes equations (RANS). When the equations are averaged and solved in transient simulations, the resulting equations are called URANS (Unsteady Reynolds Averaged Navier-Stokes equations). However, there are some situations where RANS and URANS approaches are not adequate, as for example unsteady flow with coherent structures or unstable flow with

highly anisotropic turbulence, etc. Alternative approaches, such as Large Eddy Simulation (LES), Detached Eddy Simulation (DES) or Direct Numerical Simulation (DNS) can be adopted.

With LES and DNS methods, time dependent equations are solved for the turbulent flow with either no approximations and all relevant scales resolved for DNS (see Verzicco *et al.*, 2004), or the equations are filtered to remove the very small spatial length scales and time differencing removes the very short temporal scales for LES (see Moin, 2002). These approaches require very fine grids and the use of very small time-steps, and simulation for a large number of time-steps is necessary to generate statistically meaningful correlations for the fluctuation velocity components (ANSYS CFX 11.0 user guide). However, these methods can give information on the very detailed structure of turbulent flow. For mixing vessels, the capability of the LES approach has been demonstrated in many studies (Dersksen and Van den Akker (1999), Yeoh *et al.*, 2005)). According to Menter *et al.* (2003a), "it was estimated [in 1997] that viable LES solutions for high Reynolds number industrial flows will not be feasible in the next 3-4 decades, even making optimistic assumptions". This point of view in not shared by all, and many researchers are very optimistic about the future of LES, see, for example, Van den Akker (2006). In contrast, the use of DNS at high Reynolds numbers, characteristic of most of engineering applications, is limited to academic research work due to the huge computational costs required (Nishino *et al.*, 2007) to resolve the wide range of scales of the turbulent flow.

Another approach, proposed initially by Spallart (1997), is a hybrid approach which combines features of the classical RANS formulation with elements of LES methods. The concept has been termed Detached Eddy Simulation (DES) and is based on the idea of simulating the flow in the boundary layer by a RANS model and switching to an LES model in regions of detached flow (see Spalart (2000), Squires (2004)). Although very interesting results have been obtained using DES, for example for the turbulent flow over a sphere and turbulent flow around aircrafts (Squires, 2004), this approach has received much less attention than LES. A possible reason may be because the switch between the RANS and LES region can be very grid dependent, which introduces an unacceptable level of uncertainty in the simulation results, particularly for unstructured meshes (Menter et al., 2003).

During this thesis, computer intensive methods such as LES, DES and DNS were not used because they were considered impractical with the time available. Nevertheless, it would be a very interesting and challenging task for future investigations. If the computer power increases with the same rate as observed during the past ten years, there is no reason why LES cannot be performed as easily as URANS is nowadays. In addition, academic research project using LES can be helped with the assistance of large computer resources (as or example the super-calculator ALTIX-SGI, CALMIP® - 120 processors, 240G RAM - used during this study to generate the results given in Chapter 8). From the author's point of view, researchers have to maintain and increase their know-how with LES and DNS methods. Nevertheless, it is not sufficient to wait for many years to perform accurate unsteady simulations and other methods or attractive concepts to compute unsteady simulations should be tested. The Scale-Adaptive Simulation (SAS) approach is one of the best promising alternative methods.

12.1.2. <u>The Scale-Adaptive Simulation approach used with the SST model</u>

To find an alternative between the URANS methods which does not provide the correct spectrum of turbulent scales, and the LES methods which is still prohibitive for many engineering problems due to the large computer resources needed, F. Menter, in association with various researchers, has developed a new Scale-Adaptive Simulation (SAS) concept (Menter *et al.* (2003a), Menter and Egorov (2004a, b), Menter and Egorov (2005a, b), Menter *et al.* (2006)). This model, based on the introduction of the von Karman length scale into the turbulence equations, allow the resolution of the turbulent spectrum in unsteady flow conditions. The von Karman length scale is defined in Eq. (12.1):

$$L_{vK} = \kappa \left| \frac{\partial U / \partial y}{\partial^2 U / \partial y^2} \right| \quad \text{with } \kappa = 0.41 \text{(von Karman constant)} \quad (12.1)$$

In the case of a logarithmic wall velocity profile this gives the familiar turbulent length-scale of $L_t = \kappa y$.

The information provided by the von Karman length-scale concering the scale of boundary and shear layers allows the SAS model to dynamically adjust to resolve turbulence structures in an LES-like manner in unsteady regions of the flow field, where the mesh is fine enough to

resolve them. At the same time, the model provides the RANS capabilities in stable flow regions, such as boundary layers, where it performs very well. This model appears not to be as prohibitive as LES or DES simulations in terms of the required computer resources. In addition, the SAS approach can operate in RANS and LES without an explicit grid dependency, which is a major advantage compared with DES. Finally, this modelling approach can be used with a one equation (e.g. Spalart-Allmaras, KE1E (see Menter *et al.*, 2003a)) or two equation turbulence models.

Two-equation turbulences models are based on the assumption that the minimum information required for a statistical description of turbulence are two independent scales obtained from two independent transport equations. A discussion concerning the two-equation models can be found in Menter (1994). Over the years, all the various two-equation turbulence models developed can be classified into three main groups: the first group of models is based on the k-ω model, as proposed by Kolmogorov (1942) (see Spalding (1991) for an English translation from the original Russian paper) and later extended by Saffman (1970) and Wilcox (1993). The second group is derived from the k-ε model proposed initially by Launder and Spalding (1974). The third group is built on the integral length scale of Rotta (1972) and is typically formulated as a k-kL model (Menter and Egorov, 2004a). As discussed in Menter and Egorov (2004b), standard RANS models derived from the k-ω and the k-ε models can only determine a turbulence frequency ω and the length scale is determined by turbulent diffusion and the applied boundary conditions. The only RANS model which uses two independent turbulent scales is the k-kL model of Rotta (Menter and Egorov, 2004b). Therefore, the k-kL model of Rotta, which has been reformulated as k-$\sqrt{k}\,$L model for practical considerations (see Menter *et al.*, 2006), was used to develop the basis of the SAS approach. A re-evaluation of Rotta's theory resulted in the retention of an additional term in the equation for the turbulent length scale, which introduces a second scale in the equations, the von Karman length scale L_{vK}, which has the property that it allows the model to recognize and adjust to already resolved scales in the simulation (Menter *et al.*, 2006). The equations solved in the model are detailed in Menter and Egorov (2004a) and will therefore not be repeated here. The approach has been applied with the Shear Stress model (Menter and Egorov, 2005a) in order to base the SAS model on an existing and technically-proven two equation model (Menter and Egorov, 2004b). For further details on the SST model, the reader is referred to Menter (2003b). The SST-SAS model has be tested directly by the authors on

different cases reported in Menter and Egorov, (2005a). The comparison with existing experimental data showed good agreement and, according to Menter, has demonstrated the viability of this approach.

Although this concept appears as an attractive tool, this model was implemented only very recently, in 2006, in the latest version of the CFD code ANSYS-CFX 11.0. This explains reason why few published papers have been found which used this modelling approach, and particularly why there are none for mixing vessels. Therefore, the simulation of the highly unsteady flow in the partially-baffled agitated vessel use in this study was computed with the SAS modelling used with the Shear-Stress Transport (SST) model, not because the model was new, but because the approach offers the potential to provide significantly better resolution of the unsteady phenomena (e.g. Macro Instabilities) observed in this type of mixing vessel. The results of SST-SAS simulations were compared with both the velocities predictions obtained using the classical RANS approach used with the k-ε and RSM-SSG turbulences models, and with PIV experimental data.

12.1.3. <u>SAS-SST simulation strategy</u>

The geometry modelled was the partially-baffled vessel that was used in Chapter 5 for single phase studies. The unstructured mesh used is composed by 957,846 elements, and is shown in Figure 12.1(a). The SAS simulation was initialised with results obtained by using the k-ε model generated after 30 agitator rotations. After the initialization, five agitator rotations were made to allow the model to transition, before the transient averaging statistics were recorded. Then, the results were averaged during 15 agitator rotations using a time step equal to $\Delta t = 0.3$ ms. After these 15 rotations, the timestep was multiplied by a factor 10 ($\Delta t = 3$ ms), and the averaging variable were reset to zero and averaged results were obtained over 30 agitator rotations. Contour plots of the blending function values obtained with the SAS simulation are presented in Figure 12.1(b). In regions where the function is zero, the LES-like (SAS) model is used and the regions where its value is one, the RANS model (SST) is activated.
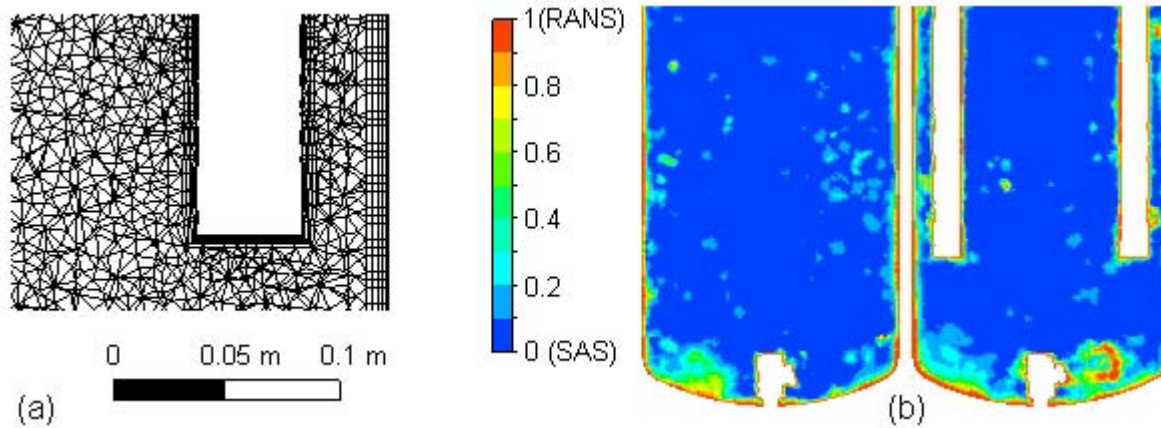
Figure 12.1. (a) details of the mesh used in the SAS simulations around the bottom tip of the right baffle; (b) RANS-SAS blending function on the vertical orthogonal baffle plane and on the baffle plane.

As shown in Figure 12.1(b), the RANS model is activated near the walls and elsewhere the value of the blend function is zero, meaning that the SAS mode is used.

12.1.4. SAS-SST results and comparison with the k-ε and the RSM-SSG

For the partially-baffled vessel modelled in this study, simulations using the standard k-ε turbulence model have highlighted that the flow is very complex and highly unsteady, with an internal rotating structure of vorticity filaments characterized by low frequencies (see Chapter 5). However, the k-ε model is known not *to perform well* in highly unsteady, rotating flows. The nature of the problem to solve, as mentioned previously in Chapter 5 and also by numerous authors who have worked with unbaffled vessels (e.g. Ciofalo *et al.* (1996)), is characterized by strong turbulence anisotropy and streamline curvature, and provides a severe benchmark for turbulences models. However, it is generally admitted than the second order Reynolds Stress Model (RSM-SSG) performs better than the k-ε for swirling flows. The two models have been tested and compared in Chapter 5. Surprisingly, the RSM gave unphysical results for the velocities near the axis and the numerical predictions were in poor agreement with the experimental PIV data, whilst the k-ε gave very good agreement (particularly for the axial velocity). Therefore, it was interesting to perform simulations with the Scale-Adaptive Simulation approach and to compare the results obtained with the previous obtained in Chapter 5.

Figure 12.2 compares the numerical instantaneous velocity field obtained, using the same mesh, for the k-ε model, the Reynolds Stress Model (RSM-SSG) and the SST-SAS. Two time-steps has been tested with the SST-SAS to see if this modification produces a noticeable effect on the observed flow patterns
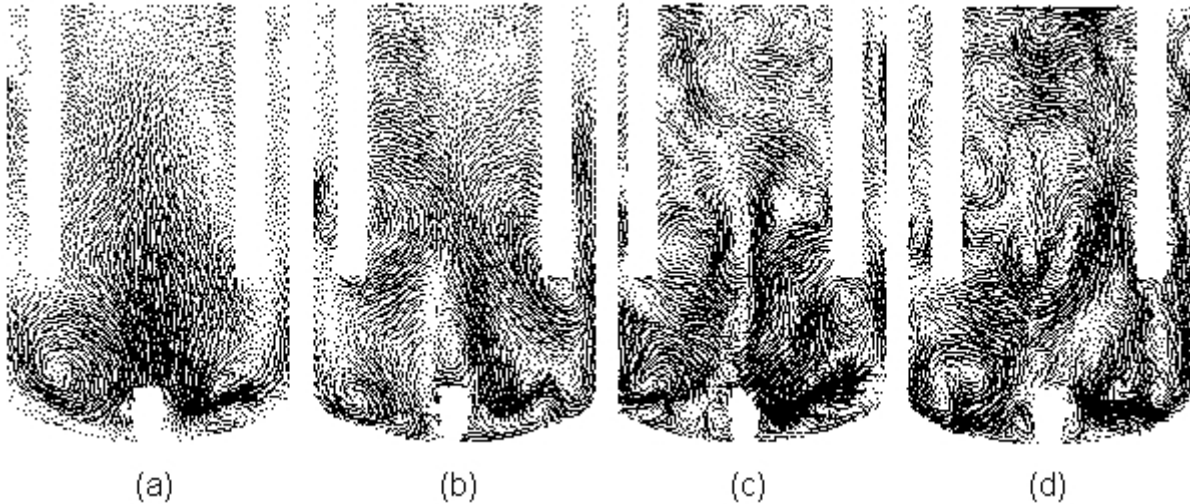
Figure 12.2. Axial-radial vector plots of the instantaneous velocity field obtained by CFD using different turbulence models (on the same grid): (a) k-ε; (b) RSM-SSG; (c) SST-SAS, $\Delta t = 0.3$ ms; SST-SAS, $\Delta t = 3$ ms.

The k-ε model leads to the lowest level of detail in the flow structures. This model predicts the existence of large turbulent structures but their temporal and spatial scales are often incorrect. In addition small-scale features are absent because of the chosen mesh size and the well-known tendency of the k-ε model to over-predict the eddy viscosity. The RSM-SSG model provides slightly more detail in the flow structure than the k-ε model as it can model the anisotropy of the turbulence structure. The smallest scales are observed is the SAS-SST results due to a better resolution of the turbulent spectrum and the detachment of many turbulent eddies from the blades and baffles. It was expected that the increase of the time step in the SAS-SST simulations may have an influence on the size of the turbulent structures. No visible differences were observed by changing the time step on the SAS simulations as shown in Figures 12.2(c) and 12.2(d). This suggests that the temporal resolution of the simulations is adequate.

Figure 12.3 shows contours plots of the predicted averaged axial velocity for the four cases of Figure 12.2, and also the experiment data obtained by PIV measurements. It was shown previously in Chapter 5 that the Reynolds Stress model gave numerical results close to

the vessel axis which disagree with the experimental data. In contrast, the experimental data were in good agreement with the numerical predictions obtained using the k-ε model. These previous results are complemented by the results of the two SST-SAS simulations (time steps equal to 0.3 and 3 ms). The numerical predictions were compared with each other and with experimental PIV data in a qualitative manner in Figures 12.3(c) and (d), and quantitatively on two horizontal lines located at different heights in the vessel in Figure 12.4.
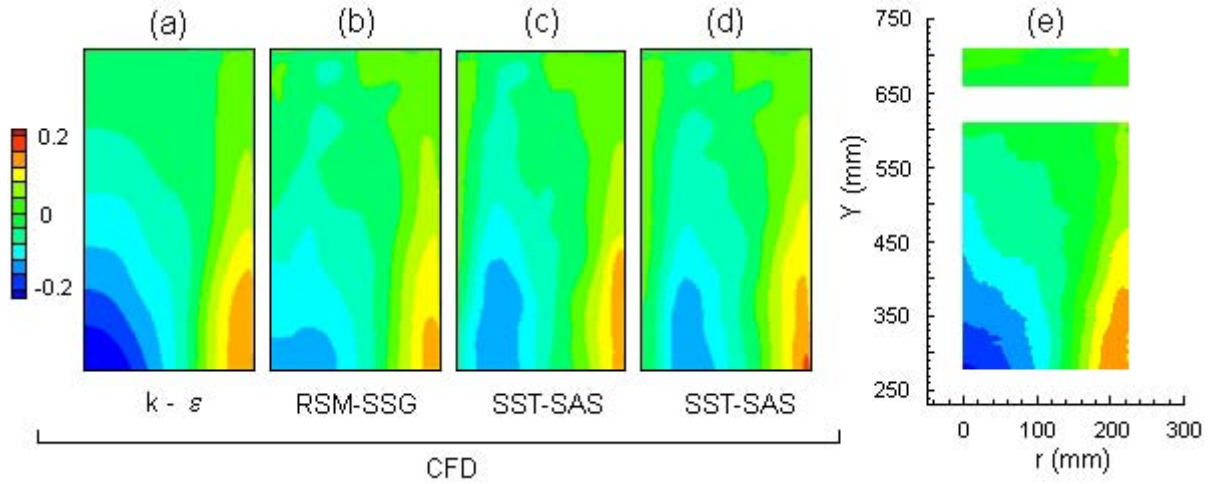
Figure 12.3. Contour plot of the averaged axial velocity obtained on the PIV plane and comparison with the experimental data. (a) k-ε model, averaging over 15 agitator rotations.; (b) RSM-SSG, averaged over 15 agitator rotation; (c) SST-SAS, Δt = 0.3 ms, averaged during 15 agitator rotations., (d) SST-SAS, Δt = 3 ms, averaged over 30 agitator rotations; (e) experimental PIV data.
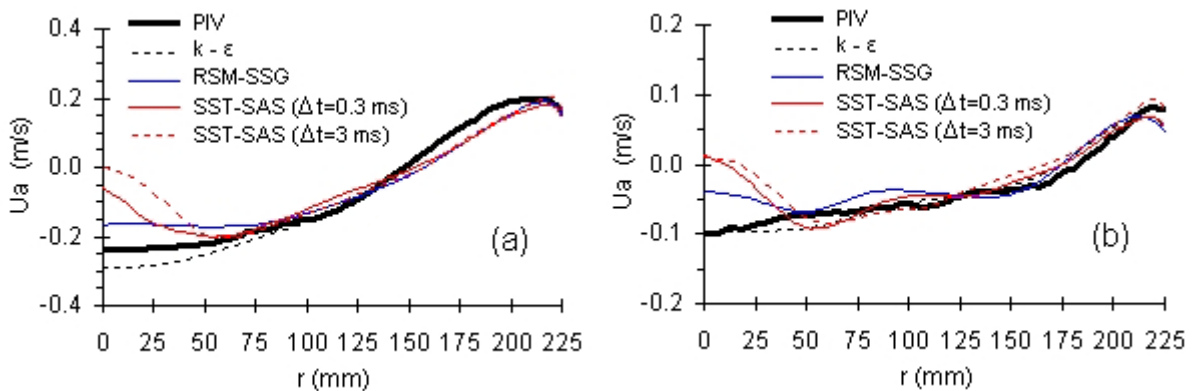
Figure 12.4. Comparison of the experimental PIV data and averaged numerical CFD predictions for the axial velocity values along the vessel radius at two different heights: (a) Y = 318 mm; (b) Y= 528 mm.

Although, the SST-SAS provides the finest flow details, as shown in Figure 12.2, it leads to a region of near zero velocity close to the vessel axis. This observation is presented for the axial velocity but it is also the case with the other velocity components. This feature looks

unphysical and is in contradiction with the experimental PIV data of Figure 12.3(e). The SAS model gives worse predictions than the RSM. In addition, these SAS conclusions are independent of the time-step as only minor differences are observed between Figures 12.3(c) and (d) and Figures 12.4(a) and (b).

In spite of the discrepancies observed close to the vessel axis for a radius below 60 mm, the numerical predictions in the other vessel regions are in good agreement with the experimental data. Unfortunately, the reasons why the SAS model produces a near-zero velocity region close to the vessel axis have not yet been understood. In our case, the k-ε model remains the best of the turbulence model tested, as it gives the best agreement with the PIV data.

12.1.5. <u>Concluding remarks</u>

The SAS modelling approach is one of the most promising turbulence approaches for the future. It has been shown that this model enables a very detailed velocity field to be obtained due to a partial resolution of the turbulent spectrum. This model may be a cost-effective alternative to LES methods, which are still difficult to perform due to the computer resources needed. Concerning the case investigate here, the predicted near-zero velocities close to the vessels axis seemed to be unphysical and are not in agreement with the experimental PIV data. Surprisingly, the simplest k-ε model gave the best agreement with experimental data for the velocity field. Currently there are no published data for rotating flows so it may be that this defect is appearing in simulations involving a rotating frame of reference.

A theoretical analysis and additional simulations for different cases need to be performed. An unbaffled, stirred vessel equipped with an eight-blade paddle impeller, which has been modelled recently by Haque *et al.* (2006), is currently being studied using the SST-SAS. The numerical results obtained will be compared with the experimental data given in the paper of Haque *et al.* (2006) in order to determine if the discrepancies observed are particular to this case or occur more generically in rotating flows.

12.2. A NOVEL APPROACH TO FREE-SURFACE MODELLING

It was demonstrated previously in Chapters 4 and 5 that an inhomogeneous multiphase model used with simplified physics can predict the vortex shape accurately. However, the complexity of the multiphase modelling approach, requiring one continuity equation and three momentum equations per phase plus equations for the turbulence variables, make this type of simulation computationally demanding. If the simulation is run in transient mode, as presented in Chapter 6 for an agitator stopping, the computational demand becomes very high (but much less than for example required by LES, DES or DNS in comparison). Although it was demonstrated that the use of this method gives good results, the major limitation may be the difficulty of adding much more complexity to the present modelling. For the particular interest of this study, the injection of a liquid jet in the gaseous space which impacts the free-surface leads to several numerical problems. The free-surface being defined as an isosurface of liquid volume fraction, the simulation of a case with a free-surface feed would imply the need to define "a priori" a jet entry position on an as yet undetermined free-surface or to simulate the passage of the jet though the gas space. Since the use of the inhomogeneous approach considers the gas phase as dispersed, the injection of a liquid in this region would require a more complex model that can treat air as a continuous phase in one part of the flow and as gas bubbles in another.

For the reasons given above it is difficult to combine the free-surface shape determination using the inhomogeneous approach and jet injection in the same simulation. To avoid the problem, the whole simulation has been split into two parts. Firstly, the inhomogeneous model was used to determine the free-surface shape for the stirred vessel. The coordinate of this free-surface were exported and input into a CAD-package. Then, all the volume above the free-surface was cut-away to make a new geometry which includes the real free-surface shape. The details of the free-surface construction procedure are presented in Appendix E.

Figure 12.5(a) shows the 3D geometry of the free-surface which corresponds to an isosurface of water volume fraction equal to 0.9 obtained with an agitator rotation speed of 275 RPM (this case has been detailed previously in Chapter 4). Figure 12.5(b) shows the final geometry and the virtual surface obtained with the free-surface cut away.

Figure 12.5. The mixing vessel with a free-surface: (a) free-surface shape calculated from an isosurface of water volume fraction equal to 0.9, N = 275 RPM, inhomogeneous approach; (b) the modified geometry with the free-surface used to cut away the gas space.

The smoothing process used for the generation of the free-surface is responsible for a lower level of detail compared with the initial free-surface shape. Figure 12.6 shows the comparison between mesh on the predicted free-surface (Figure 12.6(a)) and the virtual one (Figure 12.6(b)).
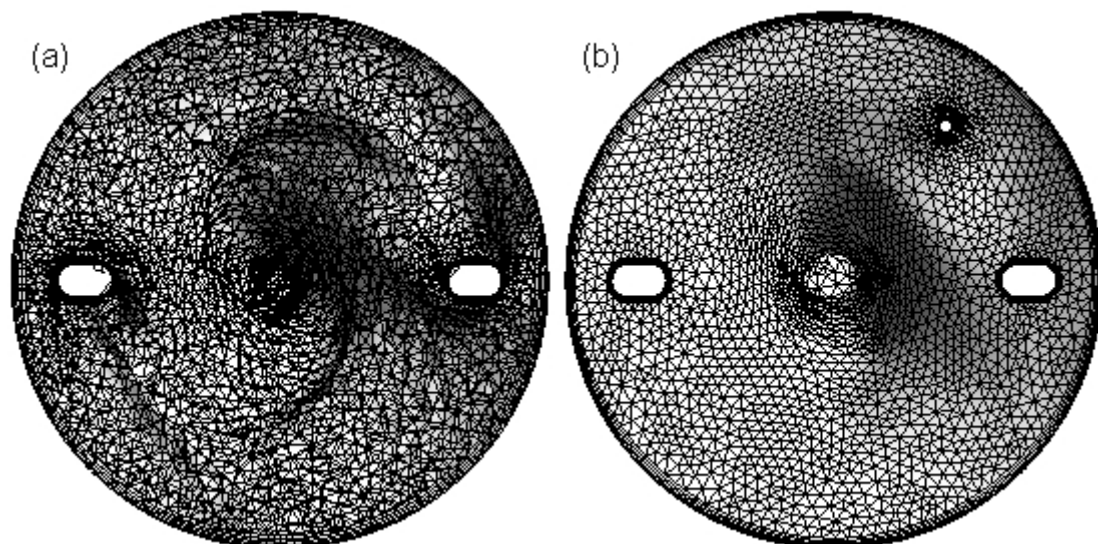
Figure 12.6. Details of the mesh on the free-surface shown from above: (a) inhomogeneous approach; (b) free-surface cut-away, note the jet injection location in the top right quadrant.

It is obvious that the global shape is respected, but the smaller details, for example, the wake at the rear of the baffles, are not conserved. The main target of this test was to generate a virtual surface which allowed a good quality mesh to be generated rather than to take account of all of the fine-scale detail of the free-surface.

12.2.1. <u>Details of the CFD modelling</u>

A test was made to determine the answer to the following question: are the calculated hydrodynamics results accurate if the free-surface is replaced by a solid boundary? To answer this question, a simulation was performed with the geometry having the free-surface cut away. The mesh was composed of 496,550 nodes, arising from more than two millions elements (2,113,082 exactly). Although no grid independency study have been performed with this case due to time constraints, the mesh was finer than in the previous cases where grid independency was performed. The mesh has been refined in the jet injection area, on a vertical line below the injection point (using the same settings as given in Chapter 8) and inflation meshing has been used at all walls to capture the boundary layer. The simulation was performed in steady-state (frozen rotor approach), using a single phase model (water at 25 °C), standard k-ε model and automatic wall functions. The agitator rotation speed was set to 275 RPM in order to compare the results obtained with previous simulations. A no-slip boundary condition was applied at all walls except the new free-surface where a free-slip condition was used (zero shear stress at the boundary). For the simulations that consider jet injection, the inlet surface was the imprint on the free-surface of a vertical cylinder of diameter d = 10 mm, centred on the "*Initial*" injection point (see Chapters 7 and 8). The mass flow rate was calculated using the initial jet diameter and a jet velocity equal to 6 m s^{-1}. The direction of the jet was set on the inlet surface (located on the free-surface) to have velocity directed vertically downwards. The timestep was set to 1 ms and the simulation was deemed to be converged when the normalized residuals fell below 10^{-5}.

12.2.2. <u>Results</u>

The liquid velocity results obtained with the inhomogeneous model are shown in Figure 12.7(a) and have been compared with the results of Figure 12.7(b) obtained using the free-surface cut-away strategy. It is readily observed that the free-surface strategy has not

introduced any significant differences compared with the original case. Although the gas column on the vessel axis is not present in Figure 12.7(b), the velocities in the central vessel region are comparable. A good agreement is also obtained for the velocities close to the free-surface.
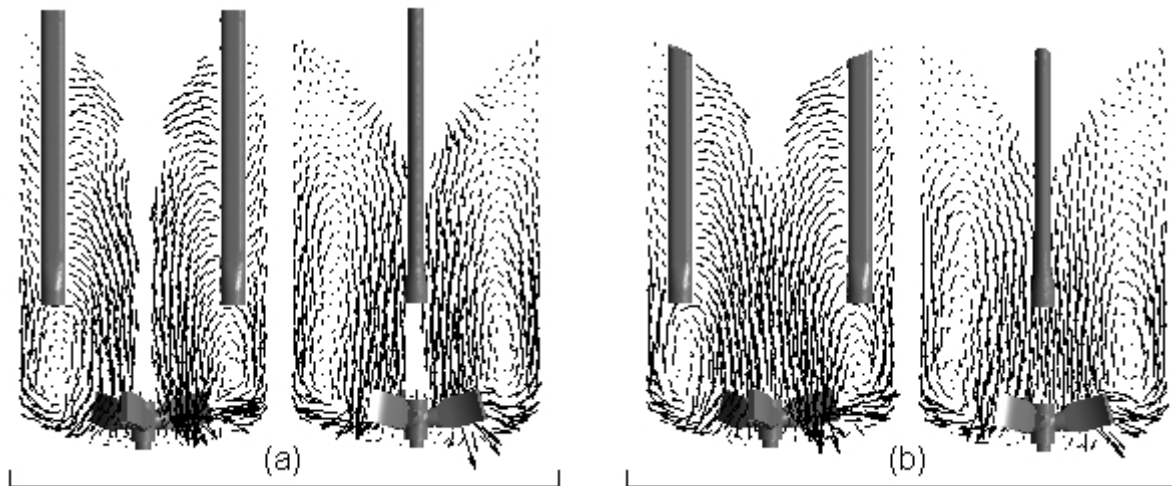
Figure 12.7. Axial-radial velocity vector plots: (a) inhomogeneous approach; (b) free-surface cut-away strategy.

A more quantitative comparison is proposed in Figure 12.8, where the three components of the velocity (U_x, U_y and U_z) are compared on four different lines located in the baffle plane. Three are horizontal at $Y = 0.2$, 0.4 and 0.6 m from the bottom tank, and one is vertical line at $r = 75$ mm from the vessel axis.

Minor differences only are observed and a very good agreement is obtained. It can be concluded that the modelling using the single phase approach gives the same results concerning the velocities as the inhomogeneous approach. As, the inhomogeneous model has proved to give a free-surface shape and velocity fields in good agreement with experimental data in Chapter 4 and in Chapter 5, respectively, it may be assumed that using a free-surface cut-away strategy allows the accurate calculation of the velocity field in the vessel.
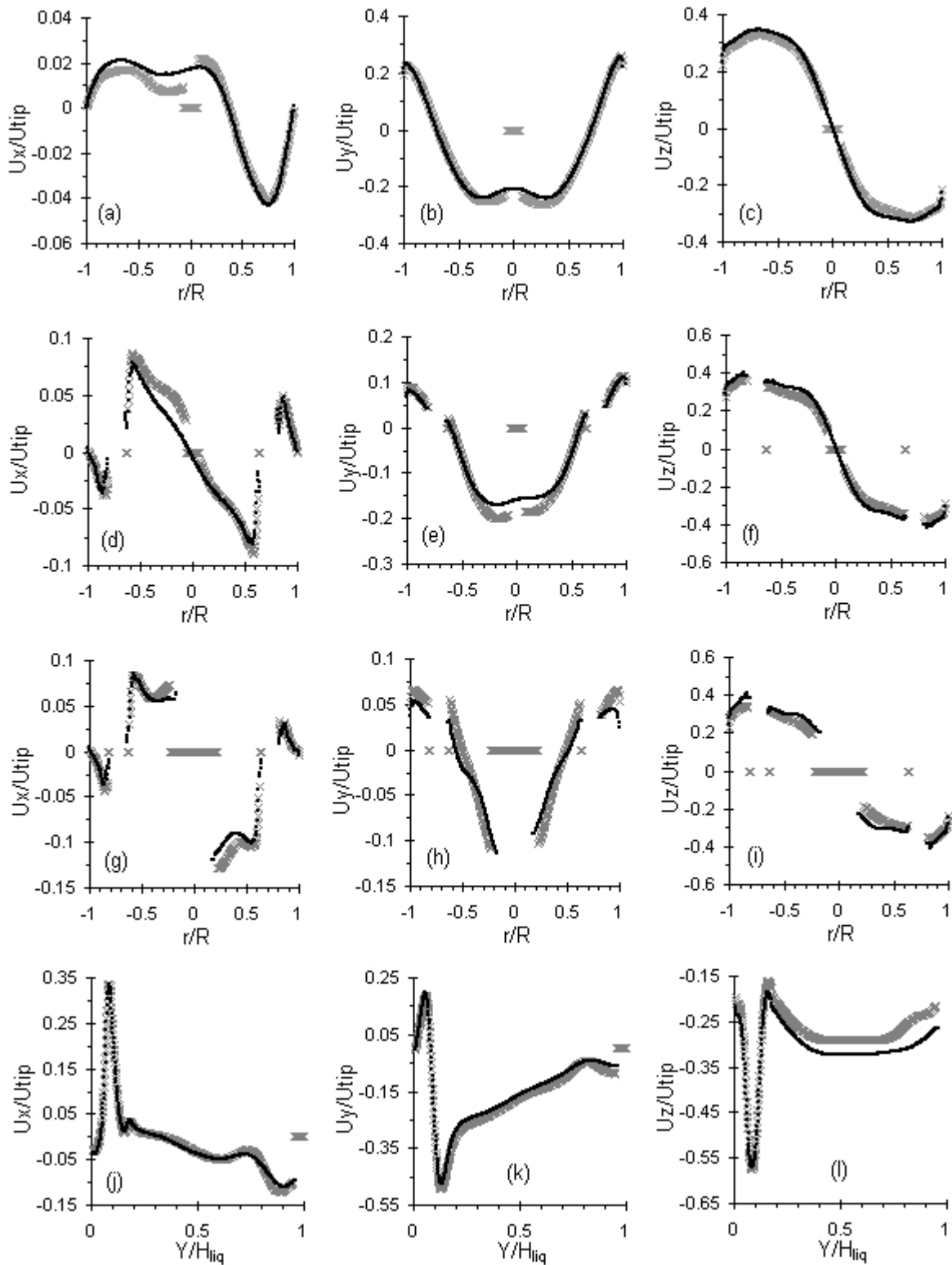
Figure 12.8. Comparison of the radial U_x, axial U_y and circumferential (U_z) velocity values on different locations on the baffle plane (N = 275 RPM) for the inhomogeneous model (black symbols) and the free-surface cut strategy (grey symbols). (a), (b),(c): Y = 200 mm; (c), (d), (e): Y = 400 mm; (f), (g), (h): Y = 600 mm, (i), (j), (k): vertical line at r = 75 mm from the vessel axis.

The last step was to run a simulation with jet injection located on the virtual free-surface. The results are shown in Figure 12.9.
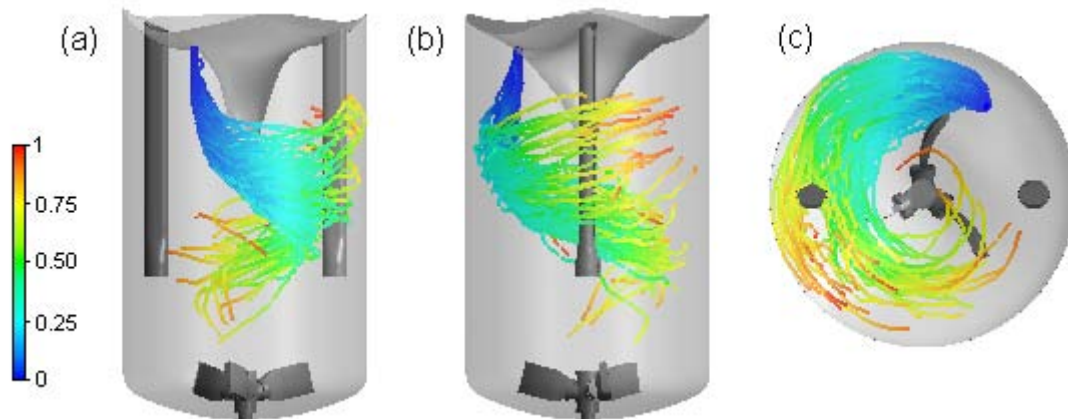
Figure 12.9. Jet injection on a deformed free-surface. Lagrangian jet trajectories coloured by the Lagrangian particle travel time normalized by T_{inj}, for d = 10 mm, V = 6 m s^{-1} and N = 275 RPM, plotted at T_{inj} with 200 particles. (a) XY lateral; (b) YZ lateral view; (c) top view.

As the main purpose was to demonstrate the feasibility of the proposed methodology, no further calculations have been made with this simulation.

12.2.3. **Concluding remarks**

Therefore, to simplify the simulation of mixing vessels with a deformed free-surface, the process can be decomposed into two steps. Instead of trying to do everything in the same simulation (quasi-impossible) or make the wrong assumption of a flat free-surface, the proposed methodology is as follows:

- first, use the inhomogeneous approach to predict the free-surface shape;
- then, use a CAD package to generate a new geometry with a virtual free-surface;
- finally, a complex simulation can be carried out (blending solids, jet mixing…) using the real free-surface shape.

From the author's point of view, this opens up a different and interesting way of thinking about the simulation of agitated vessels with deformed free-surfaces.

Chapter 13

GENERAL CONCLUSION

The mixing vessels investigated in this study are partially-baffled systems. The baffling effect is not sufficient to prevent the high swirling movement of the fluid imparted by the agitator, and therefore the free-surface is deformed and a vortex is created. The experimental characterization and the numerical prediction of this vortex was an important component of the work presented in this thesis, as this vortex shape differs significantly from the classical and usual vortex shapes obtained in unbaffled agitated vessels. The strong instability of the free-surface due to the complex entrainment/disentrainment of air bubbles at the air/water interface lead to the development of an original experimental imaging process to determine this very unusual vortex shape. A video acquisition method based on the superposition of images was used and shown to have the capability to determine accurately the shape of the vortex at different rotation speeds. This vortex shape has been predicted numerically by using a new simulation strategy for the prediction of free-surface deformation in stirred vessels. An inhomogeneous multiphase approach, which considers the water as the continuous phase and the air as the disperse phase, was used with simplified physics (single bubble diameter and constant drag coefficient) and coupled with homogeneous k-ε turbulence model. This model was able to predict a vortex shape in very good agreement with the experimental data. In steady-state, it was shown that the best agreement is obtained considering a water isosurface of volume fraction equal to 0.9, due to the presence of the dynamical equilibrium zone of intense gas/liquid exchange which occurs around the free-surface. However, as it was shown that this inhomogeneous approach does not converge well at low rotation speeds, transient simulations using the sliding-mesh approach had to be performed.

Important results were obtained from transient simulations performed at constant agitator speed using a single phase or multiphase approach. After initialization with a steady-state result, it was shown that at 100 RPM the system required simulation of at least five impeller rotations to break down the initial flow pattern and that meaningful averaging could only begin after around fifteen revolutions. This averaging process must be maintained during fifteen more agitator rotations. One important conclusion was to determine that such transient

sliding-mesh simulations require a significant number (here at least thirty) of agitator rotations to obtain reliable results. Due to the constant increase of pressure to deliver industrial results quickly, everyone has to keep in mind that performing reliable transient simulations of mixing vessels highlights the need to be vigilant concerning the total number of agitator rotations to be performed. The time-averaged results show a similar flow structure to the steady-state results but, in addition, highlight the complex, unsteady nature of flow. The simulation of the transient flow structure showed vorticity filaments which rotate in the vessel at low frequency, and an in-depth analysis of the variation of the local instantaneous velocity revealed the presence of macro-instabilities. Using single-phase flow and a flat free-surface, transient simulations allowed the comparison of experimental PIV data with numerical results obtained with different turbulence models: the Reynolds-Stress model (RSM-SSG) which is known to perform well for swirling flows as it takes in account the turbulence anisotropy, and the standard k-ε model. Surprisingly, the RSM predicted axial velocities which disagree with experimental data near the vessel axis. In contrast, the k-ε provided the best agreement with experimental PIV data and was therefore preferred for the configurations tested. Finally, power input studies were performed in terms of the power number of the agitator and good agreement was obtained between the experimental values and numerical predictions.

The transient modelling with free-surface deformation has been extended to the case where the agitator is stopping, this situation being frequently encountered industrially after a power failure of the plant. The simulations carried out with the inhomogeneous approach have demonstrated the accuracy of this numerical strategy even in these severe conditions of gas disengagement and decreasing agitator speed. The hydrodynamics in the vessels were able to be predicted during the stopping phase, as well as during the inertial period after the agitator has stopped. It was demonstrated that the agitator stopping introduced inertial effects in the flow implying that this type of simulation cannot be conducted as a succession of steady-states. In addition, the dynamics of the free-surface evolution and the predicted gas disentrainment from the agitator region to the free-surface during the stopping phase were in good agreement with experimental data.

More generally, the inhomogeneous multiphase approach used here for modelling a partially-baffled vessel with a free-surface, in steady-state, transient with constant or decreasing agitator rotation speed, shows very promising result for the computation of hydrodynamics in other stirred vessels which have non-negligible free-surface deformation.

This method remains numerically affordable and allows the numerical assumption of a flat free-surface, often made in computational studies, to be relaxed.

Mixing time experiments were carried out with a colouring/decolouring technique and revealed other important results of this study. A Design of Experiments (DoE) approach, coupled with an analysis of variance, allowed the construction of an experimental mixing time model which included five operating parameters: agitation speed, injection pressure, pipe injection diameter and injection location characterized by two Cartesian coordinates. This polynomial-based model generalized here the classical dimensionless mixing time model and allowed it to be used as an optimization tool. Firstly, that current industrial injection location was shown to be non-optimal but is acceptable if the jet velocity and jet diameter are optimized. Secondly, there exists a strong coupling effect between the injection pressure and the pipe diameter.

Therefore, the effects of the jet diameter and the jet velocity have been studied both experimentally and numerically, maintaining the injection location at its initial position. Experimentally, the jet trajectories have been visualized using UV fluorescence to limit the uncertainties associated with the entrainment of air bubbles by the free-falling jet. This method was shown to perform well, and allowed the liquid jet penetration behaviour into the bulk during the injection period to be visualised. Numerically, an Eulerian-Lagrangian approach, that used a single-phase flow model in which the modification of the bulk hydrodynamics by the jet momentum was taken in account, has been developed to investigate the effect of the jet injection parameters on the jet trajectory. At the same time, the transport of a passive scalar was used in order to correlate the influence of the jet trajectory with the quenching efficiency, by analysing the scalar concentration distribution versus time. Lagrangian particle tracks were used to highlight very clearly the jet trajectories in the mixing vessel. It was demonstrated that an optimum jet momentum flux exists to maximize the quenching efficiency of the vessel. A jet momentum flux significantly below the optimal value lead to weak penetration of the jet into the bulk, implying a rapid deflection of the jet plume towards the centre of the vessel where it enters a swirling flow. In contrast, a jet momentum significantly above the optimal momentum flux results in the injected fluid accumulating in the reactor base thus creating zones that are not quenched in the upper part of the reactor. Two separate ways to compare the effect of different injections conditions or more generally to quantify the reactor quenching, have been proposed: (i) the establishment

and the analyse of quenching curves giving the percentage of the quenched vessel volume versus time; (ii) the use of new global mixing criteria adapted for safety issues, denoted t_{50} and t_{90} which gives the time to quench 50% and 90% of the reactor volume, respectively. The results demonstrated that it is not necessary to use a very high momentum driven jet to decrease the quenching time and revealed that the optimized injection condition has to be set in order to maximize the mixing benefits of the bulk flow patterns.

Finally, the numerical know-how and background learnt for pilot-scale simulations was used to investigate, with confidence in the developed models, the hydrodynamics, free-surface-shape, power input, jet trajectories and reactor quenching at the industrial scale. Two different industrial synthesis reactors of Tessenderlo Group were studied using CFD simulations. The suspension PVC synthesis reactors, located either in the French PVC plant of Mazingarbe or the Dutch plant of Beek, are both partially-baffled but equipped with different agitators and baffles. CFD simulations for the two different reactors allowed analysis of the hydrodynamics of the two vessels, and their vortex shapes to be determined. For the Mazingarbe reactor, two configurations of baffle positions have been tested, allowing their influence on the vortex shape and power input to be studied.

Jet mixing studies have been performed using CFD in one of the industrial reactor where experimental data on the current injection conditions were available. Experiments carried out at the Mazingarbe plant have demonstrated that the contents of the synthesis reactor are in contact with the killer agent quasi-instantaneously as the rupture disk of the injection system bursts immediately (< 1 s) after the killer vessel is pressurised. In addition, calculations were made for the current killer jet velocity equal to 1.55 m/s (corresponding to a total draining time of 15 seconds). By using the CFD methods validated previously at the pilot reactor scale, four different jet velocities, chosen as multiples of the current injection velocity V_o, have been tested for two agitator speeds (equal to the nominal agitator speed and half of this value). The CFD simulation allowed prediction of the killer jet trajectory in the industrial stirred vessels and quantification of the quenching efficiency. For the current jet injection velocity equal to $V_o = 1.55$ m/s, very weak downward jet penetration was predicted, leading to an immediate bending of the jet plume very close to the free-surface due to the combined effects of the high tangential movement of the stirred fluid in this region and the weak jet momentum flux. From these injection conditions, the injected fluid is constrained to follow the tangential bulk flow, leading to very rapid entrapment by the swirling flow at the vessel centre. It was demonstrated

for the pilot reactor that this type of injection is not favourable for efficient mixing. The optimized industrial jet velocity was found to be equal to ten times the current velocity to maximize the benefits of the reactor hydrodynamics. For the actual nominal agitator rotation speed, since increasing the current velocity by a factor of five lead to a reduction of the value of t_{90} by 36%, the optimized jet velocity is reached for $V = 10V_o$ where the value of t_{90} is reduced by 57% compared with the current injection conditions. Finally, the author proposed a scale-up method of the optimized jet velocity by using the tangential momentum flux of the agitator and the jet momentum flux. This method allowed predictions of the jet velocity with relatively good agreement with the industrial simulation results.

For both for the pilot and the industrial scales, the analysis of the numerical Lagrangian tracks used for the jet modelling allow construction of a correlation to quantify the jet trajectory. By using an analogy derived from jet in cross-flow literature studies, the non-linear fitting of the cloud of points generated by the Lagrangian particle tracks allowed description of the jet trajectory in the form of a non-dimensional correlation, which is only a function of the jet velocity, the jet diameter and the jet injection location coordinates. One very interesting result is that the correlation is found to be independent of the reactor scale. This analysis allowed definition of a penetration depth which was used to quantify the jet penetration provided by of the current industrial injection conditions and to estimate the potential of improvement which could be reached by increasing the jet injection velocity. The optimized velocity of $10V_o = 15.5$ m/s, found by using the quenching curves, gives a penetration depth of 47 % of the total liquid height instead of 7% with the actual jet velocity of 1.55 m/s. This means that the liquid jet would penetrate to a depth of 2.3 m below the free-surface instead 0.32 m as it does at the present (visualized on the vessel axis) which is seven times better than the present configuration. Finally, a dimensionless quantity, based on the ratio between the jet momentum flux and the tangential momentum flux of the agitator, has been proposed for scaling-up the results of the optimized industrial injection velocity.

Therefore, the actual killer system allows the bursting of the rupture disk within a second but the total draining time of the killer is so high (15 seconds) that the current system prevents an efficient quenching of the PVC reactors. To improve the actual industrial system it was demonstrated that the jet injection velocity must be increased, the optimized jet velocity being found to be equal to ten times the current velocity (15.5 m/s instead of 1.55 m/s). Technical

and practical industrial proposals have been submitted to Tessenderlo Group (Torré, 2007) that can easily improve the current injection system of the Mazingarbe industrial reactors.

Chapter 14

LOOKING TOWARDS THE FUTURE

Some interesting perspectives of this work have begun to be tested during this thesis, but should be investigated in more depth in future studies.

A new turbulence modelling approach, named Scale Adaptive Simulation, used with the Shear Stress Transport turbulence model has been tested in single phase with a flat free-surface, and the results were compared with both the previous numerical results and the PIV data. It was shown that this approach, which can operate in RANS and LES-mode without an explicit mesh dependency, allows very fine details of the instantaneous velocity field to be resolved due to the partial resolution of the turbulent spectrum. However, the reasons why the numerical predictions of the axial velocity close to the vessel axis were not in agreement with experimental data remain unexplained. As this modelling approach appears very promising for the future, a different mixing vessel (unbaffled) is currently being investigated to see if the problem encountered here is directly linked to the case studied here or, more generally, is linked to the rotating flow or reference frame.

A new way of thinking about the simulation of the mixing vessel with a free-surface was proposed. Instead of doing everything in the same simulation, or worse, making the wrong assumption of flat free-surface, the method proposed is: (i) to determine the free-surface shape with the use of the inhomogeneous approach and export its coordinates to a CAD package; (ii) modify the initial geometry by cutting away the volume above the free-surface; and (iii) a perform a single-phase simulation using a geometry which has the real free-surface shape. This single phase simulation, carried out with a free-slip surface having the real-free-surface shape lead to velocity fields identical to those obtained with the inhomogeneous model (validated previously by PIV experimental data). Finally, jet injection was simulated with this free-surface-cut geometry, which demonstrated the feasibility of this method. However, further analysis must be performed with this approach. For example, the effect of the free-surface deformation on the reactor quenching, in cases where the jet velocity is such

that the injected fluid is entrained in the centre vessel region (where the swirl develops), should be investigated.

Other interesting outcomes could also be proposed as future work of this study.

The inhomogeneous approach could be completed by refining the physical model used with addition of non-drag forces in the model as lift, virtual mass, etc. The model used in this study was built using really simplified physics, as the main purpose was to describe the vortex shape and not to model the gas/liquid process in detail but numerical improvements could be made using information from the paper of Lane *et al.* (2005). One can imagine also replacing the single bubble diameter by a gas bubble distribution as proposed in Laakkonen *et al.* (2007). With these refinements, the dynamics of the flattening process of the free-surface during the agitator stopping phase (for example) should be improved.

The results obtained in this study with water as the working fluid bring useful understanding to many situations in the real reactors since turbulent flow is maintained. Both experimentally and numerically, the real physical properties of the bulk fluid should be taken in account. It was noted during the literature surveys of this thesis that physical property data of the bulk fluid during PVC polymerization, particularly the viscosity, are very hard to find. The reasons for this lack of data are mainly due to: (i) difficulties in sampling the bulk medium as the PVC synthesis reaction is done in a pressurized autoclave (the vinyl chloride monomer is gaseous at ambient temperature); (ii) the well-known hazards linked to the monomer (extremely flammable and may cause cancer by inhalation); and (iii) the changing nature of the bulk fluid during polymerization from a fine liquid-liquid dispersion of monomer droplets to a final slurry of PVC. However, the published results of Cebollada *et al.* (1989) and especially those of Maggioris *et al.* (2000) and Kiparissides *et al.* (1997) could be used as a good starting point for future studies to evaluate the bulk physical properties. Numerically, it would be very interesting to study the influence of the viscosity on the scalar mixing and the reactor quenching. The problem is more difficult experimentally with the pilot installation designed for this study as it poses the problem of the use of a large quantity of viscous model fluid and its recycling.

In addition, the injected fluid could be made immiscible in the stirred fluid, as for example the injection of an organic solvent into water. This would enable the study of the trajectory of

a buoyant liquid jet injected into the stirred vessel, which is closer to the current industrial case. Experimentally, a harmless organic product, which has physical properties close to the organic killer agent currently used industrially, must be chosen. A previous literature survey carried out during the pilot reactor conception phase (not reported in this manuscript) has shown that the N-penthyl propionate (an ester used as pineapple artificial flavour) was one of the best substitute solvents for this purpose. Numerically, the case of the multiphase simulation of a free-surface injection of a buoyant jet into a mixing vessel would be very interesting and challenging. No published papers on this topic have been found.

The behaviour of a tracer mixing in a liquid-liquid dispersion, or a liquid-solid suspension, will be different to the studies carried out here for a homogeneous medium. This poses the question as to what extend the mixing process in a dispersed two-phase system differs from a single phase system. In addition, critical conditions are obtained where the liquid-liquid dispersion is transformed in two separated phases. This phenomenon, which occurs generally after an agitator failure (and in the worst case with the agitator functioning normally), is named phase separation. In processes involving liquid-liquid dispersions, a lot of problems are due to these phase separations. In the case considered in this study, the monomer droplets are less dense than the water phase and when phase separation occurs at the beginning of the polymerization (the most critical case), the reaction mass is located on top while the water phase drains to the bottom of the reactor. It would be interesting to compare the mixing time to the phase separation time, and to study the quenching process in these conditions. It would also be very interesting to study, as a first step, how jet injection and tracer mixing behave in normal liquid-liquid dispersion conditions – for example using a suspension of 1-chlorobutane in water (see Hong *et al.* (2006), Padovan and Woods (1986)) – and, in a second step, to extend the study to the case of a phase separation.

As presented at the beginning of this manuscript, the entire problem which concerns the quenching of runaway reactions is very complex as it touches various scientific domains. The studies carried out in this thesis were focussed mainly on hydrodynamics, as the macro-mixing of the species in the mixing vessel is the first step to achieve. The next step to satisfy is the mixing at the molecular scale (micro-mixing). A lot of experimental work has been done concerning the micro-mixing but few papers are available in the literature concerning the coupling between chemical reactions and CFD. Several progressive levels of complexity could be considered: the first is the introduction of the kinetics of the exothermic reaction

function of the scalar concentration to predict the temperature distribution with considering only the macro-mixing (e.g. Dakshinamoorthy and Louvar, 2007). A second and much more complicated step would be to integrate micro-mixing models, chemical reactions and advanced turbulence models into the simulations (e.g. van Vliet *et al.*, 2007). The final level would be to use these models coupled to safety process criteria to study critical runaway conditions.

REFERENCES

- A -

Abbott, M. B. & Basco, D. R. (1989). *Computational fluid dynamics: an introduction for engineers.* Longman.

Abid, R. & Speziale, C. G. (1993). Predicting equilibrium states with Reynolds stress closures in channel flow and homogeneous shear flow. *Physics of Fluids A*, 5 (7), 1776-1782.

Abramovich, G. N. (1963). The theory of turbulent jets. *English translation published by M.I.T. Press, Massachusetts.*

Adrian, R. J. & Yao, C. S. (1985). Pulsed laser technique application to liquid and gaseous flow and the scattering power of seed materials, Applied Optics, 24(1), 44.52.

Adrian, R. J., (1991). Particle imaging techniques for experimental fluid mechanics. *Annual Rev. Fluid Mech.*, 23, 261-304.

Adrian, R. J. (2005). Twenty years of particle image velocimetry. Experiments in Fluids, 39, 159-169.

Aggarwal, M. L., Goel, A. & Chowdhury, S. R. (1997). Catalogue of group structures for two-level fractional factorial designs. *J. Applied Statistics.* 24(4), 437-451.

Alcamo, R., Micale, G., Grisafi, F., Brucato, A. & Ciofalo, M. (2005). Large-eddy simulation of turbulent flow in an unbaffled stirred tank driven by a Rushton turbine. *Chem. Eng. Sci.*, 60 (8-9), 2303-2316.

Alexis, J. (1995). *Pratique industrielle de la méthode Taguchi.* Ed. Afnor, Paris.

Alliet-Gaubert, M., Sardeing, R., Xuereb, C., Hobbes, P., Letellier, B. & Swaels, P. (2006). CFD analysis of industrial multi-staged stirred vessels. *Chem. Eng. and Process.*, 45(5), 415-427.

Allsopp, M. W. & Vianello, G. (1992). Poly(Vinyl Chloride). *Ullmann's encyclopaedia of industrial chemistry*, A21, 717-742.

ANSYS-CFX 10.0 (2006). User's guide (http://www.ansys.com).

Armenante, P. M. & Chou, C.-C. (1994). Experimental LDV measurement and numerical CFD determination of the fluid velocity distribution in an unbaffled mixing vessel. *A.I.Ch.E. Symposium Series*, 90 (299), 33-40.

Armenante, P. M. & Huang, Y. T. (1992). Experimental determination of the minimum agitation speed for complete liquid-liquid dispersion in mechanically agitated vessels. *Ind. Chem. Chem. Res.*, 31(5), 1398-1406.

Armenante, P.M., Luo, C., Chou, C.-C., Fort, I. & Medek, J. (1997). Velocity profiles in a closed, unbaffled vessel: comparison between experimental LDV data and numerical CFD predictions. *Chem. Eng. Sci.*, 52 (20), 3483-3492.

Aslan, N. & Cebeci, Y. (2007). Application of Box–Behnken design and response surface methodology for modeling of some Turkish coals. *Fuel*, 86(1-2), 90-97.

Aubin, J. (2001). Mixing capabilities of down and up pumping axial flow impellers in single phase and gas liquid systems: experimental and CFD studies. *PhD Thesis, INP,* Toulouse.

Aubin, J., Fletcher D. F. & Xuereb, C. (2004). Modeling turbulent flow in stirred tanks with CFD: the influence of the modeling approach, turbulence model and numerical scheme. *Exp. Therm. Fluid Sci.*, 28(5), 431-445.

Aubin, J., Kresta, S. M., Bertrand, J., Xuereb, C. & Fletcher, D. F. (2006). Alternate operating methods for improving the performance of continuous stirred tank reactors. *Chem. Eng. Res. Des.*, 84(A7), 569-582.

- B -

Bakker, A. & Gates, L. E. (1995). Properly choose mechanical agitators for viscous liquids. *Chem. Eng. Prog.*, 91 (12), 25-34.

Balasubramanian, S. G., Dakshinamoorthy, D. & Louvar, J. F. (2003). Shortstopping runaway reactions. *Process Safety Progress*, 22(4), 245-251.

Balasubramanian, S. G. & Louvar, J. F. (2002). Study of major accidents and lessons learned. *Process Safety Progress*, 21(3), 237-244.

Baldyga, J., Bourne, J. R. & Yang Yang (1993). Influence of feed pipe diameter on mesomixing in stirred tank reactors. *Chem. Eng. Sci.*, 48(19), 3383-3390.

Bałdyga J. & Pohorecki, R. (1995). Turbulent micromixing in chemical reactors - a review. *The Chem. Eng. J. and the Biochem. Eng. J.*, 58(2), 183-195.

Barclay, L. M. (1976). Formation and structure of PVC particles. *Die Angew. Makromol.* Chem., 52, 1-20.

Barton, J. A. & Nolan, P. F. (1989). Incidents in the chemical industry due to thermal runaway chemical reactions. *Hazards X: Process safety in fine and specialty chemical plants, Symposium series*, 115, 3-18.

Basara, B. & Younis, B. A. (1995). Assessment of the SSG pressure-strain model in two-dimensional turbulent separated flows. *Appl. Sci. Res.*, 55(1), 39-61.

Baudou, C., Xuereb, C. & Bertrand, J. (1997). 3-D Hydrodynamics generated in a stirred vessel by a multiple propeller system. *The Canadian Journal of Chemical Engineering*, 75, 653-663.

Bhattacharya, S. & Kresta, S. M. (2006). Reactor performance with high velocity surface feed. *Chem. Eng. Sci.*, 61 (9), 3033-3043.

Bidone, G. (1829). Expériences sur la forme et sur la direction des veines et des courants d'eau lances par diverses ouvertures. *Imprimerie Royale*, Turin, 1-136.

Bin, A. K. (1993). Gas entrainment by plunging liquid jets. *Chem. Eng. Sci.*, 1993, 48(21), 3585-3630.

Bovey, F. A. & Winslow, F. H (1979). *Macromolecules - An introduction to Polymer Science.* Academic Press, Inc.

Box, G. E. P. & Behnken, D. W. (1960). Some new three level designs for the study of quantitative variables. *Technometrics*, 2(4), 455-475.

Braga Jr., L. R., Brooman, J. H. P., Alves, J. J. N., Vasconcelos L. G. S. & Brito, R. P. (2006). Modelling and simulation of inhibition-injection systems applied to polymerization reactors. *Journal of Loss Prevention in the Process Industries*, 19(6), 736-742.

Brennan, D. J. (1976). Vortex geometry in unbaffled vessels with impeller agitation. *Trans. Instn. Chem. Engrs.*, 54, 209-217.

Brennan, D. J. & Lehrer, I. H. (1976). Impeller mixing in vessels experimental studies on the influence of some parameters and formulation of a general mixing time equation. *Trans. Instn. Chem. Engrs.*, 54, 209-213.

Brooks, B. W. (1997). Why are polymerizations reactors special? *Ind. Eng. Chem. Res.*, 36, 1158-1162.

Brucato, A., Ciofalo, M., Grisafi, F. & Micale, G. (1998). Numerical prediction of flow fields in baffled stirred vessels: a comparison of alternative modelling approaches. *Chem. Eng. Sci.*, 53 (21), 3653-3684.

Budwig, R. (1994). Refractive index matching methods for liquid flow investigations. *Exp. in Fluids*, 17(5), 350-355.

Burgess, R. H. (1982). *Manufacture and processing of PVC*. Applied Science Publishers, London.

Butcher, M. & Eagles, W. (2002). Fluid mixing re-engineered. *Chem. Eng.*, 733, 28-29.

Church, J. C. & Shinnar, R. (1961). Stabilizing liquid-liquid dispersions by agitation. *Ind. and Eng. Chemistry*, 53(6), 479-484.

- C -

Cabaret, F., Bonnot, S., Fradette, L. & Tanguy, P. A. (2007). Mixing time analysis using colorimetric methods and image processing. *Ind. Eng. Chem. Res.*, 46(14), 5032-5042.

Campolo, M., Paglianti, A. & Soldati, A. (2002). Fluid dynamic efficiency and scale-up of a retreated blade impeller CSTR, *Ing. Eng. Chem. Res.*, 41, 164-172.

Campolo, M., Sbrizzai, F. & Soldati, A. (2003). Time-dependent flow structures and Lagrangian mixing in Rushton-impeller baffled-tank reactor. *Chem. Eng. Sci.*, 58(8), 1615-1629.

Campolo, M. & Soldati, A. (2002). Appraisal of fluid dynamic efficiency of retreated-blade and turbofoil impellers in industrial-sizes CSTRs. *Ind. Eng. Chem. Res.*, 41, 1370-1377.

Cartland Glover, G. M. & Fitzpatrick, J. J. (2007). Modelling vortex formation in an unbaffled stirred tank reactors. *Chem. Eng. J.*, 127, 11-22.

Cebollada, A. F., Schmidt, M. J., Farber, J. N., Capiati, N. J. & Vallés, E. M. (1989). Suspension polymerization of vinyl chloride: I. Influence of viscosity of suspension medium on resin properties. *J. Appl. Polym. Sci.*, 37, 145-166.

Chanson, H., Aoki, S. & Hoque, A. (2004). Physical modelling and similitude of air bubble entrainment at vertical circular plunging jets. *Chem. Eng. Sci.*, 59(4), 747-758.

Chung, S. Y., Landsittel, D., Chon, C. H., Ng, C. S. & Fuchs, G. J. (2005). Laparoscopic skills training using a webcam trainer. *The Journal of Urology*, 173(1), 180-183.

Ciofalo, M., Brucato, A., Grisafi, F. & Torraca, N. (1996). Turbulent flow in closed and free-surface unbaffled tanks stirred by radial impellers, *Chem. Eng. Sci.*, 51(14), 3557-3573.

Cokljat, D., Slack, M., Vasquez, S. A., Bakker, A. & Montante, G. (2006). Reynolds-Stress model for Eulerian multiphase. *Progress in Computational Fluid Dynamics*, 6(1/2/3), 168-178.

- D -

Dakshinamoorthy, D., Khopkar, A.R., Louvar, J.F. & Ranade, V.V. (2004). CFD simulations to study shortstopping runaway reactions in a stirred vessel. *Journal of Loss Prevention in the Process Industries*, 17, 355-364.

Dakshinamoorthy, D., Khopkar, A.R., Louvar, J.F. & Ranade, V.V. (2006). CFD simulation of shortstopping runaway reactions in vessels agitated with impellers and jets. *Journal of Loss Prevention in the Process Industries*, 6, 570-581.

Dakshinamoorthy, D. & Louvar, J. F. (2007). Shortstopping and jet mixers in preventing runaway reactions. *Chem. Eng. Sci.*, *in press*, doi:10.1016/j.ces.2007.05.008.

Dakshinamoorthy, D. & Louvar, J. F. (2006). Hotspot distribution while shortstopping runaway reactions demonstrate the need for CFD models. *Chem. Eng. Comm.*, 193, 537-547.

Danckwerts, P. V. (1952). The definition and measurement of some characteristics of mixtures. *Appl. Sci. Res.,* A(3), 279-296.

Davidson J. A. & Witenhafer, D. E (1980). Particle structure of suspension Poly(Vinyl Chloride) and its origin in the polymerization process. *J. Polym. Sci.*, 18, 51-69.

Davoust, L., Achard, J. L. & El Hammoumi, M. (2002). Air entrainment by a plunging jet: the dynamical roughness concept and its estimation by a light absorption technique. *Int. J. Multiphase Flow*, 28(9), 1541-1564.

Derksen, J. J. (2003). Numerical simulation of solids suspension in a stirred tank. *AIChE. Journal*, 49, 2700-2714.

Derksen, J. J., Van den Akker, H. E. A. (1999). Large Eddy Simulations on the flow driven by a Rushton impeller. *AIChE Journal*, 45(2), 209-221.

Dickey, D.S., Bittorf, K. J, Ramsey, C. J & Johnson, K. E. (2004). Understand flow patterns in glass-lined reactors. *Chem. Eng. Progress*, November Vol., 21.25.

Doehlert, D. H. (1970). Uniform shell designs. *Journal of the Royal Statistical Society*, 19(C), 231-239.

Dong, L., Johansen, S. T. & Engh, T. A. (1994a). Flow induced by an impeller in an unbaffled tank (I): experimental. *Chem. Eng. Sci.*, 49 (4), 549-560.

Dong, L., Johansen, S. T. & Engh, T. A. (1994b). Flow induced by an impeller in an unbaffled tank (II): numerical modelling. *Chem. Eng. Sci.*, 49 (20), 3511-3518.

Dorr, R., Ozu M. & Parisi, M. (2007). Simple and inexpensive hardware and software method to measure volume changes in Xenopus oocytes expressing aquaporins. *Journal of Neuroscience Methods*, 161(2), 301-305.

Dhotre, M. T. & Smith, B. L. (2007). CFD simulation of large-scale bubble plumes: comparisons against experiments. *Chem. Eng. Sci.*, 62(23), 6615-6630.

Ducci, A. & Yianneskis, M. (2007). Vortex tracking and mixing enhancement in stirred processes. *AIChE Journal*, 53(2), 305-315.

Duhamel, P. & Vetterli, M. (1990). Fast Fourier transforms: A tutorial review and a state of the art. *Signal Processing*, 19(4), 259-299.

- E -

El Hammoumi, M., Achard, J. L. & Davoust, L. (2002). Measurements of air entrainment by vertical plunging liquid jets. *Exp. in Fluids*, 31, 624-638.

Endo. K. (2002). Synthesis and structure of poly(vinyl chloride). *Prog. Polym. Sci.*, 27, 2021-2054.

Esch, T. & Menter, F. R. (2003). Heat transfer predictions based on two-equation turbulence models with advanced wall treatment. *Turbulence, Heat and Mass Transfer 4,* Begel House, Inc.

Etchells, J. C. (1996). Runaway. *Chem. Eng.*, Sept. 1996, 17-21.

Etchells, J. C. (1997). Why reactions run away? *Organic Process Research & Development*, 1, 435-437.

- F -

Fall, A., Lecoq, O. & David, R. (2001). Characterisation of mixing in a stirred tank by Planar Laser Induced Fluorescence (PLIF). *Trans. IChemE.*, 79, 876-882.

Fangary, Y. S., Barigou, M., Seville, J. P. K. & Parker, D. J. (2000). Fluid trajectories in a stirred vessel of non-newtonian liquid using positron emission particle tracking. *Chem. Eng. Sci.*, 55(24), 5969-5979.

Ferreira, S. L. C., Bruns, R. E., Ferreira, H. S., Matos, G. D., David, J. M., Brandão, G. C., da Silva, E. G. P., Portugal, L. A., dos Reis, P. S., Souza, A. S. & Dos Santos, W. N. L. (2007). Box-Behnken design: An alternative for the optimization of analytical methods. *Analytica Chimica Acta*, 597(2), 179-186.

Févotte, G. & Puel, F. (2003). Application de la spectroscopie moyen infrarouge in situ au développement et au contrôle des procédés de cristallisation en solution. *Actes Cristal Toulouse*, 2, 69-74.

Fisher, R. A. (1949). *The design of experiments*. 5th edition, Olivier and Boyd, Ed. Edinburgh.

Fletcher, D. F. & Xuereb, C. (2004). Mécanique des fluides numérique. *Techniques de l'Ingénieur*, J1 050, 1-11.

Fox, E. A. & Gex, V. E. (1956). Single-phase blending of liquids. *AIChE J.*, 2(4), 539-544

Fowler, A. H. K. & Baxter, A. (2000). Fires, explosions and related incidents at work in Great Britain in 1996/97 and 1997/98. *Journal of Loss Prevention in the Process Industries*, 13(6), 547-554.

Fowler, A. H. K. & Hazeldean, J. A. (1998). Fires, explosions and related incidents at work in Great Britain in 1994/95 and 1995/96. *Journal of Loss Prevention in the Process Industries*, 11(5), 347-352.

Freudig, B., Hogekamp, S. & Schubert, H. (1999). Dispersion of powders in liquids in a stirred vessel. *Chem. Eng. and Processing*, 38, 525-532.

- G -

Gaskey. S. Vacus. P. David. R. Villermaux. J. & André. J. C. (1990). A method for study of turbulent mixing using fluorescence spectroscopy. *Exp. in Fluids*, 9, 137-147.

Gordier, R. L. (1963). Studies on fluid jets discharging normally into moving liquid. *St. Anthoni Falls Hydraulics Lab., Univ. of Minnesota, Minneapolis, Tech. Paper.*, 28, Ser. B.

Goupy, J. (1999). *Plans d'expériences pour surface de réponse.* Ed. Dunod, Paris.

Goupy, J. (2005). *Pratiquer les plans d'expériences.* Ed. Dunod, Paris.

Grotjans, H. & Menter, F. R. (1998). Wall functions for general application CFD codes. *In ECCOMAS 98, Proceedings of the Fourth European Computational Fluid Dynamics Conference*, 1112-1117.

Guillard. F. & Trägårdh. C. (2003). Mixing in industrial Rushton turbine-agitated reactors under aerated conditions. *Chem. Eng. and Processing.*. 42. 373–386.

Gustin, J. L. (1991). Runaway reactions, their courses and the method to establish safe process conditions. *J. Phys. III France*, 1, 1401-1419.

- H -

Hackl, A. & Wurian, H. (1979). Determination of mixing time. *Ger. Chem. Eng.*, 2, 103-107.

Haque, J. N., Mahmud, T. & Roberts, K. J. (2006). Modeling turbulent flow with free-surface in unbaffled agitated vessels. *Ind. Eng. Chem. Res.*, 45, 2881-2891.

Harris, C. K., Roekaerts, D., Rosendal, F. J. J., Buitendijk, F. G. J., Daskopoulos, Ph., Vreenegoor, A. J. N. & Wang, H. (1996). Computational fluid dynamics for chemical reactor engineering. *Chem. Eng. Sci.*, 51(10), 1569-1594.

Hartmann, H., Derksen, J. J., Montavon, C., Pearson, J., Hamill I. S. & Van den Akker, H. E. A. (2004). Assessment of large eddy and RANS stirred tank simulations by means of LDA. *Chem. Eng. Sci.*, 59(12), 2419–2432.

Hartmann, H., Derksen, J. J. & Van den Akker, H. E. A. (2006). Numerical simulation of a dissolution process in a stirred tank reactor. *Chem. Eng. Sci.*, 61, 3025-3032.

Harvey, A. D., Lee, C. K. & Rogers, S. E. (1995). Steady-state modelling and experimental measurement of a baffled impeller stirred tank. *AIChE Journal*, 41(10), 2177-2186.

Hasal, P., Montes, J. L. Boisson, H. C. & Fořt, I. (2000). Macro-instabilities of velocity field in stirred vessel: detection and analysis. *Chem. Eng. Sci.*, 55(2), 391-401.

Hendricks, F. & Aviram, A. (1982). Use of zinc iodide solutions in flow research. *Rev. Sci. Instrum.*, 53(1), 75-78.

Hiby, J. W. (1985). Problems with measuring mixing time. *Proceedings of the Fifth European Conference Mixing*, Wurzburg, West Germany, 10-12 June, 555-561.

Hiby, J. W. (1981). Definition and measurement of the degree of mixing in liquid mixtures. *Int. Chem. Eng.*, 21(2), 197-204.

Hitomi, D., Kato, Y., Kubo, T., Okuzaki, S. & Sugiyama, H. (2006). Finite element analysis of a flow induced by a Rushton turbine in an unbaffled stirred vessel. Journal of. Chem. Eng. of Japan, 39(3), 275-283.

Holden, P. J., Wang, R., Mann, R., Pickin, F. J. & Edwards, R. B. (1988). Imaging stirred-vessel macromixing using electrical resistance tomography. *AIChE J.*, 44(4), 780-790.

Hong, S., Albu, R., Labbe, C., Lasuye, T, Stasik, B. & Riess, G. (2006). Preparation and characterization of colloidal dispersions of vinyl alcohol-vinyl acetate copolymers: application as stabilizers for vinyl chloride suspension polymerization. Polymer international, 55(12), 1426-1434.

Hoogendoorn, C. J. & Den Hartog, A. P. (1967). Model studies on mixers in the viscous flow regime. *Chem. Eng. Sci.,* 22. 1689-1699.

Houcine, I., Vivier, H., Plasari, E., David, R. & Villermaux, J. (1996). Planar laser induced fluorescence technique for measurements of concentration fields in continuous stirred tank reactors. *Exp. in Fluids*, 22, 96-102.

Hristov, H. V. & Mann, R. (2002). Fluid mixing and the safe quenching of runaway reaction in a stirred autoclave. *Trans IChemE*, 80(A), 872-879.

Huang, H. Dabiri, D. & Gharib, M. (1997). On errors of digital particle velocimetry. *Meas. Sci. Technol.*, 8, 1427-1440.

- J -

Javed, K. H., Mahmud, T. & Zhu, J. M. (2006). Numerical simulation of turbulent batch mixing in a vessel agitated by a Rushton turbine. *Chem. Eng. and Process.*, 45(2), 99-112.

Jaworski, Z., Bujalski, W., Otomo, N. & Nienow, A. W. (2000). CFD study of homogenization with dual Rushton turbines - comparison with experimental results. Part I Initial studies. *Chem. Eng. Res. Des.,* 78, 327-333.

Jaworski, Z., Dyster, K. N., Moore, I. P. T., Nienow, A. W. & Wyszynski, M. L. (1997). The use of angle resolved LDA data to compare two different turbulence models applied to sliding mesh CFD flow simulations in a stirred tank. *Récents Progrès en Génie des Procédés,* 11(51), 187-194.

Jaworski, Z. & Zakrzewska, B. (2002). Modelling of the turbulent wall jet generated by a pitched blade turbine impeller - The effect of turbulence model. *Chem. Eng. Res. Des.*, 80(A8), 846-854.

Jenne, M. & Reuss M., (1999). A critical assessment on the use of k–ε turbulence models for simulation of the turbulent liquid flow induced by a Rushton-turbine in baffled stirred-tank reactors. *Chem. Eng. Sci.*, 54(17), 3921-3941.

Jeong, J. H. & Yang D. Y. (1998). Finite element analysis of transient fluid flow with free surface using the VOF (Volume-Of-Fluid) method and adaptative grid. *Int. J. Numer. Meth. Fluids*, 26, 1127-1154.

Joosten, G. E. H., Schilder, J. G. M. & Broere, A. M. (1977). The suspension of floating solids in stirred vessels. Trans IChemE, 55, 220-222.

Joshi, J. B. & Ranade, V. V. (2003). Computational fluid dynamics for designing process equipment: expectations, current status, and path forward. *Ind. Eng. Chem. Res.*, 42, 1115-1128.

Ju, K. K. & Chase, G. G. (1992). Improved scale-up strategies of bioreactors. *Bioprocess Eng.*, 8, 49-53.

- K -

Kammel, U., Schlüter, S., Steiff, A. & Weinspach, P. M. (1996). Control of runaway polymerization reactions by injection of inhibiting agents – A contribution to the safety of chemical reactors. *Chem. Eng. Sci.*, 51(10), 2253-2259.

Kersten, B., Ohl, C. D. & Prosperetti, A. (2003). Transient impact of a liquid column on a miscible liquid surface. Physics of Fluids, 15(3), 821-824.

Kim, S., Ngansib Nkaya, A. & Dyakowski, T. (2006). Measurement of mixing of two miscible liquids in a stirred vessel with electrical resistance tomography. *Int. Com. in Heat and Mass Transfer*, 33(9), 1088-1095.

Kiparissides, C., Daskalakis, G., Achilias, D. S. & Sidiropoulou, E. (1997). Dynamic simulation of industrial poly(vinyl chloride) batch suspension polymerization reactors. *Ind. Eng. Chem. Res.*, 36, 1253-1267.

Kolmogorov, A. N. (1942). Equations of turbulent motion of an incompressible fluid. *Izv. Akad. Nauk SSSR, Seria fisicheska VI*, No 1-2, 56-58.

Kramers, H., Baars, G. M. & Knoll, W. H. (1953). A comparative study on the rate of mixing in stirred tanks. *Chem. Eng. Sci.*, 2, 35-42.

- L -

La Fontaine, R. F. & Shepherd, I. C. (1996). Particle Image Velocimetry applied to a stirred vessel. *Exp. Therm. Fluid Sci.*, 12, 256-264.

Laakkonen, M., Moilanen, P., Alopaeus, V. & Aittamaa, J. (2007). Modelling local bubble size distributions in agitated vessels. Chem. Eng. Sci., 62(3), 721-740.

Laakkonen, M., Moilanen, P. & Aittamaa, J. (2005). Local bubble size distributions in agitated vessels. *Chem. Eng. J.*, 106 (2),133-143.

Lamberto, D. J., Alvarez, M. M. & Muzzio, F. J. (1999). Experimental and computational investigation of the laminar flow structure in a stirred tank. *Chem. Eng. Sci.*, 54(7), 919-942.

Lane, G. L., Schwarz, M. P. & Evans, G. M. (2005). Numerical modelling of gas-liquid flow in stirred tanks. *Chem. Eng. Sci.*, 60, 2203-2214.

Lane, G. L., Schwarz, M. P. & Evans, G. M. (2000). Comparison of CFD methods for modelling of stirred tanks. *Proc. 10th Eur. Conf. on Mixing (Delft, 2-5 July)*, 273-280.

Launder, B. E. & Spalding, D. B. (1974). The numerical computation of turbulent flows. *Comp. Meth. Appl. Mech. Engn.*, 3, 269-289.

Le Lan, A. & Angelino, H. (1972). Etude du vortex dans les cuves agitées. *Chem. Eng. Sci.*, 27 (11), 1969-1978.

Leclercq, E. (2005). Mesures de puissance sur moteurs. *Internal report,* 18-19-20 December 2005, ref. 05H1202, 1-14.

Lee, K. C. & Yianneskis, M. (1997). A liquid crystal thermography technique for the measurement of mixing characteristics in stirred vessels. *Chem Eng. Res. Des.*, 75(A8), 746-754.

Legault, T. (2007). Astrophotographie. Ed. Eyrolles.

Lesek, F. & Eichler, J. (1975). Mixing problems in suspension polymerisation. Chemicky Prumysl, 25(6), 299, T/28-T/33.

Levenberg, K. (1944). A Method for the Solution of Certain Non-Linear Problems in Least Squares. *Quart. Appl. Math.*, 2(2), 164-168.

Li, M., White, G., Wilkinson, D. & Roberts, K. J. (2004). LDA measurements and CFD modelling of a stirred vessel with a retreat curve impeller. *Ind. Eng. Chem. Res.*, 43, 6534-6547.

Li, M., White, G., Wilkinson, D. & Roberts, K. J. (2005). Scale up study of retreat curve impeller stirred tanks using LDA measurements and CFD simulation. *Chem. Eng. J.*, 108 (1-2), 81-90.

Louvet, F. & Delplanque, L. (2005). Design of experiments: the French touch. *Témoignage de l'association experimentique [1996-2005]*, Orléans.

Lu, W. M., Wu, H. Z., Tsai, F. Y. & Wang, C. Y. (1997a). Effect of baffle design on the fully baffled condition in aerated stirred tanks with Rushton turbine impeller. *Journal of the Chin. I. Ch. E.*, 28(1)69-72.

Lu, W. M., Wu, H. Z. & Ju, M. Y. (1997). Effects of baffle design on the liquid mixing in an aerated stirred tank with standard Rushton turbine impellers. *Chem. Eng. Sci.*, 52(21-22), 3843-3851.

Lundén, M., Stenberg, O & Andersson, B. (1995). Evaluation of a method for measuring mixing time using numerical simulation and experimental data. *Chem. Eng. Comm.*, 139. 115-136.

Luo, J. Y., Issa, R. I. & Gossman, A.D. (1994). Prediction of Impeller induced flows in mixing vessels using multiple frames of reference. *IChemE Symp. Series*, 139, 549-556.

- M -

Mahouast, M. (1993). Mesure des champs de concentration et de température dans un réacteur agité par traitement des images de la fluorescence induite par une nappe laser. *Récents Progrès en Génie des Procédés*, 24, 53-60.

Maggioris, D., Goulas, A., Alexopoulos, A. H., Chatzi, E. G. & Kiparissides, C. (2000). Prediction of particle size distribution in suspension polymerization reactors: effect of turbulence nonhomogeneity. *Chem. Eng. Sci.*, 55(20), 4611-4627.

Malmonges, S. M. & Santos, L. R. (1996). Emergency stopper for VCM suspension polymerization. *J. Vinyl Additive Tech.*, 2(3), 211-215.

Manna, L. (1997). Comparison between physical and chemical methods for the measurement of mixing times. *Chem. Eng. Journal*, 67(3), 167-173.

Margason, R. J. (1993). Fifty years of jet in cross flow research. *Proc. AGARD, Computational and Experimental Assessment of Jets in Cross Flow*, 1.1-1.41.

Markopoulos, J. & Kontogeorgaki, E. (1995). Vortex depth in unbaffled single and multiple impeller agitated vessels. *Chem. Eng. Technol.*, 18, 68-74.

Marquardt, D. (1963). An Algorithm for Least-Squares Estimation of Nonlinear Parameters. *SIAM J. Appl. Math.*, 11, 431-441.

Mavros, P. (2001). Flow visualization in stirred vessels, a review of experimental techniques. *Trans. Inst. Chem. Eng.*, 79(A), 113-127.

Mavros, P. & Baudou, C. (1997). Quantification of the performance of agitators in stirred vessels: definition and use of an agitator index. *Trans IChemE*, 75(A), 737-745.

McCarthy, M. J. & Molloy, N. A. (1974). Review of stability of liquid jets and the influence of nozzle design. *Chem. Eng. J.*, 7, 1-20.

McIntosh, R. D. & Nolan, P. F. (2001). Review of the selection and design of mitigation systems for runaway chemical reactions. *Journal of Loss Prevention in the Process Industries*, 14(1), 27-42.

McKeogh, E. J. (1978). A study of air entrainment using plunging water jets. PhD thesis, Queen's University of Belfast, Ireland.

McKeogh, E. J. & Ervine, D. A. (1981). Air entrainment rate and diffusion pattern of plunging liquid jets. *Chem. Eng. Sci.*, 36, 1161-1172.

Mejdell, T., Pettersen, T., Naustdal, C. & Svendsen, H. F. (1999). Modelling of industrial S-PVC reactor. *Chem. Eng. Sci.*, 54, 2459-2466.

Melton, L. A., Lipp, C. W., Spradling, W. & Paulson, K. A. (2002). DISMT – Determination of mixing time through color changes. *Chem. Eng. Comm.*, 189(3), 322-338.

Menter, F. R. (1994). Two-equation eddy-viscosity turbulence models for engineering applications. *AIAA Journal*, 32(8), 15981605.

Menter, F. R. & Egorov, Y. (2004a). Revisiting the turbulent scale equation. *IUTAM Symposium: "One hundred years of boundary layer research"*, Göttingen, Germany, 1-11.

Menter, F. R. & Egorov, Y. (2004b). Turbulence models based on the length-scale equation. Fourth International Symposium on Turbulent Shear Flow Phenomena, Langley 2004, paper TSFP4-268, 1-6.

Menter, F. R. & Egorov, Y. (2005a). A Scale-Adaptive Simulation model using two equation models. *AIAA*, 2005-1095, 1-13.

Menter, F. R. & Egorov, Y. (2005b). SAS turbulence modelling of technical flows. *DLES 6, 6th ERCOFTAC Workshop on Direct and Large Eddy Simulation*, September, Poitiers, France, 1-8.

Menter, F. R., Egorov, Y. & Rusch, D. (2006). Steady and unsteady flow modelling using the k-$\sqrt{k}$ L model. *Turbulence, Heat and Mass Transfer 5*, Editors: K. Hanjalić, Y. Nagano and S. Jakirlic, 1-20.

Menter, F. R., Kuntz, M. & Bender, R. (2003a). A Scale-Adaptive Simulation model for turbulent flow predictions. *AIAA*, 2003-0767, 1-11.

Menter, F. R., Kuntz, M. & Langtry, R. (2003b). Ten years of industrial experience with the SST turbulence model. *Turbulence, Heat and Mass Transfer 4*, Editors: K. Hanjalić, Y. Nagano and M. Tummers, 1-8.

Milewska, A. & Molga, E. J. (2007). CFD simulations of accidents in industrial batch stirred tank reactors. *Chem. Eng. Sci.*, 62(18-20), 4920-4925.

Mixing Equipment Co. (1981). Impeller comparison A310 vs. retreat blade "crowfoot" impeller., Mixing Equipment Co., Inc., Rochester, NY, 1-13.

Moin, P. (2002). Advances in large eddy simulation methodology for complex flows. *Int. J. of Heat and Fluid Flow*, 23, 710-720.

Montante, G., Bakker, A, Paglianti, A. & Magelli, F. (2006). Effect of the shaft eccentricity on the hydrodynamics of unbaffled stirred tanks. Chem. Eng. Sci., 61(9), 2807-2814.

Muhr, H., Leclerc, J. P. & David, R. (1999). Fluorescent UV dye: a particularly well-suited tracer to determine residence time distributions of liquid phase in large industrial reactors. *Analusis*, 27, 541-543.

Muppidi, S. & Mahesh, K. (2005). Study of trajectories of jets in crossflow using direct numerical simulations. *J. Fluid Mech.*, 530, 81-100.

Murthy Shekhar, S. & Jayanti, S. (2002). CFD study of power and mixing time for paddle mixing in unbaffled vessels. *Trans. Inst. Chem. Eng.*, 80 (A), 482-498.

Myers, K. J., Reeder, M. F. & Fasano, J. B. (2002). Optimize mixing by using the proper baffles. *Chem. Eng. Progress*, 91 (12), 25-34.

- N -

Nagata, S. (1975). *Mixing: principles and applications.* Wiley, New York.

Narasimha, M., Brennan, M. & Holtham, P. N. (2007). A review of CFD modelling for performance predictions of hydrocyclone. *Eng. Appl. Compt. Fluid Mech.*, 1(2), 109-125.

Nere, N. K., Patwardhan, A. W. & Joshi, J. B. (2003). Liquid-phase mixing in stirred vessel: turbulent flow regime. *Ind. Eng. Chem. Res.*, 42, 2661-2698.

Nikiforaki, L., Yu, J., Baldi, S., Genenger, B., Lee, K. C., Durst, F. & Yianneskis, M. (2004). On the variation of precessional flow instabilities with operational parameters in stirred vessels. *Chem. Eng. J.*, 102(3), 217-231.

Nikiforaki, L., Montante, G., Lee, K. C. & Yianneskis, M. (2003). On the origin, frequency and magnitude of macro-instabilities of the flows in stirred vessels. *Chem. Eng. Sci.*, 58(13), 2937-2949.

Nishikawa, M., Okamoto, Y., Samejima, M., Fujieda, S. & Hashimoto, K. (1979). *Kagaku Kogaku Ronbunshu*, 5, 535.

Nishino, T., Roberts, G. T. & Zhang, X. (2007). Unsteady RANS and detached-eddy simulations of flow around a circular cylinder in ground effect. *Journal of Fluids and Structures*, doi:10.1016/j.jfluidstructs.2007.06.002, *in press*.

Novák, V. & Rieger, F. (1973). Mixing in vessels of square cross-section. *Chem. Commun.*, 38, 350-358.

- O -

Okamoto, K. (2005). Editorial of the 6th International Symposium on Particle Image Velocimetry, Pasadena, California, 21–23 September 2005, *Meas. Sci. Technol.*, 17**,** 7.

Oldshue, J. Y, Mechler, D. O. & Grinnell, D. W (1982). Fluid mixing variables in suspension and emulsion polymerization. Chem Eng. Prog, May 1982, 68-74.

Ozkaya, N., Erbay, E., Bilgic, T. & Savasci, T. (1993). Agitation scale-up model for the suspension polymerization of vinyl chloride. *Die Angew. Makromol. Chem.*, 211, 35-51.

- P -

Padovan, D. & Woods, D. R. (1986). Polyvinyl alcohol as a suspending agent for PVC production. *AIChE Symp. Ser.*, 82, 91-99

Paglianti, A., Montante, G. & Magelli, F. (2006). Novel experiments and a mechanistic model for macroinstabilities in stirred tanks. *AIChE Journal*, 52(2), 426-437.

Patankar, S. V. (1980). *Numerical Heat Transfer and Fluid Flow*. Taylor & Francis.

Patil, S. M., Gogate, P. R., Patwardhan, A. W. & Pandit, A. B. (2001). Mixing time studies in mechanically agitated contactor. *Int. Symp. on Mixing in Ind. Processes ISMIP4*, 14-16 May. Toulouse (France).

Patrick, M. A. (1967). Experimental investigation of the mixing and penetration of a round turbulent jet injected perpendicularly into a transverse stream. *Trans. Inst. Chem. Eng.*, 45, T, 16-31.

Paul, E. L., Atiemo-Obeng, V. A. & Kresta, S. M. (2004). *Handbook of industrial mixing: science and practise.* Wiley, Hoboken, New Jersey.

Pedersen, A. G., Nielsen, J. & Villadsen, J. (1994). Characterization of bioreactors using isotope tracer techniques. *Proceedings of the 6th European Congress of Biotechnology*, Amsterdam, 931-934.

Pfaudler (1992). Pfaudler-Symposium: Rühren and Mischen, Anwendungstechnik, Leistungscharakteristik beim Impellerrührer (ohne Einbauten), p12.

Pfleger, D. & Becker, S. (2001). Modelling and simulation of the dynamic flow behaviour in a bubble column. *Chem. Eng. Sci.*, 56(4), 1737-1747.

Pillet, M. (1997). *Les plans d'expériences par la méthode Taguchi.* Les éditions d'organisation, Paris.

Pineault, G. & Cloutier, L. (1972). Fonction de transfert d'un réservoir agité en système continu: I. Détermination à l'aide d'un traceur fluorescent. *Can. J. Chem. Eng.*. 50. 736-742.

Plackett, R. L. & Burman, J. P. (1946). The design of optimum multifactorial experiments. *Biometrika*, 33, 305-325.

Platkowski, K. & Reichert, K. H. (1999). Short stopping of runaway methyl methacrylate polymerizations. *Chem. Eng. Technol.*, 22(12), 1035-1038.

Polhemus, N. W. (1999). *Quality Control & Experimental Design using Statgraphics Plus*, Ed. Statpoint, Chapter 13: Screening Designs, 1-62.

Pope, S. B. (2000). *Turbulent Flows.* (Cambridge University Press), Cambridge, UK.

- R -

Raffel, M., Willert, C. & Kompenhans, J. (1998). Particle Image Velocimetry: a pratical guide. Experimental fluid mechanics, Springer.

Raghav Rao, K. S. M. S. & Joshi, J. B. (1988). Liquid phase mixing in mechanically agitated vessels. *Chem. Eng. Commun.*, *74*, 1-25.

Rajaratnam, N. (1976). *Developments in Water Science: Turbulent Jets.* (Elsevier Scientific Publishing Co.), New York, USA.

Reschtschaffner, R. L (1967). Saturated fractions of 2^n and 3^n factorial designs. *Technometrics*, 9(4), 569-575.

Rewatkar, V. B. & Joshi, J. B. (1991). Effect of impeller design on liquid phase mixing in mechanically agitated reactors. *Chem. Eng. Commun.*, 102, 1-33.

Rieger, F., Ditl, P. & Novák, V. (1979). Vortex depth in mixed unbaffled vessels. *Chem. Eng. Sci.*, 34 (3), 397-403.

Rielly, C. D. & Britter, R. E. (1985). Mixing times for passive tracers in stirred tanks. *Proceedings of the Fifth European Conference Mixing,* Wurzburg, West Germany, 10-12 June, 365-375.

Rielly, C. D., Habib, M. & Sherlock J. P. (2007). Flow and mixing characteristics of a retreat curve impeller in a conical-based vessel. Chem. Eng. Res. Des., 85(A7), 953-962.

Rouland E. (1994). Etude et développement de la technique de velocimetrie par intercorrélation d'images de particules. Application aux écoulements en tunnel hydrodynamique. *Ph.D. Thesis, Université de Rouen*, France.

Rousseaux, J. M., Muhr, H. & Plasari, E. (2001). Mixing and micromixing times in the forced vortex region of unbaffled mixing devices. *The Canadian Journal of Chemical Engineering*, 79, 697-707.

Roussinova, V., Kresta, S. M. & Weetman, R. (2003). Low frequency macroinstabilities in a stirred tank: scale-up and prediction based on large eddy simulations. *Chem. Eng. Sci.*, 58(11), 2297-2311.

Roustan, M., Pharamond, J.-C. & Line, A. (1997). Agitation - mélange. Concept théoriques de base. *Techniques de l'Ingénieur, traité Génie des Procédés*, J3 800, 1-22.

Rushton, J. H., Costich, E. W. & Everett, H. J. (1950a). Power characteristics of mixing impellers – Part 1. *Chem. Eng. Prog.*, 46(8), 395-404.

Rushton, J. H., Costich, E. W. & Everett, H. J. (1950b). Power characteristics of mixing impellers – Part 2. *Chem. Eng. Prog.*, 46(9), 467-476.

Ruszkowski, S. W. & Muskett, M. J. (1985). Comparative mixing times for stirred tank agitators*. Proceedings of the Fifth European Conference Mixing*, Wurzburg, West Germany. 10-12 June, 89-104.

- S -

Saeki, Y. & Emura, T. (2002). Technical progress for PVC production. *Prog. Polym. Sci.*, 27, 2055-2131.

Saffman, P. G. (1970). A model for inhomogeneous turbulent flow. *Proc. Roy. Soc Lond., Series A: Mathematical and Physical Sciences,* 317(1530), 417-433.

Sahu, A. K., Kumar, P. Patwardhan, A. W. & Joshi, J. B. (1999). CFD modelling and mixing in stirred tanks. *Chem. Eng. Sci.*, 54, 2285-2293.

Sallam, K. A., Dai, Z. & Faeth, G. M. (2002). Liquid breakup at the surface of turbulent round liquid jets in still gases. *Int. J. Multiphase Flow*, 28, 427-449.

Sano, Y. & Usui, H. (1987). Effects of paddle dimensions and baffle conditions on the interrelation among discharge flow rate, mixing power and mixing time in mixing vessels. *J. Chem. Eng. of Japan*, 20(4), 399-404.

Savart, F. (1833). Mémoire sur la constitution des veines liquides lancées par des orifices circulaires en mince paroi. *Ann. Chim. Phys.*, 53, 337-386.

Sbrizzai, F., Lavezzo, V., Verzicco, R., Campolo, M. & Soldati. A. (2006). Direct numerical simulation of turbulent particle dispersion in an unbaffled stirred-tank reactor. *Chem. Eng. Sci.*, 61(9), 2843-2851.

Scardovelli, R. & Zaleski, S. (1999). Direct numerical simulation of free-surface and interfacial flow. *Annual Rev. Fluid Mech.*, 31, 567-603.

Serra, A., Campolo, M. & Soldati, A. (2001). Time-dependent finite-volume simulation of the turbulent flow in a free-surface CSTR. *Chem. Eng. Sci.*, 56 (8)**,** 2715-2720.

Shang, J. S. (2004). Three decades of accomplishments in computational fluid dynamics. *Prog. Aero. Sci.*, 40, 173-197.

Siddiqui, H. (1993). Mixing Technology for buoyant solids in a nonstandard vessel. AIChE Journal, 39(3), 505-509.

Smit, L. & Düring, J. (1991). Vortex geometry in stirred vessel. *Proc. 7th European Congress on Mixing, part II*, Brugge, Belgium, 633-639.

Smith, F. G. (1997). A model of transient mixing in a stirred tank. *Chem. Eng. Sci.*, 52(9), 1459-1478.

Snee, T. J. & Cusco, L. (2005). Pilot-scale evaluation of the inhibition of exothermic runaway. *Trans IchemE, Part B, Process Safety and Environmental Protection*, 83(B2), 135-144.

Sommerfeld, M. & Decker, S. (2004). State of the art and future trends in CFD simulation of stirred vessel hydrodynamics. *Chemical Engineering and Technology*, 27, 215-224.

Souvay. P. (1995). *Les plans d'expériences: méthode Taguchi.* Ed. Afnor, Paris.

Spalart, P. R. (2000). Strategies for turbulence modelling and simulations, *Int J. of Heat and Fluid Flow*, 21, 252-263.

Spalart, P.R, Jou, W.-H., Strelets, M. & Allmaras, S.R. (1997). Comments on the feasibility of LES for wings, and on a hybrid RANS/LES approach. *1st AFOSR Int. Conf. on*

DNS/LES, Aug.4-8, Ruston, LA. In *Advances in DNS/LES*, C. Liu & Z. Liu Eds., Greyden Press, Colombus, OH.

Spalding, D. B. (1991). Kolmogorov's Two-Equation Model of Turbulence. *Proc. Roy. Soc Lond., Series A: Mathematical and Physical Sciences, Turbulence and Stochastic Process: Kolmogorov's Ideas 50 Years*, 434(1890), 211-216.

Speziale, C. G., Sarkar, S. & Gatski, T. B. (1991). Modelling the pressure-strain correlation of turbulence: an invariant dynamical systems approach. *J. Fluid Mechanics*, 277, 245-272.

Squires, K. D. (2004). Detached Eddy Simulation: current status and future perspectives. *Proc. DLES5 conference*, München, 1-16.

Statgraphics Centurion XV 15.0.10. user's guide. StatPoint. Inc., 1982-2006.

Steffin, M. (2005). Power measures on the Beek reactor. (Action 02-07/05, MS). *Internal memo # TS.05423.MS, 05-10-05.*

Steffin, M. (2006). Vortex shape and data acquisition for Beek reactors, (Action 04-22/03, MS). *Internal memo # TS.06417.MS, 27-06-06.*

Storr, G. J. & Behnia, M. (1999). Experiments with large diameter gravity driven impacting liquid jets. *Exp. in Fluids*, 27, 60-69.

- T -

Taguchi, G. & Konishi, S. (1987). Taguchi methods: orthogonal arrays and linear graphs. American Supplier Institute Inc.

Tang, H., Wrobel, L. C. & Fan, Z. (2004). Tracking of immiscible interfaces in multiple-material mixing processes. *Comp. Mater. Sci.*, 29 (1), 103-118.

Togasaki, D. M., Hsu, A., Samant, M., Farzan, B., DeLanney, L. E., Langston, J. W., Di Monte, D. A. & Quik, M. (2005). The Webcam system: a simple, automated, computer-based video system for quantitative measurement of movement in nonhuman primates. *Journal of Neuroscience Methods*, 145(1-2), 159-166.

Torré, J.P. (2007). How to achieve better quenching of industrial S-PVC synthesis reactors? *Internal LVM memo*, QID 131-2007-JPT, 1-3.

Torré, J.P., Fletcher, D. F., Lasuye, T. & Xuereb, C. (2007a). An experimental and computational study of the vortex shape in a partially baffled agitated vessel. *Chem. Eng. Sci.*, 62(7), 1915-1926.

Torré, J.P., Fletcher, D. F., Lasuye, T. & Xuereb, C. (2007b). Transient hydrodynamics and free surface capture of an under-baffled stirred tank during stopping. *Chem. Eng. Res. Des.*, 85(A5), 626-636.

Torré, J.P., Fletcher, D. F., Lasuye, T. & Xuereb, C. (2007c). Single and multiphase CFD approaches for modelling partially baffled vessels: comparison of experimental data with numerical predictions. *Chem. Eng. Sci.*, 62(22), 6246-6262.

Torré, J.P., Fletcher, D. F., Lasuye, T. & Xuereb, C. (2008). An experimental and CFD study of liquid jet injection into a partially-baffled mixing vessel: a contribution to process safety by improving the quenching of runaway reactions. *Chem. Eng. Sci.*, 63, 924-942.

Tort, A. B.L., Neto, W. P., Amaral, O. B., Kazlauckas, V., Souza, D. O. & Lara, D. R. (2006). A simple Webcam-based approach for the measurement of rodent locomotion and other behavioural parameters. *Journal of Neuroscience Methods*, 157(1), 91-97.

Tüdós, F. & Földes-Berezsnich, T. (1989). Free-radical polymerization: inhibition and retardation. *Prog. Polym. Sci.*, 14, 717-761.

Tukey, J. W. (1977). *Exploratory Data Analysis.* EDA, Reading, MA, (Addison-Wesley).

- U -

Uhl, V. W. & Gray, J. B. (1966). *Mixing theory and practise*, *Vol. 1.* Academic Press, London, UK.

U.S. CSB (2003). Chemical Safety and Hazards Investigation Board. *Incident data – Reactive Hazard Investigation*, No 2003-15-D, September 2003, 1-37.

- V -

Van den Akker, H. E. A. (2006). The details of the turbulent mixing process and their simulation. *Advances in Chemical Engineering*, 31, 151-229.

van Vliet, E., Derksen, J. J., van den Akker, H. E. A. & Fox, R.O. (2007). Numerical study on the turbulent reacting flow in the vicinity of the injector of an LDPE tubular reactor. *Chem. Eng. Sci.*, 62(9), 2435-2444.

Vasconcelos, J. M. T., Alves, S. S., Nienow, A. W. & Bujalski, W. (1998). Scale-up of mixing in gassed multi-turbine agitated vessels. *Can. Journal. of Chem. Eng.*, 76, 398-404.

Verschuren, I., Wijers, J. & Keurentjes, J. (2000). Mixing with a Pfaudler type impeller: the effect of micromixing on reaction selectivity in the production of fine chemicals. *Proc. 10th Eur. Conf. on Mixing*, July 2-5, Delft, The Netherlands, 69-75.

Verschuren, I. L. M., Wijers, J. G. & Keurentjes, J. T. F. (2002). Large-scale oscillations of a feedstream inside a stirred tank reactor. *AIChE Journal*, 48(9), 1888-1995.

Verschuren, I. L. M., Wijers, J. G., Schoenmakers G. J. H. A., Jeurissen, F. G. H. & Keurentjes, J. T. F. (2001). Determination of the mixing rate of a high velocity feed stream in agitated vessels. *Chem. Eng. Comm.*, 188, 59-79.

Versteeg, H. K. & Malalasekera, W. (1995). A*n introduction to computational fluid dynamics, the finite volume method.* Longman.

Verzicco, R., Fatica, M., Iaccarino, G. & Orlandi, P. (2004). Flow in an impeller-stirred tank using an immersed-boundary method. *AIChE Journal*, 50(6), 1109-1118.

Vigier, M. G. (1988). Pratique des plans d'expériences: méthodologie Taguchi. Les éditions d'organisation, Paris.

- W -

Westerterp, K. R. & Molga, E. (2004). No more runaways in chemical reactors. *Ind. Eng. Chem. Res.*, 43, 4585-4594.

Westerterp, K. R. & Molga, E. (2006). Safety and runaway prevention in batch and semibatch reactors - a review, *Chem. Eng. Res. Des.*, 84(A7)**,** 543-552.

Westerweel, J. (1994). Efficient detection of spurious vectors in particle image velocimetry data*, Exp. in Fluids*, 16, 236-247.

Wilcox, D. C. (1993). *Turbulence Modelling for CFD*, DCW Industries, LA Canada, CA.

Willert, C. E. & Gharib, M. (1991). Digital particle Velocimetry, *Exp. in Fluids*, 10, 181-193.

Williams, R. A., Mann, R, Dickin, F. J., Ilyas, O. M., Ying, P., Edwards, R. B. & Rushton, A. (1993). Application of electrical impedance tomography to mixing in stirred vessels. *IChE Symp. Ser.*, 293(89), 8-15.

- X -

Xie, T. Y., Hamielec, A. E., Wood, P. E. & Woods, D. R. (1991a). Experimental investigation of vinyl chloride polymerization at high conversion: mechanism, kinetics and modelling. *Polymer*, 32(3), 337-557.

Xie, T. Y., Hamielec, A. E., Wood, P. E. & Woods, D. R. (1991b). Experimental investigation of vinyl chloride polymerization at high conversion: molecular-weight development. *Polymer*, 32(6), 1098-1111.

Xie, T. Y., Hamielec, A. E., Wood, P. E. & Woods, D. R. (1991c). Experimental investigation of vinyl chloride polymerization at high conversion: effect of polymerization on polymer properties. *Polymer*, 32(9), 1696-1702.

Xuereb, C., Poux, M. & Bertrand J. (2006). *Agitation et mélange : aspects fondamentaux et applications industrielles.* Paris, Dunod, l'Usine nouvelle.

- Y -

Yeoh, S. L., Papadakis, G., Lee, K. C. & Yianneskis, M. (2004). Large eddy simulation of turbulent flow in a Rushton impeller stirred reactor with sliding-deforming mesh methodology. *Chemical Engineering and Technology*, 27, 257–263.

Yeoh. S.L. Papadakis. G. & Yianneskis. M. (2005). Determination of mixing time and degree of homogeneity in stirred vessels with large eddy simulation. *Chem. Eng. Sci.*, 60(8-9). 2293-2302.

- Z -

Zaldívar, J. M., Cano, J., Alós, M. A., Sempere, J., Nomen, R., Lister, D., *et al.* (2003). A general criterion to define runaway limits in chemical reactors, *Journal of Loss Prevention in the Process Industries*, 16(3), 187-200.

Zerfa, M. & Brooks, B. W. (1996a). Predictions of Vinyl Chloride drop sizes in stabilised liquid-liquid agitated dispersions. *Chem. Eng. Sci.*, 51(12), 3223-3233.

Zerfa, M. & Brooks, B. W. (1996b). Vinyl chloride dispersion with relation to suspension polymerisation. *Chem. Eng. Sci.*, 51(14), 3591-3611.

Zlokarnik, M. (1971). Trombentiefe beim rühren in unbewehrten behältern. *Chemie Inger. Techn.*, 43 (18), 1028-1030.

APPENDIXES

APPENDIX A. Details of the preparation of iodine and thiosulphate solutions for experiments using the colouring/decolouring method.

APPENDIX B. Experimental matrix and results for the Design of Experiments relative to the mixing time.

APPENDIX C. Correlation of the jet velocities with the jet injection pressure and the injection pipe diameter.

APPENDIX D. Jet injection profiles for the industrial Mazingarbe reactor at nominal agitator speed.

APPENDIX E. Free-surface construction procedure

APPENDIX A.

Details of the preparation of iodine and thiosulphate solutions for experiments using the colouring/decolouring method.

A.1. Redox reaction

Oxidation-reduction reaction for the colouration/decolouration reaction: I_2/I^- (iodine/iodide) and $S_4O_6^{2-} / S_2O_3^{2-}$ (tetrathionate/thiosulphate).

$$I_2 + 2S_2O_3^{2-} \quad \rightarrow \quad 2I^- + S_4O_6^{2-}$$
$$\textit{(orange – brown)} \qquad \textit{(colourless)}$$
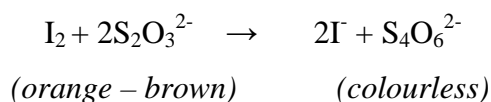
A.2. Operating protocol to make the iodine and thiosulphate solution

It is necessary to introduce into the vessel twice as many moles of thiosulphate as of iodine to have decolouration:

At the equivalence → $n_{thio} = \alpha \; n_{I2}$ with $\alpha_{eq} = 2$

It is necessary to have a small excess of thiosulphate (e.g. 5-10%) to have a visible decolouring → $\alpha > 2$

To have a 10% thiosulphate excess → $\alpha = 2.2$

- ▪ ***Preparation of 500 ml of iodine solution at 1 mol/L***

→ $m_{I2} = C_{I2} * M_{I2} * V_{I2}$

Application :

$V_{I2} = 0.5 \; L$

$C_{I2} = 1 \; mol/L$

$M_{I2} = 253.8 \; g/mol$

→   *m_{I2} = 1* 253.8 * 0.5 = 126.9 g*

To help the dissolution of iodine (solid) in water it is necessary to add about 90g of potassium iodide (KI) for 250 ml of iodine solution at 1 mol/L (adjusted with the volume).

$$I_2 + 2KI \quad \rightarrow \quad I_3^- + I^- + 2K^+$$

With V_{I2} = 500 ml:

→ *m_{KI} = 500/250 * 90 = 180 g*

- ### *Preparation of 20 litres of thiosulphate solution*

Volume of thiosulphate introduced in the vessel = V_{thio}^{intro}
Volume of iodine introduced in the vessel = V_{I2}^{intro}
10% excess of thiosulphate → α = 2.2

→ $n_{thio}^{intro} = \alpha\ n_{I2}^{intro} = \alpha C_{I2} * V_{I2}^{intro}$

Thiosulphate concentration : $C_{thio} = n_{thio}^{intro} / V_{thio}^{intro} = \alpha\ C_{I2} * V_{I2}^{intro} / V_{thio}^{intro}$
To make a volume V_{thio} of thiosulphate solution the masses are:

$m_{thio} = C_{thio} M_{thio} V_{thio} = = \alpha\ (\ C_{I2} * V_{I2}^{intro} / V_{thio}^{intro}\ ) * M_{thio} V_{thio}$

Application:
V_{thio} = 20 L
M_{thio} = M(Na_2SO_4. $5H_2O$) = 248 g/mol

→ *m_{thio} = 2.2 * (1*10/533) * 248* 20 = 204.72 g*

A.3. Summary

▪ **500 ml of a solution at 1 mol/L of iodine:**

In a volumetric flask of 500 ml:

→ 126.9 g of $I_{2\ (s)}$ + 180 of $KI_{(s)}$ + qsp H_2O

▪ **20 litres of a solution of sodium thiosulphate:**

such as :

- the thiosulphate excess was 10%

- the initial volume of iodine solution at 1 mol/L was 10 ml

- the introduced volume of thiosulphate solution was 533 ml

→ 204.72 g of $Na_2SO_4.5H_2O(s)$ + 20 litres H_2O

APPENDIX B.

Experimental matrix and results for the Design of Experiments relative to the mixing time.

	rotation speed (RPM)	pressure (bar relative)	pipe diameter (mm)	X position (mm)	Y position (mm)	mixing time (s)
exp1	100	1	12.5	47	64.7	9.79
exp2	100	1	7.2	0	64.7	11.72
exp3	100	2	7.2	47	64.7	10.56
exp4	50	1	12.5	47	0	14
exp5	100	0	12.5	94	64.7	9.78
exp6	100	1	12.5	0	0	9.65
exp7	100	0	12.5	47	0	12.81
exp8	100	1	12.5	94	0	9.23
exp9	100	1	12.5	47	64.7	10.56
exp10	100	0	12.5	0	64.7	8.03
exp11	100	1	12.5	47	64.7	11.06
exp12	150	0	12.5	47	64.7	5.5
exp13	150	1	12.5	94	64.7	5.12
exp14	150	1	17.8	47	64.7	5.91
exp15	150	1	12.5	0	64.7	7.18
exp16	50	0	12.5	47	64.7	12.84
exp17	150	1	7.2	47	64.7	6.19
exp18	100	1	12.5	47	64.7	7.72
exp19	100	2	17.8	47	64.7	9.62
exp20	100	1	7.2	94	64.7	9
exp21	100	1	17.8	47	129.4	7.73
exp22	100	2	12.5	0	64.7	10.74
exp23	150	1	12.5	47	0	8.59
exp24	150	2	12.5	47	64.7	7.28
exp25	50	1	12.5	0	64.7	15.72
exp26	100	1	12.5	0	129.4	8.21
exp27	100	1	17.8	0	64.7	9.03
exp28	150	1	12.5	47	129.4	6
exp29	50	2	12.5	47	64.7	12.25
exp30	100	0	7.2	47	64.7	10.77
exp31	50	1	17.8	47	64.7	13.07
exp32	100	0	12.5	47	129.4	9.47
exp33	100	0	17.8	47	64.7	7.65
exp34	50	1	12.5	47	129.4	11.59
exp35	100	1	17.8	47	0	9.09
exp36	100	1	7.2	47	0	10.44

exp37	100	2	12.5	47	129.4	7.31
exp38	50	1	7.2	47	64.7	14.63
exp39	100	2	12.5	47	0	9.84
exp40	100	2	12.5	94	64.7	8.13
exp41	100	1	12.5	47	64.7	10.28
exp42	100	1	12.5	94	129.4	7.395
exp43	50	1	12.5	94	64.7	10.79
exp44	100	1	7.2	47	129.4	8.66
exp45	100	1	17.8	94	64.7	6.81
exp46	100	1	12.5	47	64.7	8.82
exp47	50	0	17.8	94	129.4	13.00
exp48	50	0	17.8	94	129.4	17.91
exp49	50	0	17.8	94	129.4	19.07
exp50	50	2	17.8	94	129.4	11.31
exp51	100	0	17.8	94	129.4	8.61
exp52	50	1	17.8	94	129.4	15.63
exp53	150	2	17.8	94	129.4	5.37
exp54	100	0	12.5	94	129.4	9.21
exp55	50	2	12.5	94	129.4	15.03
exp56	150	1	12.5	94	129.4	6.22
exp57	50	0	7.2	94	129.4	18.37
exp58	150	2	7.2	94	129.4	5.19
exp59	150	0	7.2	94	129.4	11.91
exp60	100	1	7.2	94	129.4	7.4
exp61	50	0	17.8	94	129.4	17.81
exp62	100	2	12.5	94	129.4	8.25
exp63	50	0	17.8	0	121.49	20.14

APPENDIX C.

Correlation of the jet velocities with the jet injection pressure and the injection pipe diameter.

C.1. Experimental data

ΔP (bar) (d = 7 mm)	V (m/s) (d = 7 mm)	ΔP (bar) (d = 10 mm)	V (m/s) (d = 10 mm)	ΔP (bar) (d = 15 mm)	V (m/s) (d = 15 mm)
0	2,08	0	2,14	0	2,38
0.25	5,58	0.25	5,38	0.25	4,82
0.35	6,2	0.4	6,01	0.45	5,91
0.5	8,03	0.5	7,25	0.5	6,4
0.75	10,16	0.7	7,94	0.75	7,54
1	12,1	0.75	8,34	1	7,9
1.25	13	1	9,6	1.25	8,1
1.5	14,79	1.25	9,8	1.5	9,46
1.75	16,47	1.3	9,9	1.75	8,5
2	16	1.50	10,99	2	9
		1.75	10,8		
		2	13		

C.2. Non-linear fitting

As shown in Figure C.1 for each jet diameter, the experimental jet velocity data is well fitted by a law of the type $V = \alpha(\Delta P + \beta)^{\chi}$, with V in m s^{-1} and ΔP in bars.
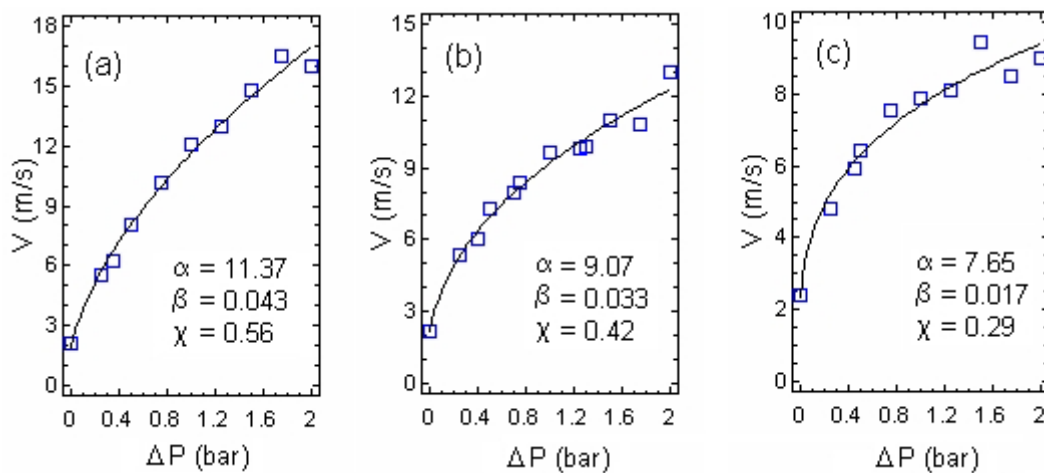

Figure C.1. Non-linear fitting of the jet velocity experimental data for the three jet diameters fitted by a law of the type $V = \alpha(\Delta P + \beta)^{\chi}$: (a) d = 7.2 mm; (b) d = 10 mm; (c) d = 15 mm.

APPENDIX D.

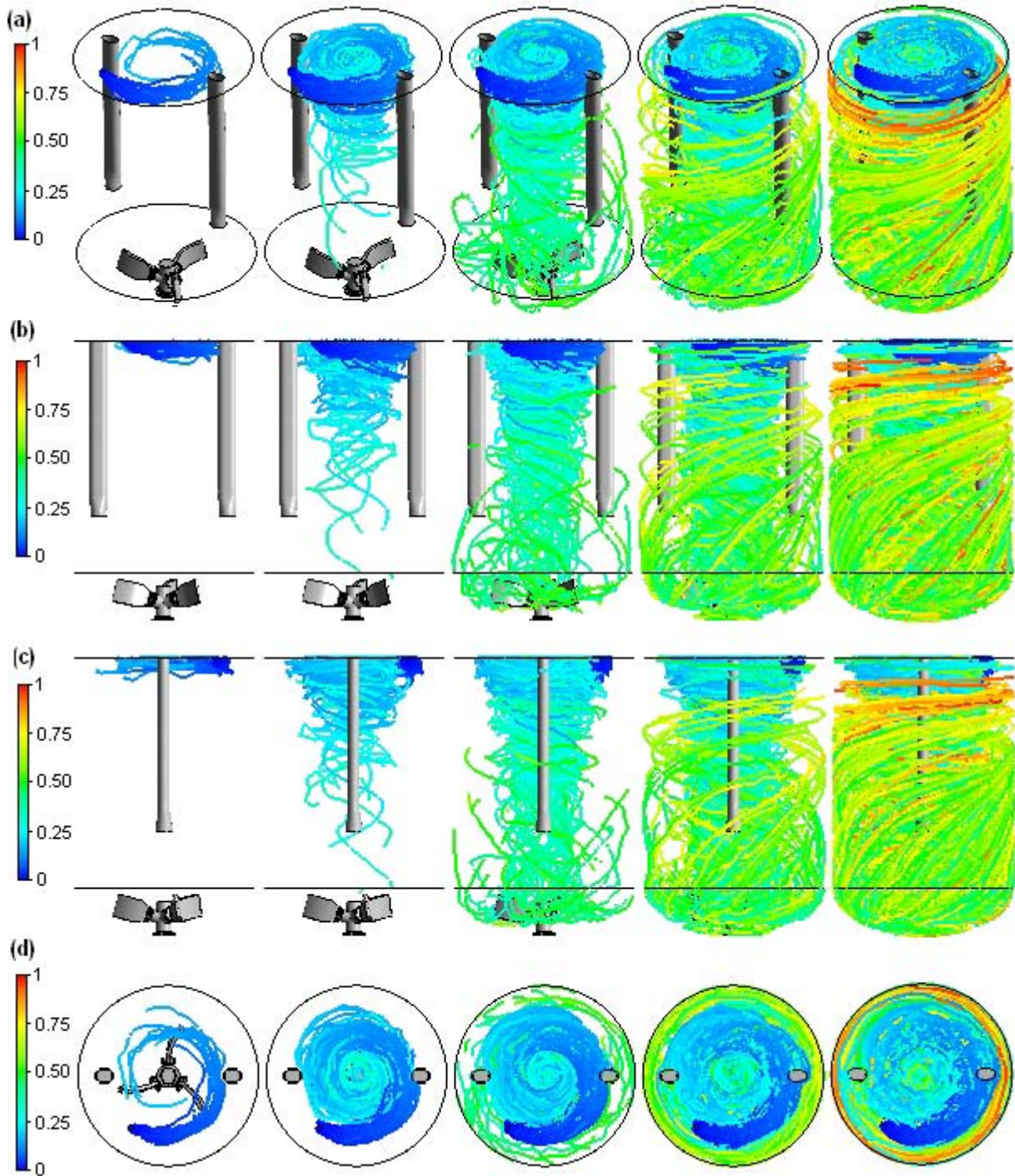## Jet injection profiles for the industrial Mazingarbe reactor at nominal agitator speed.

Figure D.1. Lagrangian jet trajectories coloured by the Lagrangian particle travel time normalized by T_{inj}, for d = 0.1 m, V = $20V_o$ = 1.55 m s^{-1} and Re = 5×10^6, plotted at $0.2T_{inj}$, $0.4T_{inj}$, $0.6T_{inj}$, $0.8T_{inj}$ and T_{inj}. (a) 3D view; (b) XY lateral view; (c) YZ lateral view; (d) top view.
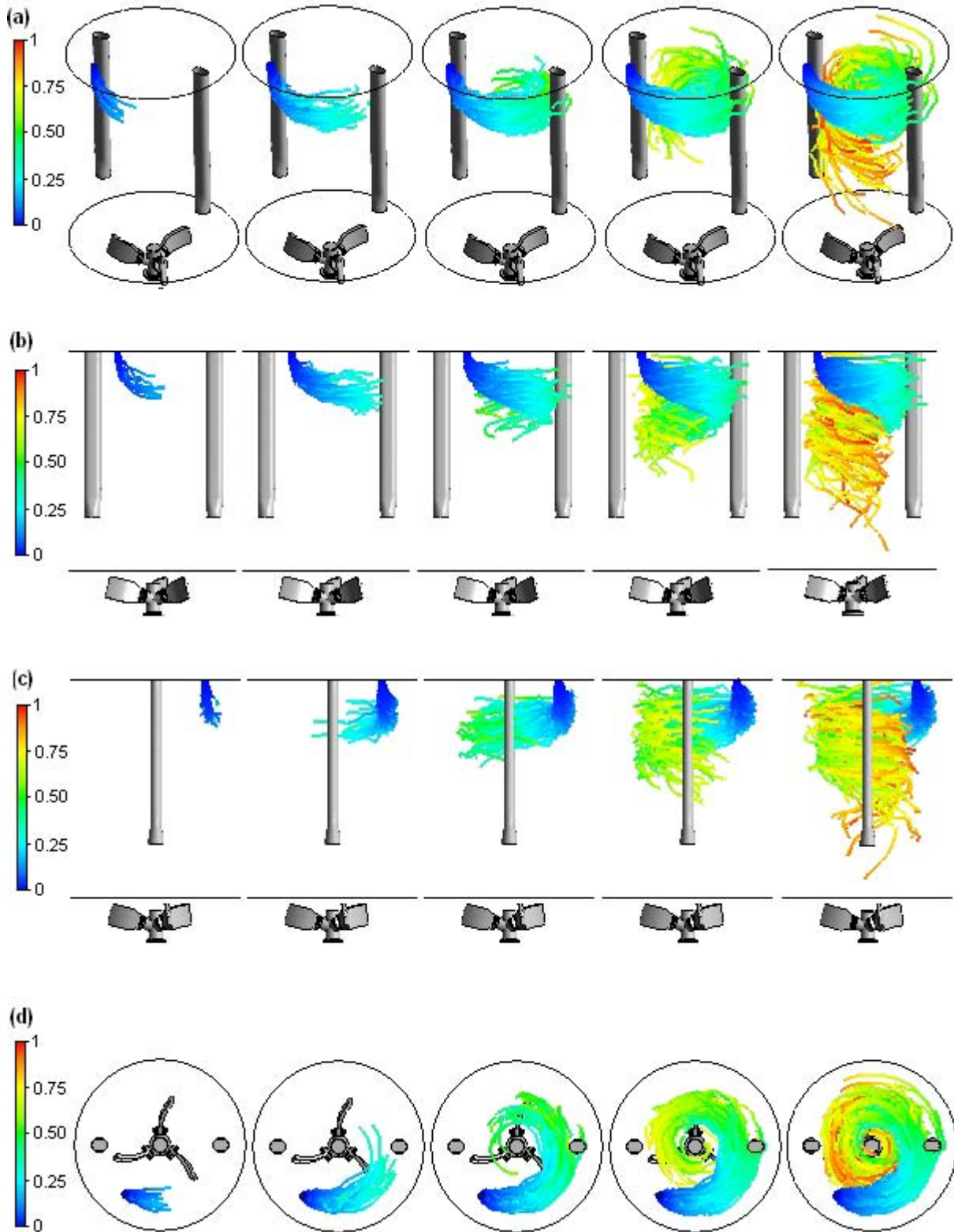
Figure D.2. Lagrangian jet trajectories coloured by the Lagrangian particle travel time normalized by T_{inj}, for $d = 0.1$ m, $V = 20V_o = 7.75$ m s^{-1} and Re $= 5\times10^6$, plotted at $0.2T_{inj}$, $0.4T_{inj}$, $0.6T_{inj}$, $0.8T_{inj}$ and T_{inj}. (a) 3D view; (b) XY lateral view; (c) YZ lateral view; (d) top view.
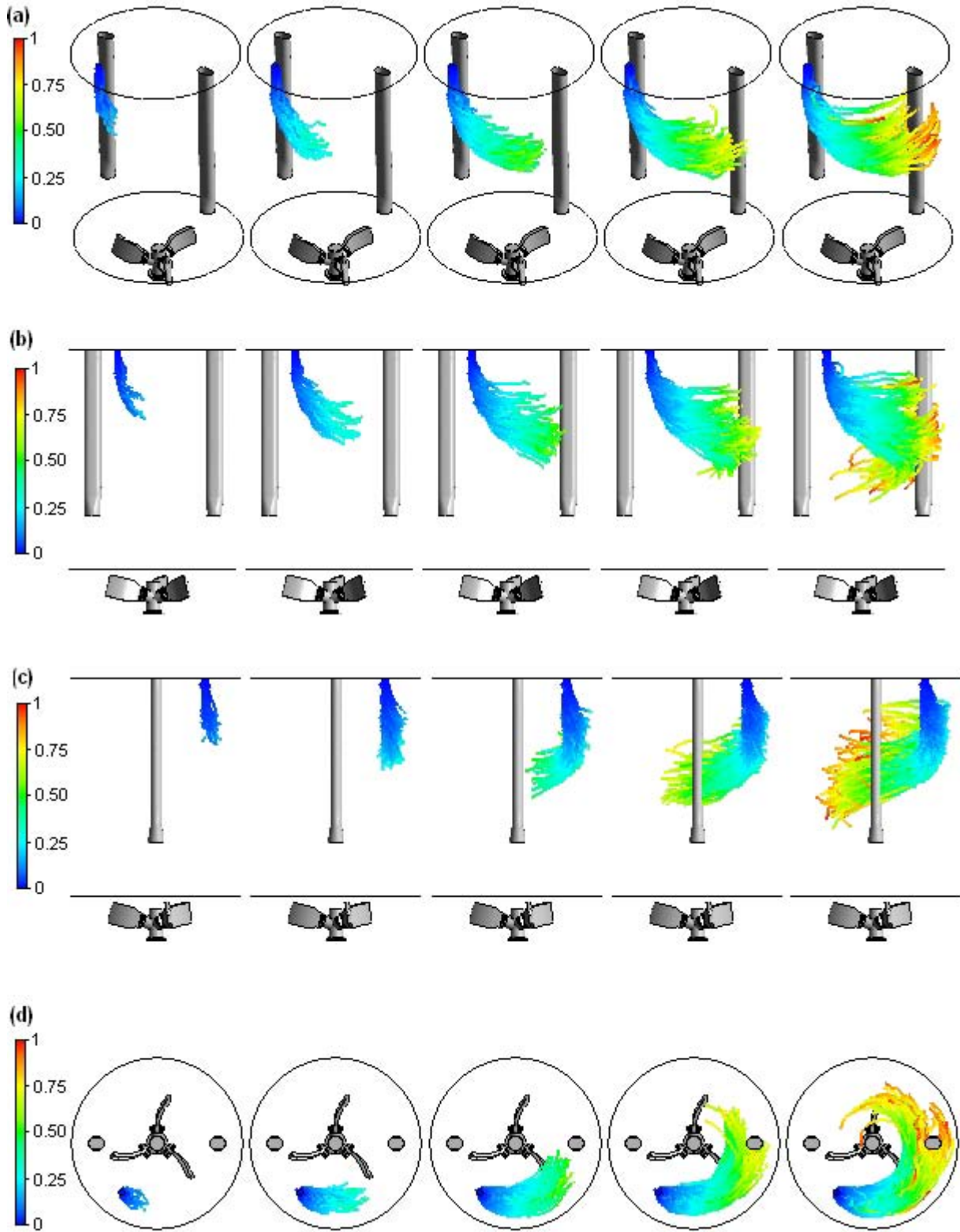
Figure D.3. Lagrangian jet trajectories coloured by the Lagrangian particle travel time normalized by T_{inj}, for d = 0.1 m, V = $20V_o$ = 15.5 m s^{-1} and Re = 5×10^6, plotted at $0.2T_{inj}$, $0.4T_{inj}$, $0.6T_{inj}$, $0.8T_{inj}$ and T_{inj}. (a) 3D view; (b) XY lateral view; (c) YZ lateral view; (d) top view.

Figure D.4. Lagrangian jet trajectories coloured by the Lagrangian particle travel time normalized by T_{inj}, for d = 0.1 m, V = $20V_o$ = 31 m s^{-1} and Re = 5×10^6, plotted at $0.2T_{inj}$, $0.4T_{inj}$, $0.6T_{inj}$, $0.8T_{inj}$ and T_{inj}. (a) 3D view; (b) XY lateral view; (c) YZ lateral view; (d) top view.
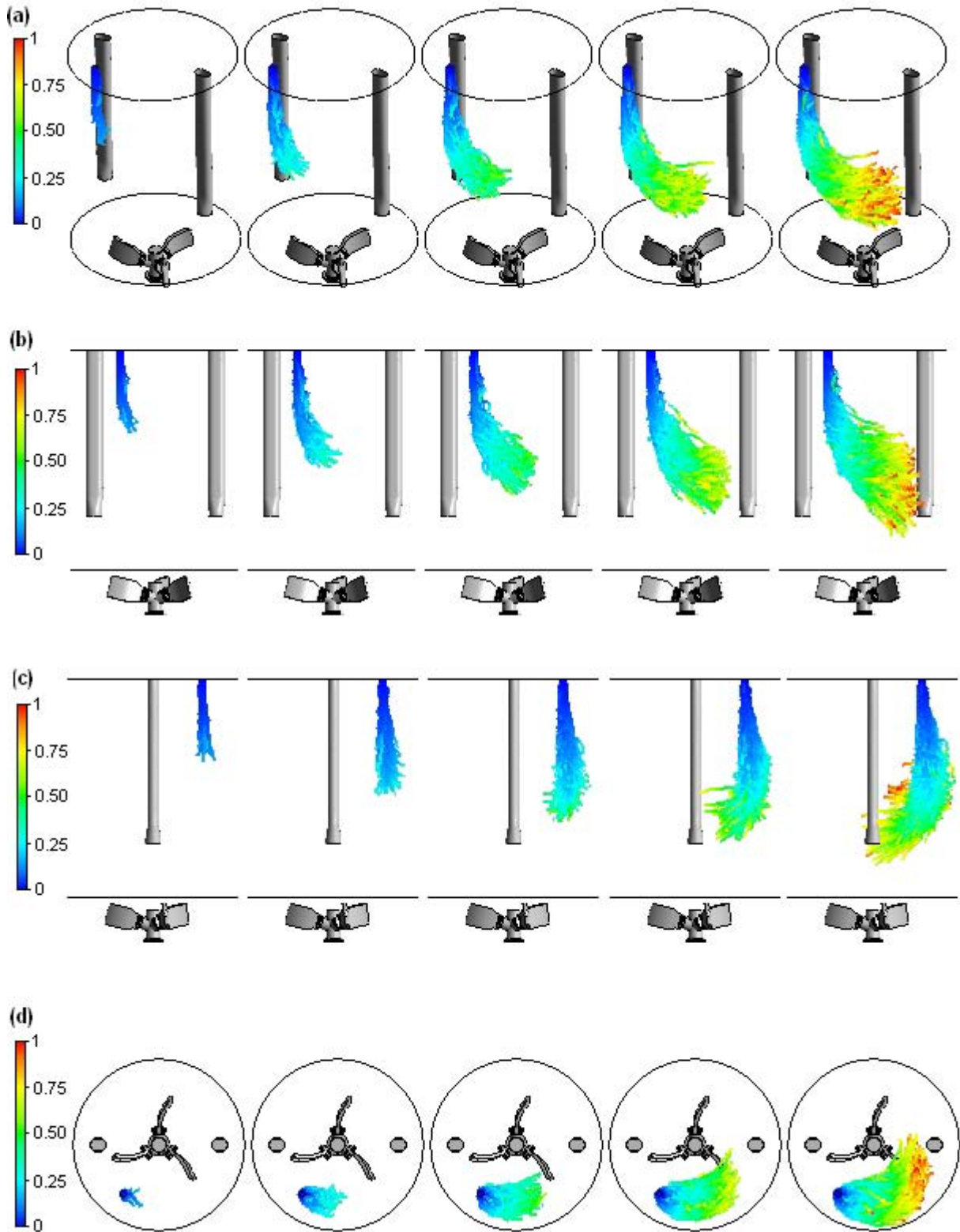
APPENDIX E.

Free-surface construction procedure.

The methodology for generating the free-surface profile was developed by Peter Higgins of LEAP Australia.

The process required a number of different steps as given below:

1. The iso-surface determining the location of the free-surface was plotted in CFX Post and the locations of the point on this surface were exported to a text file. The total number of points used to describe the free-surface was equal to 15,550 in the case presented here. Only the free-surface (obtained with the inhomogeneous approach) having $Y > 500$ mm from the bottom of the vessel was considered to avoid the gas column which links the top region of the vessel to the bottom dish.

2. The point cloud data were imported into the CAD package. The final set of points kept was a subset of those imported, with errant points (outliers) removed and a more uniform distribution of points was saved. By orienting the model to give a view from the top, an elliptical selection tool was used to acquire and delete all of the points around the baffles. Then the remaining filtered point set was used to create a triangular facet mesh which resulted in a contiguous facet representation of the surface made by joining the points. Finally, the two elliptical holes where the baffles are located were filled using a curvature-continuous facet patch.

3. The STL file (geometry file) resulting from the above procedure was used in the Reverse Engineering Extension of ProEngineer (Pro/E) to create a series of curves which attach automatically to the facet model. A "spider's web" was created where these lines cross. A copy of the curve where the lines met the vessel wall was created and offset outwards, by eye, to assist in the creation of an extended surface later.

4. The resulting "cobweb" of curves was written out as an IGES file and then read back into a new Pro/E part file. The Interactive Surface Design Extension for Pro/E was used to trace over the "cobweb" scaffold to create high quality, curvature-continuous B-spline curves. The position of the points on the curves and the tangency vectors at the curve ends could be controlled. From these curves surface patches were generated that inherit their "curvature-continuity across the boundary" attributes from the parent curves.

5. The result was a very smooth quilt which was again written out in a neutral format. The vessel component was opened in Pro/E and the new quilt was read in, and the co-ordinate system was manipulated to put the surface in the correct place. The quilt was then used in a Boolean operation to remove the upper part of the vessel.

The entire process was undertaken with Pro/E and the REX and ISDX add-ins.